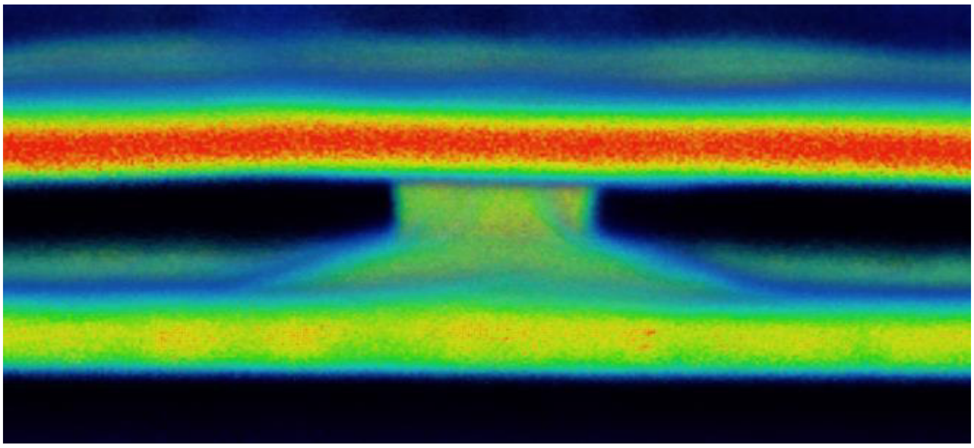

Spin-transfer-torque nano-oscillators: fabrication, characterization, and dynamics

José Diogo Teixeira Barbosa Costa
Física
Departamento de Física e Astronomia
2017

Orientador
João Ventura, Investigador Principal, Faculdade de Ciências da Universidade do Porto

Coorientador
Ricardo Ferreira, Investigador Principal, International Iberian Nanotechnology Laboratory

José Diogo Teixeira Barbosa Costa: *Spin-transfer-torque nano-oscillators: fabrication, characterization and dynamics,* , © November 2016

“(...) and Thales, according to what is related of him, seems to have regarded the soul as something endowed with the power of motion, if indeed he said that the loadstone has a soul because it moves iron.”

Aristotle on Thales of Miletus,
about the first recorded description of magnetism.

ABSTRACT

Spin transfer torque nano-oscilators (STNOs) are spintronic devices that explore the spin transfer torque (STT) mechanism to operate. More precisely, the STT effect enables the magnetization control through polarized electrical currents. Hence, STNOs take profit of the current-induced persistant magnetic dynamics to obtain novel radiofrequency (RF) sources designed for microelectronic applications, such as chip-to-chip or wireless communications and phase-array transceivers. Despite the notorious advantages of STNOs, such as broadband output, frequency tunable by current and/or magnetic fields, possibility of integration with CMOS, and small device footprint, some requirements still have to be fulfilled. Namely, the need for large output powers (above 1 μW) and narrow linewidths (below 1 MHz), so that this technology can be pushed into the market.

Magnetic tunnel junction (MTJ)-based STNOs constituted the bedrock of this thesis, from their fabrication to physical studies. In fact, one of the milestones consisted in the development of the nanofabrication process necessary to achieve high-quality STNOs. State-of-the-art MTJs with resistance × area products (RA) below 1 Ωμm^2 and tunnel magnetoresistance ratios (TMR) above 100% with diameters down to 50 nm were achieved. Such nanofabrication process incorporates a novel ion beam planarization (IBP) step to confer electrical and physical stability to the MTJ nanopillars.

Moreover, the effect of the MgO barrier thickness on the performance of STNOs was also unveilled. In particular, it was found that there is an intermediate MgO thickness (RA between 7.5 and 12.5 Ωμm^2) that maximizes the output power up to 200 nW without affecting the signal linewidth. Such methodology is cumulative with other improvements of the STNOs (such as magnetic vortices, incorporation of perpendicular magnetic anisotropy or oscillator synchronization).

The MTJ fabrication process was also adapted to different geometries of STNOs. More precisely, nanopillar structures with nano-constrictions for current confinement, STNOs with magnetic vortex configurations and MTJs with homogeneous in-plane magnetization incorporating a perpendicular polarizer, were successfully implemented.

Finally, fundamental physical studies using THz spectroscopy on magnetoresistive materials, were performed. A strong correlation between the THz transmission and the resistance of materials used in spintronic applications was demonstrated. These results pave a way to THz probing of the magnetoresistance and push spintronics to the THz regime.

RESUMO

Nano-osciladores por transferência de spin (NOTS) são dispositivos de spintrónica que exploram o mecanismo de transferência de spin-torque (TST) para operar. Mais concretamente, o efeito de TST possibilita o controlo da magnetização através de correntes elétricas polarizadas. Desta forma, os NOTS usam a dinâmica magnética pesistente induzida por corrente para obter novos geradores de sinais de radiofrequência (RF) concebidos para aplicações de microeletrónica, como comunicações chip-para-chip ou sem fios e transceptores de fase. Apesar das notórias vantagens dos NOTS, como sinal de banda larga, frequência sintonizável por corrente e/ou campos magnéticos, possibilidade de integração com CMOS e pequena pegada de dispositivo, alguns requisitos ainda têm que ser cumpridos. Nomeadamente, a necessidade de elevada potência de saída (acima de 1 μW) e larguras de banda estreitas (abaixo de 1 MHz), para que esta tecnologia possa ser introduzida no mercado.

NOTS baseados em junções de efeito de túnel (JET) constituem o alicerce desta tese, desde o seu fabrico até aos seus estudos físicos. De facto, um dos marcos desta tese consistiu no desenvolvimento do processo de nanofabricação necessário para atingir NOTS de elevada qualidade. Conseguiu-se obter JETs do estado-da-arte com produtos de resistência × área (RA) abaixo de 1 $\Omega\mu m^2$ e magnetorresistência de túnel (MRT) acima dos 100 % com dimensões até os 50 nm. Este processo de nanofabricação incorpora um novo passo de planarização por feixe de iões (PFI) para conferir estabilidade elétrica e física para os nanopilares de JET.

Além disso, o efeito da espessura da barreira de MgO na performance dos NOTS foi também desvendada. Em particular, foi descoberto que existe um valor intermédio de espessura da barreira de MgO (RA entre 7.5 e 12.5 $\Omega\mu m^2$) que maximiza o sinal de saída até 200 nW sem afetar a largura de banda do sinal. Tal metodologia é cumulativa com outros aperfeiçoamentos dos NOTS (como vórtices magnéticos, incorporação de anisotropia magnética perpendicular ou sincronização de osciladores).

O processo de fabricação de JETs foi também adaptado a diferentes geometrias de NOTS. Mais precisamente, estruturas de nanopilares com nanoconstrições para confinamento de corrente, NOTS com configurações de vortices magnéticos e JETs com magnetização homogénea no plano incorporando um polarizador perpendicular, foram implementadas com sucesso.

Finalmente, estudos físicos fundamentais, usando espectroscopia de THz em materiais magnetorresistivos, foram efetuados. Uma forte correlação entre a transmissão de THz e a resistência de materiais usados em aplicações de spintrónica foi demonstrada. Estes resultados abrem caminho para sondas de THz para magnetorresistência, encaminhando a spintrónica para o regime dos THz.

PUBLICATIONS

[1] A path for high power, low critical current density spin-transfer nano-oscillators: the impact of MgO thickness, J. D.Costa, S. Serrano-Guisan, B. Lacoste, A. S. Jenkins, T. Böhnert, M. Tarequzzaman, E. Paz, J. Borme, J. Ventura, R. Ferreira, P. P. Freitas, submitted to Nano Letters.

[2] High yield, full magnetoresistance nanofabrication process of magnetic tunnel junctions over 200 mm wafers, J. D. Costa, J. Borme, M. Tarequzzaman, E. Paz, F. L. Deepak, J. Ventura, R. Ferreira, P. P. Freitas, under preparation.

[3] Enhancing the injection locking range of spin torque oscillators through mutual coupling, M. Romera, P. Talatchian, R. Lebrun, K. J. Merazzo, P. Bortolotti, L. Vila, J. D. Costa, R. Ferreira, P. P. Freitas, M.-C. Cyrille, U. Ebels, V. Cros, J. Grollier, Appl. Phys. Lett. 109 (2016) 252404.

[4] Femtosecond control of electric currents in metallic ferromagnetic heterostructures, T. J. Huisman, R. V. Mikhaylovskiy, J. D. Costa, F. Freimuth, E. Paz, J. Ventura, P. P. Freitas, S. Blügel, Y. Mokrousov, Th. Rasing, and A. V. Kimel, Nat. Nanotech., 11 (2016) 455-459.

[5] Electrocatalytic performance and stability of nanostructured Fe–Ni pyrite-type diphosphide catalyst supported on carbon paper, J. D. Costa, J. L. Lado, E. Carbó-Argibay, E. Paz, J. Gallo, M. F. Cerqueira, C. Rodríguez-Abreu, K. Kovnir, and Y. V. Kolen'ko, J. Phys. Chem. C, 120, 16537-16544 (2016).

[6] Terahertz dynamics of spins and charges in CoFe/Al2O3 multilayers, J. D. Costa, T. J. Huisman, R. V. Mikhaylovskiy, I. Razdolski, J. Ventura, J. M. Teixeira, D. S. Schmool, G. N. Kakazei, S. Cardoso, P. P. Freitas, Th. Rasing, and A. V. Kimel, Phys. Rev. B, 91, 104407 (2015).

[7] Impact of MgO thickness on the performance of spin transfer torque nano-oscillators, The cyclic nature of porosity in anodic TiO2 nanotube, J. D. Costa, S. Serrano-Guisan, J. Borme, F. L. Deepak, M. Tarequzzaman, E. Paz, J.Ventura, R. Ferreira and P.P. Freitas, IEEE Trans. Magn., 51, 11 (2015).

[8] Observation of spin-dependent quantum well resonant tunneling in textured CoFeB layers, J.M. Teixeira, J.D. Costa, J. Ventura, J.B. Sousa, P. Wisniowski, and P.P. Freitas, Appl. Phys. Lett., 104, 112414 (2014).

[9] Giant intrinsic thermomagnetic effects in thin MgO magnetic tunnel junctions, J. M. Teixeira, J. D. Costa, J. Ventura, M. P. Fernandez-Garcia, J. Azevedo, J. P. Araujo, J. B. Sousa, P. Wisniowski, S. Cardoso, and P. P. Freitas, Appl. Phys. Lett., 102, 212413 (2013).

[10] The influence of annealing on the bimodal distribution of blocking temperatures of exchange biased bilayers, J. Ventura, J.M. Teixeira, E. Paz, J.S. Amaral, J. D. Costa, A. Apolinario, J. P. Araujo, S. Cardoso, R. Ferreira, and P. P. Freitas, Phys. Stat. Solidi RRL, 1-5 (2013).

ACKNOWLEDGMENTS

First and foremost I would like to thank my supervisors Dr. João Ventura, Dr. Ricardo Ferreira and Prof. Dr. Paulo Freitas for their guidance throughout my PhD. With their complementary knowledge they advised and supported me during my research work, and for that I am grateful.

I am specially grateful to my colleagues from the spintronics group Elvira Paz, Tareq Zaman, Santiago Serrano, Bertrand Lacoste, Tim Boehnert and Alex Jenkins. They witnessed my learning curve, in particular, an exponential increase (linear perhaps) of my patience level during these years. Also, to José Teixeira who helped me to launch my PhD during its early stage.

I would also like to thank Jérôme Borme, Margaret Costa, Mariam Debs, Hélder Fonseca, Leonard Francis, Hefu Han, Enping Tu, Lianwei Wang, Luana Benetti, and Roberta Dutra. Their help made my work so much easier.

Thanks to Noel Garcia and José Lado for interrupting my work so often for fruitful coffee breaks.

I am also grateful to the Nijmegen group that received me for four months. A special thanks to Dr. Alexey Kimel, Thomas Huisman and Rostislav Mikhaylovskiy that made this time so fruitful. Also, to Ilya Razdolski, Tonnie Toonen and Prof. Theo Rasing for all their help and support. Finally, to Dima Afanasiev for the free Russian lessons.

My gratitude goes also to Prof. Yuriy Pogorelov with whom I learned so much.

Thanks to Fundação para a Ciência e Tecnologia for their funding of my doctoral years (SFRH/BD/79393/2011).

I am deeply thankful to Noelia Guldris, who is always by my side, during the good moments and the most difficult steps.

To my friends Pedro Lebre, Olga Sousa, Sara Bastos, Lúcia Vaz, João Rodrigues, Paulo Barbosa, Rita Silva, Rita Moreira, José Camarinha and Ana Magalhães (+ Benedita). Moreover, this thesis is somehow dedicated to Miguel Galvão since, as an irresponsible teenager, I promised him that I would dedicate him my first book.

The path that we take and, ultimately, who we are, depend on who helped us take our first steps. Hence, I would like to thank my grandparents Teixeira and Cesário. Also, my godmother Anitas, that recently passed, who had a vision of the world a lot different than mine.

Thanks to my brother and friend Daniel.

Finally, to my parents, Aida and Cesário, who supported me throughout all the stages of my life. This achievement, or any other in my life, is as mine as it is yours...

CONTENTS

LIST OF FIGURES

LIST OF TABLES

ACRONYMS

MR - magnetoresistance
STT - spin transfer torque
STNO - spin transfer nano oscillator
AMR - anisotropic magnetoresistance
AP - antiparallel
P - parallel
GMR - giant magnetoresistance
FM - ferromagnetic
NM - non-magnetic
DOS - density of states
CPP - current perpendicular to the plane
MTJ - magnetic tunnel junctions
TMR - tunnel magnetoresistance ratio
RT - room temperature
SPT - spin-polarized tunneling
RKKY - Ruderman-Kittel-Kasuya-Yosida
PMA - perpendicular magnetic anisotropy
OOP - out-of-plane
IP - in-plane
AFM - antiferromagnetic
IEC - interlayer exchange coupling
LLGS - Landau-Lifshitz-Gilbert-Slonczewski
MRAM - magnetic random access memory
VCO - voltage-controlled oscillator
CMOS - complementary metal oxide semiconductor
PVD - physical vapor deposition
MTM - multi target mode
FTM - flexible target module
SIMS - secondary ion mass spectrometer
PR - photoresist
DWL - Direct Write Lithography
SEM - Scanning electron microscopy

EDS - energy dispersive spectroscopy
TEM - transmission electron microscopy
FIB - Focused ion beam
XRD - X-ray diffraction
MRD - materials research diffractometer
VSM - vibrating sample magnetometer
CIPT - current in-plane tester
BW - bandwidth
CMP - chemical-mechanical polishing
IBP - ion beam planarization
HE - high energy
LE - low energy
BC - bottom contact
CL - capping layer
SAF - synthetic antiferromagnet
PSD - power spectral density
TDS - time domain spectroscopy
DMIM - discontinuous metal-insulator multilayer
MOKE - magneto-optical Kerr effect
PEM - photoelastic modulator

1

INTRODUCTION

The term spintronics refers commonly to phenomena in which it is the spin and not the charge of electrons that plays the major role in electronic components. More precisely, the phenomenon known as magnetoresistance (MR), which consists in the dependence of the electrical resistance on the magnetic state of a material or device, is the key element that enabled most of the stunning progress observed in this research field during the last decades. In this chapter we outline the technological progress triggered by the field of spintronics along with their physical explanation, culminating in novel spin transfer torque (STT)-based technologies such as the spin transfer nano oscillators (STNOs).

1.1 ANISOTROPIC MAGNETORESISTANCE (AMR)

Although the above definition of MR is quite general, the nature and physical mechanisms which result in the MR effect are broad. The first observation of magnetoresistive effects occurred in 1857 when Lord Kelvin discovered the anisotropic magnetoresistance (AMR). This effect is observed in 3d transition metals and their alloys. It consists in a change of the electrical resistance with the orientation of the magnetization with respect to the direction of the electrical current flowing in the material. The origin of AMR is related with the simultaneous action of the d-band splitting and the spin-orbit effect [1, 2, 3]. For most materials, the electrical resistance depicts a $cos^2(\theta)$ dependence, where θ is the angle between the current and the magnetization, given by:

$$\rho(\theta) = \rho_\perp + (\rho_\parallel - \rho_\perp)cos^2(\theta), \tag{1.1}$$

where $\rho_\perp$ and $\rho_\parallel$ are the resistivities for $\theta = 90^o$ and $\theta = 0^o$, respectively. In bulk materials AMR ratios can go up to 6% while in thin films they are limited to around 3%. Despite its early discovery, it was only more than one century later that the AMR effect found its greatest use in hard disk drive read heads for data retrieving. The large need for such application at the time, due to the growing demand for storage capacity, fueled the research in magnetoresistive effects [4].

1.2 GIANT MAGNETORESISTANCE (GMR)

As the storage density in hard disk drives (HDDs) escalated, the demand for a larger magnetoresistive effect ignited extended research worldwide. In 1988, Albert Fert [5] and Peter Grünberg [6] independently observed that the antiparallel (AP) magnetic configuration of Fe/Cr/Fe multilayers depicted a higher resistance that the parallel (P) one. For the discovery of this phenomenon, denominated as giant magnetoresistance (GMR), they were both awarded with the Nobel Prize in Physics in 2007. GMR ratios up to 20% could be achieved in ferromagnetic (FM) layers separated by a non-magnetic (NM) metal (FM1/NM/FM2; spin valves). This higher MR ratio quickly launched the spin valve use in read heads and magnetic sensor applications.

To understand the physical nature of the GMR effect, let us consider the simplest trilayer case (spin valve). A small thickness of the NM spacer (d) is required so that electrons traveling through this layer undergo negligible spin-flip processes (spontaneous flip of the electron). If we consider the case where electron transport occurs in the direction orthogonal to the FM1/NM/FM2 interface, the electron current traveling through the spin valve can be divided into two independent channels of spin up and down electrons (relatively to the axis parallel to the magnetization of the FM layers). The magnetization orientation of the FM layers leads to different densities of states (DOS) and thus to differently populated spin channels. More precisely, the majority (minority) spin channel is constituted by electrons whose spins have the same (opposite) direction of the magnetization of the FM. Since these majority and minority channels are differently populated, they also depict different scattering rates and thus different channel resistances ($R_\uparrow$ and $R_\downarrow$, respectively). Therefore, the GMR effect is caused by a spin-dependent scattering cross section, *i.e.* electrons with spin opposite to the magnetization of the FM layer they travel in are usually more easily scattered than electrons with spins in the same direction as the magnetization of the FM layer. Therefore, when the magnetization of both layers has the same direction (P orientation) the majority channel experiences a weak scattering (resistance of $2R_\uparrow$) while the minority channel is highly scattered [resistance of $2R_\downarrow$; Fig. 1.1(a)], leading to an equivalent resistance of:

$$R_P = \frac{2R_\uparrow R_\downarrow}{R_\uparrow + R_\downarrow}. \tag{1.2}$$

When the magnetizations of the FM layers have opposite orientations (AP orientation) both conduction channels are strongly scattered [Fig. 1.1(b)] each having a resistance of $R_\uparrow + R_\downarrow$, so that the total equivalent resistance is:

$$R_{AP} = \frac{R_\uparrow + R_\downarrow}{2}. \tag{1.3}$$

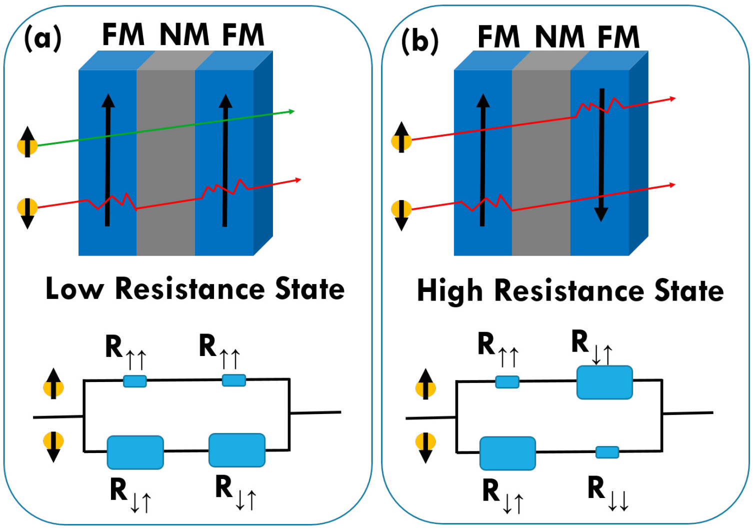

Figure 1.1: Schematic representation of the spin dependent scattering for the (a) P and (b) AP states in a spin valve. The spin↑ and ↓ have different scattering rates that give rise to different electric resistances.

Hence, spin dependent scattering leads to a magnetic control of the resistance state in spin valves being the resistance in the AP state (R_{AP}) usually higher than the resistance in the P state (R_P). The magnitude of this variation is given in percentage by the magnetoresistive ratio:

$$MR = \frac{R_{AP} - R_P}{R_P}(\%). \tag{1.4}$$

Only two configurations (P and AP) were considered here, but in fact the magnetoresistance can be computed for arbitrary magnetic orientations between FM layers [7]. A considerable advantage of spin valves relies on their simple fabrication process due to the metallic nature of all the layers. However, the GMR ratio is limited to around 20% and they have a low resistance (mΩ to Ω), making them difficult to integrate into complementary metal oxide semiconductor (CMOS) technology.

1.3 TUNNEL MAGNETORESISTANCE (TMR)

So far, we have only considered fully metallic structures. Nevertheless, magnetoresistive effects had been previously observed in magnetic tunnel junctions (MTJs) which are structures that consist in a thin insulating barrier sandwiched between two FM layers (FM1/I/FM2). In fact, prior to the discovery of the GMR effect, Jullière reported in 1975 tunnel magnetoresis-

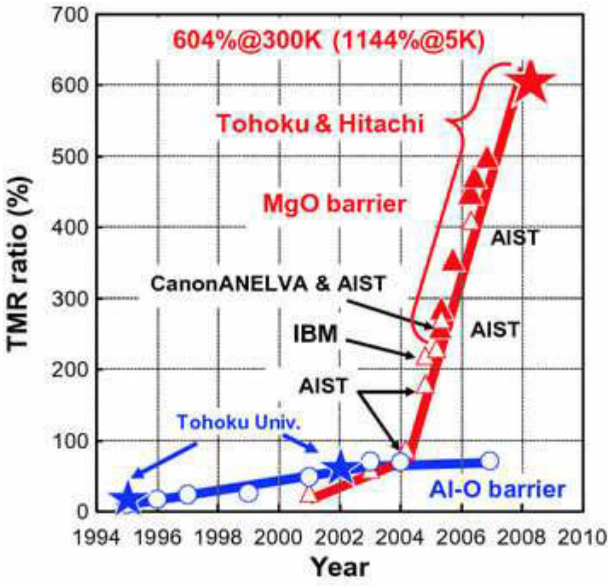

Figure 1.2: Development of the TMR ratio at RT for Al-O and MgO-based MTJs [12].

tance (TMR) in Fe/Ge-O/Fe MTJs [8]. The insulating barrier of an MTJ has to be very thin (of the order of the nm or below) to enable the transport of electrons through the insulating layer through tunneling. Similarly to the case of spin valves, the magnetization of a FM layer can be pinned while the other rotates freely upon the application of an external applied magnetic field, allowing us to easily control the corresponding magnetic configuration (P or AP). Despite its early discovery, in this first experiment the TMR was limited to 14% at 4.2 K. The low temperatures necessary to observe the TMR greatly reduced the interest in this effect. With the discovery of the GMR, extensive experimental and theoretical efforts were performed to achieve sizable TMR at room temperature (RT). In 1995 Miyazaki et al. [9] and Modera et al. [10] used MTJs incorporating an insulating layer of aluminum oxide (Al-O) and 3d ferromagnetic electrodes, achieving TMR ratios as high as 18% at RT. The optimization of the FM electrodes and of the fabrication conditions of the Al-O barrier led to an increase of the TMR to about 70% [11].

In 2001, first principle calculations performed by Butler et al. [13] and Mathon and Umerski [14] pointed out the possibility of achieving TMR ratios as high as 1000% for MTJs with fully ordered (001)-oriented MgO barrier layers and Fe, Co and FeCo FM electrodes. This giant TMR originates from the fact that, in these epitaxial MTJs, the tunneling across the MgO is dominated by $\Delta 1$ Bloch states which are spin-polarized, enhancing the TMR ratio. These theoretical predictions were soon followed by their experimental verification [15, 16]. In Fig.

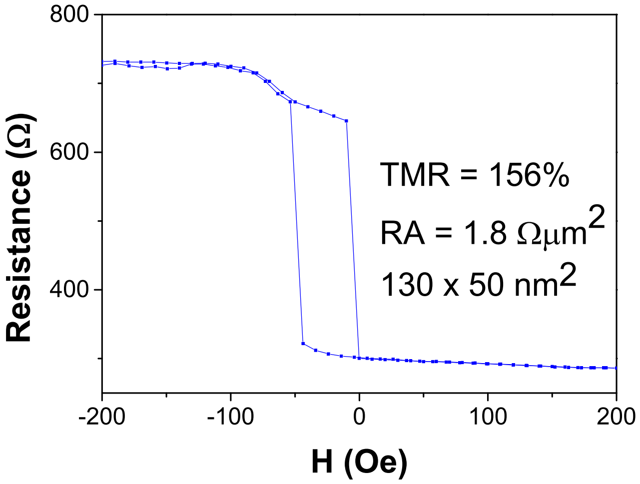

Figure 1.3: Transfer curve of an MTJ with a TMR of 156%, an *RA* of 1.8 $\Omega\mu\mathrm{m}^2$ and lateral dimensions of 130×50 nm^2.

1.2 we show the development of the TMR ratio for Al-O and MgO-based MTJs at RT. In 2004, Yuasa et al. reported TMR ratios of 88% at RT in fully epitaxial Fe/MgO-based MTJs prepared using molecular beam epitaxy [17]. This surpassed the highest value reported in Al-O-based MTJs of 70% [11]. Subsequent experiments demonstrated TMR ratios up to 600% at RT and 1144% at 5 K in CoFeB/MgO/CoFeB-based MTJs without an antiferromagnetic layer and for resistance × area (*RA*) product of the order of 10^4 $\Omega\mu\mathrm{m}^2$ [18]. In the lower *RA* region, which is the most relevant for applications, we were able to reach TMR ratios above 150% for an *RA* of 1.8 Ω $\mu\mathrm{m}^2$ (Fig. 1.3). The reason for this drastic TMR ratio increase when compared with AlO_x-based MTJs is related with the different physical mechanisms of the TMR effect in both cases.

1.3.1 *Jullière model*

The physical phenomenon responsible for the magnetoresistance observed in MTJs is spin-polarized tunneling (SPT) [19, 20, 21]. SPT consists in an imbalance of the electrical current (I) carried by up- (↑) and down-spin (↓) electrons that tunnel through an insulating barrier. The spin polarization (P) of the tunneling current is then given by:

$$P = \frac{I^{\uparrow} - I^{\downarrow}}{I^{\uparrow} + I^{\downarrow}}. \tag{1.5}$$

This phenomenon originates from the fact that the probability of electron tunneling through the barrier depends on the corresponding Fermi wave vector. In FM metals the electronic bands are exchange-split. The consequent different Fermi vectors of spin up and spin down electrons naturally results in a spin dependent tunneling probability. A model that explains the TMR effect based on SPT was proposed by Jullière [8]. This model is based in two assumptions. (1) Since the wave function of the electrons is the same in both electrodes, all the quantum numbers of the electrons are conserved in the tunneling process. Consequently, electrons are only able to tunnel between states of equal spin. This first assumption implies that the tunneling of up and down spin electrons takes place through two independent spin channels [22, 23, 24]. This means that electrons originating from one spin state of FM1 will only undergo tunneling to unfilled states of the same spin in FM2. (2) According to the Fermi's golden rule, the current for a particular spin orientation is proportional to the product of the effective DOS of the initial and final FM layers. Following these assumptions, one easily concludes that the tunneling probabilities between FM1 and FM2 are different for the P and AP configurations. For the P case, the minority spins tunnel to the minority states and the majority spins to the majority states [Fig. 1.4(a)]. However, in the AP case, the minority spins tunnel to the majority states and the majority spins to the minority states [Fig. 1.4(b)]. Therefore, using assumption (2), the tunneling current density through the insulating layer from FM1 to FM2 for the P (J_P) and AP (J_{AP}) configurations are given by:

$$J_P \propto D_1^{\uparrow} D_2^{\uparrow} + D_1^{\downarrow} D_2^{\downarrow}, \tag{1.6}$$

and

$$J_{AP} \propto D_1^{\uparrow} D_2^{\downarrow} + D_1^{\downarrow} D_2^{\uparrow}, \tag{1.7}$$

where D_i^s is the DOS at the Fermi level (the electrons at the Fermi level contribute to almost all of the tunneling conduction) of the FM$_i$ with spin s. From Eq. (1.6) and (1.7), it is clear that the P and AP states have different resistances. Therefore, using these equations, the spin polarization P_i can be written as:

$$P_i = \frac{D_i^{\uparrow} - D_i^{\downarrow}}{D_i^{\uparrow} + D_i^{\downarrow}}. \tag{1.8}$$

Hence, the TMR is given by:

$$TMR = \frac{R_{AP} - R_P}{R_P} = \frac{J_P - J_{AP}}{J_{AP}}, \tag{1.9}$$

allowing us to arrive at Jullière's formula:

$$TMR = \frac{2P_1P_2}{1 - P_1P_2}, \tag{1.10}$$

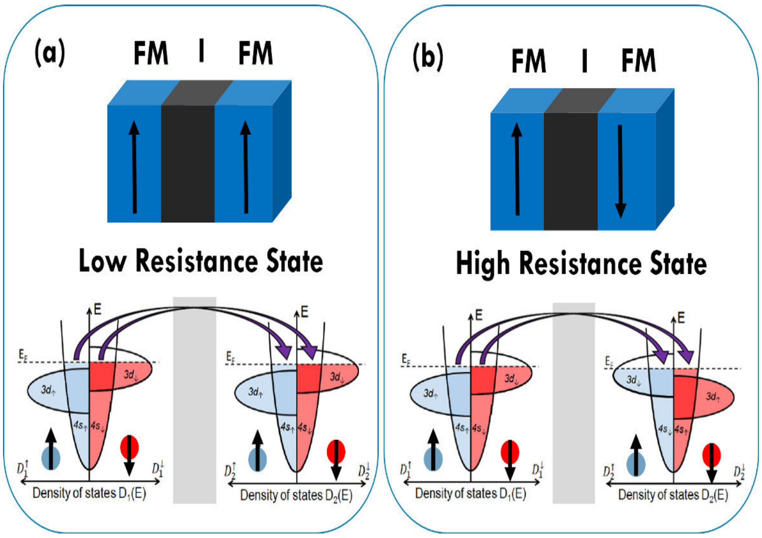

Figure 1.4: Schematic representation of the spin dependent tunneling for the (a) P and (b) AP states in an MTJ. In the P state the majority-majority and minority-minority transitions result in a high tunneling probability (low resistance). In the AP state the majority-minority and minority majority transitions result in smaller tunneling probability (high resistance).

where P_1 and P_2 are the spin polarizations of FM1 and FM2, respectively. Equation 1.10 has been widely used to infer the polarization of several FM using the measured TMR values. Despite the simplicity of the model and the fact that it only takes into account the polarization of the FM layers, and not the influence of the tunnel barrier, it describes well the tunneling transport across many usual tunnel barrier materials such as TaO_x [25], HfO_x [26], $LaSrMnO_3$ [27], ZrO [28], ZrAlO [28], AlN [29] and AlO_x.

It was later shown that the value of P depends not only on the FM electrodes but also on the nature of the insulating barrier [30, 31]. The interfacial bonding and the importance of the spin symmetry have a fundamental role in determining the hybridization between the Bloch states of the metal and the slowly decaying states in the insulating layer [13, 32, 33, 34, 35]. More precisely, different barriers depict different symmetry rules that select different wave functions for each spin direction. Insulating barriers that depict coherent tunneling, such as MgO, generate spin dependent tunneling that increases the TMR up to 600% at room temperature [18]. A deep understanding of the main difference between incoherent and coherent tunneling is thus required for us to understand the effect of the insulating barrier on the TMR.

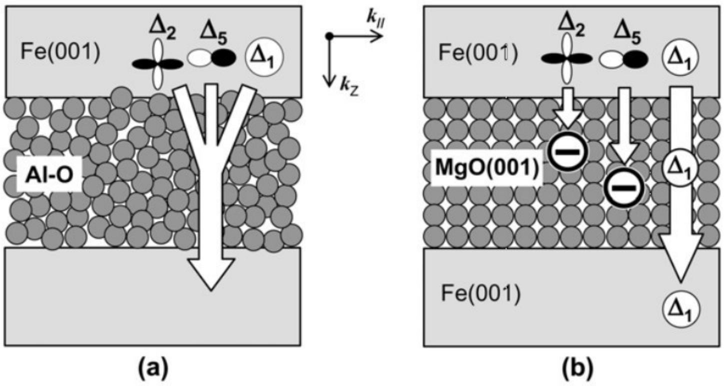

Figure 1.5: Schematic representation of the (a) incoherent tunneling through an amorphous Al-O barrier and (b) coherent tunneling through a crystalline MgO barrier [36].

1.3.2 *Incoherent Tunneling through amorphous barriers*

Electrons traveling through a crystal can depict several wave functions (Bloch states) with different symmetries. Let us first consider the case of an amorphous barrier. These electrons, having different Bloch states that arise from the FM layers of an MTJ, will tunnel through the insulating layer. However, due to the lack of crystallographic symmetry of the amorphous barrier, all the Bloch states have the same tunneling probability (incoherent tunneling) where neither the momentum nor the coherence of the Bloch states are conserved. Figure 1.5(a) illustrates the effect of incoherent tunneling for Fe (0 0 1)/AlO_x-based MTJs. Since all the states have the same tunneling probability, incoherent tunneling is well described by Jullière's model.

Nevertheless, for AlO_x barriers, there are important discrepancies between the experimentally measured values of TMR and the ones calculated using known polarization values and Jullière's model. In fact, tunneling through an AlO_x barrier is not completely incoherent as described by Jullière's model nor as coherent as the tunneling through crystalline MgO barriers.

1.3.3 *Coherent tunneling through crystalline barriers*

For an accurate description of tunnel barriers one needs to take into account the realistic electronic band structure both for the barrier and electrodes. In that respect, an MgO barrier has four electronic bands: $\Delta 1$, $\Delta 5$, $\Delta 2$ and $\Delta 2'$, which correspond to different symmetries of the Bloch states. Contrary to the case of the incoherent tunneling, in the coherent case the

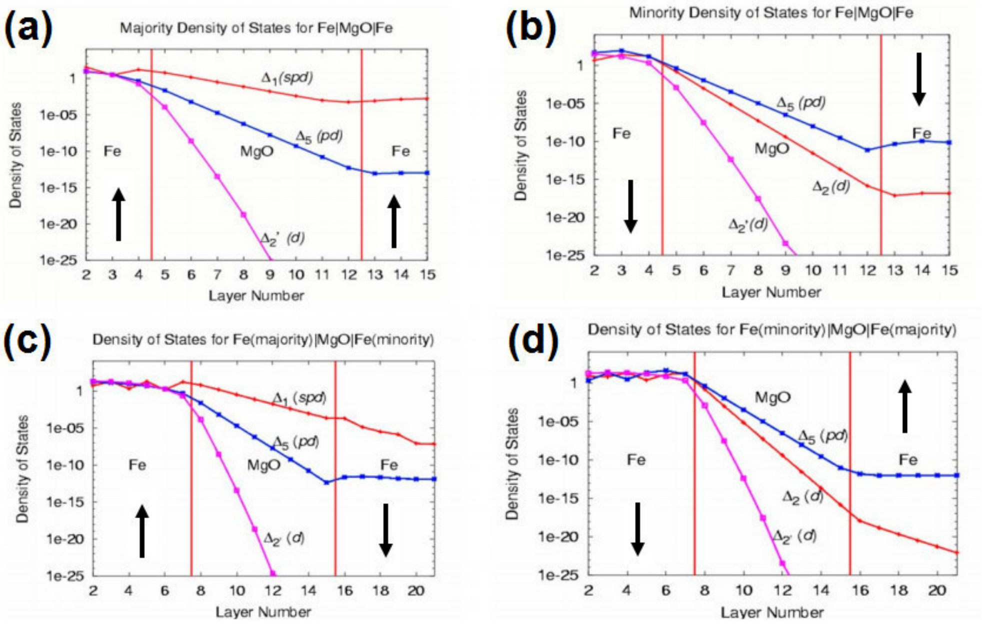

Figure 1.6: Tunneling DOS calculated across a Fe(100)\MgO(100)\Fe(100) trilayer for the four possible transitions. The top images (bottom) represent the P (AP) state for (a) majority-majority, (b) minority –minority, (c) majority-minority and (d) minority-majority transitions [37].

different bands have distinct decay rates within the barrier [Fig. 1.5(b)]. Figure 1.6 shows the calculated DOS available for electrons tunneling from the left to the right electrode in Fe/MgO/Fe MTJs [13, 37]. The P and AP states are considered for all the possible transitions [majority-majority (a) and minority-minority (b) in the P configuration and majority-minority (c) and minority-majority (d) in the AP configuration]. For the P configuration in the majority-majority transitions most of the tunnel current is performed by the Δ1 electrons [Fig. 1.6(a)]. As for the AP configuration, the Δ1 Bloch state is also dominant in the majority-minority transitions [Fig. 1.6(c)], while the Δ5 dominates in the minority-majority transitions [Fig. 1.6 (d)]. However, since the Δ1 band in the majority-minority transition is by far the one with more electronic states available in the second electrode, the transport in the AP configuration is also dominated by the Δ1 Bloch states.

The important feature of this symmetry selection consists in the fact that the Δ1 states are highly spin-polarized at the Fermi level, not only in bcc Fe (0 0 1), but also in many other bcc FM metals and alloys based on Fe and Co (e.g. bcc CoFe and some of the Heusler alloys). In Fig. 1.7 it is shown the band structure for Fe (0 0 1) and Co (0 0 1). Since the Δ1 states of Fe and Co are fully spin-polarized at the Fermi level and the conductance across the MgO

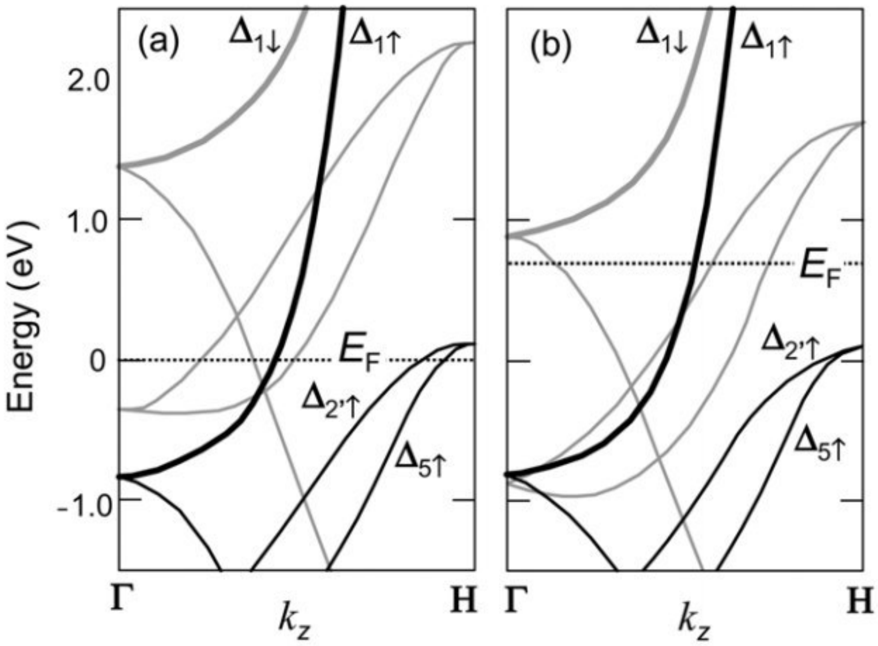

Figure 1.7: Band dispersion in Fe and Co. (a) Band dispersion of Fe bcc in the (0 0 1) direction and (b) of Co bcc in the (0 0 1) direction. The thick black and gray lines represent the majority-spin and minority-spin bands (Δ1 bands), respectively.

barriers is dominated by these Bloch states, highly spin-polarized tunneling takes place in Fe (0 0 1)/MgO (0 0 1)/Fe (0 0 1) and Co (0 0 1)/MgO (0 0 1)/Co (0 0 1) epitaxial MTJs. This spin-polarized tunneling resulting from symmetry filtering led to the prediction of enhanced TMR ratios [13, 38] of more than 1000% with (100)-Fe electrodes and even higher for CoFe electrodes. Experimentally, a TMR of 600% at RT was reported in CoFeB/MgO/CoFeB stacks [39, 18]. The main advantage of CoFeB that leads to these high TMR values consists in the amorphous nature of this material. If an annealing is performed to CoFeB/MgO/CoFeB MTJs, the MgO imposes its crystallographic structure leading to epitaxial structures that result in the selection of the Δ1 states and thus to the high TMR values.

1.4 MAGNETIZATION EQUATION OF MOTION

Magnetic fields allow the control of magnetic moments. For instance, applying magnetic fields to MTJs we are able to change from the P to the AP configuration, or vice versa. The effect of the magnetic fields on the magnetization can be described if we approximate individual magnetic moments to an average over a small region of volume V. Then, the magnetization (magnetic moment per unit of volume) can be written as $\boldsymbol{M} = M_s \boldsymbol{m}(\boldsymbol{r})$ where M_s is the magnetization saturation (expressed in A/m) and $\boldsymbol{m}(\boldsymbol{r})$ is the unit vector of the magnetization direction. The effective magnetic field ($\boldsymbol{H_{eff}}$) exerts a torque on the magnetization which is given by:

$$\dot{\boldsymbol{m}}(\boldsymbol{r}) = -\mu_0 \boldsymbol{m}(\boldsymbol{r}) \times \boldsymbol{H_{eff}}(\boldsymbol{r}), \tag{1.11}$$

where the notation $\dot{\boldsymbol{X}}$ stands for $\frac{\partial \boldsymbol{X}}{\partial t}$ for any function $\boldsymbol{X}$, $\boldsymbol{\mu_0}$ is the magnetic permeability and t and $\boldsymbol{r}$ are the time and position, respectively. The local effective magnetic field consists in the contributions of the external applied magnetic field and the field created by the neighbouring magnetic moments and thus depends on the position. The local magnetic field can be derived from the Gibbs free energy (E):

$$\boldsymbol{H_{eff}} = -\frac{1}{\mu_0 M_s V} \frac{\partial E}{\partial \boldsymbol{m}(\boldsymbol{r})}, \tag{1.12}$$

that leads to the Larmor equation:

$$\dot{\boldsymbol{m}}(\boldsymbol{r}) = \frac{\gamma}{M_s V} \boldsymbol{m}(\boldsymbol{r}) \times \frac{\partial E}{\partial \boldsymbol{m}(\boldsymbol{r})}, \tag{1.13}$$

where γ is the gyromagnetic ratio. In a complex magnetic structure there are several energy contributions to the Gibbs free energy. For instance, the free layer magnetization of an MTJ is subjected to internal and external fields arising from adjacent layers and applied fields. These different contributions to the energy are schematically depicted in Fig. 1.8 and can be separated in the following terms:

$$E = E_Z + E_{an} + E_{dem} + E_{bias} + E_{dip} + E_{RKKY} + E_{ex}, \tag{1.14}$$

where E_Z is the Zeeman energy generated by the interaction with an external magnetic field, E_{an} is the magnetocrystalline or anisotropy energy, E_{dem} the demagnetizing field energy, E_{bias} the exchange bias energy, E_{dip} the dipolar field energy, E_{RKKY} the energy arising from the Ruderman-Kittel-Kasuya-Yosida (RKKY) interaction and E_{ex} the exchange energy.

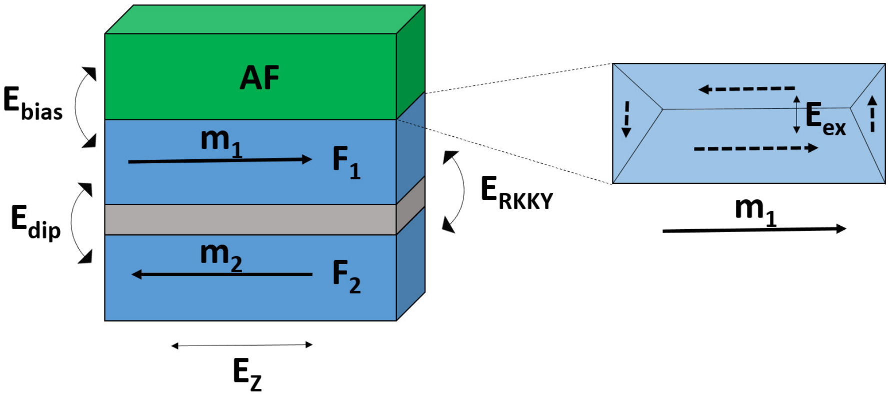

Figure 1.8: Schematic representation of the interactions involved in a magnetic stack. The layer-layer interaction fields (left): exchange bias (E_{bias}), dipolar (E_{dip}) and RKKY interaction (E_{RKKY}) along with the external applied field that leads to the Zeeman energy (E_Z). Detail of the magnetic domains in a FM layer (right) which result from the competition between the exchange field (E_{ex}), the demagnetizing field (not shown) and E_Z.

1.4.1 *Zeeman energy (E_Z)*

An applied external magnetic field interacts with the magnetic moments of a magnetic material leading to an energetic contribution designated as Zeeman energy (E_Z). This contribution is minimized when the spins are aligned to the applied field ($\boldsymbol{H_a}$) and is given by:

$$E_Z = -\mu_0 M_s V \boldsymbol{H_a} \cdot \boldsymbol{m}. \tag{1.15}$$

1.4.2 *Anisotropy energy (E_{an})*

Different crystallographic orientations change the geometry of the lattice and the distance between neighbouring atoms. Therefore, the interactions between the magnetic moments are also changed and one or several directions for the magnetization might be favoured. In the case of uniaxial anisotropy (only one favoured direction) the anisotropy energy is given by:

$$E_{an} = K_{an} V[1 - (\boldsymbol{u_k} \cdot \boldsymbol{m})^2], \tag{1.16}$$

where K_{an} is the anisotropy per unit of volume caused by the crystalline induced magnetic orientation and $\boldsymbol{u_k}$ is the favoured direction. From Eq. (1.16) we can conclude that the energy is minimal when the magnetization has the same direction as $\boldsymbol{u_k}$ (and is the same for both orientations). The anisotropy field can then be written as:

$$H_{an} = \frac{2K_{an}}{\mu_0 M_s}. \tag{1.17}$$

One of the cases with more relevance for applications in spintronics is that of perpendicular magnetic anisotropy (PMA). In this case, a magnetic layer has a crystallographic orientation that favors an out-of-plane (OOP) magnetization. This anisotropy energy has a bulk ($K_V^{\perp}$) and a surface ($K_S^{\perp}$) contribution and is expressed as:

$$E_{\perp} = (K_V^{\perp} V + K_S^{\perp} S)[1 - (\boldsymbol{u}_{\perp} \cdot \boldsymbol{m})^2], \tag{1.18}$$

where S is the surface responsible for the anisotropy and $\boldsymbol{u}_{\perp}$ is the direction normal to the surface. In MTJs this anisotropy can be achieved through two different approaches. (1) By depositing materials with the proper crystalline growth such as Co/Pt multilayers. The (100) texture of these multilayers has a strong PMA and, when coupled to the MTJ, can induce such anisotropy to the CoFeB electrodes. (2) PMA also arises from the interface between a metal and an oxide. In particular, the MgO/CoFeB interface generates PMA in the magnetic layers. Since this is an interfacial effect only thin CoFeB layers (below ~ 1.0 nm) are perpendicularly magnetized. The amplitude of $K_S^{\perp}$ was found to be related with the TMR (increasing for larger TMR values) [40, 41, 42, 43, 44].

1.4.3 *Demagnetizing field energy (E_{dem})*

The demagnetizing field ($\boldsymbol{H_{dem}}$) is a field of magnetostatic origin generated by the shape of the magnet. It follows from the laws of Maxwell that state that the divergence of a magnetic field ($\boldsymbol{B}$) must be zero:

$$\nabla \boldsymbol{B} = 0, \tag{1.19}$$

where $\boldsymbol{B}$ is the sum of the magnetization and the demagnetizing field ($\boldsymbol{H_{dem}}$):

$$\boldsymbol{B} = \mu_0(\boldsymbol{M} + \boldsymbol{H_{dem}}). \tag{1.20}$$

Therefore, the demagnetizing field is equivalent to a field that counters the magnetization, closing the flux lines. The demagnetizing field energy corresponds to the interaction of the magnetization with $\boldsymbol{H_{dem}}$ and can be expressed as:

$$E_{dem} = -\frac{1}{2}\mu_0 M_s V \boldsymbol{H_{dem}} \cdot \boldsymbol{m}. \tag{1.21}$$

Since the demagnetizing field depends on the magnetic configuration and shape of the magnet, it is quite difficult to determine. If we assume that the sample is an ellipsoid, $\boldsymbol{H_{dem}}$ is uniform and corresponds to the tensorial product between the magnetization $\boldsymbol{M}$ and a constant symmetric tensor $\boldsymbol{N}$:

$$\boldsymbol{H_{dem}} = -M_s \boldsymbol{N} \cdot \boldsymbol{m}. \tag{1.22}$$

The tensor $\boldsymbol{N}$ is diagonal in the basis of the Cartesian axes of the ellipsoid (u_x, u_y, u_z) with unit trace. Thus, in this case $\boldsymbol{H_{dem}}$ can be written as:

$$\boldsymbol{H_{dem}} = -M_s N_{xx} m_x - M_s N_{yy} m_y - M_s N_{zz} m_z, \tag{1.23}$$

where $N_{xx} + N_{yy} + N_{zz} = 1$ are the diagonal values of the tensor. The thinner the ellipsoid in the directions $\boldsymbol{u_i}$, the larger is the corresponding N_{ii} element. For instance, if we have an elliptical magnetic thin film with the longer direction along $\boldsymbol{u_x}$ and the thickness along $\boldsymbol{u_z}$, we will have $N_{xx} < N_{yy} \ll N_{zz}$. Hence, the demagnetizing field would benefit an in-plane (IP) magnetization along the $\boldsymbol{u_x}$ direction.

1.4.4 *Exchange bias energy (E_{bias})*

An antiferromagnet (AFM) is a magnetic material possessing spin lattices that point in opposing directions, leading to a zero total magnetic moment. When an AFM layer is in contact with a FM, the first atomic planes of the AFM pin the FM causing a shift in the hysteresis curve. More precisely, the FM layer is pinned in a certain direction which is set when the sample is annealed and cooled down under applied magnetic field from a temperature above the Néel temperature. Thus, during annealing the AFM temperature rises above the Néel temperature losing its magnetic order. Since the Curie temperature of the FM is usually higher, it will be aligned along the external field direction. During cooling, the first atomic layer of the AFM aligns with the FM moments saturated by the external field. Therefore, upon cooling a higher field will be required to rotate the FM layer. As a first approximation, the exchange bias energy is equivalent to the energy generated by an additional constant field ($\boldsymbol{H_b}$). Thus, it can be written as:

$$E_{bias} = -\mu_0 M_s V \boldsymbol{H_b} \cdot \boldsymbol{m}. \tag{1.24}$$

The strength of this field $\boldsymbol{H_b}$ depends on the nature of the AFM and defects on the interface. This effect is used in a large variety of spintronic nanodevices [45, 46] and novel magnetoresistive structures where the AFM plays an active role in the transport mechanism [47].

1.4.5 *Dipolar field energy (E_{dip})*

The dipolar field energy has the same origin as the demagnetizing field energy but it concerns the interaction between the magnetization of one layer with the field created by another layer. This contribution is caused by the closure of the lateral magnetic flux arising from the magnetic layers. This coupling becomes more pronounced for smaller lateral dimensions of the MTJs [48].

1.4.6 *Ruderman-Kittel-Kasuya-Yoshida (RKKY) energy*

The Ruderman-Kittel-Kasuya-Yoshida (RKKY) interaction consists in the coupling of two magnetic layers separated by a thin metallic spacer and is mediated by the conduction electrons. This indirect exchange coupling occurs when the nuclear spin of one atom interacts with a conduction electron through the hyperfine interaction and moves to another layer, interacting with another nuclear spin and generating a correlation between the nuclear spins of different layers. The energy associated with this coupling can be written in the macrospin approximation [49] as:

$$E_{RKKY} = -J_{RKKY} S \boldsymbol{m_1} \cdot \boldsymbol{m_2}, \tag{1.25}$$

where J_{RKKY} is the interaction energy per unit area, S the interface area and m_i the magnetization of the magnetic layers interacting with each other. The value of J_{RKKY} depends on the non-magnetic spacer and has an oscillating nature with the spacer thickness. It can be both positive and negative, inducing a FM or AFM coupling, respectively.

1.4.7 *Exchange energy (E_{ex})*

The exchange energy is an interaction between unpaired electrons in nearby atoms. This is a short distance spin-spin quantum interaction deriving from the fact that the wave function of indistinguishable particles is subjected to exchange energy. The energy associated with this interaction can be written as:

$$E_{ex} = J_{ex}(\boldsymbol{S_1} \cdot \boldsymbol{S_2}), \tag{1.26}$$

where $\boldsymbol{S_1}$ and $\boldsymbol{S_2}$ are the spins of two neighboring unpaired electrons and J_{ex} is the exchange constant. The sign of J_{ex} can be both positive and negative inducing a P or AP alignment, respectively. Hence, this interaction is responsible for collective ordering in FMs. Despite the fact that in FMs the exchange interaction induces a homogeneous alignment between spins, the presence of a magneto-static energy can lead to the formation of domain walls and consequently magnetic domains such as the ones schematized in Fig. 1.8 (right).

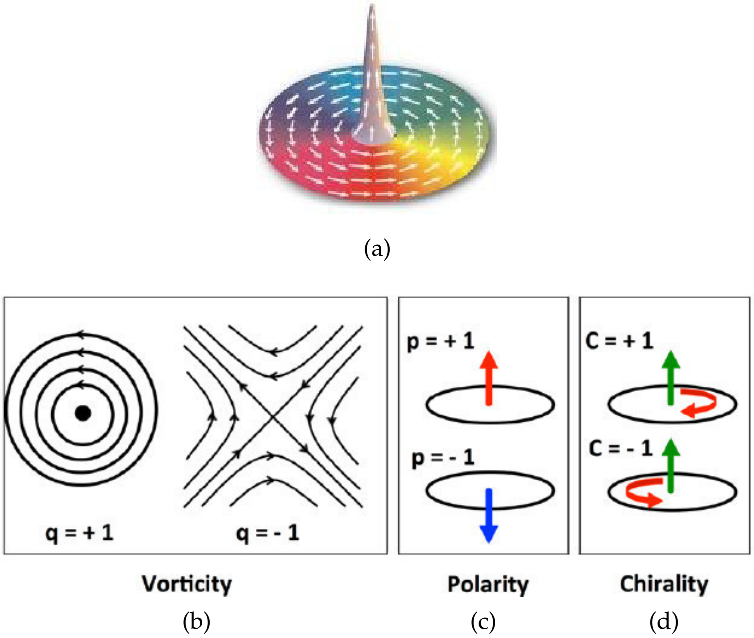

(a)

(b) (c) (d)

Figure 1.9: Magnetic vortices. (a) Schematic representation of a vortex magnetization configuration. Topological charges of a FM vortex: (b) vorticity, (c) polarity and (d) chirality [52].

1.5 MAGNETIC VORTICES

The interplay between the different magnetic energy terms can generate non-trivial magnetic configurations. One of the most studied of magnetic configurations are magnetic vortices, which are a consequence of the interplay between the dipolar and the exchange energies. This configuration consists on a curling spin structure in the plane of the magnetization around a central region (core), where the magnetic moments are pointing OOP to avoid creating a singularity [Fig. 1.9(a)]. A vortex can be described by three topological charges: the vorticity q [Fig. 1.9(b)], the polarity p [Fig. 1.9(c)] and the chirality c [Fig. 1.9(d)] [50]. The vorticity describes the curling of the magnetic moments, being $q = 1$ associated with the vortices and $q = -1$ associated with the anti-vortices (other geometries are described for different q values [51]). The polarity defines the orientation of the vortex core with respect to the plane of the FM (with values of $p = \pm 1$). The chirality indicates the rotation of the moments and can be clockwise ($c = 1$) or counterclockwise ($c = -1$).

To obtain a vortex configuration a soft FM with a weak magneto-crystalline anisotropy (such as NiFe) is required. In Fig. 1.10 the phase diagram of the magnetic states is shown

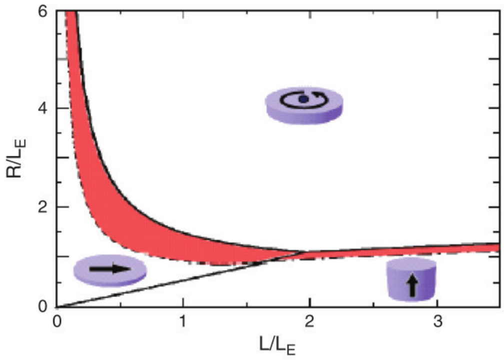

Figure 1.10: Phase diagram of nano-sized discs. The different ground states are: vortex state, magnetized uniformly IP and magnetized uniformly OOP. The red region marks the range where the vortices are metastable, below that region no complete vortices can be present [54].

[53, 54]. If the disc thickness (L) is much larger than its radius (R), the demagnetizing field will favour the OOP homogeneous magnetization state. On the other hand, if R is much larger than L, the IP homogeneous magnetization state is favored. If, however, the radius is larger than the exchange length (L_E; typically 5-10 nm) and if the L/R ratio is neither too large (OOP magnetization) or too low (IP magnetization), a vortex magnetization can be achieved. Note also that metastable states, where both homogeneous and vortex magnetization states are energy minima can occur (red area of Fig. 1.10). Furthermore, if the lateral size becomes too large, multiple domains may appear.

1.6 GILBERT DAMPING TORQUE

Starting from the free energy E we are able to determine the Larmor equation [Eq. (1.13)]. This equation describes a precessional magnetization with constant energy. However, in a real material, energy dissipation takes place as well. This dissipation converts the energy coming from the magnetic excitations into phonons and ultimately heat. Therefore, a phenomenological torque has to be added in order to account for magnetic energy dissipation (Gilbert damping). The magnetic motion equation becomes:

$$\dot{\boldsymbol{m}} = \frac{\gamma}{M_s V}\boldsymbol{m} \times \frac{\partial E}{\partial \boldsymbol{m}} + \alpha \boldsymbol{m} \times \dot{\boldsymbol{m}}, \tag{1.27}$$

where α is the adimensional phenomenological Gilbert damping constant. If now we make the vectorial product of $\boldsymbol{m} \times \dot{\boldsymbol{m}}$ and since $\boldsymbol{m}$ is a unitary vector with constant norm, we arrive to the Landau-Lifshitz-Gilbert equation:

$$\dot{\boldsymbol{m}} = \frac{\gamma}{1+\alpha^2}\frac{1}{M_s V}\boldsymbol{m} \times \frac{\partial E}{\partial \boldsymbol{m}} + \frac{\gamma}{1+\alpha^2}\frac{\alpha^2}{M_s V}\boldsymbol{m} \times (\boldsymbol{m} \times \frac{\partial E}{\partial \boldsymbol{m}}). \tag{1.28}$$

If now we define a modified gyromagnetic ratio as $\gamma^* = \frac{\gamma}{1+\alpha^2}$ and considering that α is small (approximately 0.02 in transition metals) the change of the gyromagnetic ratio is negligible and we can re-write Eq. (1.28) as:

$$\dot{\boldsymbol{m}} = \frac{\gamma}{M_s V}\boldsymbol{m} \times \frac{\partial E}{\partial \boldsymbol{m}} + \alpha\frac{\gamma}{M_s V}\boldsymbol{m} \times (\boldsymbol{m} \times \frac{\partial E}{\partial \boldsymbol{m}}). \tag{1.29}$$

The effect of the damping then consists in decreasing the energy of the system until an energy minimum (global or local). The relaxation time of this process is given by:

$$\tau_D = \frac{1}{\alpha \mu_0 \gamma H_{eff}}. \tag{1.30}$$

The time corresponding to the precessional dynamics of a magnetic moment can also be estimated from Eq. (1.29) and lies in the ns range, corresponding to the GHz in the frequency domain. This is the reason why spintronic devices can be used as radiofrequency (RF) emitters as will be discussed later.

1.7 SPIN-TRANSFER-TORQUE (STT)

Magnetic fields are not the only mechanism that allows the control of the magnetization. In fact, the angular momentum of the electron spins can be absorbed by spin-dependent scattering and other processes in a lattice, leading to a spin transfer torque (STT) which is equal to the rate of change of angular momentum in the lattice [55]. Therefore, the total angular momentum of the electron current and lattice is conserved and can only be transferred within these systems. Hence, STT allows the excitation of magnons [56], to move domain walls [57, 58], reverse the magnetization of magnetic materials [59, 60] and induce magnetic precession [61, 62]. Note that even an initially unpolarized current can become spin polarized by spin dependent scattering in a FM material and exert a torque in another FM layer. For instance, consider an MTJ (FM1/I/FM2) where FM1 has its magnetization pinned (e.g. by exchange bias) in direction $\boldsymbol{m_1}$ and FM2 has a free magnetization direction $\boldsymbol{m}$ (for simplicity). An unpolarized electrical current passing from left to right would become spin polarized after passing through FM1 [Fig. 1.11(a)]. As they are injected into FM2, electron spins realign

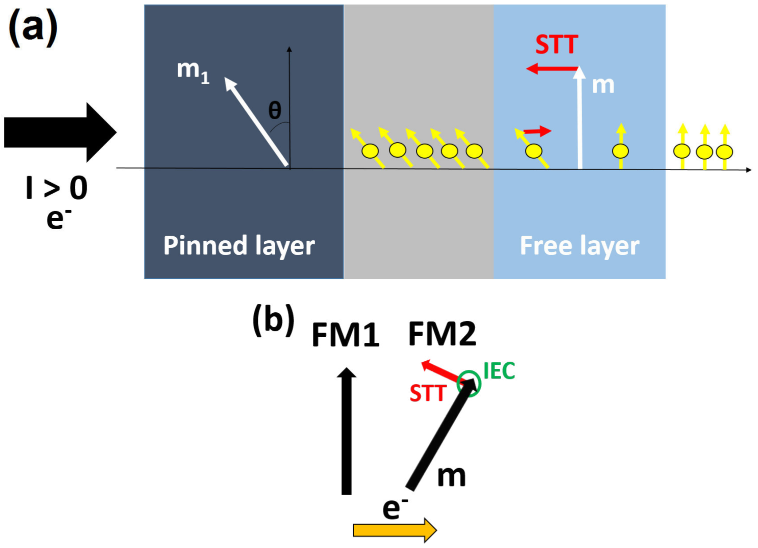

Figure 1.11: Schematic representation of the torques induced in the free layer of a MTJ. (a) In the case of electrons traveling from the pinned to the free layer the induced STT favors the P state [63]. (b) Representation of the STT and IEC torques applied to the free magnetic layer.

towards the direction of $\boldsymbol{m}$. However, due to the conservation of angular momentum, the momentum of the spins is also transferred to FM2. Thus the magnetization $\boldsymbol{m}$ feels a torque with the same direction of $\boldsymbol{m}_1$. Note that the STT effect is also present when the electrons pass through FM1. However, since FM1 is pinned the effect is negligible. The STT effect also depends on the direction of the current: when the current flows from right to left (from the free to the pinned layer) it becomes spin polarized in FM2 along the direction of $\boldsymbol{m}$. However, when the current passes through FM1, it realigns in the direction of $\boldsymbol{m}_1$, and the electron spins transmitted through FM1 will have the same direction as $\boldsymbol{m}_1$. On the other hand, the spins reflected at the interface will have the opposite spin orientation and thus induce a torque in FM2. Note that the torque induced to the free layer has different orientations depending on the current direction. In particular, for the P state, electrons traveling from the pinned to the free layer favor the P state and electrons traveling from the free to the pinned layer induce the AP configuration. Therefore, a larger magnetic precession or even full magnetization reversal is obtained in the last case. For analogous reasons, in the AP case, electrons flowing from the pinned to the free layer favour the magnetization dynamics.

Hence, the STT effect depends on the angle between the magnetic orientation of the two FM layers (θ), the current density (J) and material parameters such as the TMR. It can be expressed as:

$$\boldsymbol{\tau_{STT}} = a_J(J,\theta)\boldsymbol{m} \times (\boldsymbol{m} \times \boldsymbol{m_1}), \tag{1.31}$$

where a_J is the STT amplitude that depends on the used material and TMR.

Another contribution to the electron-induced magnetization dynamics is the field-like torque, or interlayer exchange coupling (IEC) torque, that has the same form as the torque applied by an external magnetic field and can be written as:

$$\boldsymbol{\tau_{IEC}} = b_J(J,\theta)\boldsymbol{m} \times \boldsymbol{m_1}, \tag{1.32}$$

where b_J is the STT amplitude. Therefore, $\boldsymbol{\tau_{STT}}$ and $\boldsymbol{\tau_{IEC}}$ are orthogonal to each other [Fig. 1.11(b)], being the maximum value of $b_J \sim 30\%$ of a_J. Thus, despite the fact that both torques are present, $\boldsymbol{\tau_{STT}}$ has the main contribution. The value of b_J is proportional and opposite to a_J and is usually written as:

$$b_J = -\alpha\beta_{IEC}a_J. \tag{1.33}$$

This definition is used because the coefficient β_{IEC} is 1 when only the damping related to the STT is considered [64].

By adding these contributions to Eq. (1.29) we arrive at the Landau-Lifshitz-Gilbert-Slonczewski (LLGS) equation:

$$\dot{\boldsymbol{m}} = \frac{\gamma}{M_s V}\boldsymbol{m} \times \frac{\partial E}{\partial \boldsymbol{m}} + \alpha\frac{\gamma}{M_s V}\boldsymbol{m} \times (\boldsymbol{m} \times \frac{\partial E}{\partial \boldsymbol{m}}) + \gamma\mu_0 a_J \boldsymbol{m}(\boldsymbol{m} \times \boldsymbol{m_1}) - \gamma\mu_0\alpha\beta_{IEC}a_J\boldsymbol{m} \times \boldsymbol{m_1}. \tag{1.34}$$

The LLGS equation describes the behaviour of the magnetic moment of the free magnetic layer for a certain current density J and effective field $\boldsymbol{H_{eff}}$. The first term describes the precession of $\boldsymbol{m}$ around $\boldsymbol{H_{eff}}$. The second describes the damping due to the loss of magnetic energy and will act to align the magnetic moment to $\boldsymbol{H_{eff}}$. The third is the STT effect that can either act along or against the damping torque, depending on the direction of the applied current. The last term models the IEC torque which can be often neglected since STT has the main effect of the current induced dynamics. In Fig. 1.12(a) we show a representation of the torques applied to $\boldsymbol{m}$ (neglecting the IEC torque). Depending on the direction and strength of the current, magnetization dynamics can follow three different types of paths. If the damping and the STT have the same direction, their joint effects will align $\boldsymbol{m}$ with $\boldsymbol{H_{eff}}$ [Fig. 1.12(b)]. If the current is applied in the opposite direction and the damping and STT compensate each other, the magnetization reaches a steady magnetic precession [Fig. 1.12(c)]. Note that in this case different values of J can lead to steady precessions with different amplitudes. Finally, when the STT is stronger than the damping, the complete switching of the magnetic moment

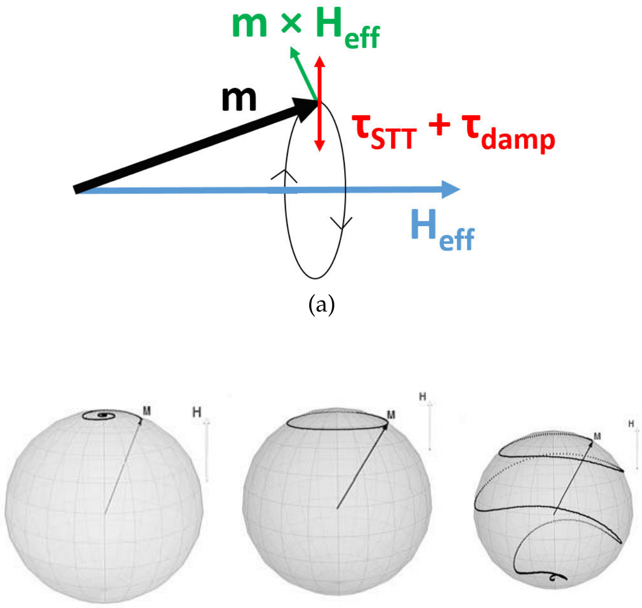

(a)

(b) Damping (c) Precession (d) Switching.

Figure 1.12: (a) Schematic representation of the torques exerted in the magnetization of the free layer: conservative torque ($\boldsymbol{m} \times \boldsymbol{H_{eff}}$), damping and STT. Different trajectories that can be performed by the magnetization: (b) damped oscillation, (c) magnetic precession and (d) magnetic switching.

can be achieved. In this case, $\boldsymbol{m}$ will move away from $H_{\boldsymbol{eff}}$ until a critical angle is reached, at which point it will change direction and spiral to the opposite orientation and magnetic switching is achieved [Fig. 1.12(d)].

Hence, the STT effect allows the effective control of the magnetization of nano-magnets using spin-polarized electrical currents. Contrary to the case of magnetic fields, the STT effect is intrinsically scalable since higher current densities increase the magnitude of the STT effect opening the possibility of devices with small footprint and high density. Therefore, novel technologies that use this effect to operate promptly appeared, such as STT controlled magnetic random access memories (STT-MRAM) or spin transfer torque nano-oscillators (STNOs). In the scope of this thesis, we mainly explored magnetic precessions [Fig. 1.12(c)] that allow the fabrication of STNOs.

1.8 STT-INDUCED DYNAMICS IN MAGNETIC VORTICES

Similarly to the homogeneous magnetization case, STT can also induce dynamics in more intricate magnetic structures, such as magnetic vortices [65] or skyrmions [66]. In the case of the magnetic vortices (see section 1.5), its core is "trapped" to the central region since this is the magnetic configuration that minimizes the energy. It can, however, be moved from its equilibrium position using magnetic fields or the STT effect leading to the gyrotropic motion of the core. In fact, the core can then be treated as a domain wall and starting from the LLGS equation [Eq. (1.34)] the Thiele equation for the vortex core position ($\mathbf{X}$) can be derived [67]:

$$-\frac{\partial W}{\partial \mathbf{X}} + \mathbf{G} \times \frac{d\mathbf{X}}{dt} - D\frac{d\mathbf{X}}{dt} + \mathbf{F_{STT}} = 0, \tag{1.35}$$

where $\mathbf{G} = -2pLM_s/\gamma \mathbf{e_z}$ is the gyrovector, L the thickness of the FM layer, M_s the saturation magnetization, p the core polarity, γ the gyromagnetic ratio and $\mathbf{e_z}$ the unit vector along the normal direction. $W(\mathbf{X})$ is the potential of the off-centre vortex, and D is the damping factor. In Fig. 1.13 these four contributions are depicted schematically, along with the core position and trajectory (red line). The first two terms, corresponding to the restoring force and gyrotropic force, respectively, are radial with respect to the core trajectory and their compensation defines the motion frequency. The last two terms, corresponding to the viscous damping and the effect of the STT ($\mathbf{F_{STT}}$), respectively, are tangent to the trajectory and their balance sets the the orbit amplitude. Here, $\mathbf{F_{STT}}$ only accounts the effect of the Slonczewski term of the STT. The smaller effect of the field-like term would be equivalent to an additional magnetic field directed along the current polarization. The gyrovector, directed perpendicular to the disc plane, is responsible for the vortex core oscillation. If the excitation is turned off, the core goes back to its equilibrium position in a spiral movement. The vortex core precession frequencies are located in the range of the hundreds of MHz.

1.9 SPIN-TRANSFER-TORQUE NANO-OSCILLATORS (STNOS)

The current driven magnetic precession induced by STT enables the fabrication of novel RF generators. These STNOs use the persistent magnetic dynamics of the free magnetic layer of an MTJ or spin valve to retrieve the RF electrical signal (Fig. 1.14) [69]. They have several advantages over standard LC-tank voltage-controlled oscillators (VCOs). They depict a broadband output and can be biased at low voltages (< 1 V) and their frequency is tunable by current and/or magnetic fields. In STNOs the oscillation frequency can be tuned over several GHz just by changing the current and up to 40 GHz by an external magnetic field for particular configurations [70], while VCOs only allow a 20% frequency change compared to the carrier frequency.

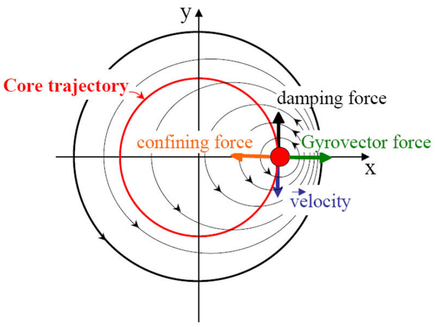

Figure 1.13: Schematic representation of the different forces acting on the vortex core [68].

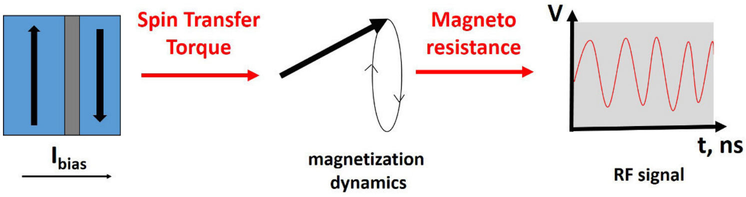

Figure 1.14: General concept of the STNO operation. A current passes through a spin valve or MTJ, the STT excites the magnetization dynamics and the resistance variation caused by the device magnetoresistance leads to a RF signal.

STNOs are amongst the smallest RF emitters developed, over 50 times smaller than a VCO in CMOS technology [71]. They also work over a large temperature range. STNOs are thus versatile and compact RF emitters which can be fabricated on chip and used in applications such as chip-to-chip or wireless communications, local on-chip clocks for very-large-scale integration applications, microwave sources for nanosensors, phase array transceivers and high density parallel microwave signal processors [72, 73]. The main limitations of STNOs are the need for a large output power ($P_{out} \sim 1\ \mu$W is needed while typical STNOs show P_{out} in the nW range) and narrow linewidths ($\Gamma < 1$ MHz). Several configurations have been pursued in order to fulfill these objectives.

1.9.1 *Geometry*

Accordingly to sample patterning, several geometries have been developed to obtain efficient STNOs [74], being the most relevant nanopillars [Fig. 1.15(a)] and point-contacts [Fig. 1.15(b)].

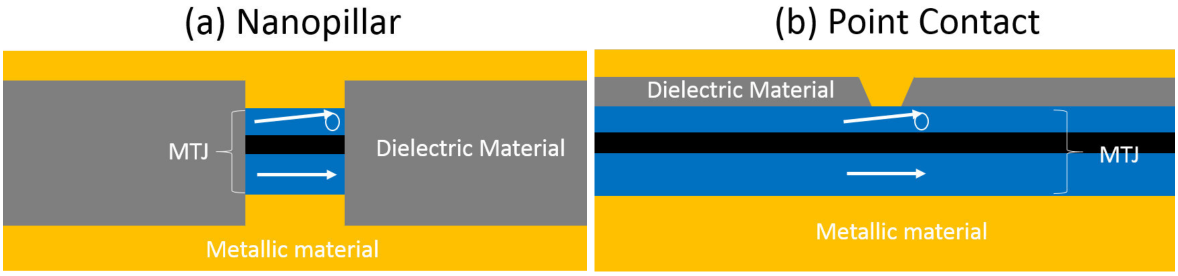

Figure 1.15: STNOs geometries. (a) Nanopillar, (b) point contact.

In the case of a nanopillar, the free magnetic layer has a finite lateral size and reflecting boundaries in the plane of the layer. In the case of a point-contact, the free magnetic layer is not bounded in the layer plane but a dielectric constriction (typically 10-80 nm) leads to localized current densities that excite propagating spin waves. The nanopillars usually show a higher amplitude signal while the linewidth is usually smaller in structures incorporating point contacts. However, since MTJs are more resistive than spin valves, in a point contact with an MTJ stack the electrons will spread along the FM layer, leading to smaller current densities. Therefore, point-contacts are mainly used in spin valves but in principle can also be implemented with MTJs with low RA product. In fact, a particular type of point-contact, the "sombrero-shaped" point contact was used in MTJs and a large P_{out} (2 μW) was reported [75].

It is important to stress that in both geometries the cross section of the bias current must be nano-sized (current densities of the order of 10^6 - 10^7 A/cm^2). Such high current densities are necessary for the STT effects to manifest, compensating magnetic damping in the free layers to generate RF emission. Nevertheless, the continuous device miniaturization is not always beneficial. In fact, it has been shown that larger nanopillars (diameters of 300 nm) maximize P_{out} [76].

1.9.2 *Magnetic stack*

It is widely accepted that CoFeB/MgO/CoFeB MTJs with a thin dielectric layer are the best option to achieve STNOs with large P_{out} due to their large TMR that enhances the RF emission. The first significant result of a pronounced narrow peak (linewidth of 21 MHz at a frequency of 7 GHz) was obtained in 2006 [77]. Despite the fact that a relatively thin MgO barrier (RA < 50 $\Omega \mu m^2$) is necessary to achieve sufficiently high current densities, it was shown that high and low resistance STNOs have distinct dynamic behaviours [78, 79, 80, 81]. Furthermore, several magnetic configurations for STNOs have been tried. These include homogeneous IP magnetization structures, where both the free and the pinned magnetic layers have an IP easy axis [Fig. 1.16(a)] [61, 70, 79]. Usually, this configuration requires a relatively large magnetic field a few degrees away from the magnetic easy axis in circular samples [61] or with a larger angle in samples with shape anisotropy [80] to produce a high microwave signal. This configuration explores the large TMR obtained in IP epitaxial MTJs, but the same orientation of both FM layers hampers large amplitude and well-defined magnetic precessions. Magnetic layers with PMA can also be incorporated in STNOs. A fully perpendicular device (with both free and pinned layers perpendicularly magnetized) can be fabricated using materials with strong PMA [Fig. 1.16(b)] [82]. In this case, the relative orientation of both layers is also the same and thus it also requires an external magnetic field to achieve oscillations and does not present significant advantages for STNO applications. To maximize the STT induced in the free layer, MTJs with IP reference layer and free layer depicting PMA have also been developed. The configuration with fully OOP free layer is not beneficial for STNOs since the induced STT will damp the magnetic oscillations in some regions of its trajectory. Nevertheless, a tilted free layer magnetization [Fig. 1.16(c)] has been shown to excite large precessions amplitudes and decreased linewidths even without applied magnetic fields [83, 84, 85]. Very recently, large P_{out} values up to 2.8 μW have been reported through the conjugation of free layers with PMA and OOP fields [76]. The PMA can be further explored to obtain oscillators with a fully planar MTJ and perpendicular polarizer [Fig. 1.16(d)] [86]. STNOs with non-homogeneous magnetization, such as the vortex configuration have also been successfully implemented [Fig. 1.16(e)] [68, 87]. This configuration can be obtained using thick layers of soft FM materials such as NiFe. In this case, large amplitude (in the μW range) with low linewidth (below 1 MHz) oscillations could be achieved but with frequencies below 1 GHz, making them less attractive for applications. Moreover, a large OOP magnetic field was necessary to trigger large P_{out}. This need for a large field can be solved by using vortex oscillators incorporating a perpendicular polarizer. Such configuration led to a large P_{out} values (0.6 μW) without applied field [Fig. 1.16(f)] [88].

The different types of STNOs can cover different frequency ranges and can thus be used in different applications. In Fig. 1.17 we summarize the different features of the existing STNO types, based on vortex magnetization, homogeneous magnetization (nanopillar shaped) and point-contacts. Vortex-based STNOs cover the lowest frequency range (< 1 GHz), while STNOs cover the intermediate frequency window (2-10 GHz) and nanocontacts achieve the largest frequencies (> 20 GHz). However, usually the amplitude is higher for the vortex-based STNOs, decreases for the homogeneous magnetization STNOs and decreases further for the nanocontact ones. The decrease of amplitude observed for the point-contact geometries is related to the fact that spin valves are mostly used. The quality factor ($Q = P_{out}/\Gamma$), however, is usually smaller in STNOs with uniform magnetization. Despite the larger Q values obtained for vortices and point-contacts, the former STNOs are restricted in terms of frequency and the latter

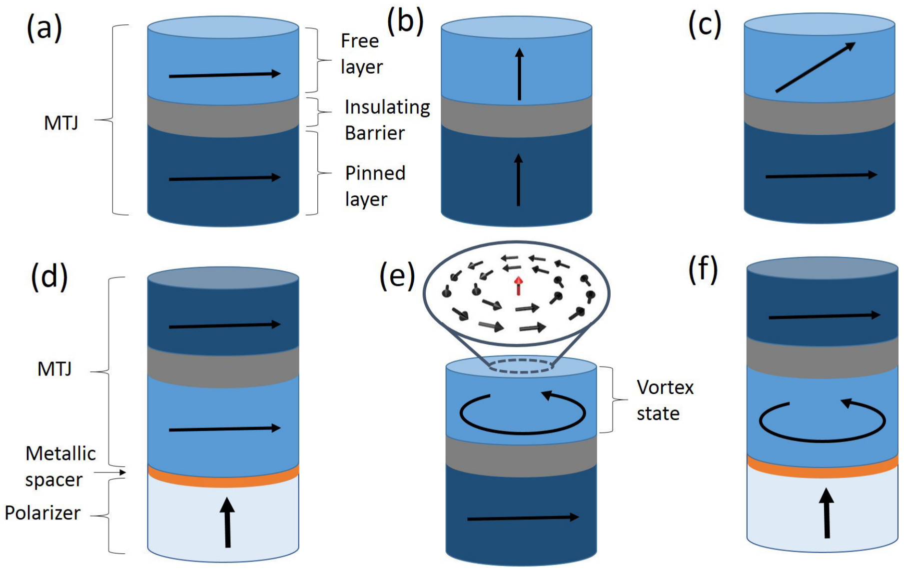

Figure 1.16: Magnetic configurations used in STNOs. (a) In plane anisotropy; (b) fully perpendicular; (c) in plane reference layer and free layer with PMA; (d) in plane with perpendicular polarizer; (e) magnetic vortex; (f) magnetic vortex with perpendicular polarizer.

would have to be implemented with MTJs to increase P_{out}. Hence, each type of STNO has margin for further study and improvement in order to push this technology into the market.

1.9.3 *Output power* (P_{out})

The RF signal emitted by a STNO can be characterized accordingly to parameters such as P_{out}, linewidth and frequency. The P_{out} is one of the most important figures of merit since values above 1 μW are required for STNOs to reach commercial applications. As discussed before, the P_{out} value depends on the magnetic configuration, the sample geometry and is usually higher for MTJs than spin valves. Large P_{out} values of 0.28, 0.6 and 2 μW were reported for devices with a homogeneous magnetic layer with PMA [84], magnetic vortices incorporating a perpendicular polarizer [88], and for a particular case of point contacts with MTJs [75], respectively. P_{out} arises from the temporal voltage variation caused by the current (I_{bias})-induced magnetic precession of a magnetoresistive structure. This voltage variation is given by:

$$V_{out}(t) = \Delta R \cdot cos(wt) I_{bias}, \tag{1.36}$$

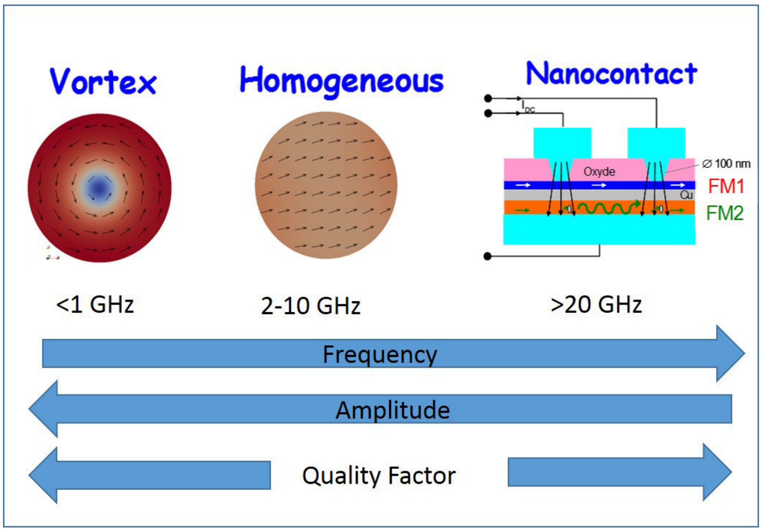

Figure 1.17: Representation of the region of operation of different STNOs. From the vortices, to the homogeneous magnetization, to the nanocontact STNOs, the frequency increases and the amplitude decreases. The Q factor is usually higher for the homogeneous magnetization STNOs.

where ΔR corresponds to the peak-to-peak amplitude of the STNO impedance variation during an oscillation period (that depends on the MTJ resistance, TMR and magnetic precession amplitude). Hence, the power generated by an MTJ with resistance R, is then delivered to a load of impedance R_L and is given by [69, 73]:

$$\langle P_{out} \rangle \approx \frac{\langle V_{out}^2 \rangle}{R_L} = \frac{I_{bias}^2 \Delta R^2 R_L}{2(R+R_L)^2}. \tag{1.37}$$

From Eq. (1.37) it is clear that the maximization of P_{out} is complex since it depends on interconnected variables. The magnetic precession amplitude depends on the I_{bias} value, that is limited by the MTJ resistance (breakdown voltage ~ 1 V). On the other hand, P_{out} also depends explicitly on R and the TMR. These two quantities are also dependent on each other since a thicker MgO usually leads to larger TMR values. Thus, P_{out} is approximately proportional to TMR, the precession amplitude and the impedance mismatch ratio R/R_L. Despite the fact that some works achieved large P_{out} values with relatively thick MgO barriers ($RA > 4$ Ωµm^2) [84, 85, 81, 88], most reports still rely on very thin MgO barriers ($RA \sim 1$ Ωµm^2) [68, 89, 78, 80, 90, 91, 92, 93].

The two limitative factors still preventing the realization of high power oscillators are the MTJ endurance and the critical current density for STT-induced magnetic precession (J_{STT}).

The MTJ endurance is limited by the dielectric breakdown of the MgO insulating layer under voltage or current stresses. While higher currents can be sustained with thinner MgO, a continuous and more crystalline barrier can endure higher breakdown voltages. This is particularly important in STNOs because in this case a continuous and large current density is required, while in e.g. STT-MRAMs, current pulses can be used (RF breakdown > DC breakdown). A very low J_{STT} is also required to achieve large amplitude oscillations before dielectric breakdown. In fact, it was shown theoretically that P_{out} increases with J/J_{STT} [94]. In the macrospin approximation, J_{STT} can be written as [74]:

$$J_{STT} = \frac{2e\mu_0 M_s \alpha d}{\hbar}\left(\frac{M_{eff}}{2} + H_a\right) \cdot \frac{1}{P} \tag{1.38}$$

where e is the charge of the electron, μ_0 is the permeability of free space, $\hbar$ the Planck constant, M_s the magnetization saturation, α the Gilbert damping constant, d the thickness of the free layer, M_{eff} the effective demagnetizing field (given by the demagnetizing factor minus the interface perpendicular magnetic anisotropy), H_a the applied field and P the spin polarization. From Eq. (1.38) we can see that J_{STT} can be decreased by decreasing α or M_{eff} or by increasing P. The damping α can be decreased, for instance, by using softer FMs (which will also decrease the TMR), M_{eff} can be decreased by using materials with strong PMA and P can be increased by increasing the TMR. Such critical current is usually larger than 10^6 A/cm^2 and had so far only been decreased by using free layers with large PMA [84, 85]. However, such strategy, usually achieved using thin CoFeB layers, also leads to the decrease of P_{out}. Therefore, new approaches to decrease the value of J_{STT}, while maintaining (or increasing) P_{out} are of fundamental importance for STNO applications.

1.9.4 *Linewidth* (Γ)

The linewidth (full width at half maximum of the power spectra; Γ) is a measure of the coherence of the precession of an oscillator. In the case of an ideal oscillator, a Dirac function with $\Gamma = 0$ would be obtained in the frequency domain. However, in a real oscillator there is always a finite Γ, which, in the case of the STNOs for commercial applications, should be below 1 MHz. In practice, Γ is a measure of the phase noise of the oscillator, i.e. short-term random phase fluctuations [95]. In the case of linear or quasi-linear oscillators the phase noise is decoupled from the power noise. However, in STNOs the effective field applied on the magnetization leads to a coupling between the phase and the power noise. This coupling leads to an additional contribution to the phase noise from a renormalization of the power noise through a non-linear frequency shift [96]. It was also shown that there is a strong dependence of Γ with the IP field angle, consistent with the minimization of the coupling between phase and power noise [97, 98].

The Γ of a STNO can vary depending on the geometry used, materials and operation conditions. In MTJ based STNOs with homogeneous magnetization, Γ can go down to the tens of MHz [78, 80, 84, 85, 77, 99]. Nevertheless, lower Γ values, down to a few MHz were obtained in spin valve-based point-contact geometries [70, 83, 100]. This can be related with the fully metallic nature of this STNO, but also with the geometry, since defects and inhomogeneities are inherent to the nanopillar definition, broadening the RF emission. Vortex based STNOs also depict smaller Γ (associated to a smaller emission frequency). In fact, even sub-MHz Γ could be obtained using magnetic vortices [68, 87, 88]. However, the most promising way to decrease Γ, in conjugation with a P_{out} increase, is based on STNO synchronization.

1.9.5 *Synchronization*

The synchronization of oscillators is a deeply studied physical phenomenon. From the synchronization of pendulums, to the acoustic waves and more recently in systems such as arrays of superconducting Josephson junctions [101] and neuronal networks [102]. The synchronization occurs when two or more oscillators are pushed to the same frequency. Furthermore, for N synchronized oscillators the linewidth drops as $1/N$ and the output power increases as N^2, when compared to a single unsynchronized oscillator [103]. It is worth noting that if only a single peak is observed when measuring the signal of more than one oscillator, but an accentuated linewidth decrease and power increase is not observed, most likely the oscillators have the same resonant frequency but are not synchronized. In the case of STNOs, the linewidth decreases by at least one order of magnitude when compared to the unsynchronized case. To obtain phase locked oscillations, the oscillators have to share the information concerning their respective phases, and be able to influence the other's phases, i.e. they have to be coupled. This mediation could be achieved through spin waves (Fig. 1.18) [104, 62] and, in vortices, mediated by antivortices [105]. The present record is the synchronization of 5 STNOs through spin waves, leading to a linewidth as small as 11.2 MHz [106]. This is an efficient coupling scheme allowing a significant linewidth reduction. However, it requires the same FM layer to be used in all the phase locked STNOs for the spin waves to propagate. Hence, this is a local mechanism and a relatively small separation between contacts ($<$ 1000 nm) is necessary. Furthermore, it requires the nanocontacts to be connected in parallel. This shunts the total emitted power so that, even if the oscillators are perfectly synchronized, the final power is equal to or less than the emission of a single nanocontact. Moreover, the requirement of the nanocontacts makes it difficult to incorporate with MTJ stacks.

Another phase locking mechanism consists in the coupling between a STNO to the frequency of an injected RF signal. The phase locking of an oscillator with an external RF current whose frequency is a multiple or integer fraction of the oscillator frequency was demonstrated

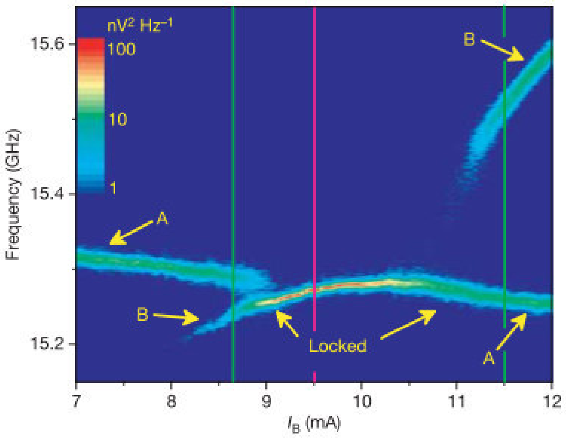

Figure 1.18: Phase locking. Combined spectrum for two nanocontacts: contact A with fixed current (I_A = 8 mA) and as a function of the current in contact B (I_B). The spectral density (color map) is in logarithmic scale [62].

[107, 108, 90]. Very small linewidths down to 3 kHz and large locking ranges (up to 1/3 of the oscillator frequency) were obtained [108]. Furthermore, the phase locking of a STNO with a reference clock was achieved and a very low linewidth (< 1 Hz) observed [109].

1.10 CONCLUSIONS

The development of spintronics along the last decades culminated in the development of novel technologies that use the STT effect to operate. Within these technologies, STNOs are one of the best positioned to reach commercial applications in the next years. However, the technological requirements for commercialization ($P_{out} > 1\ \mu$W and $\Gamma < 1$ MHz) were still not met. MTJ-based STNOs are so far the most promising candidates to meet these needs due to their larger output powers. Besides all the encouraging results with different geometries (nanopillars and point-contacts) and magnetic configurations (magnetic vortices, homogeneous magnetization, incorporation of PMA, etc.), there is still plenty of room for research and improvement for STNOs. In this thesis, we performed highly applied research to move a step forward on the development of STNOs. Studies on material engineering, nanofabrication and magnetic dynamics, along with more fundamental research of magnetoresistive materials were performed.

2

EXPERIMENTAL METHODS

The fabrication of magnetic tunnel junctions (MTJs) with namometric dimensions is a demanding process that requires very specific and complex tools. In the scope of this thesis, a new process for the nanofabrication of MTJs was conceived and developed (Chapter 3) taking full advantage of the state-of-the-art facilities of INL. This nanofabrication procedure required a broad range of specialized systems that enabled deposition, lithographic and etching processes. Furthermore, the electrical, magnetic and structural characterization of the MTJs (both before and after nanofabrication) was also performed using the characterization tools of INL. In this chapter we provide a detailed description of the systems used to fabricate and characterize the studied MTJ devices.

2.1 DEPOSITION SYSTEMS

2.1.1 *Sputtering deposition*

Several deposition methods have been developed for the preparation of thin films and nanostructures, such as thermal evaporation, laser ablation, molecular beam epitaxy and sputtering deposition. Within these techniques, the most widely used are the methods of physical vapor deposition (PVD) which include thermal evaporation and sputtering. In general terms, PVD is a process by which a film of a material is deposited on a substrate accordingly to the following sequence of steps: 1) conversion of the material to be deposited into a vapor phase by physical means; 2) the vapor transportation across a low pressure region from its source to the substrate; and 3) the vapor condensation on the substrate to form the thin film.

The sputtering technique is the most broadly used PVD process. In this case, the atoms are pulled out from the surface of a material target as a result of the impact of high-energy particles. The main reasons that justify the mainstream use of the sputtering technique is the fact that any material can be volatized, the stoichiometry of the material to deposit is conserved, it allows a uniform deposition on large areas and the plasma can also be used to clean substrates before deposition [110, 111]. Sputtering operates by generating a plasma that will volatile a target. This is performed by controllably introducing atoms of an inert gas, usually Xe or Ar, in a vacuum chamber and applying voltage to the target. Although most of the gas atoms are electrically neutral, there are always ions present among them. Two modes can then be used: DC and RF sputtering. In DC sputtering, the target is biased with a negative voltage that accelerates the ions towards the target. If their energy is large enough, they will ionize other neutral atoms in scattering events along the way. This cascade process will eventually result in the formation of a plasma. The DC sputtering is commonly used to deposit metallic films. To deposit insulating materials, RF sputtering must be used. In this case, the target is biased by an RF power supply, otherwise the insulator becomes charged. In both modes, these accelerated ions will then sputter atoms from the surface of the target. These ions are ballistically transported to the substrate through a region of reduced pressure and condense on the substrate, forming the film.

The substrate can also be grounded or biased by an RF power supply. This creates a plasma close to the surface that partially removes the material being deposited, decreasing the effective deposition rate and reducing the roughness or the film. It can also be used before film deposition to clean metallic surfaces with a thin oxide layer (etching).

In sputtering, the down limit of pressure for deposition is imposed by the quantity of inert gas required to start a stable plasma that will pulverize the atoms of the target. One way to reduce this value of pressure consists in using a magnetron sputtering [112] (Fig. 2.1). This technique includes a magnetic field that confines the plasma in a region close to the target and induces a spiraling motion in the injected electrons (of the ionization process), increasing the probability of further gas ionization. Thus, the required pressure to sustain the plasma drops and the pulverized particles maintain most of their kinetic energy when they reach the substrate, allowing the deposition of more compact and denser films. The low pressure also reduces the redeposition of pulverized atoms in the target and allows the use of lower voltage values. Both the target and the magnets are water cooled.

2.1.1.1 *Timaris multi target mode (MTM)*

The Timaris multi target mode (MTM; Fig. 2.2) is a magnetron sputtering industrial system with 10 targets and the possibility to change from DC to RF deposition. The targets are rectangular with different lateral dimensions for each material as shown in Table 2.1. This cluster tool is located in the INL cleanroom and is especially designed for deposition of ultra–thin films, magnetic films, high–quality metallic films, conductive and insulating films and multiple film stack deposition comprising these materials without the need to break ultra-high vacuum on 200 mm wafers with good uniformity (U; in percentage). Here U is defined as:

$$U = \frac{t_{max} - t_{min}}{2t_{ave}} \times 100,$$

where t_{max}, t_{min} and t_{ave} are the maximum, minimum and average thickness, respectively. A 3% uniformity was achieved for the metallic layers, whereas a 0.5% uniformity was ob-

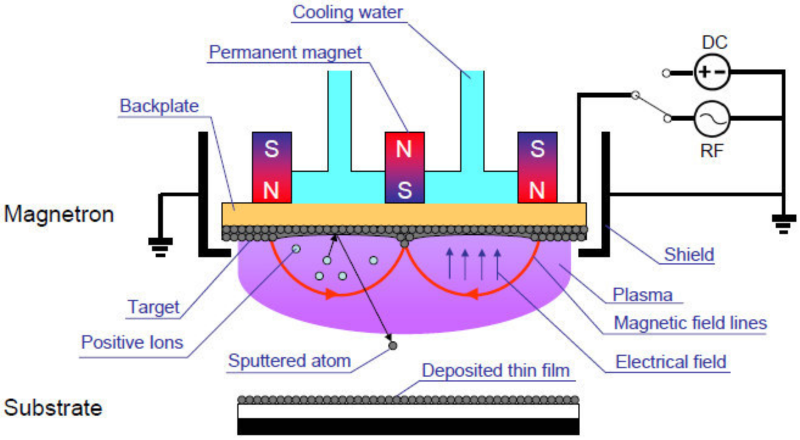

Figure 2.1: Schematic representation of a magnetron sputtering system [113].

tained for the MgO deposition [leading to a 10% uniformity of the resistance × area product (RA)]. Note that the system comprises a transport module, a multi-target PVD module, a soft etch/oxidation module and a loadlock with a cassette for 25 wafers. In the case of the RF deposition, two adjustable capacitors were used to impedance mismatch the plasma. The Timaris MTM performs depositions under an applied magnetic field. This is important to define the magnetic easy axis during the deposition of magnetic materials (which can be redefined with annealing).

The thin film deposition is performed using a linear dynamic deposition that consists of horizontal movements of the wafer under the plasma. This system allows the adjustment of the deposition rate by changing the plasma power and pressure. Moreover, one can define the number of passes (horizontal movements) and the velocity to obtain a certain thickness. In most cases the plasma power is fixed and the number of passes and the stage velocity are changed to obtain films with different thicknesses. Furthermore, by passing the wafer with an accelerated movement we are able to deposit wedge films (variable thickness along the wafer; see chapter 4). These features allow an effective and simple way to study the dependence of several parameters across the same wafer. In Appendix A we discuss further how the conditions for different film thicknesses are calculated. Once the deposition conditions for each thickness and material are determined, the deposition recipe can be defined. In Fig. 2.3 the software interface where the recipes are edited is shown (with the numbers indicating the sequence of the different steps). In step 1 the Ar flux is injected into the chamber and the

Target	Size (mm^2)
$Co_{40}Fe_{40}B_{20}$	550 × 130
$Co_{70}Fe_{30}$	550 × 130
Cu	420 × 110
$Ir_{20}Mn_{80}$	420 × 110
$Ni_{81}Fe_{19}$	550 × 130
Ta	420 × 110
Ru	420 × 110
$Mn_{62}Pt_{38}$	420 × 110
Ni	550 × 130
Co	550 × 130
MgO	550 × 110
Al	420 × 110

Table 2.1: Rectangular target sizes of each material used in the Timaris MTM.

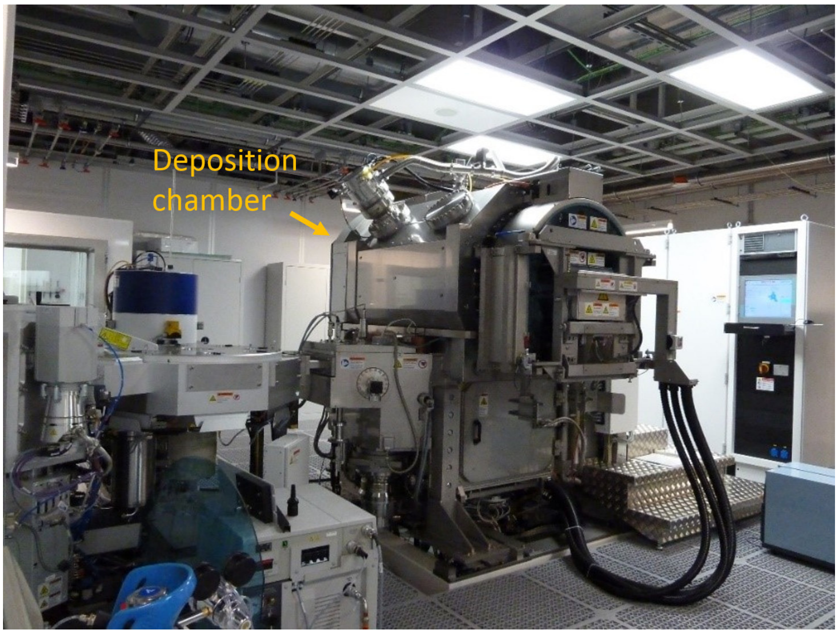

Figure 2.2: Multi-target magnetron sputtering system for MTJ depositions (INL cleanroom).

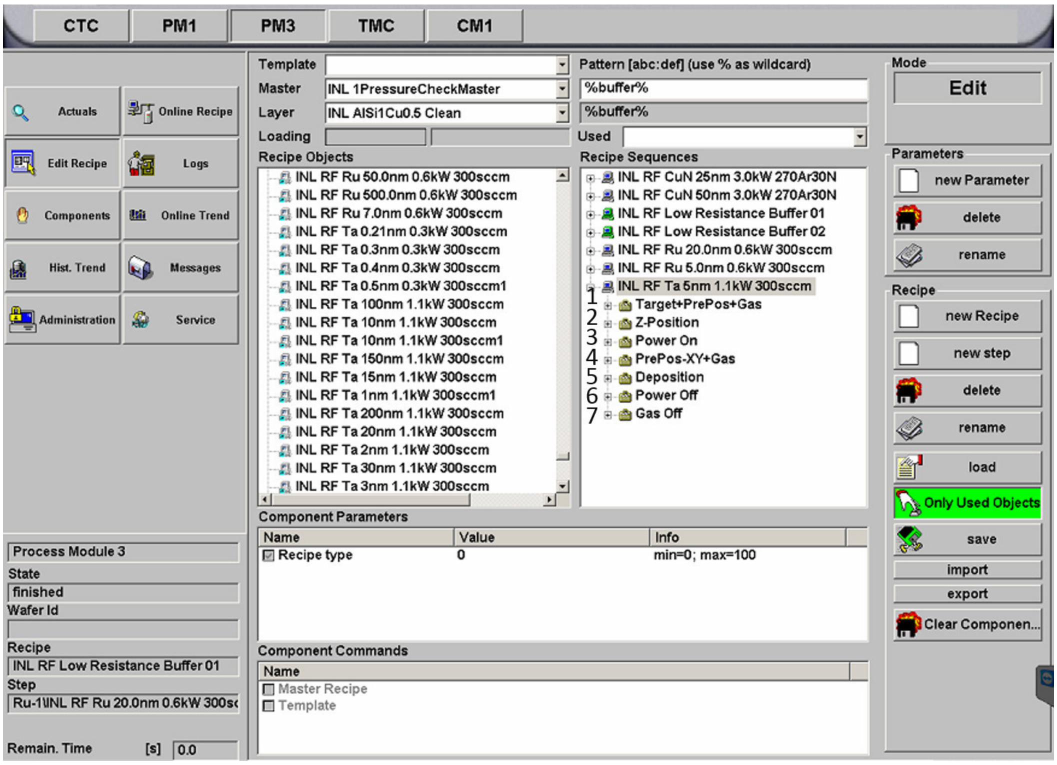

Template
Master: INL 1PressureCheckMaster
Layer: INL AlSi1Cu0.5 Clean
Loading

Pattern [abc:def] (use % as wildcard): %buffer%
%buffer%
Used

Recipe Objects
- INL RF Ru 50.0nm 0.6kW 300sccm
- INL RF Ru 500.0nm 0.6kW 300sccm
- INL RF Ru 7.0nm 0.6kW 300sccm
- INL RF Ta 0.21nm 0.3kW 300sccm
- INL RF Ta 0.3nm 0.3kW 300sccm
- INL RF Ta 0.4nm 0.3kW 300sccm
- INL RF Ta 0.5nm 0.3kW 300sccm1
- INL RF Ta 100nm 1.1kW 300sccm
- INL RF Ta 10nm 1.1kW 300sccm
- INL RF Ta 10nm 1.1kW 300sccm1
- INL RF Ta 150nm 1.1kW 300sccm
- INL RF Ta 15nm 1.1kW 300sccm
- INL RF Ta 1nm 1.1kW 300sccm1
- INL RF Ta 200nm 1.1kW 300sccm
- INL RF Ta 20nm 1.1kW 300sccm
- INL RF Ta 2nm 1.1kW 300sccm
- INL RF Ta 30nm 1.1kW 300sccm
- INL RF Ta 3nm 1.1kW 300sccm

Recipe Sequences
- INL RF CuN 25nm 3.0kW 270Ar30N
- INL RF CuN 50nm 3.0kW 270Ar30N
- INL RF Low Resistance Buffer 01
- INL RF Low Resistance Buffer 02
- INL RF Ru 20.0nm 0.6kW 300sccm
- INL RF Ru 5.0nm 0.6kW 300sccm
- INL RF Ta 5nm 1.1kW 300sccm
  1 Target+PrePos+Gas
  2 Z-Position
  3 Power On
  4 PrePos-XY+Gas
  5 Deposition
  6 Power Off
  7 Gas Off

Component Parameters

Name	Value	Info
☑ Recipe type	0	min=0; max=100

Component Commands

Name
☐ Master Recipe
☐ Template

Process Module 3
State: finished
Wafer Id:
Recipe: INL RF Low Resistance Buffer 01
Step: Ru-1\INL RF Ru 20.0nm 0.6kW 300s
Remain. Time [s] 0.0

Figure 2.3: Timaris MTM software. Steps that determine a single layer deposition recipe.

wafer positioned in the starting position. In step 2 the magnet height is adjusted, in step 3 the RF power is turned on to start the plasma, and in step 4 the magnet position is defined (the magnet follows the wafer during deposition). In step 5 the wafer moves into the deposition chamber so that the material is deposited (the number of passes and velocity will define the film thickness). Steps 6 and 7 stop the RF power and the injected gas, respectively. This example represents a low level recipe, higher level recipes are then defined and sequences with etch, alignment and multistack depositions can be performed.

2.1.1.2 *Kenosistec*

The Kenosistec deposition system (Fig. 2.4) is another sputtering magnetron tool available at INL, having eleven 2″ diameter magnetrons. It includes 11 magnetrons in a confocal geometry for the co-deposition of materials optimized for 200 mm wafers and achieving uniformities down to 5%. Since the used targets are smaller than in the case of the Timaris MTM system (previous section), the uniformity over a 200 mm wafer is also smaller. Therefore, the Kenosis-

Target	Power (W)	Voltage (V)	Current (mA)	Flux (sccm)	Press. (mbar)	Dep. rate ($\dot{A}/s$)
Pt	30	410	76	5	2.7×10^{-3}	0.492
Co	50	325	150	15	5.3×10^{-2}	0.1846
Ta	50	330	150	5	2.8×10^{-3}	0.248

Table 2.2: Deposition conditions of the materials deposited in the Kenosistec deposition.

tec tool was mainly used to test and optimize thicknesses and structures and as a backup tool for the deposition of capping layers. Moreover, since the targets in this tool are smaller, the most expensive materials, such as Pt and Pd, were only available in this system. Hence, it was used for the deposition of materials with strong perpendicular magnetic anisotropy (PMA; such as Co/Pt multilayers).

Each material has different deposition conditions, nevertheless, the same steps are used to start the deposition process. First, with the shutter closed, a plasma is injected into the chamber (usually 5 sccm more than the flux used during deposition) for a few seconds (10-15 s). Afterwards, the RF power is applied to strike the plasma (the same power value used during deposition). After the plasma strike, the Ar flux is decreased to the values that will be used during the deposition (for 15-20 s) to stabilize the plasma in the deposition conditions. The lower flux leads to a smaller pressure and, thus, a slower and more uniform deposition. Finally, the shutter is open and the deposition performed. The deposition conditions along with the deposition rates of the materials used in this thesis (Pt, Co and Ta) are shown in Table 2.2. Despite the smaller targets, the achieved uniformity in the case of materials with strong PMA was enough to enable a functional perpendicular polarizer over full 200 mm wafers (see chapter 6).

2.1.1.3 *Timaris flexible target module (FTM)*

Both the Timaris MTM and the Kenosistec are high precision tools for the deposition of ultra-thin films with sub-nm precision. However, there are several parts of the process where the required thickness of the films is higher and such accurate deposition is not necessary. In fact, for these stages of the process, a less time consuming deposition is an advantage.

The Timaris flexible target module (FTM) tool (Fig. 2.5) also located in the INL cleanroom is a magnetron sputtering system for the rapid deposition of thick films. This tool consists of a central dealer, a 200 mm-cassette load-lock, a four-target linear module (AlSiCu, TiWN, SiO_2 or Al_2O_3) with two DC and one RF sources, and a soft etch module. The targets are rectangular with dimensions of 420 × 110 mm^2. This tool allowed us to perform the steps of metallization and passivation during the nanofabrication process of MTJs.

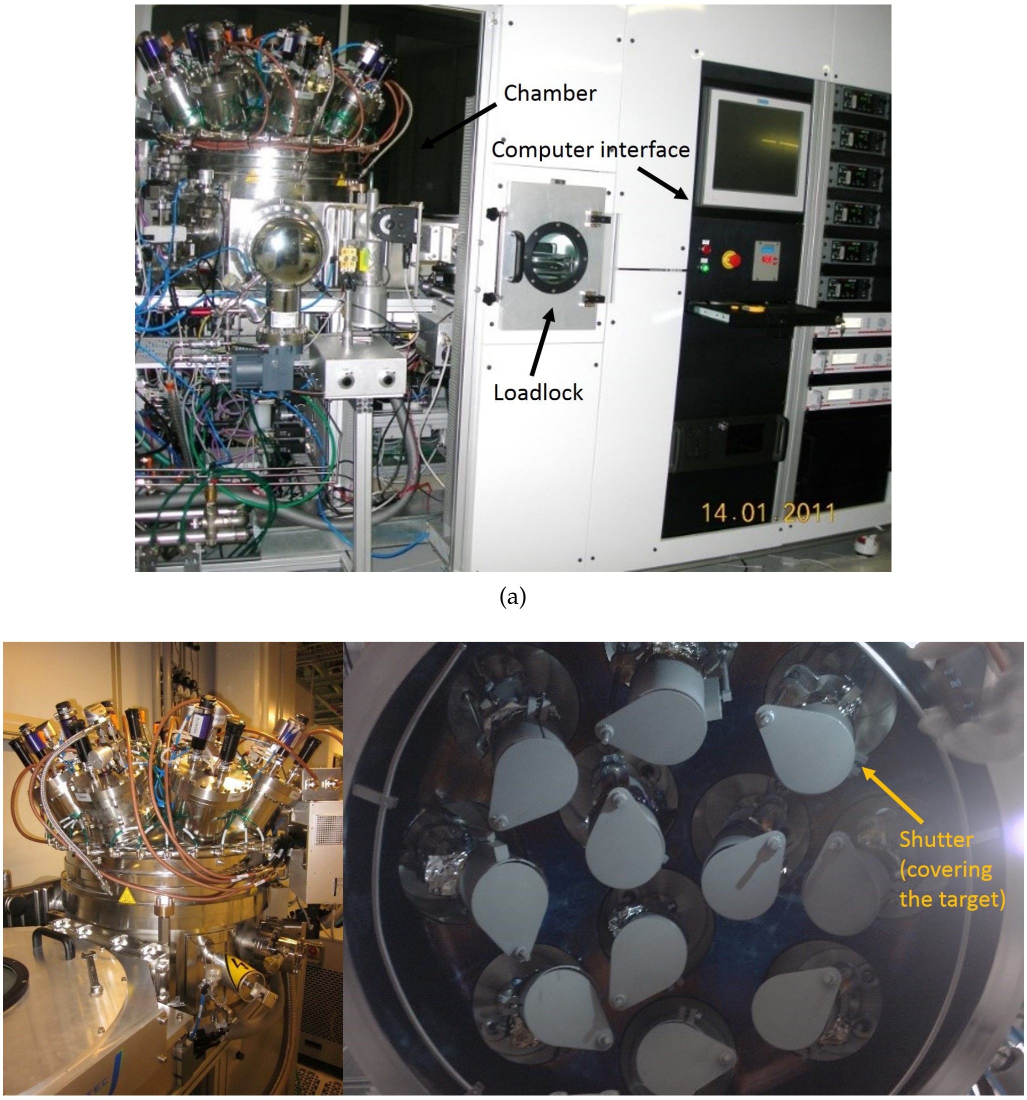

(a)

(b) (c)

Figure 2.4: Kenosistec magnetron sputtering system located in the INL cleanroom. (a) Overview of the tool; (b) deposition chamber and (c) targets inside the chamber covered by the shutters.

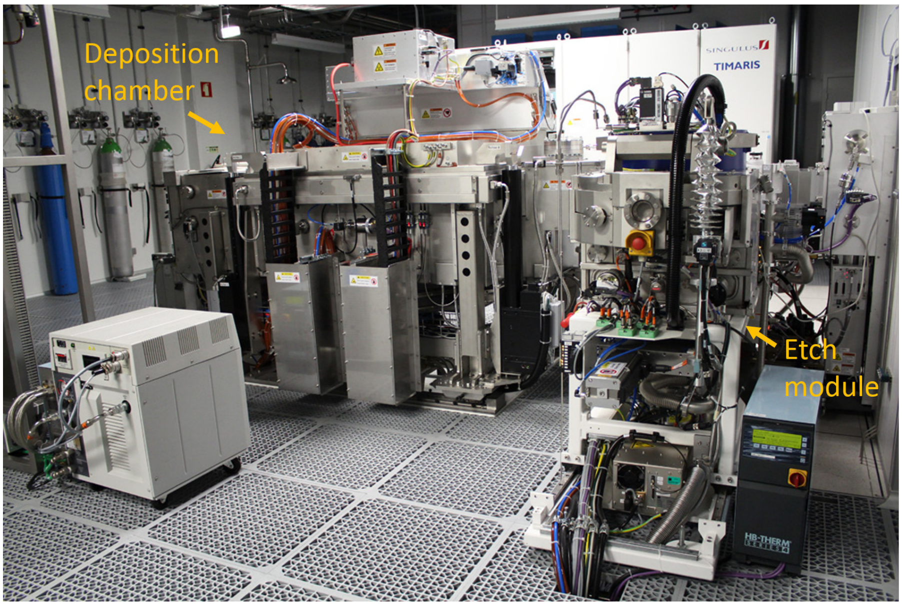

Figure 2.5: Timaris FTM sputtering system for thick layer depositions (INL cleanroom).

Figure 2.6 shows the software interface with two distinct levels of the recipe definition. Figure 2.6(a) depicts a high level recipe where an etch followed by three depositions is performed. The wafer alignment is performed only in the first step and the angle can also be defined. In Fig. 2.6(b) the detailed steps performed in each layer deposition is shown. These steps define several parameter, such as stage speed, number of passes, Ar flux, or process time. This allows a high control of the deposition rates that can be adapted depending on the needs.

2.2 ETCHING SYSTEMS

The fabrication process developed during this thesis was mostly based on etching (only one step of the process based on lift-off). Etching processes are a fundamental part of micro and nanofabrication procedures to ensure the transfer of the pattern from the lithography to the deposited materials (see section 2.3). They allow the fabrication of well-defined structures with sharp features and the definition of multilayers, being usually faster and cleaner (fewer residues) than lift-off processes.

MTJ TiWN 15nm/AlSiCu 300nm/TiWN 50nm with Etch

Step	Master Name	Modul Type	Align	Angle	Step Ex...	Step
1	Etch 100W 200sccm 120s	Etch	True	0.0	1	
2	INL MEMS TiWN 15nm 1000W 20...	FTM	False	0.0	1	
3	INL MEMS AlSiCu 300nm 2250W ...	FTM	False	0.0	1	
4	INL TiWN 50nm	FTM	False	0.0	1	

(a)

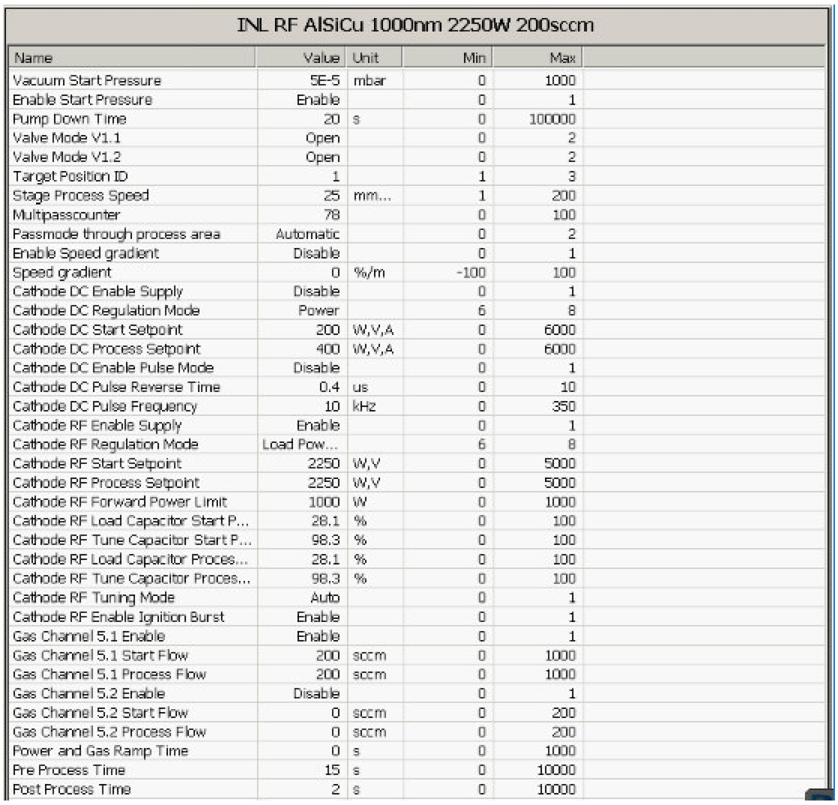

INL RF AlSiCu 1000nm 2250W 200sccm

Name	Value	Unit	Min	Max
Vacuum Start Pressure	5E-5	mbar	0	1000
Enable Start Pressure	Enable		0	1
Pump Down Time	20	s	0	100000
Valve Mode V1.1	Open		0	2
Valve Mode V1.2	Open		0	2
Target Position ID	1		1	3
Stage Process Speed	25	mm...	1	200
Multipasscounter	78		0	100
Passmode through process area	Automatic		0	2
Enable Speed gradient	Disable		0	1
Speed gradient	0	%/m	-100	100
Cathode DC Enable Supply	Disable		0	1
Cathode DC Regulation Mode	Power		6	8
Cathode DC Start Setpoint	200	W,V,A	0	6000
Cathode DC Process Setpoint	400	W,V,A	0	6000
Cathode DC Enable Pulse Mode	Disable		0	1
Cathode DC Pulse Reverse Time	0.4	us	0	10
Cathode DC Pulse Frequency	10	kHz	0	350
Cathode RF Enable Supply	Enable		0	1
Cathode RF Regulation Mode	Load Pow...		6	8
Cathode RF Start Setpoint	2250	W,V	0	5000
Cathode RF Process Setpoint	2250	W,V	0	5000
Cathode RF Forward Power Limit	1000	W	0	1000
Cathode RF Load Capacitor Start P...	28.1	%	0	100
Cathode RF Tune Capacitor Start P...	98.3	%	0	100
Cathode RF Load Capacitor Proces...	28.1	%	0	100
Cathode RF Tune Capacitor Proces...	98.3	%	0	100
Cathode RF Tuning Mode	Auto		0	1
Cathode RF Enable Ignition Burst	Enable		0	1
Gas Channel 5.1 Enable	Enable		0	1
Gas Channel 5.1 Start Flow	200	sccm	0	1000
Gas Channel 5.1 Process Flow	200	sccm	0	1000
Gas Channel 5.2 Enable	Disable		0	1
Gas Channel 5.2 Start Flow	0	sccm	0	200
Gas Channel 5.2 Process Flow	0	sccm	0	200
Power and Gas Ramp Time	0	s	0	1000
Pre Process Time	15	s	0	10000
Post Process Time	2	s	0	10000

(b)

Figure 2.6: Timaris FTM software. Definition of a deposition recipe: (a) sequence of the etching and deposition steps of a high level recipe and (b) detailed steps used to perform a single deposition.

2.2.1 *Ion Milling*

There are several etching processes, such as ion milling, reactive ion etch and wet etch. In what concerns the work performed in this thesis, the removal of material was performed using ion milling [114] [Nordiko 7500; Fig. 2.7(a)]. This ion milling tool includes a loadlock, a dealer and a process chamber for 200 mm wafer.

In an ion milling system, a physical etch induced by incident ions is performed. To do that, it is first necessary to create a plasma. The plasma is created in an ion gun outside the deposition chamber, to avoid the formation of defects. To create the plasma Ar atoms are used. A small flux (usually 20 sccm) is provided to the chamber. The power required to ionize the gas atoms is provided by an RF source. In order for the RF power to be effectively absorbed by the plasma the impedance of the RF supply circuit must be matched with the impedance of the plasma. This is performed with two adjustable capacitors, the first connected between the RF source and the power supply and the second between the power supply and the ground. The adjustment of the capacitors is done automatically when striking the ion gun by an impedance coupling circuit board. The heat excess created by the plasma is removed through a cooling water system.

The ions of the plasma beam used during the milling process will lead to charge accumulation. This charge accumulation generates a varying etching rate (the ions of the beam are decelerated by the sample charge); the charge accumulation in resist masks or thin dielectrics might cause electrostatic discharges that damage the dielectric materials; and the repulsion between ions in the beam changes its shape decreasing the etching uniformity. To minimize these effects, two neutralizers were used. These neutralizers emit electrons that neutralize the beam of positively charged ions, minimizing this repulsion effect and increasing the uniformity. Furthermore, they will also improve the convergence of the beam. The electron beam current is around 20% above the ion beam in order to neutralize the totality of the ions. Two voltages (with opposite polarities) are then used to control the plasma: one to extract the positively charged ions of the plasma after its formation and another to accelerate the ions to the required energy. This grid assembly consists of three grids with a specific hole pattern with several apertures that form the broad ion beam. The source generates a plasma, which can be extracted from the ion source through the grids with a well defined energy. The specific voltages applied between the grids provide the driving force and focusing of the ions. Therefore, the optimization of such parameters allowed us to optimize the etching rate and the uniformity of the process. Two sets of etching conditions were used during the sample fabrication: (1) high etch rate conditions and (2) low etch rate conditions (Table 2.3). The low etching rate conditions were necessary to etch the sensitive magnetic layers of the MTJs, while the higher etching rate conditions with better uniformity were used as the standard recipe.

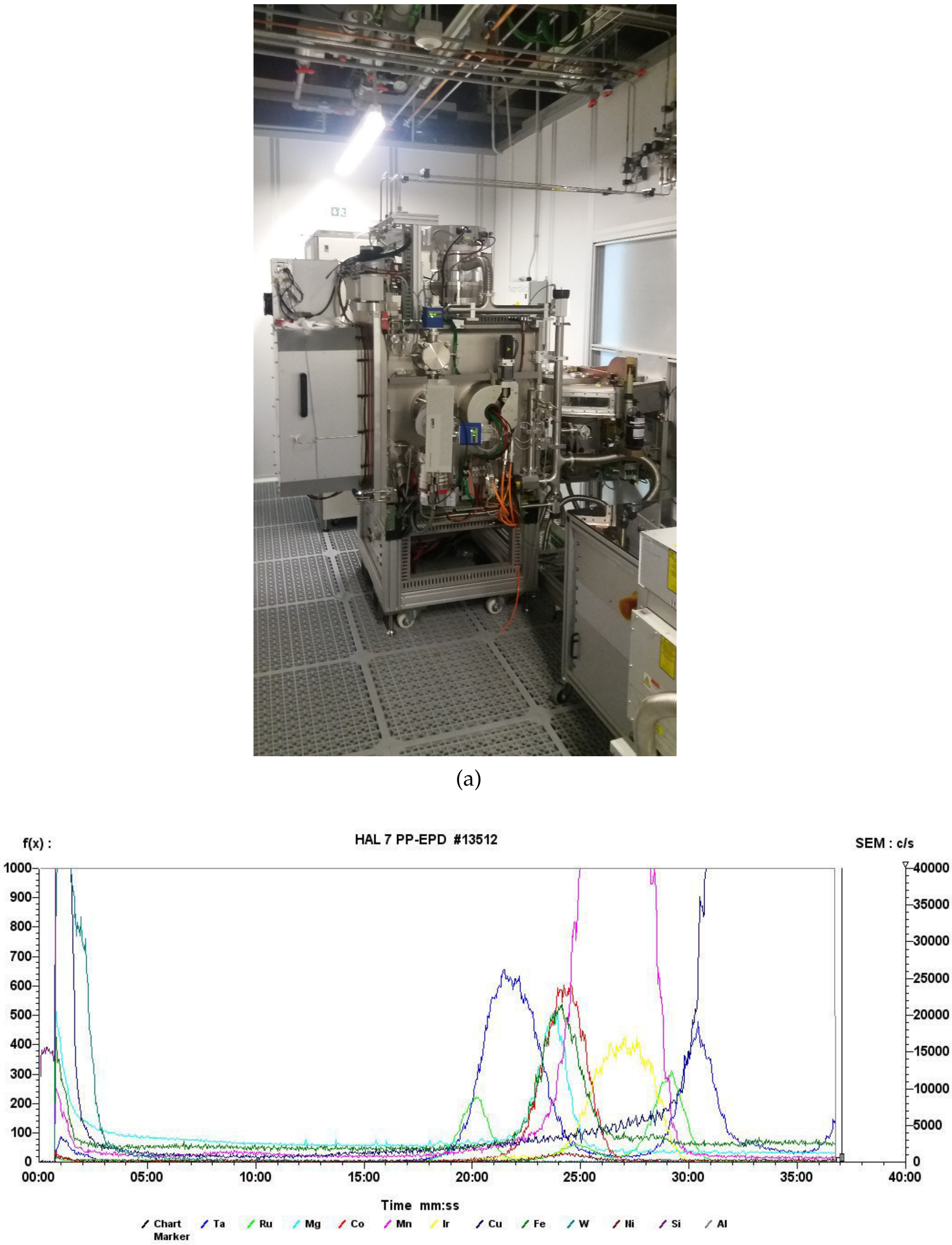

(a)

(b)

Figure 2.7: (a) Nordiko 7500 for physical ion milling (INL cleanroom). (b) SIMS plot used to determine the etching stopping point during MTJ definition.

	Power (W)	Pos. voltage (V)	Neg. voltage (V)	Intensity (mA)
High rate	360	600	-2250	235
Low rate	370	150	-1750	235

Table 2.3: Etching conditions of the high and low rate recipes.

Material	Al_2O_3	Ta	Cu
Etch rate (nm/min)	4.0	5.0	10.0

Table 2.4: Etch rate for different materials (for an incident angle of 50° and HE conditions).

Note that these conditions were fine-tuned when necessary (due to changes in the chamber conditions inherent to the use of the tool), although always within small variations of the standard parameters.

To improve the etching uniformity during process, the wafer is rotating with an adjustable speed (30 rpm were usually used). Moreover, the angle between the incident beam and the wafer normal can be controlled. The adjustment of this angle is not trivial because a normal incidence leads to a high quantity of redeposited material while a grazing angle leads to shadow effects that prevent the formation of vertical sidewalls. It was observed that an incident angle of 50° led to the most vertical sidewalls and thus this condition was used in the majority of the millings performed. For the processes where a grazing angle was necessary (sidewall cleaning and ion beam planarization), an incident angle of 10° was used (see Chapter 3). The etching angle also affected the uniformity and etch rate of the process. In fact, by changing the incident angle from 50° to 10° (at HE conditions), the etching rate in Al_2O_3 passed from 4.0 nm/min to 1.2 nm/min. Different materials also depict different etch rates, as shown in Table 2.4 (for an incident angle of 50°). The LE conditions also depict a lower etch rate when compared to the HE conditions (approximately 7 times lower for metals).

Due to the fact that the ion milling is a non-selective process that allows us to easily etch multilayers (e.g. MTJ stacks), it is critical to correctly choose the stopping point of the etching process. To do that, a secondary ion mass spectrometer (SIMS), incorporated with the etching system, was used. This detector uses an applied magnetic field to induce a parabolic path to the etched atoms. Atoms with different mass/charge ratios are then collected from different detectors and the elemental composition of the etched materials can be determined. In Fig. 2.7(b) we show an example of a SIMS plot used to determine the stopping point during the MTJ definition.

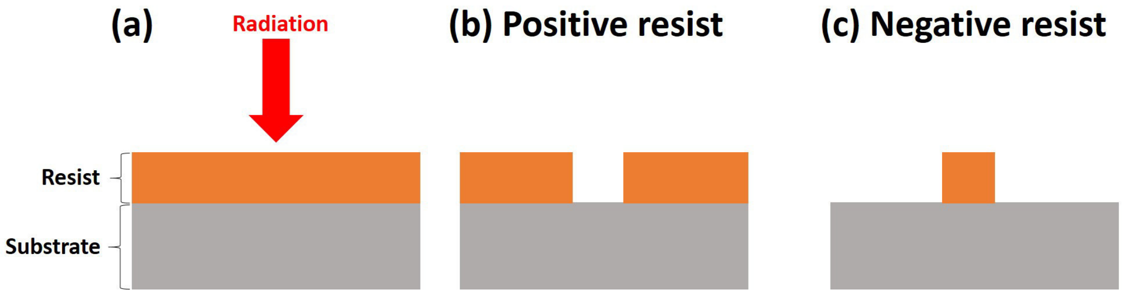

Figure 2.8: Schematic representation of the lithographic process. (a) A sample covered with resist is irradiated. Effect after development for (b) positive and (c) negative resist.

2.3 LITHOGRAPHIC TECHNIQUES

To develop devices with dimensions ranging from the µm down to the nm scale, the ability to selectively deposit or remove materials from a substrate is required. To do that, a mask with the expected features is used and a pattern can be defined [115]. This mask consists of a sensitive polymer called photoresist (PR). More precisely, when exposed to light with a specific wavelength (oprtical lithography) or electrons (e-beam lithography), a chemical reaction is triggered that can either break or induce connections between the polymer molecules and thus change the solubility of the PR in a developer solution. Thus, the PR can either become more polymerized (negative PR), or more soluble (positive PR) upon incident radiation [Fig. 2.8(a)]. This selective change of solubility can be used to engrave a mask on top of the substrate. Figures. 2.8(b) and (c) schematically represent the definition of the PR mask using a negative and positive PR, respectively. After radiation, a developer solution removes the exposed (not exposed) positive (negative) PR, thus defining the mask.

There are two ways to transfer the pattern to the substrate: etching and lift-off. In an etching process, the material to be patterned is deposited prior to the lithography step. This material is covered with a PR mask that selectively protects the deposited material [Fig. 2.9(a)]. During the etching process, the material that was not protected is removed and thus the pattern transferred [Fig. 2.9(b)]. The removal of the mask is the final part of this micro or nanofabrication process [Fig. 2.9(c)].

In a lift-off process, the first step consists in the definition of a mask that selectively covers a part of it [Fig. 2.10(a)]. Then, the material to be patterned is deposited on the substrate with the mask [Fig. 2.10(b)]. When the PR is removed, the material covering it is also removed and the pattern is transferred [Fig. 2.10(c)]. This removal of the mask is performed by leaving the sample in acetone and ultrasounds. The lift-off process has some limitations since the thicker

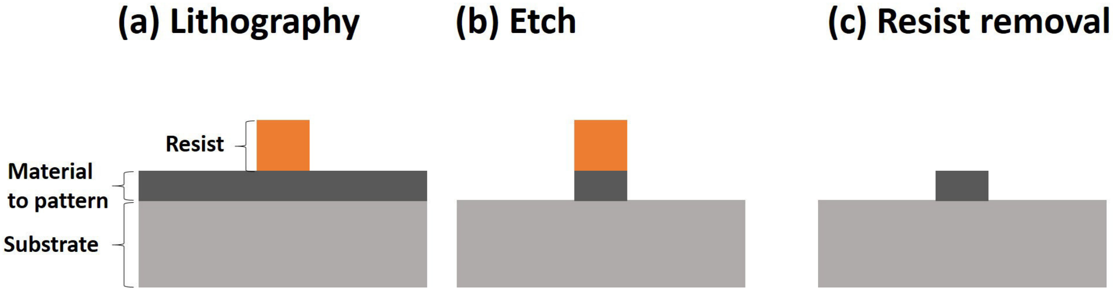

Figure 2.9: Schematic representation of the etching process. (a) Mask definition through lithography; (b) after etch; (c) after removal of the resist.

the deposited material and the smaller the features, the more difficult is the process. Also, the pointy structures ("rabbit ears"), shown in Fig. 2.10(c), are usually a consequence of this process. The lift-off time is also an issue, in particular for the smaller features such as sub-μm MTJs. Depending on the material, the lift-off time can range from a few minutes to weeks [116]. Therefore, in the critical steps, such as the nanopillar definition and the opening of the pillar, etching processes were used. The passivation of the bottom contacts (step 8 of Chapter 3), which have μm dimensions and required the deposition of 15 nm of TiWN, was the only part of the process where lift-off was used. To facilitate the lift-off, an extra chemical treatment (soaking) can be used. This treatment leads to tilted sidewalls [Fig. 2.10(d)] of the PR mask that minimize the contact between the deposited material on top of the PR and the one on top of the substrate [Fig. 2.10(e)] leading to an easier lift-off.

2.3.1 *Coating and developing*

In order to remove any moisture from the substrate and promote the adhesion of the PR and the e-beam resist to the substrate, an HMDS (hexamethyldisilizane) priming process is performed prior to PR coating [vapor prime; Fig. 2.11(a)]. It consists of a thermal treatment with HMDS to maximize the PR adhesion to the sample. This process offers the advantage of combined dehydration and priming in the same process chamber. HMDS forms a strong bond with the oxide surface of the sample, leaving at the same time free bonds to react with the resist and to improve adhesion. An initial high temperature bake and dehydration process is also needed for a uniform and stable vapor priming of the substrates. This step is of critical importance due to the ever diminishing critical feature size in both optical and e-beam lithography.

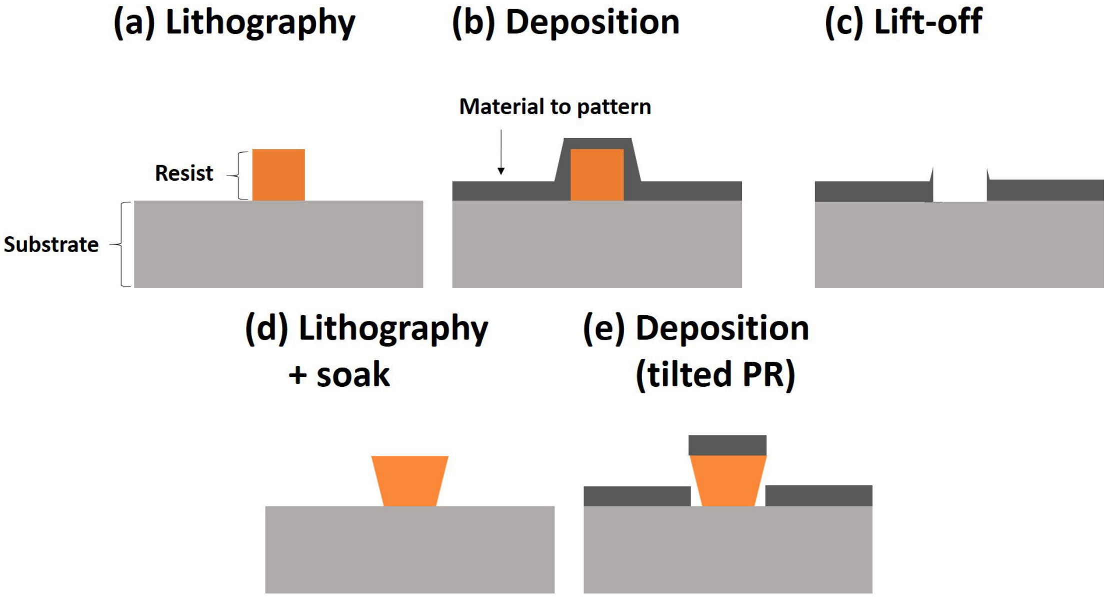

Figure 2.10: Schematic representation of the lift-off process. (a) Mask definition; (b) after material deposition; (c) after lift-off. Representation of the soaking treatment effect (d) PR profile after soak and (e) deposition.

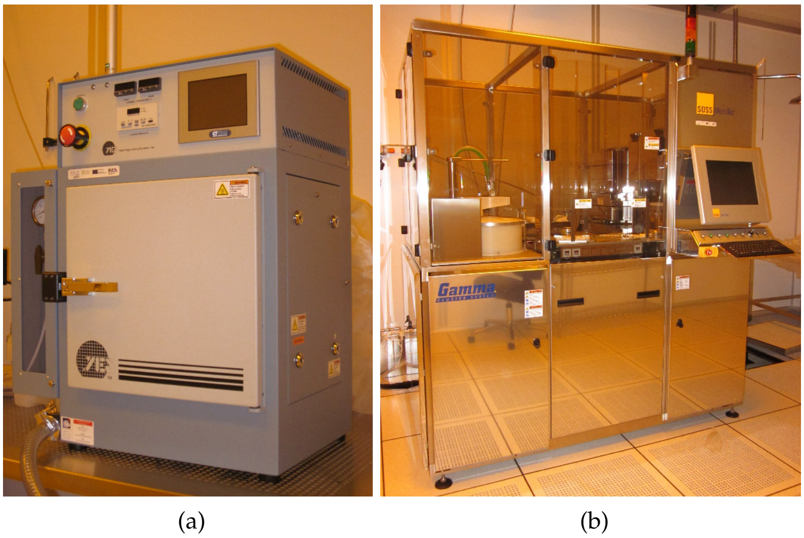
(a) (b)

Figure 2.11: (a) Vapor prime for wafer treatment prior to coating and (b) coating and developing automatic track (INL cleanroom).

To have a homogeneous pattern over a full 200 mm wafer it is essential to have uniform PR coating and developing processes. To do so, sequential spinning and thermal treatments for both coating and developing steps were performed using an industrial Karl Suss Gamma Cluster track [Fig. 2.11(b)]. These cluster tracks enable automatic spin coating and develop processes of up to 200 mm wafers and thick resist coating. They were used for all lithographic processes (both optical and e-beam) and other type of processes such as rinsing with water, developer soaks, or resist removal. The control of the resist thickness after developing [600 nm for the optical lithography and 200 nm for the e-beam lithography was performed using the Nanocalc (see section 2.5.4)].

2.3.2 *Optical Lithography*

Optical lithography [117] is a microfabrication process used to define a pattern that will be transferred to the deposited materials (either by etching or lift-off). In this case, the PR is sensitive to UV light and this radiation is thus used to define the mask (as shown in Fig. 2.8). In this work, the coatings were performed by spin coating AZ1505 photoresist (6 mL) onto a rotating wafer at 1500 rpm, followed by a 30 s rotation at 3500 rpm and a soft bake at 100 °C during 60 s. The development was performed by first cleaning with water for 3 s at 800 rpm, followed by a spin coating of the AZ400K developer (1:4 dilution in water) with a rotation of 800 rpm for 2 s, 35 rpm for 4 s, 10 rpm for 2 s and a 30 s pause (this sequence is then repeated). When required, a soak treatment [Fig. 2.10(d)] was performed after coating. This treatment was performed using the TMAH developer (4:3 dilution in water) by dispensing the TMAH with a rotation of 1500, 800 and 40 rpm for 2 s each, followed by a 40 s stop and cleaning with water (10 s at 800 rpm and 10s at 1000 rpm). Finally, a bake at 100°C for 30s is performed. This coating and developing conditions allowed the fabrication of a relatively thick mask (600 nm) with lateral dimensions down to 1 µm.

2.3.2.1 *Direct Write Lithography (DWL)*

Direct Write Lithography (DWL) allows the direct writing of a pattern in a PR by using a laser beam. This is a maskless lithographic system which offers flexibility, ease of use and cost effectiveness. A digital mask (autoCAD software) is provided to the DWL software where it is converted. Afterwards, a coated sample is prepared and aligned and the laser exposes the mask pattern. After the exposure and developing, the pattern will be transferred to the PR. This is a raster technique since the pattern is written using a UV laser that will draw the mask provided to the software.

We used a DWL 2000 (Fig. 2.12) located in the INL cleanroom which has the capability of exposing at two different wavelengths (405 and 375 nm; in the scope of this thesis 405 nm was the used wavelength). The maximum speed is 105 mm^2 per minute, with a 700 nm minimum structure size. It has the option to autofocus either pneumatically or optically, with programmable scripts for automatic measurements of critical dimensions. The autofocus capability is essential to process wafers with several steps and topography. Alignment marks are defined in each step which allows different layers of the process to be aligned during overlay. As will be shown in the next chapter, the alignment marks have a cross shape and the system detects the centre of this mark with an error $< 0.5\ \mu$m. On top of that, there is also a positioning error of the stage of $\sim 0.1\ \mu$m.

The main disadvantage of the DWL is its long exposure time. For instance, a layer exposed in a full 200 mm wafer can take up to 8 hours to be completed, depending on the number of dies. The main advantage is that it is an adaptable tool and the masks can be easily changed and adapted to each process. Thus, it is the adequate tool to develop new designs and perform complementary studies. Despite the fact that a mask aligner (next section) is a faster lithographic tool, variations and improvements of the masks used were continuously performed. Therefore, the DWL was the main tool used to perform the optical lithography steps.

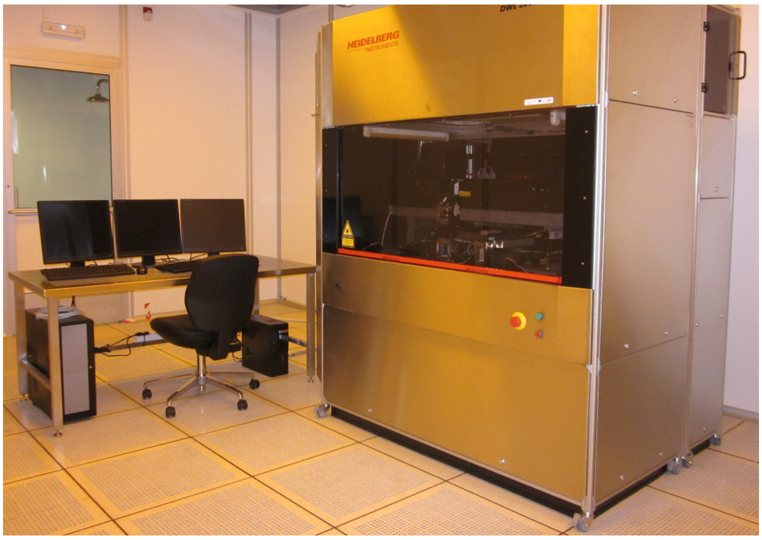

Figure 2.12: Optical lithography system DWL 2000 (INL cleanroom).

2.3.2.2 *Mask aligner*

To obtain a viable process at an industrial scale, a fast lithographic process over a full wafer is required. To achieve a fast exposure, a raster technique such as the DWL is not the best option. A different approach consists in using a physical photomask with the desired pattern [Fig. 2.13(a)]. The irradiation is performed with a UV source that covers the full wafer. The mask will selectively protect the sample upon UV incidence and thus transfer the pattern to the PR. The masks were prepared using the DWL and a transparent substrate (soda-lime) covered by a chromium/chromium oxide film. These photomasks are expensive and were therefore only used after process optimization, with masks being prepared for each of the 5 steps of the process that required optical lithography.

We used a Karl Suss MA6 BA6 mask aligner [Fig. 2.13(b)] located in the INL cleanroom. It is a high resolution mask aligner that allows us to perform vacuum contact (with vacuum between mask and sample), hard contact (mask and sample in physical contact) and proximity (small gap between sample and mask) exposures. The exposures with contact can achieve better resolution but damage the mask. Since in our process we only used the optical lithography to define the big structures of our final devices, the proximity mode exposure (with a gap of 20 μm) was used. The exposure times changed throughout the work performed in this thesis due to changes inherent to the UV light source. However, the required exposure time was always of the order of 3 s (with 15 s of contact). Moreover, contrary to the DWL system, the exposure of a larger surface of the wafer does not lead to an increase of the process time.

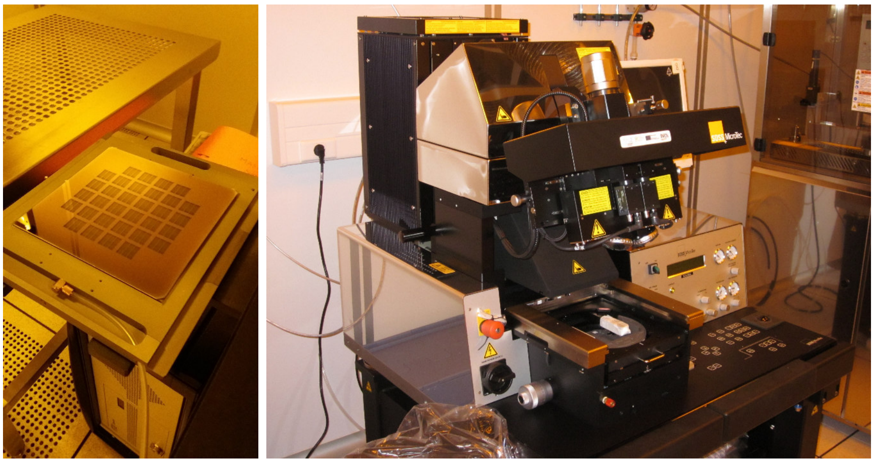

(a) (b)

Figure 2.13: (a) Photomask used in a (b) mask aligner system (INL cleanroom).

The mask aligner system also allows the alignment of different exposures provided that the alignment marks are defined.

2.3.3 *Electron-beam lithography*

The fabrication of the MTJs for STNOs applications requires a resolution in the nanometer scale that cannot be achieved using a standard optical lithography tool. The minimum feature size of a lithographic system is given approximately by:

$$d = k\frac{\lambda}{NA}, \tag{2.1}$$

where k is a constant coefficient (typically 0.4 for optical lithography production), λ the wavelength and NA is the numerical aperture as seen from the wafer. To decrease the feature size we can either increase NA (by using a tighter focused beam) or decrease the wavelength of the beam. To decrease λ we can use the wavelength characteristic of electron beams (e-beams) that arises from the particle-wave duality (de Broglie relation). In fact, the wavelength associated to the electrons is typically of the order of 3.7 pm (100 keV).

Hence, e-beam lithography [118, 119] is a technique similar to its optical counterpart but, instead of UV light sources, uses e-beams which significantly decrease the minimum feature size. This technique is more similar to the DWL in the sense that it is a raster technique instead of using a physical mask as in a mask aligner.

Other factors also contribute to an accentuated improvement of the resolution of e-beam lithography. First, the focusing of the beam is performed with electromagnetic lenses that lead to beam diameters of typically 2 nm. Also, the chemical nature of the e-beam resist differs from those for optical lithography. In the case of the negative e-beam resist (which was the type used in this thesis), the resolution is associated to the size of the molecules formed after e-beam irradiation. For the used resist (ARN7520) the minimal feature size that it can form is 30 nm. In fact, the smallest pillars obtained in this work had 50 nm of diameter, which is comparable to the minimal possible size. Furthermore, due to the competition between resist cohesion and surface energy, any resist has a certain maximum aspect ratio that can be obtained (5 in the case of the ARN7520). Thus, a thinner resist thickness allows the achievement of smaller features. Then, the use of smaller resist thicknesses in the case of the e-beam lithography when compared to the optical lithography further enables the definition of smaller structures. However, care must be taken since if the resist thickness is too small, it might be completely removed during the etching process.

We used a Vistec 5200 ES 100 kV tool (Fig.2.14). This e-beam lithography system is designed for high resolution fabrication of structures down to 8 nm (with the proper resist and exposure conditions). The used e-beam resist consisted in the diluted 1 part ARN7520-18 and 1 part AR300-12. The spin coating was performed at 2750 rpm and the soft bake at 85 °C for 60 s leading to a 200 nm thickness. The development was performed with the developer AR 300-47 diluted (4 parts developer, 3 parts deionized water). With this resist and the optimized exposure conditions (step of 2 nm, a dose of 612 $\mu C/cm^2$ and a beam current between 330 pA and 1 nA) we were able to achieve dimensions down to 50 nm (resist thickness of 200 nm). These features were used for the nanopillar definition. The exposures could be performed in glass or Si without significant changes on the final lithographic features.

2.3.4 *Resist strip*

The process of resist removal after exposure can be performed using acetone and ultrasounds (as in the case of lift-off processes). However, this system for resist removal is usually time consuming. Moreover, processes such as physical etching can modify the properties of the resist and further hamper resist removal. Therefore, a simple and fast way to selectively remove this material represents a significant improvement of the process.

The PVA Tepla GIGAbatch 360M (plasma asher; Fig. 2.15) is a system designed for the removal of PR and other polymers. It can also be used for surface activation for posterior processes. It offers, in principle, good selectivity of resist with respect to metals and oxides. However, care must be taken since we observed that it can oxidize Cu and even remove Ru. On the other hand, it works quite effectively with TiWN or oxide top layers. This system uses

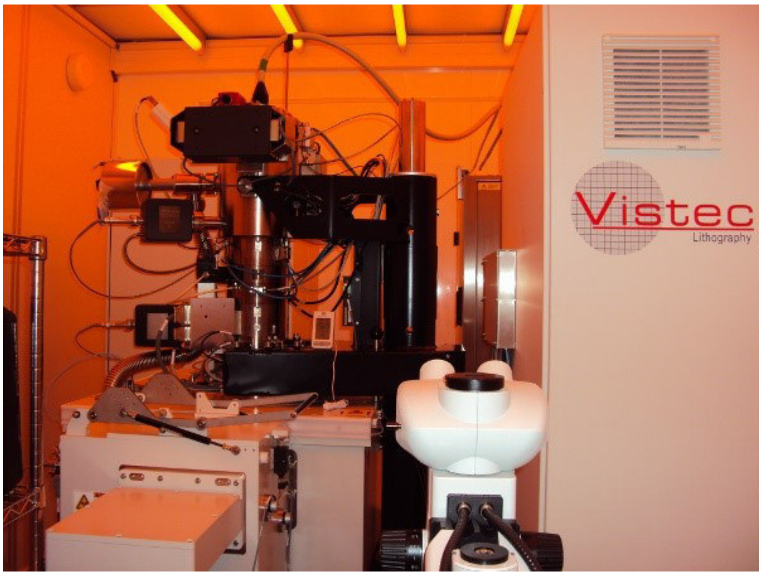

Figure 2.14: e-beam lithography system placed in the INL cleanroom.

a microwave plasma operating at 2.45 GHz with typical process pressure ranging from 0.6 to 1.5 mbar. This microwave plasma (without radio frequency power) is the reason why it is so selective to organic compounds. The design of the plasma asher is not optimized for a uniform process; for this a higher control of the temperature along the wafer would be necessary. However, since this is a selective process, the uniformity is not relevant because the process can be performed until the polymer is removed in every region of the wafer surface. The gases available are O_2, N_2, Ar, and CF_4. The resist strip process that we used consisted in an atmosphere of O_2 (200 sccm) and Ar (200 sccm), a microwave plasma with a power of 230 W and a starting pressure of 0.2 mbar (0.63 mbar during process) and a maximum temperature between 110 and 130 °C. Note that the removal rate is highly temperature dependent. The used process was optimized to remove all the resist without a significant temperature increase.

The plasma asher was used in most resist strip steps. Unfortunately, it cannot be used for lift-off since a physical mechanism (such as ultrasounds) is necessary to break the material deposited on top of the PR. Moreover, the plasma asher was found to damage the MTJ nanopillars (see Chapter 3) and thus could not be used to remove the e-beam resist after etching.

This system was also used as a pre-treatment for the wafer before coating with e-beam resist (followed by vapor prime). It was verified that the samples with this pre-treatment revealed a better adhesion of the resist allowing the definition of nanopillars with smaller sizes. This

Figure 2.15: Plasma asher system for resist removal located in the INL cleanroom.

effect is probably caused by the removal of some organic compounds that can be present on the surface of the sample due to successive lithographies. Unfortunately, it could only be used with TiWN capping layers since Ru was affected by the plasma asher.

2.4 MAGNETIC ANNEALING

The annealing step is of fundamental importance to induce the proper crystallographic orientation and achieve fully epitaxial (001)-oriented CoFeB/MgO/CoFeB MTJs that maximize the tunnel magnetoresistance (TMR). It is also important to obtain stacks with different magnetic properties [120], such as strongly pinned layers, orthogonal magnetic orientations between free and pinned layers, perpendicular magnetic anisotropy, etc. To achieve these properties, the annealing is performed under an applied magnetic field to induce the desired magnetic orientation during re-crystallization. A magnetic annealer (Fig. 2.16) that allowed uniform annealings up to 400° under controlled magnetic fields (up to 2 T), in Ar or vacuum, with programmable temperature ramps and cool down was used. The standard annealing conditions used to obtain MTJs with high TMR consisted in 330 °C at 1 T for 2 hours with cooling (with He atmosphere) while the magnetic field was still applied. An example of the software interface depicting the temperature change during this standard annealing is shown in Fig. 2.17. The tool allows not only the control of the temperature, times and magnetic fields but also the temperature slope.


(a) (b)

Figure 2.16: Magnetic annealer located in the INL magnetometry laboratory.

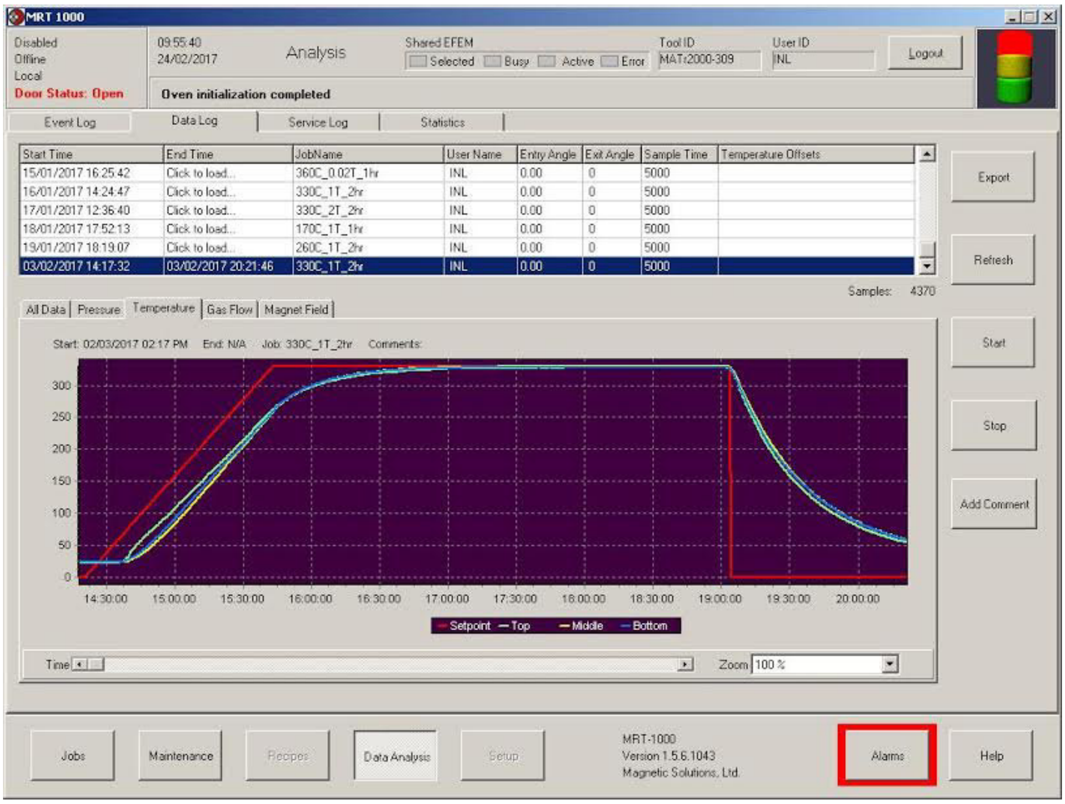

Disabled
Offline
Local
Door Status: Open

09:55:40
24/02/2017

Tool ID MAT:2000-309
User ID INL

Oven initialization completed

Start Time	End Time	JobName	User Name	Entry Angle	Exit Angle	Sample Time	Temperature Offsets
15/01/2017 16:25:42	Click to load...	360C_0.02T_1hr	INL	0.00	0	5000	
16/01/2017 14:24:47	Click to load...	330C_1T_2hr	INL	0.00	0	5000	
17/01/2017 12:36:40	Click to load...	330C_2T_2hr	INL	0.00	0	5000	
18/01/2017 17:52:13	Click to load...	170C_1T_1hr	INL	0.00	0	5000	
19/01/2017 18:19:07	Click to load...	260C_1T_2hr	INL	0.00	0	5000	
03/02/2017 14:17:32	03/02/2017 20:21:46	330C_1T_2hr	INL	0.00	0	5000	

Samples: 4370

Start: 02/03/2017 02:17 PM End: N/A Job: 330C_1T_2hr Comments:

MRT-1000
Version 1.5.6.1043
Magnetic Solutions, Ltd.

Figure 2.17: Annealing software interface depicting the temperature data of a standard annealing (330 °C at 1 T for 2 hours).

2.5 STRUCTURAL CHARACTERIZATION

The fabrication of sub-µm MTJs for STNOs applications is a complex process that involves the optimization of the electrical and magnetic counterparts for the final device fabrication. Furthermore, the miniaturization of the MTJs with low RA while maintaining high TMR is a challenging task. Hence, high quality structural characterization is a requirement to optimize MTJ nanofabrication by obtaining critical insights on the morphology and crystallinity of the nanofabricated devices.

2.5.1 *Scanning electron microscopy (SEM)*

The basis of electronic microscopy is the wavelength associated to incident electrons from the de Broglie relation. This wavelength decreases with the increase of kinetic energy and has a typical value of 0.1 nm in electronic microscopes. Therefore, the process is similar to an optical microscope but the electron beam setting and focusing is performed by electrostatic and magnetic lenses. The short wavelengths can lead to an extremely small electron beam diameter and angular aperture, allowing a much higher resolving power and field depth. Hence, scanning electron microscopy (SEM) [121, 122] was used in the scope of this thesis to study the morphology of the fabricated nanodevices, providing images with a resolution below 5 nm. SEM consists in irradiating a sample with a beam of high energy electrons focused by a set of magnetic lenses. As the electrons hit each spot of the sample, electrons and photons are emitted by the specimens in the surface. This radiation will then be used to form the SEM image, being the most commonly used the secondary electrons, backscattered electrons and X-rays. The SEM operation requires the use of high vacuum chambers.

Here, we used a NovaNanoSEM 650 (Fig. 2.18) that detects the secondary electrons (with two secondary electron detectors with accelerating voltages from 0.5 – 30 kV). These electrons are the product of ionization and provide a clear and focused topographical image of the sample. This system is capable of handling multiple sample/wafer sizes up to 200 mm. It uses a cold field emission electron source and can achieve an ultimate resolution of 1.0 nm at 15 kV and 2.0 nm at 1 kV. The NovaNano SEM is fully integrated with an automation software to enable the full control of the scanning electron microscope for metrology recipe creation, image and edge recognition, scanning and stage movements.

The SEM inspection was mostly used to control the parts of the process that concern the nanopillar fabrication and opening. It was used to inspect the morphology, control the time of the sidewall cleaning process and detect the stopping point of ion beam planarization, as will be described in the next chapter.

Figure 2.18: SEM located in the INL cleanroom.

The SEM also incorporates an energy dispersive spectroscopy (EDS) tool that analyzes the emitted X-ray spectrum determining the elemental composition of the sample. The electron beam ionizes inner shell electrons of the sample atoms and the resultant vacancy is filled by an outer electron, which emits energy in the form of Auger electrons or X-rays. Since these radiations are specific for each element, the composition of the material can be inferred. This technique allows a qualitative and/or quantitative analysis on the elements present at different points of the sample and to map the concentration of an element as a function of the position.

2.5.2 *Transmission electron microscopy (TEM)*

Similarly to the SEM, the transmission electron microscope (TEM) [123] also uses an electron beam to obtain high resolution imaging. However, in the case of the TEM, the detected electrons are transmitted through a very thin sample ($<$ 500 nm of thickness). The electrons passing through the sample interact with its structure, being more reflected in the region where the atoms are present and more easily transmitted where they are not. From the pattern of the transmitted electrons we are able to obtain microscopic images with atomic resolution. TEM requires extensive sample preparation and was thus not as extensively used as SEM. However,

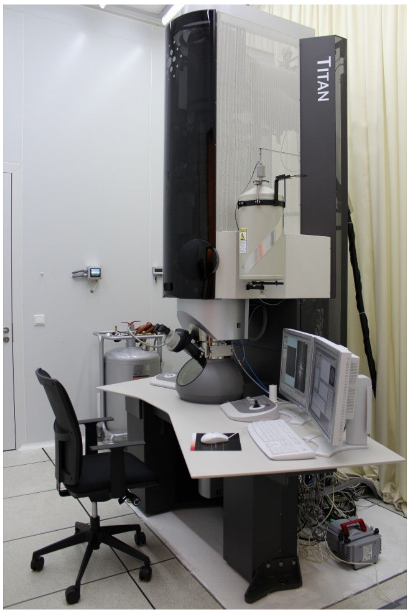

Figure 2.19: High resolution TEM located in the INL high accuracy laboratories.

its higher resolution was of fundamental importance to retrieve structural and crystallographic information of the MTJs, in particular from the thin MgO barriers.

The used high resolution TEM tool was the Titan ChemiSTEM aberration corrected electron microscope (Fig. 2.19). It allows 80-200 kV operation achieving 0.08 nm point resolution. The system is also equipped with X-ray detectors that allow the determination of the material composition (EDS analysis). In the scope of this thesis, the TEM was mainly used to observe the crystalline growth of the epitaxial MTJs, in particular the very thin (< 1 nm) MgO barriers.

2.5.3 *Focused ion beam (FIB)*

The SEM images of the surface provide useful insight regarding the morphology, topography and even composition of the nanofabricated devices. However, to access information of the stack, crystallography and material distribution in a transverse section (of patterned or unpatterned structures), it is necessary to perform a cross sectional cut of the samples. For this, a focused ion beam (FIB) [124, 125] was used to prepare lamellas employing the Helios NanoLab Dual FIB (30 kV) with SEM (Fig. 2.20). The process of lamella preparation requires the deposition of a Pt stripe to protect the structure from incurring FIB induced damage with minimum impact on the sample [Fig. 2.21(a)]. It will also confer physical stability to the struc-

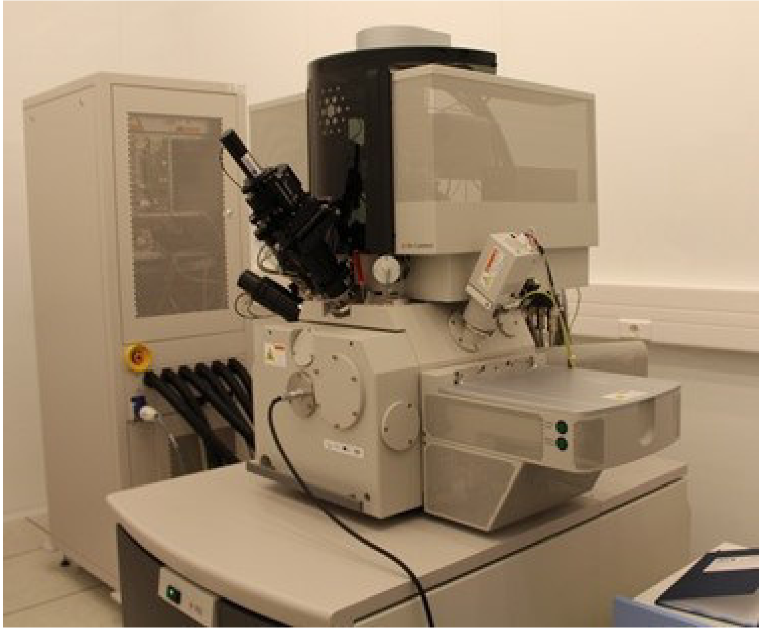

Figure 2.20: FIB with incorporated SEM located in the INL high accuracy laboratories.

ture after the thinning of the lamella [Fig. 2.21(b)]. These cross section cuts were also lifted and attached to a TEM grid. After the thinning of the lamellas, the ion beam was used, with low energy conditions (2 kV), to clean the amorphous layer damage induced by the ion beam during sample preparation.

2.5.4 *Nanocalc*

The Nanocalc [Fig. 2.22(a)] is a system used to extract the thickness of transparent layers on different substrates. It uses an interferometric technique to determine the layer thicknesses by providing an educated guess of what should be the measured stack (thickness range and optical constants - refractive index and extinction coefficient) and the substrate. The thickness of mono or multilayers can be determined through this technique. The principle of operation consists in vertically illuminating the sample with white light via an optical fiber and the measurement of the reflected light as a function of the wavelength using a spectrometer. The reflected light will have different phase shifts and superposition of amplitudes accordingly to the wavelength. This reflected signal depends on the thicknesses and optical properties of the materials being measured. Therefore, using this spectral measurement and providing to

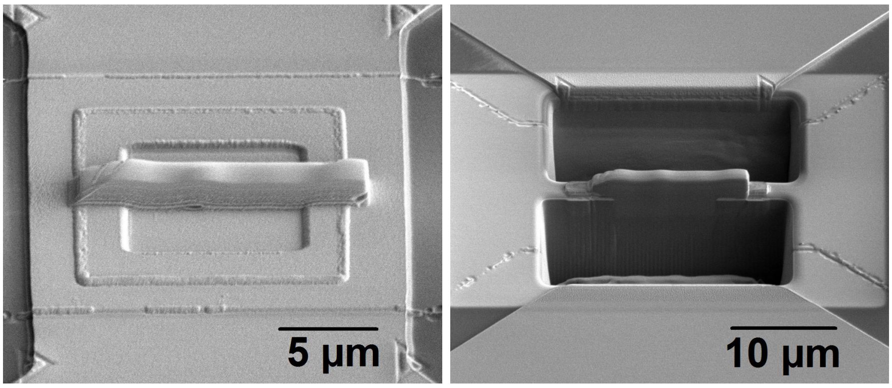

(a) (b)

Figure 2.21: Lamella preparation. (a) After ion beam Pt deposition and (b) the thinning of the lamella.

the software the substrate, materials of the stack and an estimation of their thicknesses, we can retrieve to a good approximation, the thickness of each layer. Prior to each measurement, a reference sample is used as calibration. Information regarding the quality of the fit is also provided for each measurement.

The thicknesses of each sample could be determined in isolated points or in a sequence of points along the wafer. A sequence of points uniformly distributed along a 200 mm wafer was used to perform uniformity measurements. The Nanocalc was thus mainly used to determine the deposition or etching rates and their uniformity. For this purpose, the system can also make the difference between the measurements before and after the etching or deposition. An example of these kind of measurements is shown in Fig. 2.22(b). The most commonly used material to perform these tests was Al_2O_3 deposited on top of a 200 mm Si substrate.

2.5.5 *Contact profilometer*

The contact profilometer is a surface metrology tool that provides information regarding the surface topography. It has a very simple principle of functioning: a diamond tip makes contact with the sample surface and performs a path (always in contact with the surface). From the vertical deviations of the tip, a direct measurement of the topography is obtained. The profilometer used (KLA Tencor P-16+; Fig. 2.23) is capable of performing automated step height analysis, surface contour, waviness and roughness measurements with detailed 2D or 3D topography analysis of surfaces and materials. It was mainly used to calibrate the materials' deposition rate. The achieved resolution depends on the vertical step (Table 2.5).

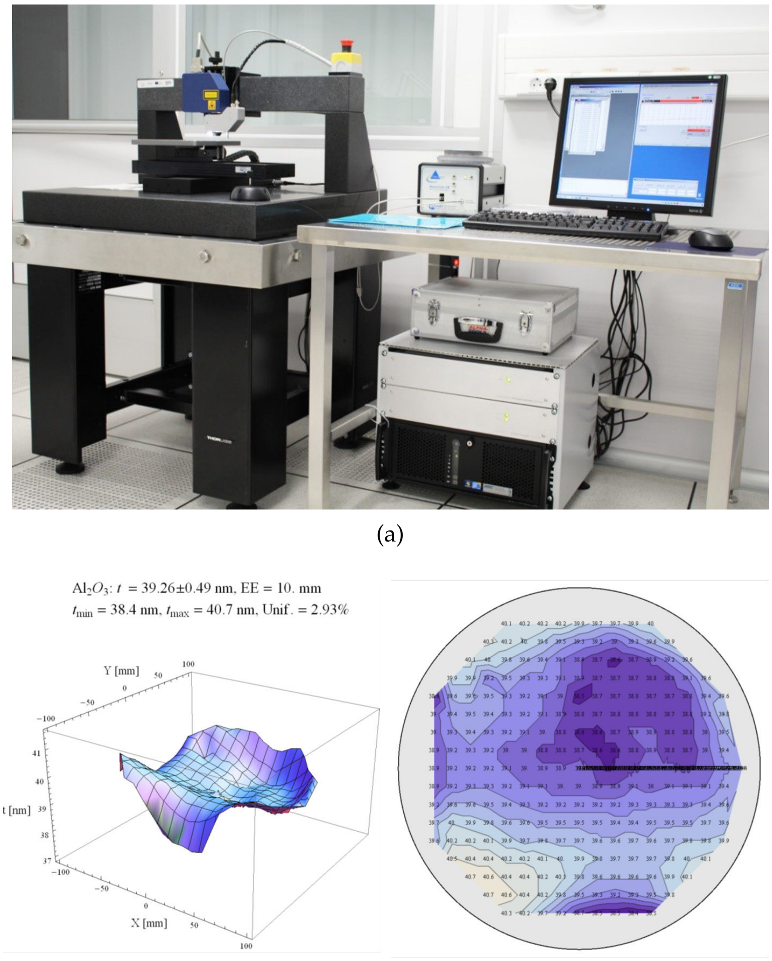

(a)

(b)

Figure 2.22: (a) Nanocalc system for the interferometric measurement of films' thicknesses (INL cleanroom). (b) Example of a uniformity measurement (of an Al_2O_3 layer on top of a Si wafer after etching with low energy conditions and an incident beam at 50°) performed using the Nanocalc.

Vertical range (μm)	Resolution (Å)
±6.5	0.008
±32	0.04
±173	0.2

Table 2.5: Profilometer resolution.

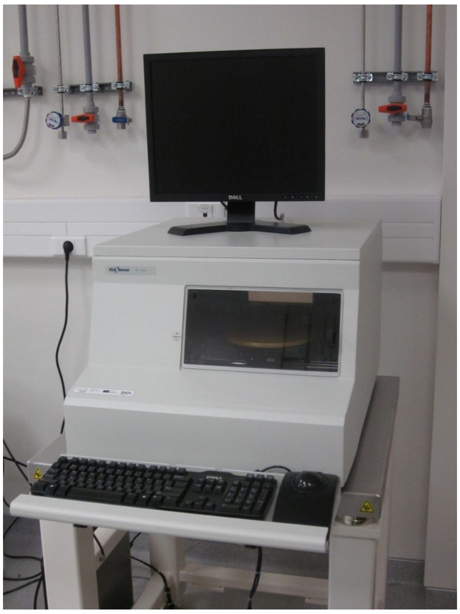

Figure 2.23: Contact profilometer for surface topography characterization (INL cleanroom).

Figure 2.24: XRD located in the INL facilities.

2.5.6 *X-ray diffraction (XRD)*

X-ray diffraction (XRD) allows the identification and structural characterization of crystalline materials. As X-ray radiation passes through the sample and interacts with the electrons in the atoms, scattering of the radiation occurs. Since the wavelength of X-rays is of the same order of magnitude of interatomic distances in a crystalline lattice, interference of the scattered particles in these solids will occur and thus form a diffraction pattern with constructive and destructive interferences. Most crystals have several atomic planes with characteristic interplanar distances. In that case, for a particular angle of X-ray incidence, an intensity peak in the diffraction pattern will appear due to constructive interference between reflections in different atomic planes. Accordingly to Bragg's law these intensity maxima of the diffraction pattern appear when:

$$n\lambda = 2d_{hkl}sin\theta, \tag{2.2}$$

where λ is the wavelength of the incident wave, d_{hkl} is the distance between planes with the Miller indexes (hkl), n an integer and θ the angle formed between the propagating vectors of the incident and scattered waves.

In this thesis, a PanAnalytical X Pert PRO materials research diffractometer (MRD) system was used (Fig. 2.24). It can be set to different configurations such as grazing incidence, in-plane diffraction, reciprocal space mapping, reflectometry, and small-angle scattering for thin film research. It allows the study of layer thicknesses, lattice constants, lattice mismatch, periodicity, mosaic spreads, lattice stress and strain, composition, etc. In this thesis, it was mainly used to determine the crystalline phase of materials with strong PMA.

2.6 MAGNETIC MEASUREMENTS

Prior to sample fabrication it is important to verify if the magnetic properties of the MTJ stack have the expected behavior. Moreover, through the measurement of the magnetization curves as a function of the applied magnetic field, it is possible to optimize the magnetic stack for a certain application before nanofabrication. Magnetic characterization tools are thus fundamentally important to the development of magnetic devices.

2.6.1 *Vibrating Sample Magnetometer (VSM)*

The Vibrating Sample Magnetometer (VSM) [126] allows the measurement of the magnetic moment as a function of the applied magnetic field of unpatterned samples. Thus, it allowed us to measure and optimize the magnetic stacks and annealings used during this project. The principle of functioning of a VSM consists on physically vibrate sinusoidally a sample, typically through the use of piezolelectric actuators. Then, through Faraday induction, a changing magnetic field will produce an electric field that will be detected by pick-up coils. This field is proportional to the magnetic moment of the sample and independent on the applied magnetic field. The induced voltage is measured using a lock-in amplifier and piezoelectrics as reference, allowing the retrieval of the magnetic moment of the sample.

The used VSM system (Fig. 2.25) can measure magnetic signals down to 5×10^{-7} emu and very low coercivities (10 mOe; field resolution) and can apply fields up to 2 T. It allows the fast and accurate measurement of the magnetic moment, not only as a function of the applied magnetic field, but also with temperature (which can be swept from 83 to 570 K). Angular and time dependences of the magnetization can be measured as well. Different recipes can be programmed using the VSM software with controllable field (range and steps per range), angle and temperature [an example of a recipe is shown in Fig. 2.26 (a)]. In Fig. 2.26 (b) an example of a magnetization curve as a function of the magnetic field is also shown.

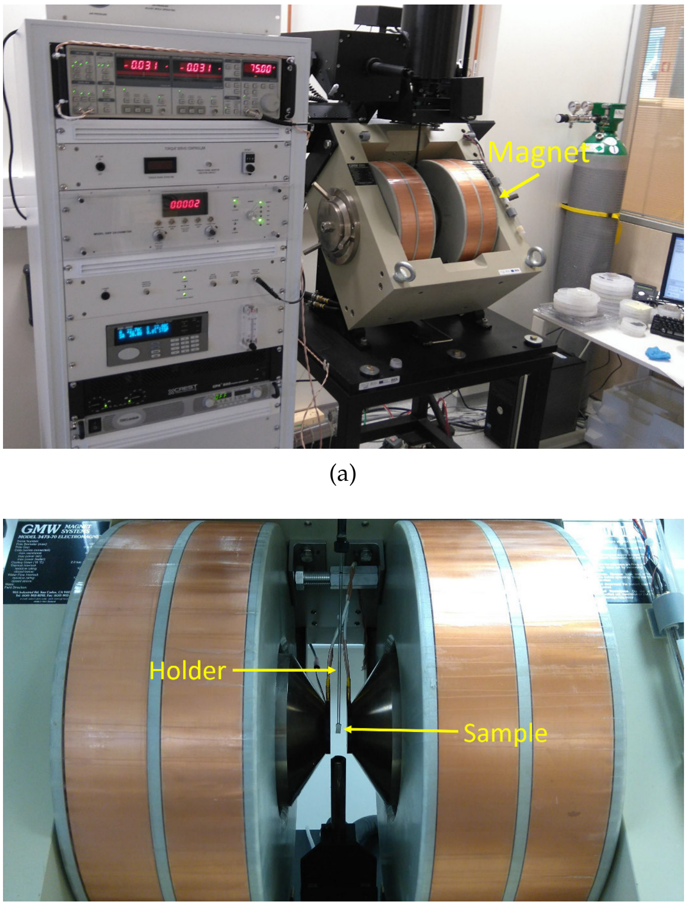

(a)

(b)

Figure 2.25: VSM placed in the INL facilities.

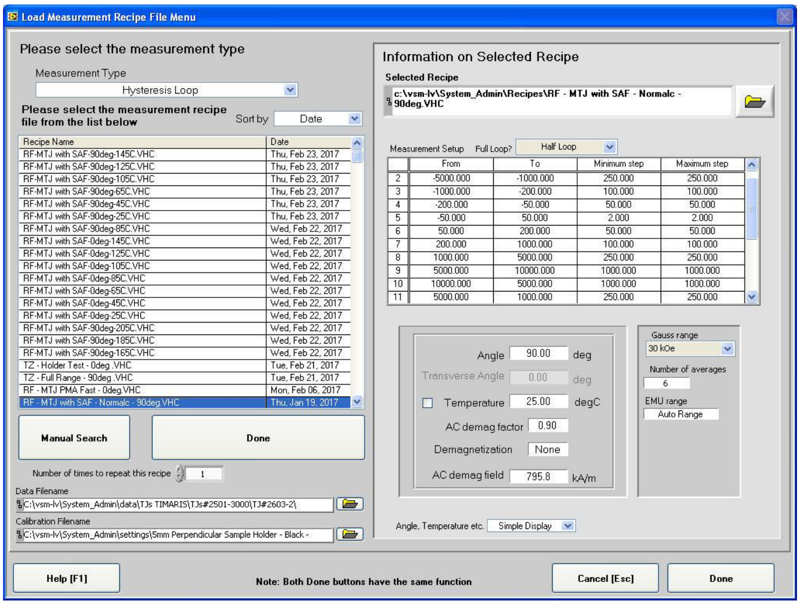

Please select the measurement type

Measurement Type: Hysteresis Loop

Please select the measurement recipe file from the list below

Sort by: Date

Recipe Name	Date
RF-MTJ with SAF-90deg-145C.VHC	Thu, Feb 23, 2017
RF-MTJ with SAF-90deg-125C.VHC	Thu, Feb 23, 2017
RF-MTJ with SAF-90deg-105C.VHC	Thu, Feb 23, 2017
RF-MTJ with SAF-90deg-65C.VHC	Thu, Feb 23, 2017
RF-MTJ with SAF-90deg-45C.VHC	Thu, Feb 23, 2017
RF-MTJ with SAF-90deg-25C.VHC	Thu, Feb 23, 2017
RF-MTJ with SAF-90deg-85C.VHC	Wed, Feb 22, 2017
RF-MTJ with SAF-0deg-145C.VHC	Wed, Feb 22, 2017
RF-MTJ with SAF-0deg-125C.VHC	Wed, Feb 22, 2017
RF-MTJ with SAF-0deg-105C.VHC	Wed, Feb 22, 2017
RF-MTJ with SAF-0deg-85C.VHC	Wed, Feb 22, 2017
RF-MTJ with SAF-0deg-65C.VHC	Wed, Feb 22, 2017
RF-MTJ with SAF-0deg-45C.VHC	Wed, Feb 22, 2017
RF-MTJ with SAF-0deg-25C.VHC	Wed, Feb 22, 2017
RF-MTJ with SAF-90deg-205C.VHC	Wed, Feb 22, 2017
RF-MTJ with SAF-90deg-185C.VHC	Wed, Feb 22, 2017
RF-MTJ with SAF-90deg-165C.VHC	Wed, Feb 22, 2017
TZ - Holder Test - 0deg .VHC	Tue, Feb 21, 2017
TZ - Full Range - 90deg .VHC	Tue, Feb 21, 2017
RF - MTJ PMA Fast - 0deg.VHC	Mon, Feb 06, 2017
RF - MTJ with SAF - Normalc - 90deg.VHC	Thu, Jan 19, 2017

Number of times to repeat this recipe: 1

Data Filename: C:\vsm-lv\System_Admin\data\TJs TIMARIS\TJs#2501-3000\TJ#2603-2\

Calibration Filename: C:\vsm-lv\System_Admin\settings\5mm Perpendicular Sample Holder - Black -

Information on Selected Recipe

Selected Recipe: c:\vsm-lv\System_Admin\Recipes\RF - MTJ with SAF - Normalc - 90deg.VHC

Measurement Setup Full Loop? Half Loop

	From	To	Minimum step	Maximum step
2	-5000.000	-1000.000	250.000	250.000
3	-1000.000	-200.000	100.000	100.000
4	-200.000	-50.000	50.000	50.000
5	-50.000	50.000	2.000	2.000
6	50.000	200.000	50.000	50.000
7	200.000	1000.000	100.000	100.000
8	1000.000	5000.000	250.000	250.000
9	5000.000	10000.000	1000.000	1000.000
10	10000.000	5000.000	1000.000	1000.000
11	5000.000	1000.000	250.000	250.000

Angle: 90.00 deg
Transverse Angle: 0.00 deg
☐ Temperature: 25.00 degC
AC demag factor: 0.90
Demagnetization: None
AC demag field: 795.8 kA/m

Gauss range: 30 kOe
Number of averages: 6
EMU range: Auto Range

Angle, Temperature etc.: Simple Display

Note: Both Done buttons have the same function

(a)

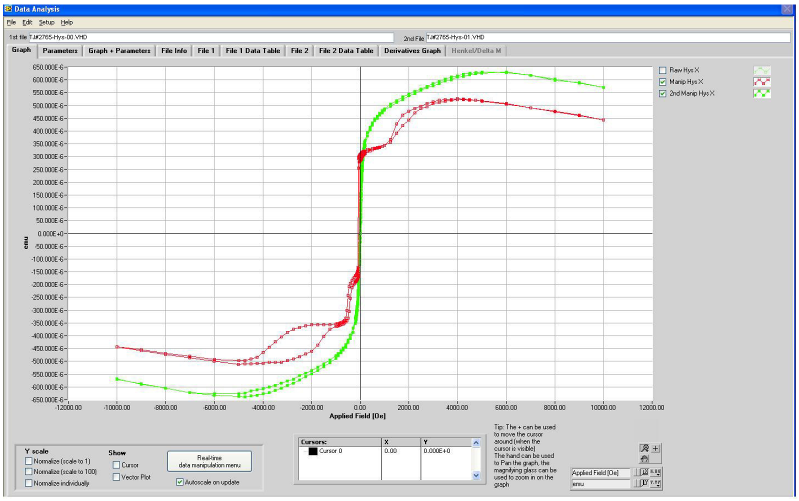

1st file: TJ#2765-Hys-00.VHD
2nd File: TJ#2765-Hys-01.VHD

☐ Raw Hys X
☑ Manip Hys X
☑ 2nd Manip Hys X

Y scale
☐ Normalize (scale to 1)
☐ Normalize (scale to 100)
☐ Normalize individually

Show
☐ Cursor
☐ Vector Plot

☑ Autoscale on update

Cursors:	X	Y
Cursor 0	0.00	0.000E+0

Tip: The + can be used to move the cursor around (when the cursor is visible) The hand can be used to Pan the graph, the magnifying glass can be used to zoom in on the graph

Applied Field [Oe]
emu

(b)

Figure 2.26: VSM software. (a) Measurement recipe and (b) measured magnetization curve as a function of the applied field.

2.7 ELECTRICAL CHARACTERIZATION

MTJs require the development and optimization of the magnetic and electrical counterpart. In fact, it is possible to have MTJ devices fully operational magnetically that do not have an electrical response (due to wrong crystalline phase, discontinuous MgO, fabrication defects, etc.). Therefore, the DC electrical characterization allows the MTJ stack optimization and constitutes the ultimate test to verify if the devices are functional after fabrication.

2.7.1 *Current in-plane tester (CIPT)*

To verify the transport properties of MTJs before nanofabrication a current in-plane tester (CIPT) was used [Fig. 2.27(a); model CIPTech M-200]. It performs TMR and RA measurements of bulk MTJ stacks. This is a very useful tool since it allows us to retrieve fundamental information of the MTJ stack prior to fabrication. To perform these measurements, the system contacts 12 cantilever electrodes with a variable spacing, down to 750 nm. It performs electrical measurements (current and voltage) through the different cantilevers with different spacing between them. Different spacings have different contributions for the measured electrical signals. For instance, a large spacing between tips allows the current to spread, receiving contributions from the top and bottom of the insulating barrier [Fig. 2.27(b)]. On the other hand, small spacing between tips leads to a larger contribution from the top layer [Fig. 2.27(c)]. By performing a fit to the measured values for the different spacings between tips, it is possible to determine the RA and TMR. The CIPT can determine RA values down to 0.1 $\Omega\mu\text{m}^2$ and measure the TMR with both in-plane and perpendicular anisotropy with in-plane fields up to 2500 Oe and perpendicular fields up to 1400 Oe.

2.7.2 *Semi-Automatic Transport Measurement Setup*

Once the MTJ fabrication process is complete, thousands of MTJ devices can be measured over the full wafer. By measuring them we can obtain statistically meaningful data regarding the device TMR, RA, shape of the transfer curves, and corresponding deviations arising from the nanofabrication process. To do that, in a fast and efficient way, a semi-automatic probe station was used [Fig. 2.28(a)]. This setup uses a system with 40 tips so that 10 MTJs can be characterized per landing in a 4-contact scheme [Fig. 2.28(b)]. Moreover, the electrical measurements across the tips can be programmed so that different types of measurement or measurements of different contact configurations can be performed. The tips have a separation of 250 µm between each other and the fabricated contacts were prepared to fit this requirement.

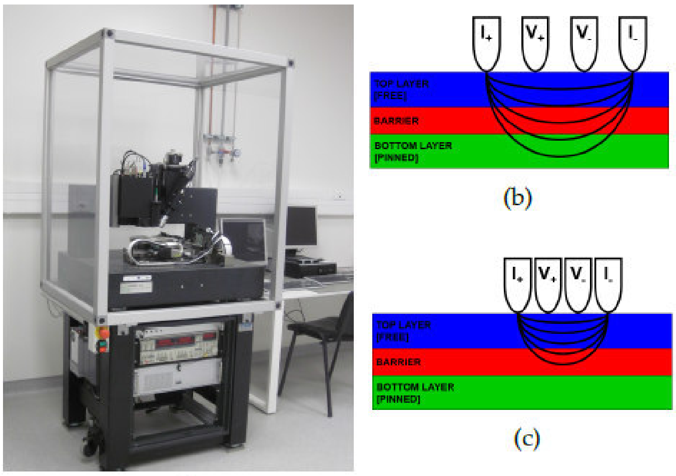

(a) (b) (c)

Figure 2.27: (a) CIPT located in the INL facilities. Representation of the current lines across an MTJ structure for (b) large and (c) small spacing between tips.

With this prober we were able to easily extract useful information from the fabricated devices, such as transfer curves, I-V curves, breakdown voltages and MTJ stability. Furthermore, a software allows a simple data treatment since we can characterize different figures of merit (TMR, RA, coercive field, linear range of the curve, etc) and organize them for different parameters (die number, pillar sizes, TMR and RA range, etc). In Fig. 2.28(c) it is shown an example of this data treatment with the analysis of a transfer curve.

2.7.3 *RF measurements*

After the MTJ fabrication and DC electrical measurements, the RF electrical properties of the STNOs were also characterized. A homemade setup and software were used to measure the RF emission of the MTJs upon current injection. This allowed us to perform studies of our devices for applications as oscillators.

2.7.3.1 *RF prober for in-plane magnetic fields*

Electrical contact to characterize RF devices was performed using special Cascade Microtech's probes. These probes allow high accuracy RF measurements with low contact resistance. Their characteristic impedance is 50 Ω and RF signals up to 67 GHz can be measured. The signal makes only one transition to the coplanar contact structure maintaining the signal integrity

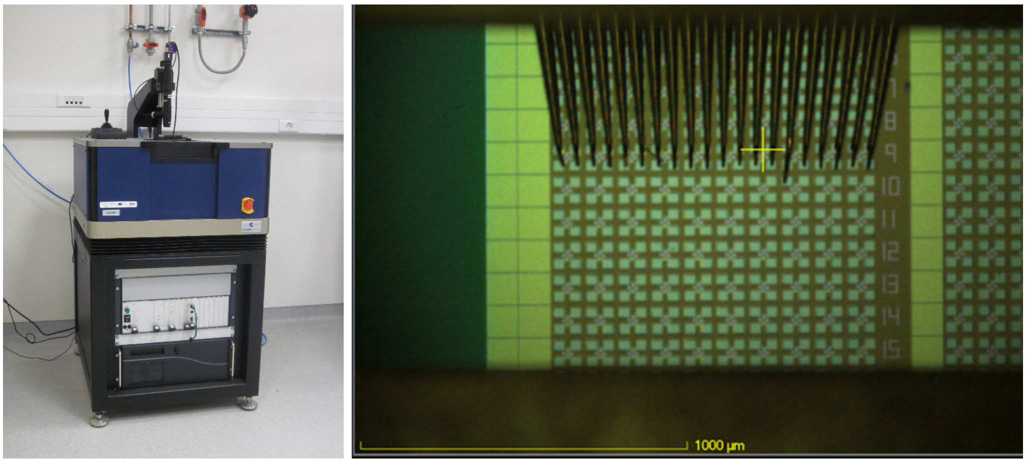

(a) (b)

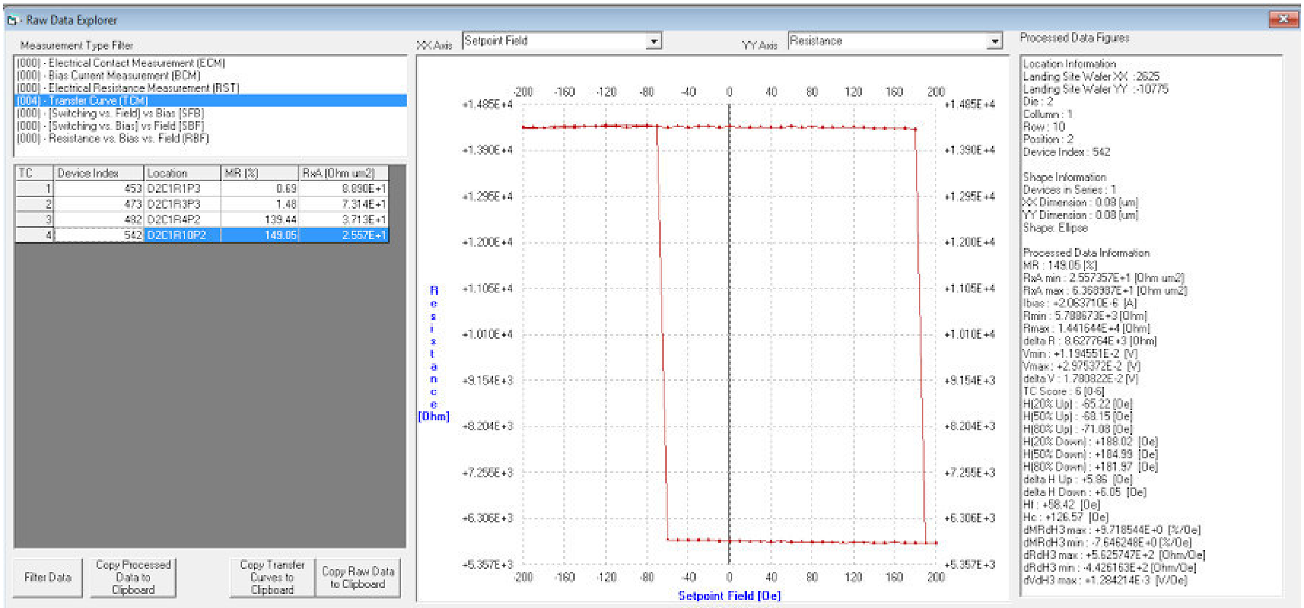

[000] - Electrical Contact Measurement (ECM)
[000] - Bias Current Measurement (BCM)
[000] - Electrical Resistance Measurement (RST)
[004] - Transfer Curve (TCM)
[000] - [Switching vs. Field] vs Bias [SFB]
[000] - [Switching vs. Bias] vs Field [SBF]
[000] - Resistance vs. Bias vs. Field (RBF)

TC	Device Index	Location	MR (%)	RxA (Ohm um2)
1	453	D2C1R1P3	0.69	8.890E+1
2	473	D2C1R3P3	1.48	7.314E+1
3	482	D2C1R4P2	139.44	3.713E+1
4	542	D2C1R10P2	149.05	2.557E+1

Location Information
Landing Site Wafer XX : 2625
Landing Site Wafer YY : -10775
Die : 2
Collumn : 1
Row : 10
Position : 2
Device Index : 542

Shape Information
Devices in Series : 1
XX Dimension : 0.08 [um]
YY Dimension : 0.08 [um]
Shape: Ellipse

Processed Data Information
MR : 149.05 [%]
RxA min : 2.557357E+1 [Ohm um2]
RxA max : 6.368387E+1 [Ohm um2]
Ibias : +2.063710E-6 [A]
Rmin : 5.788673E+3 [Ohm]
Rmax : 1.441644E+4 [Ohm]
delta R : 8.627764E+3 [Ohm]
Vmin : +1.194551E-2 [V]
Vmax : +2.975372E-2 [V]
delta V : 1.780822E-2 [V]
TC Score : 6 [0-6]
H[20% Up] : -65.22 [Oe]
H[50% Up] : -68.15 [Oe]
H[80% Up] : -71.08 [Oe]
H[20% Down] : +188.02 [Oe]
H[50% Down] : +184.99 [Oe]
H[80% Down] : +181.97 [Oe]
delta H Up : +5.86 [Oe]
delta H Down : +6.05 [Oe]
Hf : +58.42 [Oe]
Hc : +126.57 [Oe]
dMRdH3 max : +9.718544E+0 [%/Oe]
dMRdH3 min : -7.646248E+0 [%/Oe]
dRdH3 max : +5.625747E+2 [Ohm/Oe]
dRdH3 min : -4.426163E+2 [Ohm/Oe]
dV/dH3 max : +1.284214E-3 [V/Oe]

(c)

Figure 2.28: (a) Semi-Automatic Transport Measurement Setup placed in the INL facilities. (b) Tips used to perform the electrical measurements of the fabricated MTJs. (c) Software used for data treatment.

with stable performance over a wide temperature range. An optical microscope in conjugation with holders that allow high accuracy movements (both for the sample and the tips) are used to connect the contacts to the device [Fig. 2.29(a) and (b)]. The RF measurements can be performed while injecting a DC current in the MTJ. Moreover, synchronization [107, 108, 90] and spin diode torque studies [127] can also be performed since an RF signal can be provided to the MTJ and the generated DC voltage measured.

The signal is then transported through coaxial cables to a 3 Hz - 44 GHz spectrum analyzer where the emission spectrum can be acquired. Power suppliers are used to provide current both to the MTJ and the magnet. Automated control of the complete system can be performed to make sequences with different values of current and magnetic field. An amplifier is usually used to increase the measured signal, although its use was not necessary in the cases of MTJs with high output power. A bias tee is used to separate the DC and RF electrical components (being the last one sent to the spectrum analyzer). The magnetic field was applied using a small magnet. The orientation of the magnet could be manually changed but it was limited to relatively small magnetic fields (up to 200 Oe) in the in-plane direction. A schematic representation of the circuit used for this setup is shown in Fig. 2.29(c)

Using this setup a spectrum is obtained for each value of current and magnetic field. However, in order to calculate the actual power emitted from the MTJ some calculations are still required. Moreover, due to the impedance mismatch between the MTJ and the load there is some reflected power that has to be taken into account. Here, we provide an overview of the steps used in the RF prober to retrieve the data from the measured values, focusing on the determination of the integrated output power matched to the load:

1. The analyzer measures the spectrum $[V(f)]$ for a certain value of current (I_{bias}) and field (H).

2. Another measurement is performed at zero current but the same magnetic field $[V_0(f)]$.

3. In order to minimize the noise, the difference between the two measured spectra is calculated: $S = V^2(f) - V_0^2(f)$, where S is the considered signal. Negative values of S derived of fluctuations when the signal is small are made equal to zero.

4. We then divide the calculated value by the gain (g) of the amplifier $S = S/g(f)$. Despite the fact that the gain dependence on the frequency is not very pronounced, the measured $g(f)$ was used instead of a constant factor.

5. S is then divided by the bandwidth (BW) of the measurement (distance between 2 data points) because the measurement will be integrated over the full frequency range.

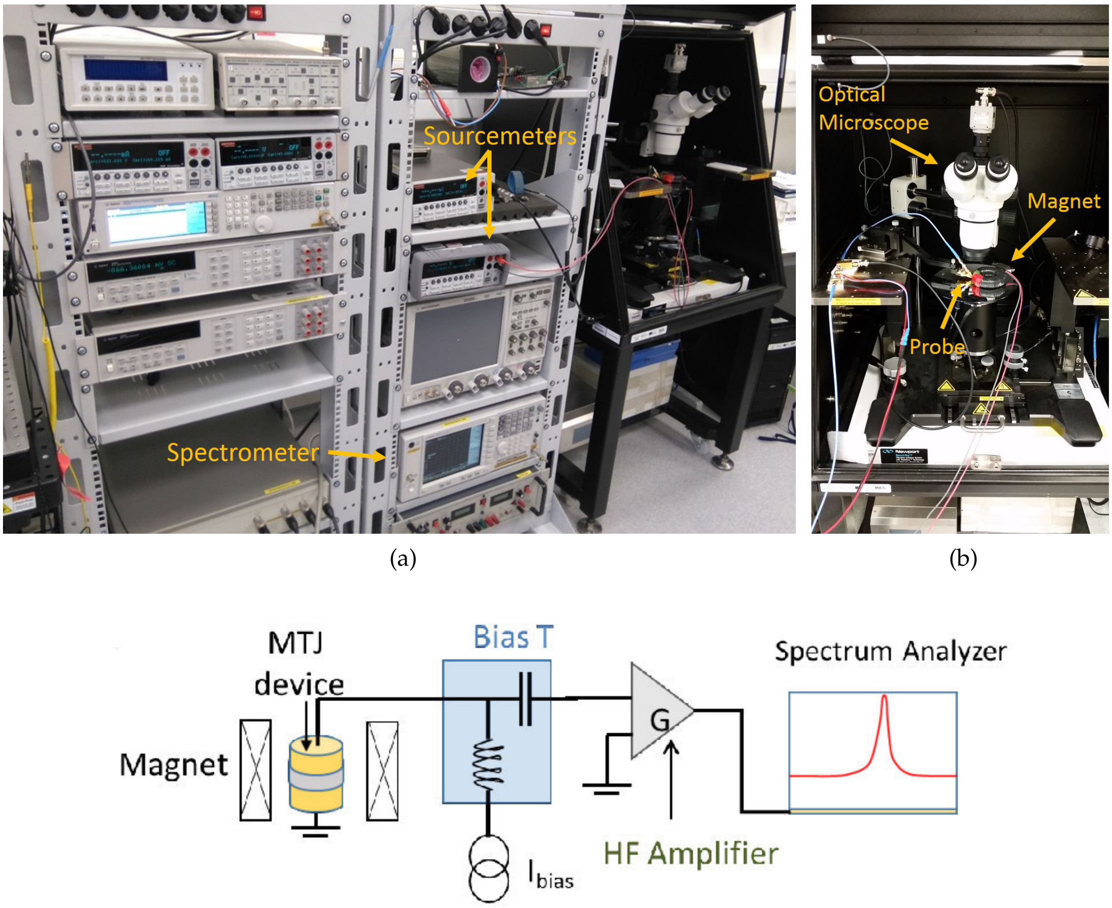

(a)

(b)

(c)

Figure 2.29: RF prober for IP magnetic fields, (a) overview with the power suppliers and the spectrum analyzer and (b) sample with the tips, the magnet and the microscope. (c) Schematic representation of the experimental setup used for the RF emission characterization.

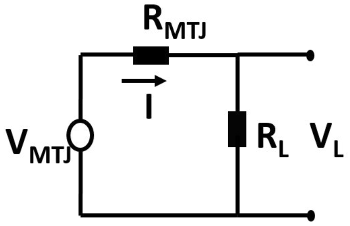

Figure 2.30: Schematic representation of the equivalent circuit of the MTJ (with resistance R_{MTJ} and voltage V_{MTJ}) that delivers RF power to a load (with resistance R_L and voltage V_L).

6. The non-matched integrated output power is then given by:

$$P_{non-matched} = \int \frac{S}{R_L} df = \int \frac{V^2(f) - V_0^2(f)}{R_L} df, \tag{2.3}$$

where R_L is the load resistance ($\approx 50\ \Omega$). The division by R_L is performed because the power is given by $P = V^2/R$, measured at the load.

7. In the case of the power matched to the load, we have to consider the equivalent circuit shown in Fig. 2.30. From this equivalent circuit, we can write the voltage delivered by the MTJ at the load as:

$$V_{MTJ} = \frac{V_L}{R_L}(R_L + R_{MTJ}). \tag{2.4}$$

Now, if we consider that we have a matched load ($R_L' = R_{MTJ}$), we obtain that the voltage delivered to the matched load is given by:

$$V_L' = \frac{R_L + R_{MTJ}}{2R_L} V_L. \tag{2.5}$$

Hence, the power delivered by the MTJ to a matched load is given by:

$$P_{matched} = P_{non-matched} \cdot \frac{(R_{MTJ} + R_L)^2}{4R_{MTJ}R_L}. \tag{2.6}$$

Using this procedure we were able to determine both the measured output power and the power matched to the load. The power matched to the load is more meaningful since it describes the actual power emitted by the MTJ.

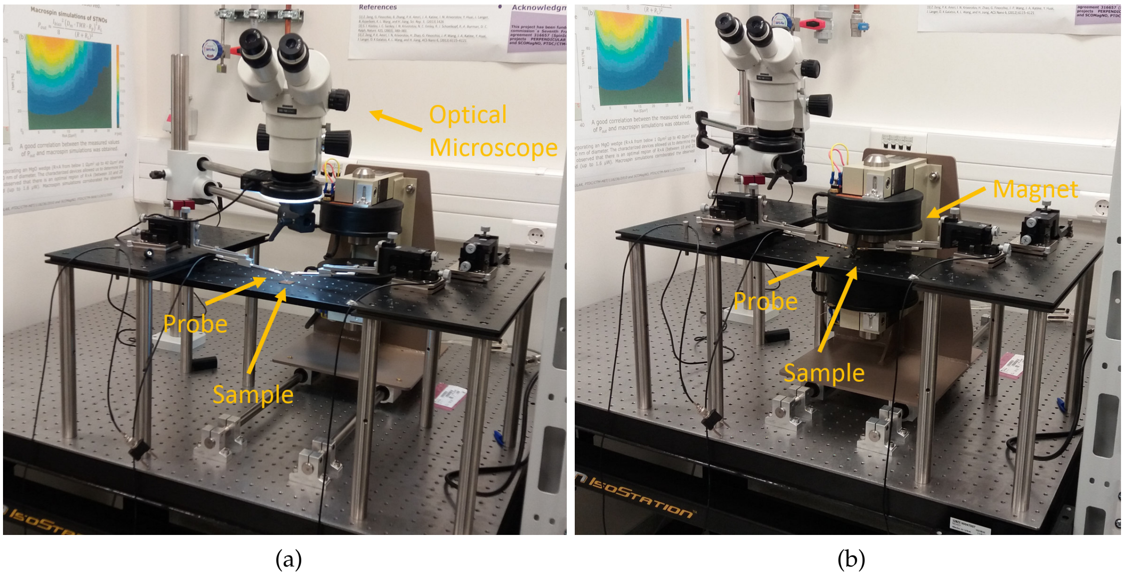

Figure 2.31: RF prober for OOP magnetic fields; (a) use of the optical microscope to position the tips and (b) positioning of the magnet for the magnetic field dependent measurements.

2.7.3.2 *RF prober for out-of-plane magnetic fields*

A similar homemade RF prober (same power supplies and spectrum analyzer), but for out-of-plane magnetic fields, was also used (Fig. 2.31). The improvement of this setup when compared with the previous one is the achievement of stronger magnetic fields (up to 1.6 T) in the out-of-plane direction. Moreover, the applied magnetic field value is measured directly using a gaussmeter. The setup requires the positioning of the tips with the aid of an optical microscope [Fig. 2.31(a)]. After the tips are properly connected to the contacts the microscope is easily displaced and the magnet positioned in the sample position [Fig. 2.31(b)].

3

NANOFABRICATION PROCESS

With the announced end of Moore's law, it becomes increasingly important to develop efficient, high yield and uniform nanofabrication processes that can work at an industrial scale. Moreover, novel technologies, such as magnetoresistive nanosensors and spin transfer torque-based applications, rely on the possibility to nanostructure magnetic components. In particular, the nanofabrication of magnetic tunnel junctions (MTJs) is particularly challenging, due to the conjugation of the electric and magnetic counterparts and the effect of the nanofabrication on both. Hence, one of the main goals of this thesis was to develop a nanofabrication process of MTJs with large tunnel magnetoresistance (TMR; above 100%) that works in the low resistance × area product (RA) region (down to ~ 1 Ωµm^2). In this chapter, we describe the developed nanofabrication process used to obtain the state-of-the-art sub-μm MTJs. The nanopillar definition was performed with a three-step etching: a high energy etching of the capping layers with a beam incidence that leads to vertical sidewalls (50° with respect to the wafer surface); a low energy etching at normal incidence used for the etching of the sensitive magnetic layers; and a low energy etching with a grazing angle (10°) to clean re-deposited material side walls of the nano-pillar. Usually, after the nanopillar definition, MTJ nanofabrication processes are based either on lift-off or chemical-mechanical polishing (CMP) steps to gain electrical access to the top part of the MTJ nano-pillar. While lift-off processes, at the nanoscale, are very time consuming (up to weeks) and have very poor yield and reproducibility for smaller nanopillars, CMP processes are hard to implement with a good enough control of the end-point, and create a significant amount of residues. As an alternative, an ion beam planarization (IBP) process was developed and successfully implemented of an Al_2O_3 dielectric through a grazing angle etching. Furthermore, we perform a detailed analysis of the nanopillar definition variables (etch angle, sidewall cleaning, resist strip and capping layer composition) and their effect on the nanopillar morphology. With this process, performed in 200 mm industrial wafers, we were able to achieve nanodevices depicting TMR values up to 156% in the low RA region (below 2 Ωµm^2), with a typical total process time of 2 weeks (which could be reduced to 4 days in the best possible conditions). A statistical analysis of the MTJ performance over the full wafer was also performed. Yields up to 80% were achieved for dimensions down to 100 × 100 nm^2. The goal of this thesis consisted in using these devices for applications in spin transfer nano-oscillators (STNOs). In fact, the studies detailed on the next chapters used STNOs fabricated using this process. Nevertheless, this is a transversal process that has already been applied at INL to different applications, such as nanosensors and novel devices controlled by pure spin currents.

3.1 NANOFABRICATED MAGNETIC TUNNEL JUNCTIONS: APPLICATIONS

Spintronics is a well-established field that jointly explores spin and charge degrees of freedom to operate [128, 69, 129]. With the development of nanofabrication tools and techniques, new applications emerged, being the most relevant nanosensors and novel spin transfer torque (STT)-based technologies. Moreover, magnetoresistive sensors have been developed both in the micrometric [130, 131, 132, 133, 134] and the nanoscale [135, 136]. Such nanosensors find applications in the areas of biomedical imaging, magnetic mapping, read heads and single nanoparticle detection. Furthermore, the recently discovered possibility to effectively and selectively manipulate the magnetization of nano-magnets using spin polarized electrical currents instead of magnetic fields promptly led to the appearance of novel technologies. This capability is based on the STT effect which consists of the transfer of angular momentum from polarized currents to the magnetic layers [55]. However, the large current densities required to observe STT-related phenomena demands the nanofabrication of magnetoresistive structures. The first STT-based devices that emerged were STT-MRAM which are based on the current-induced switching of the magnetic state [60, 59] and spin-transfer-torque nano-oscillators (STNOs) which are RF emitters triggered by the magnetic precession of the free magnetic layer [61, 62, 137]. In what concerns STT-MRAMs, with the continuous increase of the storage capacity, the size of the recording bits decreased to the order of tens of nm. Moreover, the announced end of Moore's law [138] further increases the need to push the process to its technological limits. As for the STNOs, different families have been developed. In particular the ones based on homogeneous magnetization which work in the GHz range [81, 84, 85] and the ones based on magnetic vortices that depict a lower frequency range (below 1 GHz) [139, 105, 68, 88, 52]. Also, both point contact [62, 105, 75] and nanopillar [81, 68] geometries have been used. Furthermore, the recently discovered possibility to control the magnetization with pure spin currents [140, 141, 142] is quite promising since it allows the fabrication of electronic components without significant heating effects. This possibility has started to be explored both for STT-MRAM [143, 144, 145, 146] and STNOs [147, 148].

All these novel devices have in common the need for a magnetoresistive component with nanometric dimensions. MTJs consisting of MgO tunneling barriers and CoFeB magnetic layers are regarded as the most suitable for such applications due to their large TMR of up to 600%, (for an RA of 104 $\Omega\mu m^2$ and without antiferromagnetic layer) [18]. However, for STT-based applications, a lower RA product is required to achieve large current densities before barrier breakdown. Such low RA region leads to a degradation of the MgO layer quality (higher roughness, presence of pin-holes and crystallinity loss) that severely decrease the TMR [39]. In fact, even in state-of-the-art MTJs (prior to nanofabrication) the TMR drops to values below 200% in the low *RA* region (below 5 $\Omega\mu m^2$) [39, 149]. Moreover, several problems arise from the MTJ nanofabrication, being one of the most prominent material re-deposition on the sidewalls of the nanopillars during ion beam etching. This re-deposition inflates the final device critical dimension and, more importantly, causes electrical shunting across the barrier which decreases the TMR. To remove the re-deposited material, a low angle milling is usually used after pillar definition. However, this process creates damage in the device edges, generates shadowing effects that prevent the formation of vertical sidewalls and decreases process uniformity due to the clamps used at the wafer edges [150, 151]. The edge damage can be minimized by using a low beam energy milling. However, the use of low energy increases the divergence of the beam and thus a compromise must be found [152]. Therefore, after nanofabrication the TMR of state-of-the-art MTJs is usually below 120% in the low *RA* region [81, 153, 78, 80] and only few reports address process uniformity over a full wafer [154].

Another problem related to the nanofabrication process consists of separating electrically the bottom and the top part of the MTJ. This is essential to enable the microfabrication of the remaining components of the device that allow the reading/writing of the MTJ. To achieve this structure, a dielectric material is deposited after nanopillar definition that must then be removed from the top of the pillars by opening a via to the MTJs. This can be achieved using processes based on lift-off [116] or CMP [155]. Despite the simplicity of the lift-off process, the yield of the open nanopillars is relatively low and it has a process time that can go up to weeks for nanostructures. Moreover, the process is intrinsically worse for smaller nanopillars. As for the CMP, it is a very fast process that opens more easily the smaller pillars. However, a large amount of residues arise from the planarization, and a good uniformity and control of the stopping point are difficult to achieve.

In this chapter we describe sequentially all the steps developed in this thesis to fabricate the MTJ devices that will be later applied to the study of STNOs. In particular, we focus on the novel method that we used to achieve a plane insulating matrix with the MTJs open on top based on a low angle milling. The conjugation of this ion beam planarization (IBP) with the nanopillar definition by etch allowed the nanofabrication of MTJs with TMR values up to 156% in the low *RA* region (below 2 $\Omega\mu m^2$). Full 200 mm wafer yields of ~ 80% were achieved for dimensions as small as 100 × 100 nm^2. Moreover, a wide range of dimensions (from 50 to 500 nm) could be fabricated in the same wafer. A detailed description of the nanofabrication process is given, including the nanopillar definition variables (etching angles, sidewall cleaning, resist strip and capping layer) and the IBP process. A thorough analysis of the variation of the TMR and *RA* along the full range of the wafer is also shown. This nanofabrication process is transversal to different geometries and MTJ stacks and can thus be implemented for the different applications at the nano-scale. For instance, this process has been already successfully adapted for applications in spin Hall effect-based oscillators and nanosensors.

3.2 TOOLS AND CONDITIONS USED DURING FABRICATION

During the development of this nanofabrication process several MTJ stacks were deposited and fabricated. These stacks are multilayered systems that were deposited onto 200 mm Si wafers using the TIMARIS multi target mode (MTM) system (see section 2.1.1.1) with a base pressure of 2.0×10^{-9} mbar. These stacks can be composed of different materials and thicknesses depending on the application. To achieve nanopillars, we used a combination of electron-beam (e-beam) lithography and ion beam etching. The e-beam lithography was performed in a Vistec 5200 with the ARN7520 photoresist (section 2.3.3). The etching processes were performed using a Nordiko 7500 system (section 2.2.1). Two sets of conditions were used corresponding to high (low) energy etching conditions with an acceleration grid current of 235 mA, a negative acceleration grid potential voltage of 2250 (1750) V and a positive potential of 600 (150) V. The etching process could be monitored in situ using a secondary ion mass spectrometer (SIMS) which detected the material being etched. The neutralizers were set to 280 (120) mA and 10.0 (6.0) sccm for the high (low) energy conditions. In both cases a rotation of 30 rpm was used. In most of the etchings, high energy (HE) conditions with an incident angle of 50° were used. This led to a high etch rate (~ 4.0 nm/min in Al_2O_3) with a good uniformity in 200 mm (below 5%) and vertical sidewalls. During the IBP an etch with HE conditions but 10° of beam incidence was used. During the nanopillar definition, low energy (LE) conditions were necessary in order to avoid the sidewall damage of the MTJ nanopillars. The nanofabrication process was characterized using a Scanning Electron Microscope (SEM) NovaNanoSEM 650 (section 2.3.3). A semi-automatic probe station was used to perform the full wafer DC electrical characterization (section 2.7.2).

3.3 CONTACT GEOMETRIES

The MTJ fabrication process comprises not only the definition and opening of the MTJ nanopillars, but also the definition of the contacts that allow the measurement of their electrical properties. Therefore, despite the fact that the nanofabrication is the most demanding part of the process, it is also essential to define a suitable contact geometry. A 4-contact geometry allows the electrical measurements to be performed without contact resistance. Hence, 4 contacts (2 connected to the top and 2 to the bottom) were fabricated. This contact scheme allowed us to measure the actual TMR and *RA* values of the fabricated MTJs.

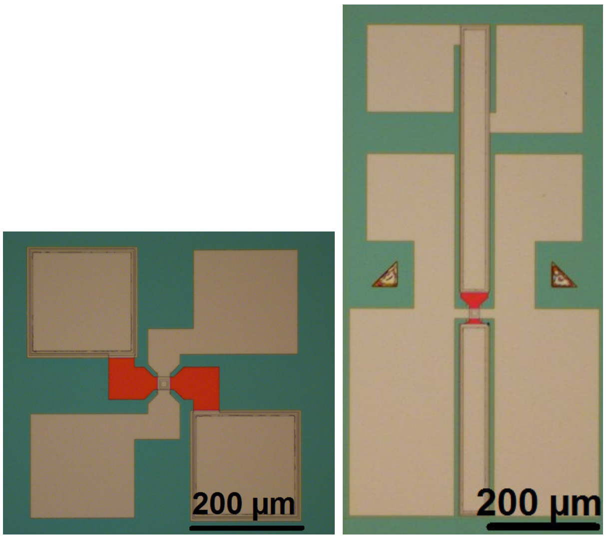

(a) DC dies (b) DCRF dies

Figure 3.1: Images obtained by optical microscopy of the types of fabricated dies after the process is finished: (a) DC and (b) DCRF.

The contact geometry can then be adapted to different needs and applications. In the scope of this thesis, two types of geometries were fabricated: a mask with a standard 4-contact geometry [DC dies; Fig. 3.1(a)] and another that incorporates wave guides [DCRF dies; Fig. 3.1(b)]. Both of them allow electrical measurements (DC and RF) but the mask with the wave guides can be used to make measurements with high frequency coplanar microprobes with bandwidths up to 40 GHz. The STNOs characterized in this thesis revealed RF signals below 10 GHz, thus, both contact geometries could be used. In both masks we were able to measure the transfer curves and no significant variation of electrical or magnetic properties was observed. For simplicity, in this chapter we describe the process for the DC dies, but the DCRF were built in an analogous way. The size and distance between contacts was chosen accordingly to the pads used in the semi-automatic DC prober (section 2.7.2).

In spite of the geometries shown here, different variants of the process can be performed, such as nanopillars with point contacts (see section 5.1), MTJs in series and MTJs with heat lines. The fabrication of these devices is almost independent on the MTJ stack, hence, no significant changes have to be introduced for the different stacks (besides the used mask and etching times). During the full fabrication process, there is only one e-beam lithography (step 5; nanopillar definition). The remaining steps were performed using optical lithography. The used photoresist (PR) for the optical lithography was the AZ1505, the developer AZ400K and both the mask aligner (section 2.3.2.2) and the direct right lithography (DWL; Section 2.3.2.1) could be used. The mask aligner only takes a few seconds to operate but the masks are not adaptable, whereas the DWL has longer exposure times but the masks can be easily changed. Since the masks were regularly altered from sample to sample, the DWL was the main lithographic tool.

This process allowed us to fabricate MTJ nanopillars with a high yield process with up to 32 dies (with dimensions of 1.9 cm per 1.9 cm each) in a 200 mm wafer. However, usually only 6 to 8 dies were fabricated per wafer since it is a good compromise between processing time and final number of devices. Each die is divided in 3 major vertical columns (C_1, C_2 and C_3), each of this major columns is divided in 10 sub vertical columns (positions; P_i) and a maximum of 35 rows (R_i) in the case of the DC dies (Fig. 3.2) and of 17 rows in the case of DCRF. In each of the intersections (R_i, P_i) an MTJ with a 4-contact scheme [such as the one of Fig. 3.1(a)] is fabricated. Thus, up to 1050 sub-μm MTJs per die and 33600 per wafer can be achieved (the number of functional devices depends on the size and position dependent yield; see section 3.5). Usually we chose to fabricate some dies with DC and others with DCRF structures, but dies with mixed structures were also fabricated. Note that different nanopillar dimensions can be defined for each position. We chose to maintain the sizes constant along the rows and change it along the positions. In each lithographic step, alignment marks were defined that are used to align the lithographies sequentially (Fig. 3.2 right inset; similar marks were defined in the dies with DCRF structures).

3.4 PROCESS STEPS

Step 1: MTJ deposition

The process starts with the deposition of 100 nm of Al_2O_3 in the TIMARIS FTM. The depositions were performed mainly in Si 200 mm wafers. This layer of Al_2O_3 is used to prevent the electric contact between the Si substrate and the MTJ. This step is followed by the MTJ stack deposition that takes place in the TIMARIS MTM tool with a base pressure of 2.0×10^{-9} mbar. Previous to any deposition the targets were cleaned by performing five MTJ depositions in a dummy wafer. Different types of stacks, such as MgO wedges, structures with perpendicular magnetic anisotropy, or stacks with thick soft ferromagnets for vortex formation, could be deposited. For the sake of simplicity we consider that every deposited stack consists of the following parts: Bottom contact (BC) / MTJ / Capping layer (CL). The BC usually consists on a CuN / Ta multilayer and different CL were used (as shown in step 5). The MTJ part is the core of the stack, here it was called MTJ for simplicity but it can be a complex structure with a synthetic antiferromagnet (SAF), perpendicular polarizers, double MgO barriers, etc.

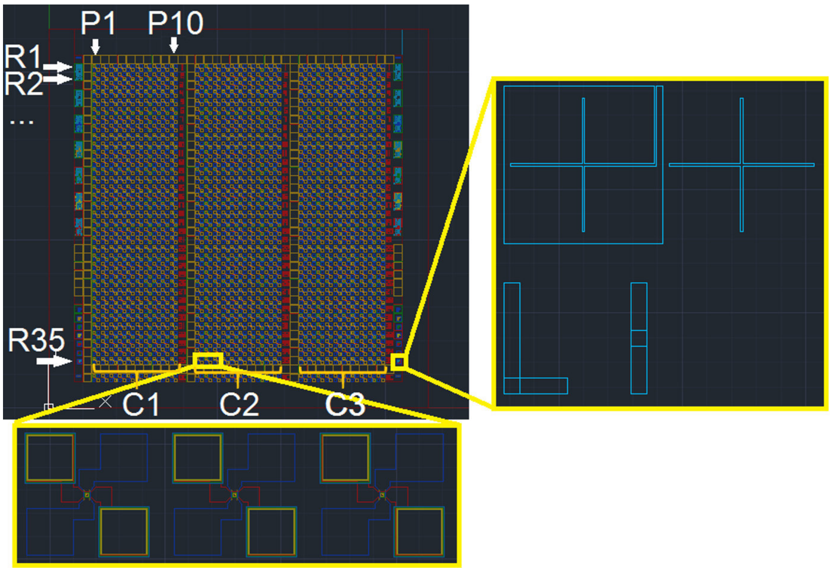

Figure 3.2: Autocad mask used to perform the lithographies of the process. Each color represents a different layer. The bottom inset shows three sequential structures whereas the right inset shows the used alignment marks.

In section 3.5 an example of a complete stack and its electrical and magnetic properties will be provided.

Step 2: Magnetic annealing

The magnetic annealing could be performed either before or after nanofabrication. Usually, it was performed before the process in order to verify the bulk electrical and magnetic properties of the MTJ before processing using the CIPT and the VSM, respectively. Moreover, it is possible that the annealing induces stresses on the fabricated device that lead to the loss of electrical contact. The annealing was performed in vacuum (to avoid oxidation) under an applied magnetic field to define the easy magnetization direction and to promote the right crystalline orientation of the CoFeB/MgO/CoFeB trilayer. Note that to achieve a large TMR an epitaxial bcc (001) MTJ crystalline structure is necessary (section 1.3.3). This is achieved by depositing amorphous CoFeB and during annealing the proper crystalline growth is induced by the MgO. The annealing that maximized the TMR consisted on 330 ºC with an applied field of 1 T for 2 hours; these conditions were the ones used in the work performed in this thesis.

Step 3: Sacrificial top contact deposition

Different CLs were deposited. In the case of AlSiCu/TiWN layers, this deposition was performed in the Timaris FTM after the annealing. However, it was verified that a CL consisting of Cu 150 nm/Ru 30 nm led to the best nanopillars' profile with less redeposition (see step 5). Therefore, after some point this was the used CL. The deposition of the Cu/Ru-based CL was performed in the Timaris MTM after the MTJ deposition (step 1) without vacuum break. However, it was observed that both Ru and Cu are affected during the plasma asher (section 2.3.4) process. Hence, when this CL was used, the photoresist had to be removed in acetone with ultrasounds. The CL is necessary since it will allow the electric contact between the MTJ and the top contacts.

Step 4: Trenches for Nanocalc

The first lithographic step consists in the die definition within the wafer. The dies are macroscopic (1.9 cm per 1.9 cm) with 0.6 cm of separation between each other. The lithography is performed using the mask shown in Fig. 3.3 and the pattern transfer is achieved through etching all the way down to the Si substrate (as shown in the inset of Fig. 3.3). The three main purposes of this step are:

1. Define the dies within the wafers. Each die can be fabricated with different purposes and using different pillar sizes or geometries. Usually, some dies were used to fabricated DC and others DCRF contact geometries.

2. During IBP (step 6) it will be necessary to determine the Al_2O_3 thickness during the etching. The space between dies etched until the Si substrate (trenches) will afterwards be used to measure the deposited Al_2O_3 thickness during IBP. Therefore, these trenches will be important for a fundamental part of the process.

3. Define the first alignment marks that will be used to align the next lithographic process (nanopillars defined through e-beam lithography). The alignment marks used for the e-beam lithography consists of a square (lateral size of 2 μm), whereas the ones used for the optical lithography are cross-shaped (right inset of Fig. 3.2). This difference is due to the different algorithms used to detect the centre of the mark.

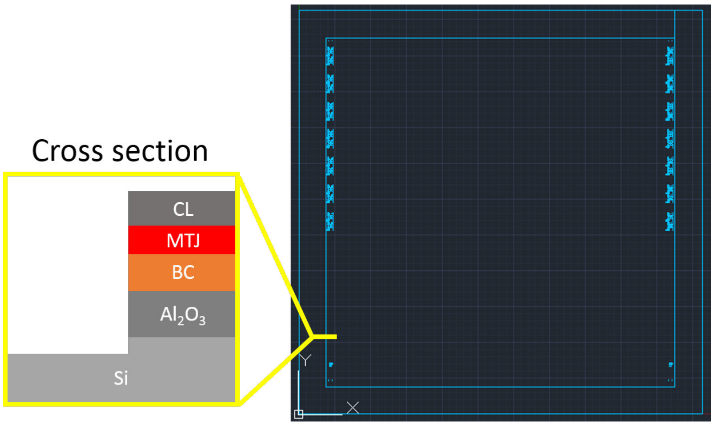

Figure 3.3: First layer for lithography of the process – trenches for Nanocalc (step 1). The inset shows the cross section after etching Si.

Step 5: Nanopillar definition

In the majority of the nanofabrication procedures, the bottom contact is defined before the nanopillar. However, in this work, the nanopillar is defined before the bottom contact (which is defined in step 7) to minimize the topography during the nanopillar definition. This improves the control and reproducibility of the process. The nanopillar characteristic dimensions (below 1 µm) cannot be accessed using optical lithography. Since the characteristic wavelength of an electron beam (e-beam) is much smaller than their optical counterpart, one can use e-beam lithography to define the nanopillars [Fig. 3.4(a) and (b)]. The e-beam resist used was the ARN7520. To define the smaller features we used a step of 2 nm, a dose of 612 $\mu C/cm^2$ and a beam of 33 pA. Lateral dimensions down to 50 nm could be achieved with resist thicknesses of 200 nm. In this step we also divide the die in the different columns and lines. In Fig. 3.4(c) we show a schematic representation of the mask used in each nanopillar position. Marks were introduced in order to find the pillars more easily in the SEM, with the triangular shape being chosen so that the wafer orientation was clear during SEM inspection.

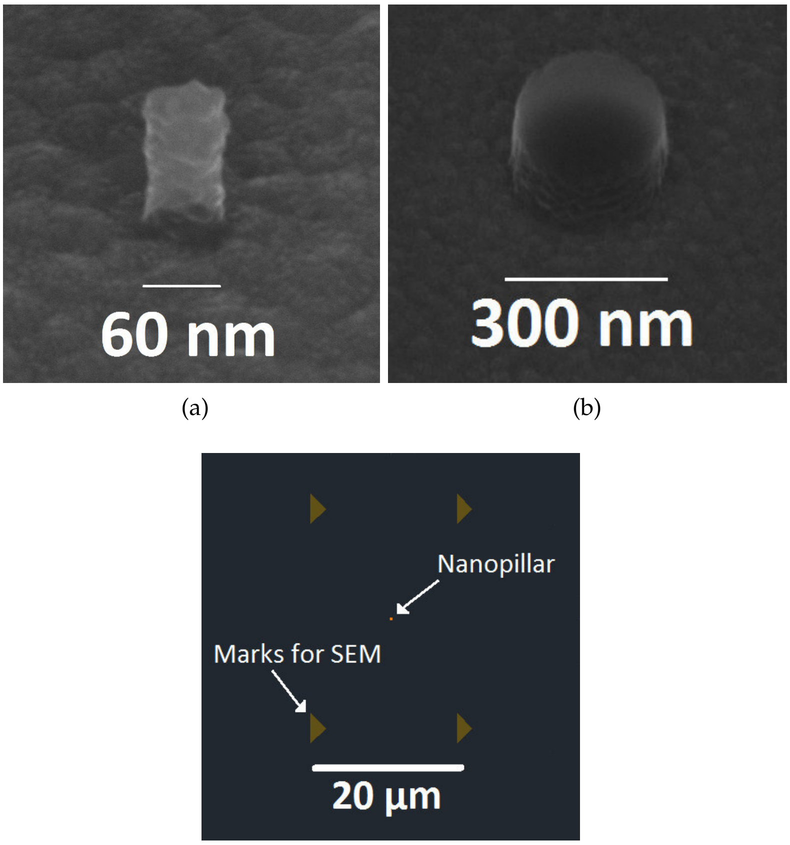

(a)

(b)

(c)

Figure 3.4: SEM images of the e-beam resist after lithography for pillar sizes of (a) 60 nm and (b) 300 nm. (c) Schematic representation of the pattern defined during the e-beam lithography for each pillar position.

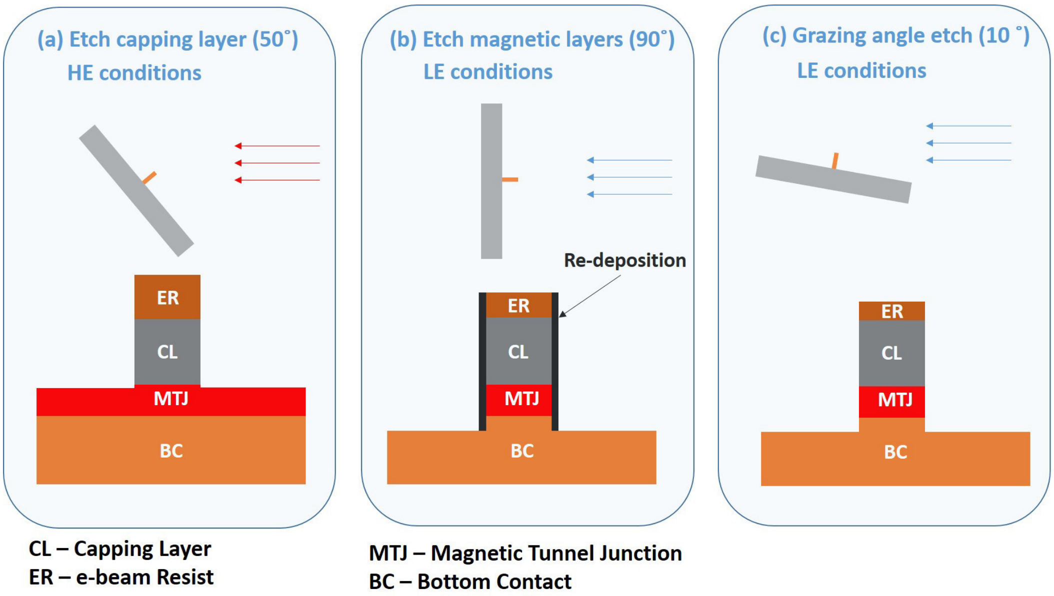

Figure 3.5: Schematic representation of the three-step milling for the nanopillars definition. (a) etch CL with best possible profile (50°) and LE conditions (red arrows); (b) etch magnetic sensitive layers with an orthogonal beam with LE conditions (blue arrows); (c) sidewall cleaning with a grazing angle of 10° and LE conditions.

The MTJ pillars fabricated in this thesis for the electrical measurements were defined using a three step milling as schematized in Fig. 3.5. (1) The CL was etched with HE conditions and the incidence angle that led to the best profile of the sidewalls (incidence angle of 50°). (2) The magnetic sensitive layers were etched with LE conditions and normal incidence, so that the transverse component of the beam would be minimized and the formation of a dead magnetic layer avoided. (3) A sidewall cleaning with LE conditions and grazing angle (10°) was performed in order to clean material re-deposited on the pillar walls.

The etching of the two first millings could be monitored using the SIMS. We chose to stop the first etch as soon as the first layer of the MTJ was detected (we usually used a Ru thin layer on top of the magnetic layers in order to define a stopping point). As for the second milling we chose to stop within the bottom contact. In Fig. 3.6 the SIMS plot used to control the stopping point during the nanopillar definition is shown (second etch at normal incidence). In this case the bottom contact consisted in a Ta layer and the etching stopped after 1h and 10 min. The signal corresponding to the other layers (Co, Fe, Ru, etc. could also be monitored). The spreading of the peaks is a consequence of the large wafer size and the very thin layers. Note that this step uses LE conditions and thus the etching rate is lower. The etching at 10°

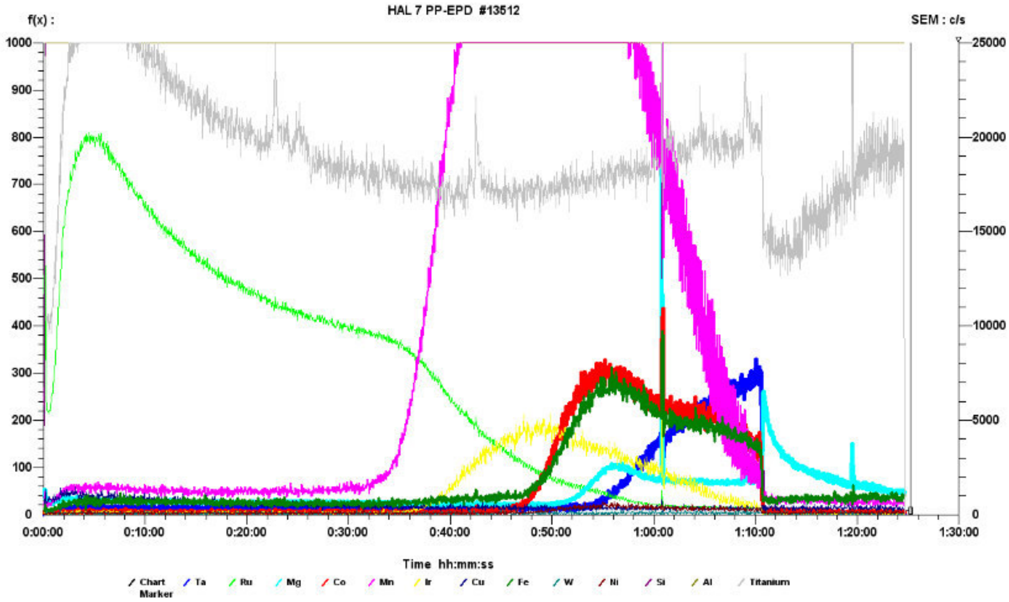

Figure 3.6: SIMS plot of the nanopillar definition etch (LE conditions and normal incidence).

of incidence angle could not be monitored using the SIMS because the signal was too low. Moreover, during the sidewall cleaning we are interested in etching the re-deposited material, which is a mixture of the various materials present in the sample. Therefore, this step of the process was controlled through time and checking the nanopillars state by using the SEM.

In the following sections, we will present a detailed overview of the steps that led us to this three-step nanopillar definition. Variables such as milling angle, resist strip and the effect of the CL were considered. This angular dependence of the etching was performed in an early stage of this thesis, when the etching conditions were still not optimized. The conditions used here were an acceleration grid current of 400 mA, a negative acceleration grid potential voltage of 3000 V and a positive potential of 500 V. The neutralizers were set to 230 mA and 4.0 sccm. The results were consistent for the optimized conditions.

Ion milling angle

Nanopillar definition using ion milling is a complex process with a large amount of variables affecting the obtained profile and, thus, the final magnetic and electrical properties. The etching angle has a strong influence on this profile by affecting the sidewall re-deposition and causing a shadow effect. Figure 3.7 shows SEM images of nanopillars etched with different milling angles (between the beam and the surface of the wafer). It is clear from Fig. 3.7(a) that an ion beam incidence at high angle (70°) leads to a high quantity of re-deposited material. This occurs because the material etched from the sample surface spreads in all directions and some eventually re-deposits on the nanopillar sidewalls. As the angle of the ion beam incidence decreases, the amount of re-deposited material decreases but the shadow effect becomes increasingly more important. [Fig. 3.7(d); etching at 40°]. It appears for lower angles because, when the incidence is not orthogonal to the sample surface, the pillar itself blocks the ion beam, causing an effect equivalent to a shadow. Also, since the beam component parallel to the sample surface becomes more relevant, the low angle milling favours the formation of nanopillars with inverted sidewalls. This strong parallel component not only makes it harder to know the exact value of the MTJ size but, more importantly, damages the MTJ sidewalls, leading to a degradation of its magnetic properties. A fine-tuning is needed to balance these factors. Figure 3.7(b) and (c) show the nanopillar after etching at 55° and 50° respectively. Despite the small variation of the milling angle, there is a significant impact on the nanopillar profile. We have then chosen to use a 50° incidence of the ion beam for most etching steps since it allowed the formation of vertical sidewalls with a small amount of re-deposition.

3.4.0.3 *Sidewall cleaning*

Even using a beam incidence that allows the formation of nanopillars with vertical sidewalls, it is difficult to avoid the presence of some re-deposition. This re-deposited material decreases the TMR of the MTJ by shunting the insulating barrier. One way to prevent this effect and clean the re-deposited material consists of using a grazing angle milling step after the nanopillar definition. Figure 3.8 shows the evolution of the profile of the same pillar with the sidewall cleaning time (under a 10° beam incidence). In Fig. 3.8(a) it is shown the nanopillar after definition with an incidence angle of 90° which leads to significant re-deposition. As the sidewall cleaning proceeds, and re-deposited material is etched, the pillar lateral dimensions decrease. It is clear from Figs. 3.8(d) and (e) that re-deposited material starts to be removed from top to bottom since the top part is affected both by the parallel and normal component of the beam, while the bottom part is only affected by the parallel component. When all re-deposited material is removed, the selectivity between different layers leads to a variation of the nanopillar dimensions along its height [Fig. 3.8(f)].

Resist strip

After the nanopillar definition there may still be e-beam resist present on top of the MTJ. This residual resist could, in principle, prevent electrical contact between the top electrode and the MTJ. We were not able to remove the exposed e-beam resist using a standard resist strip process (acetone + ultrasounds). Therefore, a plasma asher treatment was tried to remove the

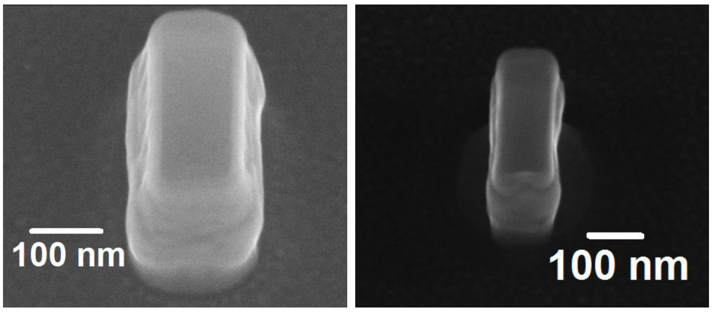

(a) θ = 70 ° (b) θ = 55 °

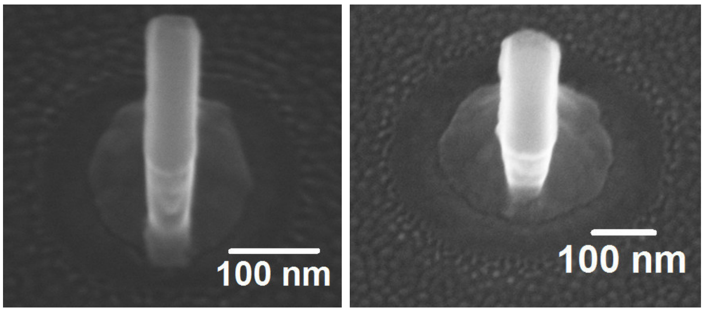

(c) θ = 50 ° (d) θ = 40 °

Figure 3.7: SEM images of nanopillars after definition with a single step ion milling with different incident beam angles: (a) 70°; (b) 55°; (c) 50°; (d) 40°. The conditions used here were an acceleration grid current of 400 mA, a negative acceleration grid potential voltage of 3000 V and a positive potential of 500 V.

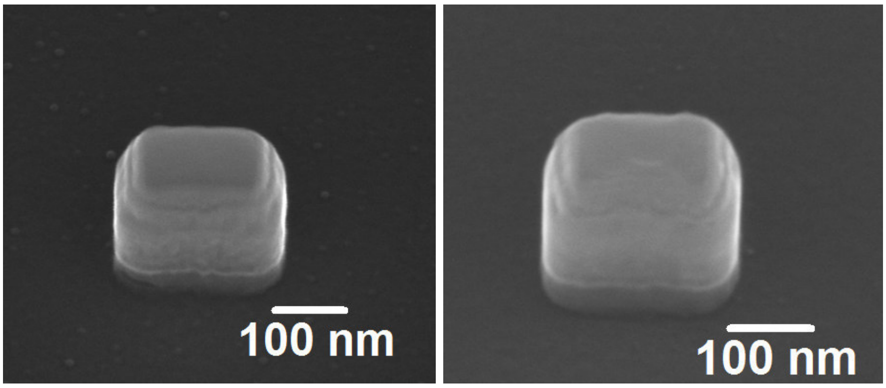

(a) t = 0 s (b) t = 400 s

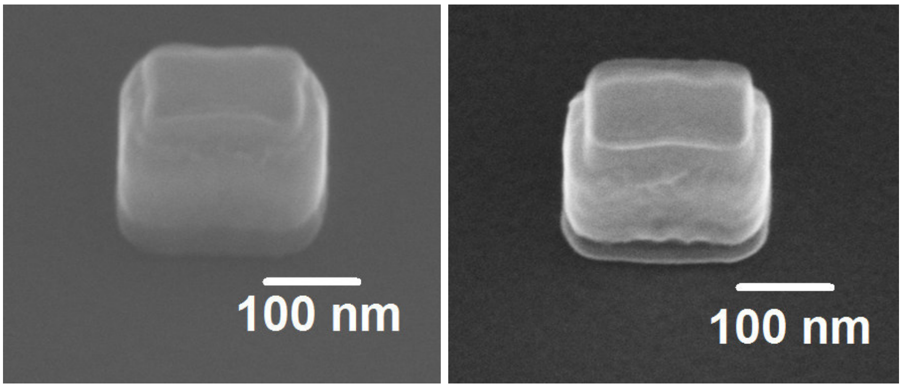

(c) t = 800 s (d) t = 2000 s

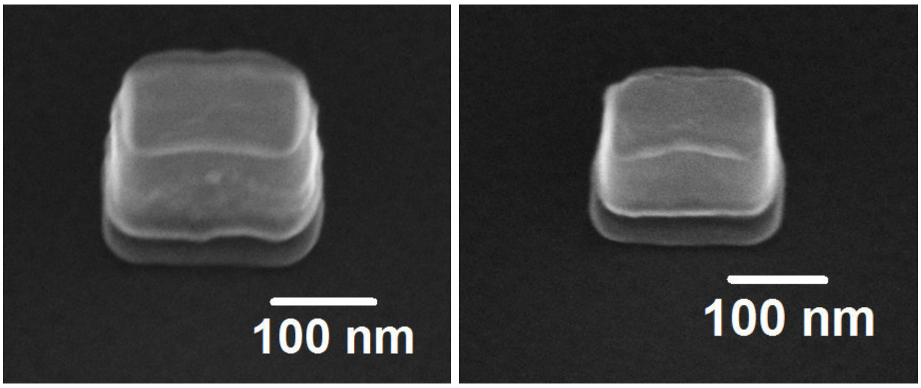

(e) t = 2800 s (f) t = 3600 s

Figure 3.8: Effect of 10° sidewall cleaning on the MTJ profile of the same device. (a) after nanopillar definition at 90° beam incidence; after sidewall cleaning with beam incidence of 10° during (b) 400 s, (c) 800 s, (d) 2000 s, (e) 2800 s and (f) 3600 s. The conditions used here were an acceleration grid current of 400 mA, a negative acceleration grid potential voltage of 3000 V and a positive potential of 500 V.

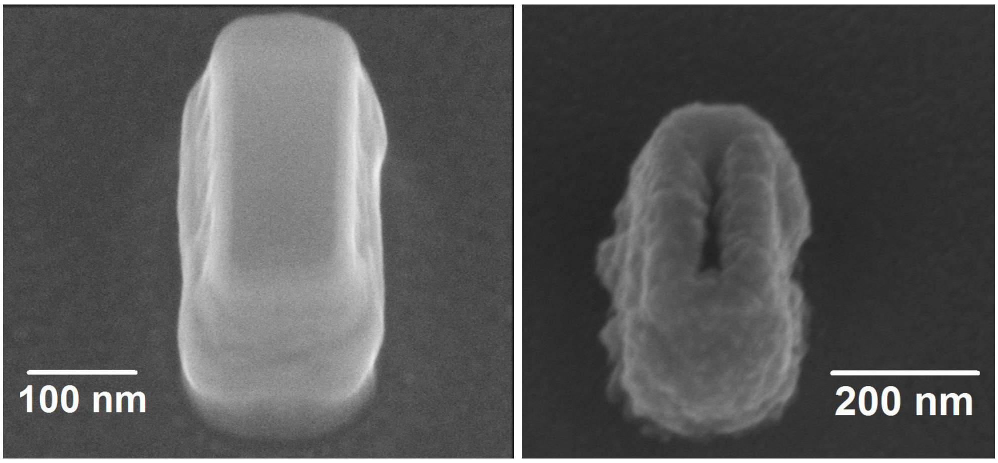

(a) Before plasma asher (b) After plasma asher

Figure 3.9: SEM image of the same nanopillar after (a) ion beam definition and (b) the same pillar after definition and plasma asher.

remaining resist. This system uses a microwave plasma to remove polymeric material. From Fig. 3.9(a) after nanopillar definition and (b) after plasma asher it is clear that the e-beam resist is indeed removed. However, this process also strongly affects the metallic materials of the nanopillar, oxidizing them and affecting the profile and, most likely, the electric properties of the MTJ. Due to this issue we chose to continue the process without this step. Furthermore, notice that this resist on top of the pillar will be residual or even absent when the process is finished. This occurs because, from the initial thickness of e-beam resist (~ 200 nm), only a small fraction will remain after the 3-step nanopillar definition. Moreover, during the IBP (step 6) we chose the stopping point to be within the thick CL and after the resist is etched away.

Capping layer

The CL plays a fundamental role in the IBP process as will be shown in step 6. However, the thickness and composition of these layers also affects the profile of the nanopillars and thus their electric and magnetic performance. Figure 3.10 shows nanopillars with different CLs after nanopillar definition (the dimensions of the pillars after e-beam lithography were 100 × 100 nm^2). In the three cases we etched the CL with HE conditions at 50° incidence and the magnetic layers with LE conditions at normal incidence. The nanopillars with a CL of AlSiCu (150 nm)/TiWN (80 nm) revealed a large amount of re-deposition that resulted in a cone-like

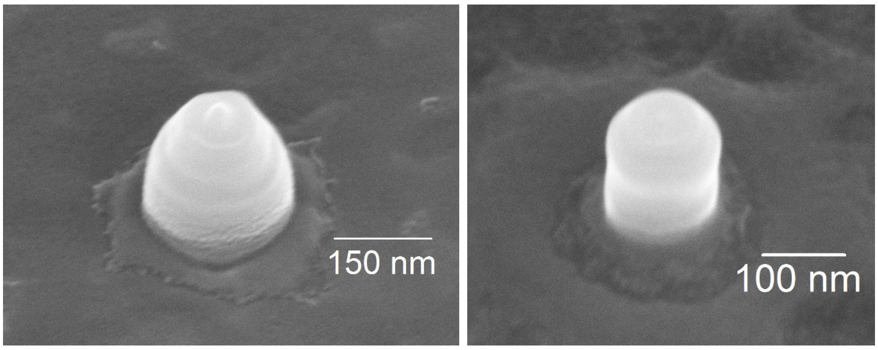

(a) AlSiCu (150 nm) / TiWN (80 nm) (b) AlSiCu (150 nm) / TiWN (5 nm)

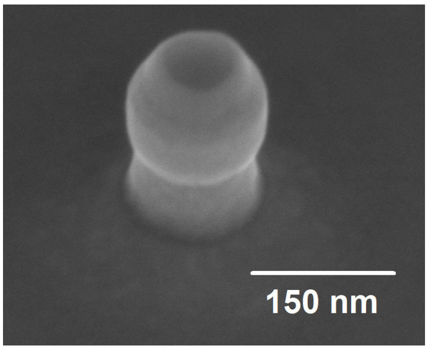

(c) Cu (150 nm) / Ru (30 nm)

Figure 3.10: SEM images nanopillars with e-beam dimensions of 100 × 100 nm^2 after etching of the CL (with LE etch and an incidence of 50°) and the magnetic layers (with LE etch and normal incidence) for different capping layers: (a) AlSiCu (150 nm) / TiWN (80 nm); (b) AlSiCu (150 nm) / TiWN (5 nm); and Cu (150 nm) / Ru (30 nm)

shape [Fig. 3.10(a)]. If the thickness of the TiWN is reduced to 5 nm [Fig. 3.10(b)] more vertical walls are obtained but still some re-deposition is present. Heavier metals (such as TiWN) are prejudicial as CLs because, after etching, they have low kinetic energy and thus will remain close to the sample surface and re-deposit on the pillars. Since a thick CL is necessary for the IBP process, the best way to reduce re-deposition is to use lighter materials. In fact, for a Cu (150 nm)/Ru (30 nm) structure we observe a significant decrease of the re-deposition [Fig. 3.10(c)]. After the optimized process, the Cu (150 nm)/Ru (30 nm) CL was the mainly used CL. Nevertheless, functional devices could be achieved with different CLs. In fact, the electrical measurements that will be shown in section 3.5 were obtained with a AlSiCu (150 nm)/TiWN (5 nm) CL.

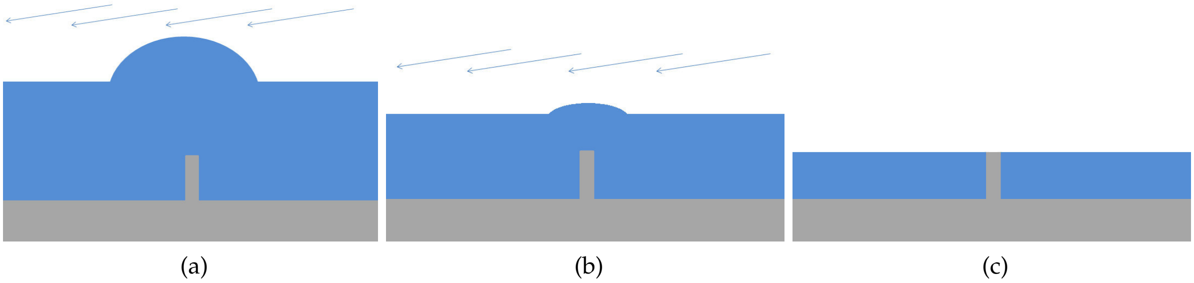

Figure 3.11: Schematic representation of the planarization process. (a) Conform deposition of the Al_2O_3; (b) the grazing angle etch (10 deg) etches and planarizes the surface; (c) when the thickness of the Al_2O_3 is smaller than the height of the pillar we were able to obtain a plane surface with the nanopillars open on top.

Step 6: Ion Beam Planarization (IBP)

After the nanopillars are defined, we have to confer physical and electrical stability to the structure, protect the sidewalls of the MTJ and isolate the bottom from the top contact. Therefore, our goal consists of obtaining a matrix of a robust insulating material, involving the pillars, which in turn are open on the top. To do that, we deposited an Al_2O_3 layer (600 nm), thicker than the height of the pillar (usually $\sim$ 200 nm) so that we have enough material to planarize. This Al_2O_3 layer deposition is conform and thus follows the profile of the nanopillars [Fig. 3.11(a)]. This occurs because the target is larger than the sample and thus the lateral walls are always exposed to the deposited material, forming a bump of Al_2O_3. To achieve the matrix of Al_2O_3 surrounding an open MTJ we have to planarize and reduce the thickness of the insulating layer. Our approach consisted in using an ion beam milling step (with HE conditions) at grazing incidence (10°). With these etching conditions, the etching rate in the direction parallel to the surface is higher than that in the direction normal to the surface. Thus, the structure becomes less conform [Fig. 3.11(b)] and eventually planarizes completely with the top CL of the pillars open [Fig. 3.11(c)]. Due to the conform Al_2O_3 deposition, the bump width will depend on the pillar size. A throughout study of this dependence was not performed, but it was observed that the 600 nm of Al_2O_3 are sufficient to planarize structures with pillars as big as 500 nm (of diameter).

In order to obtain fully operative devices, the stopping point of the IBP has to be within the CL in the full wafer. Since the open pillars do not have a significant area, SIMS cannot be used to determine the stopping point. Therefore, we use a combination of two complementary methods to determine the etching stopping point. (1) Trenches without deposited material on top of the Si substrate were defined in the first optical lithography process (step 4), so that the thickness of the Al_2O_3 layer can be measured using an optical profilometer (section 2.5.4). (2) SEM images are also taken to verify the planarization state of the Al_2O_3 layer and if the MTJ pillars are already open. Figure 3.12 shows the sequence of the IBP process for different milling times for a pillar of 100 × 100 nm^2. Figure 3.12(a) shows the pillar buried in the insulating layer after the deposition of 600 nm of Al_2O_3. The highly conform oxide leads to a high bump in the region with approximately 450 nm of diameter. As the planarization proceeds the diameter of the bump decreases and the oxide layer becomes smoother [Fig. 3.12(b)]. Note that the etch rate in the direction parallel to the surface (measured as the variation of the bump diameter per time) is close to 6 nm/min, which is higher than in the direction perpendicular to the surface (~1.5 nm/min). Finally, the Al_2O_3 is completely planarized but the nanopillar is still completely immersed in the oxide matrix [Fig. 3.12(c)]. When the CL is reached a higher contrast is observed in the SEM image [Fig. 3.12(d)] due to the presence of conductive materials. Figure 3.12(e) shows a schematic representation of the structure after IBP, with the pillar open within the CL involved in a matrix of Al_2O_3. The grazing milling and the different material selectivities lead to some profile of the top part of the pillar. This small profile helps to resolve the SEM image and might even remove residual e-beam resist.

The planarization revealed a strong dependence in the etching angle. In fact, the IBP performed with a grazing angle of 10° between the sample surface and the ion beam led to a planarized structure with the nanopillar open on top of the Al_2O_3 matrix [Fig. 3.13(a)]. On the other hand, IBP with an incidence angle of 15° already revealed an etching rate normal to the sample higher than in the parallel direction, preventing the planarization to occur [Fig. 3.13(b)]. In this case, a final plane structure could not be achieved and despite the fact that we can distinguish the profile of the pillar, it is still covered with Al_2O_3. In the structures fabricated with 15° of tilting angle during IBP open circuits were obtained, which indicates that the nanopillars were not open on top.

The IBP process allowed the fabrication of sub-μm MTJs in a 200 mm process. The uniformity of the etching with the grazing angle of 10° is ~12% in the full wafer with an etch rate of 1.5 nm/min in Al_2O_3. This uniformity is approximately 2 times worse than the one with an incidence of 50° (the angle that maximizes the etch rate to 4.4 nm/min). It is difficult to improve the uniformity at these grazing angle millings due to the presence of the clamps holding the substrate. However, during the IBP process at most 400 nm of Al_2O_3 are etched, corresponding to an error of 48 nm along the full wafer. Even taking into account extra uniformity variations arising from the stack deposition and nanopillar definition, the thick CL guarantees that all devices are open without damaging the magnetic layers in the full 200 mm wafer. The IBP process is also better suited to smaller devices since they have a smaller profile after Al_2O_3 deposition. After the IBP step is complete, 15 nm of TiWN were deposited

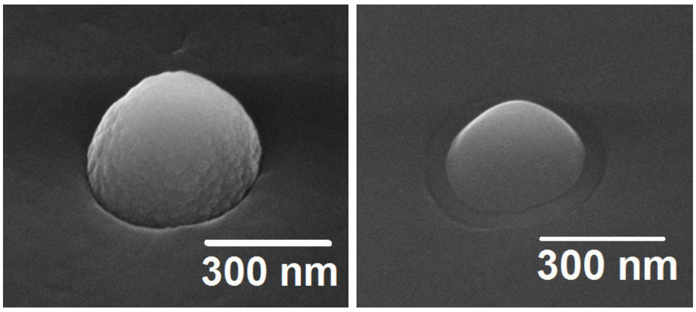

(a) t_{Al2O3} ~ 600 nm (b) t_{Al2O3} ~ 340 nm

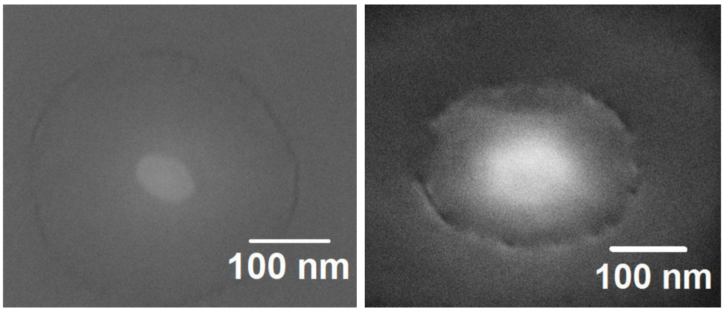

(c) t_{Al2O3} ~ 260 nm (d) t_{Al2O3} ~ 215 nm

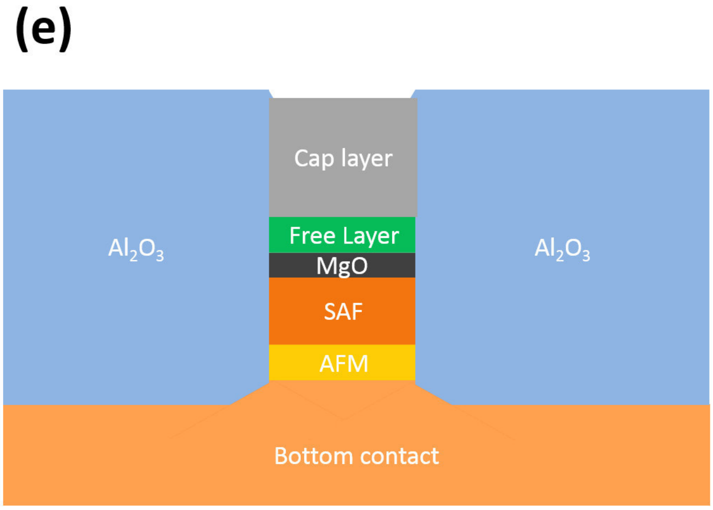

(e)

Figure 3.12: SEM images of different steps of the planarization process (at incidence angle of 10°). (a) after the depositing the thick Al_2O_3 layer (t_{Al2O3} ~ 600 nm); after planarization for (b) 1000 s (t_{Al2O3} ~ 340 nm);.(c) 2740 s (t_{Al2O3} ~ 260 nm); and (d) 3770 s (t_{Al2O3} ~ 215 nm). (e) Schematic representation of the device after IBP.

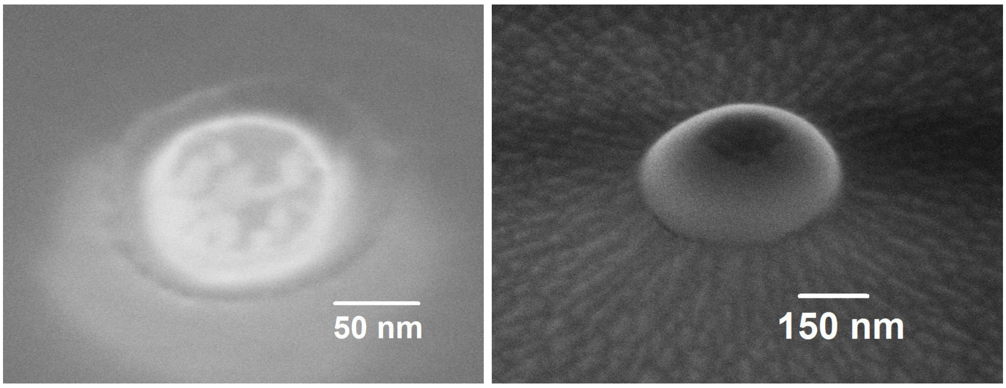

(a) θ = 10 °

(b) θ = 15 °

Figure 3.13: SEM images of MTJ pillars after the planarization process at different incident beam angles: (a) 10° and (b) 15° for HE conditions.

to protect the exposed part of the pillar and allow electrical contact (as will be shown in the following steps). Figure 3.14 shows a cross section of a nanopillar after completing the full fabrication process. Despite the presence of some shadow effect on the nanopillar profile, it was verified that the MTJ part is confined to the part with vertical sidewalls.

Step 7: Bottom contact leads definition

After the IBP, the nanofabrication process is finished and the remaining steps concern the microfabrication of the contacts required to establish electrical contact to the bottom and top of the MTJ. The structure after IBP for each position consists on an MTJ nanopillar involved by a dielectric matrix that confers stability and electrical isolation. These nanopillars are connected to a metallic layer on top (15 nm of TiWN deposited after the planarization) and to the BC below the planarized dielectric in the bottom.

Hence, the next step consists in defining the bottom contact leads. This structure will be used to define the two bottom contacts on the edge of the contact leads. This is done by defining the structure shown in Fig. 3.15(a; red part) using optical lithography and etching until the Al_2O_3 below the bottom contact [see inset of Fig. 3.15(a)]. Once again, SIMS is used to determine the stopping point [Fig. 3.15(b)]. Note that, in the center of the bottom lead, there is the MTJ connecting the top and the bottom metallic layers. Using the plasma asher, the resist is removed and we obtain MTJs electrically separated from each other and the bottom contact leads defined.

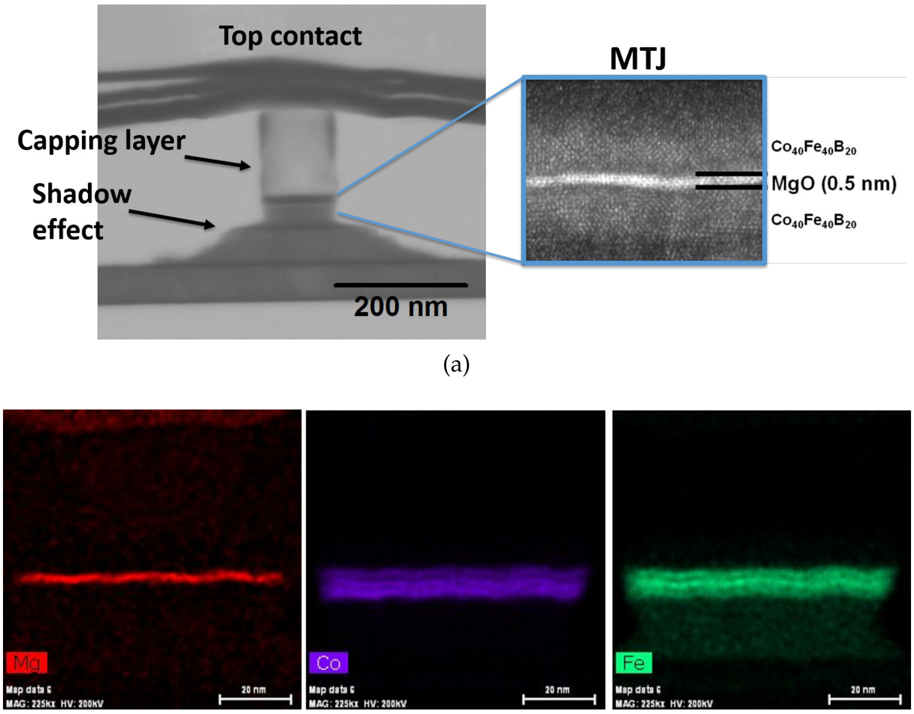

(a)

(b)

Figure 3.14: (a) Cross sectional SEM image of the MTJ final device obtained with a focused ion beam system. MTJ nanopillars with vertical sidewalls and negligible re-deposition can be seen. The shadow effect is confined to the bottom contact and so will not affect the magnetic properties of the MTJs. The inset shows a TEM image of the epitaxial MTJ. (b) TEM energy dispersive spectroscopy (EDS) images showing the material distribution of Mg, Co, and Fe in an MTJ cross-section.

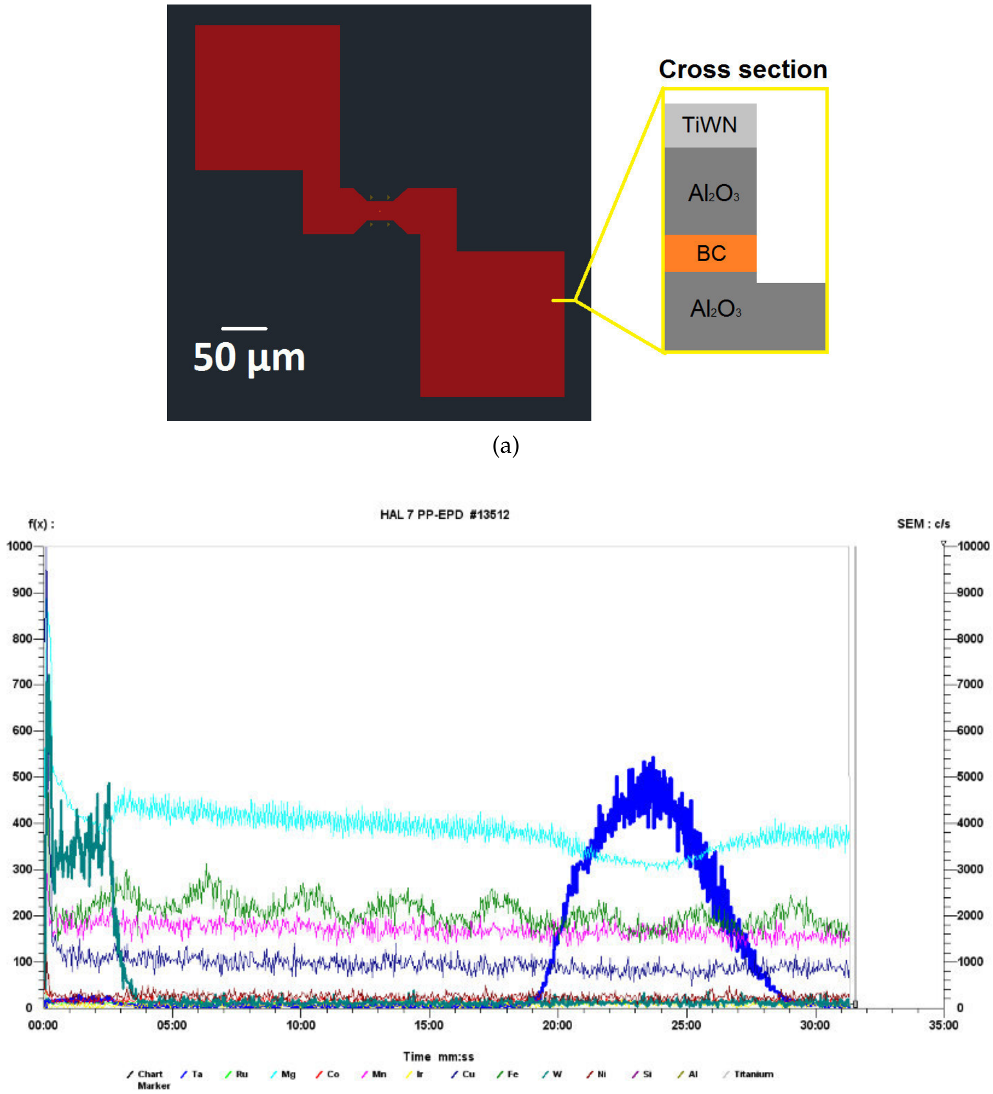

(a)

(b)

Figure 3.15: Bottom contact leads. (a) Mask used to define the bottom contact leads (red part). The brown triangles were defined during the e-beam lithography to make it easier to find the nanopillars during the SEM inspection. The orange point in the centre of the triangles is the nanopillar. The inset represents a cross sectional cut along the yellow line after step 7 is complete. (b) SIMS plot used to determine the stopping point during the bottom lead definition; the etching was stopped after the BC (Ta BC in this case).

Step 8: Vias to Bottom Contact

After the bottom contact leads are defined, the conductive layers of the BC under the planarized Al_2O_3 still have to be reached. This will allow us to electrically connect to the bottom of the MTJ allowing the bottom contact definition. To do so, the optical lithography pattern shown in Fig. 3.16(a; yellow part) is defined. Note, however, that this lithography is reversed (clear mode) and the exposed part is open and thus PR-free. The SIMS data of the previous step [Fig. 3.15(b)] will help us to determine the etching stopping point at the BC. Figure 3.16(b) shows the SIMS plot of this etching step, stopped within the BC, and with a time in agreement with the previous etch. Moreover, the lithography is performed with soak, which is a chemical treatment with a developer that leads to a tilted profile of the PR [Fig. 3.17(a)]. This type of lithography is performed to facilitate the lift-off process that will be performed in this step (see section 2.3).

Hence, the goal of this step consists of reaching the BC and protect it from the chemicals used during the process (e.g. the developer KOH reacts with Cu and Ta). To do that, after lithography an etching through the Al_2O_3 until the BC is performed [Fig. 3.17(b)]. This is a critical step since if we etch too much we will etch the BC and if we etch too little we will stop in the Al_2O_3 layer. In both cases we would not be able to establish contact with the bottom part of the MTJ. A good etching uniformity is thus required to stop in the BC in all the fabricated dies. As shown previously, we were able to stop within the BC [Fig. 3.16(b)]. Afterwards, a thin layer of TiWN (15 nm) is deposited [Fig. 3.17(c)]. The purpose of this layer is to protect the BC from subsequent chemical treatments. After deposition, a lift-off in acetone and ultrasounds is performed. This lift-off is usually fast (~30 min) since the TiWN layer is relatively thin. After the lift-off, a structure as schematized in Fig. 3.17(d), with an open vias to the bottom contact is obtained. After finishing the process, these pads will allow us to access electrically the bottom part of the MTJ.

Step 9: Sacrificial pillar cap definition

At this point, our device consists in a bottom contact lead, mainly composed by an insulating Al_2O_3 layer between two metallic layers (the BC in the bottom and TiWN layer on top). Except for the center of the lead where an MTJ nanopillar connects both metallic layers and in the bottom pads where we etched until the bottom conductive layer and deposited a protective TiWN layer. The main objective of this and the following steps is to ensure that we can define the top lead that will allow us to access electrically the top of the MTJ.

Note that the bottom contact lead was defined by etching and thus has the lateral wall exposed [inset of Fig. 3.15(a)]. Therefore, if the top contact would be deposited directly, a short

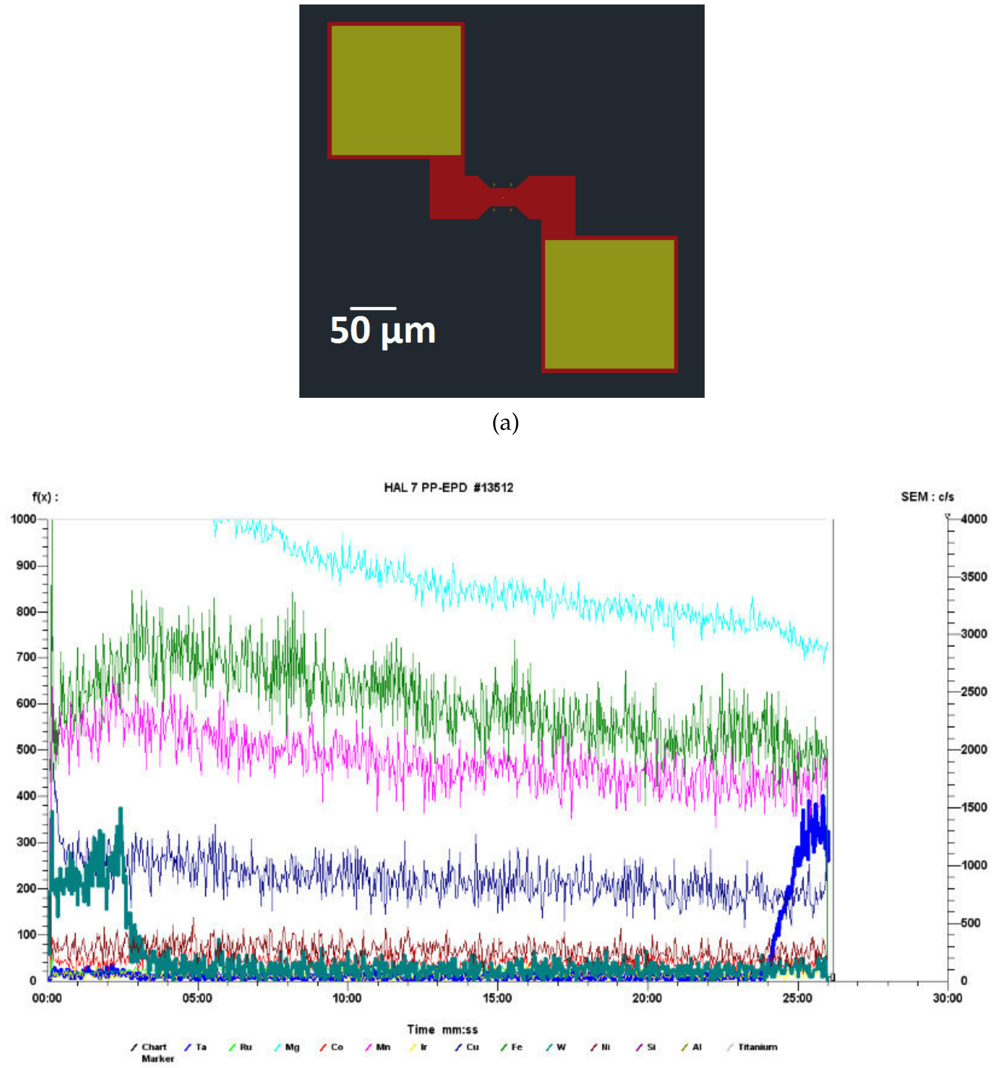

(a)

(b)

Figure 3.16: Bottom contacts. (a) Mask used to define the holes where the etch until the BC will be performed (brown part). (b) SIMS plot used to determine the stopping point during the definition of the bias to the bottom contact; the etching was within the BC.

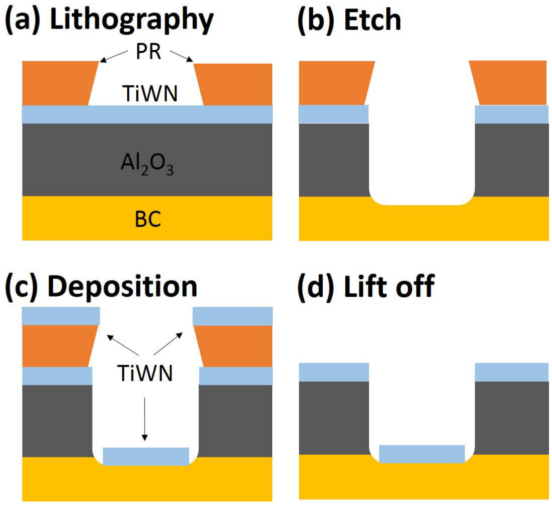

Figure 3.17: Schematic representation of the process for opening the bottom pads. (a) Lithography with soak that leads to the PR with the tilted walls; (b) etch until the BC; (c) TiWN deposition; and (d) after lift-off with acetone and ultrasounds.

circuit between the top TiWN and the BC would be obtained. To prevent this to happen, the sidewalls have to be insulated before the top lead definition. This insulation will be performed in the next step by depositing a thick Al_2O_3 layer that will cover the sidewalls. Nevertheless, first we have to make sure that we are able to access the bottom contacts and the top part of the MTJ. Thus, first a sacrificial pillar cap, that consists of a trilayer with TiWN (15 nm)/AlSiCu (10 nm)/TiWN (15 nm), has to be deposited. This trilayer structure is used so that it is easy to choose a stopping point in the following step (in between the TiWN layers). Then, again by lithography (without soak) and ion milling, three PR squares are defined: one on the top of the nanopillar and one on each bottom contact [Fig. 3.18(a); green part]. The etching stopping point is the Al_2O_3 below the sacrificial cap and the TiWN deposited after IBP [see inset of Fig. 3.18(a)] and is also controlled using SIMS [Fig. 3.18(b)]. After etching, the plasma asher is used and the sacrificial caps are obtained on top of the bottom contacts and MTJ.

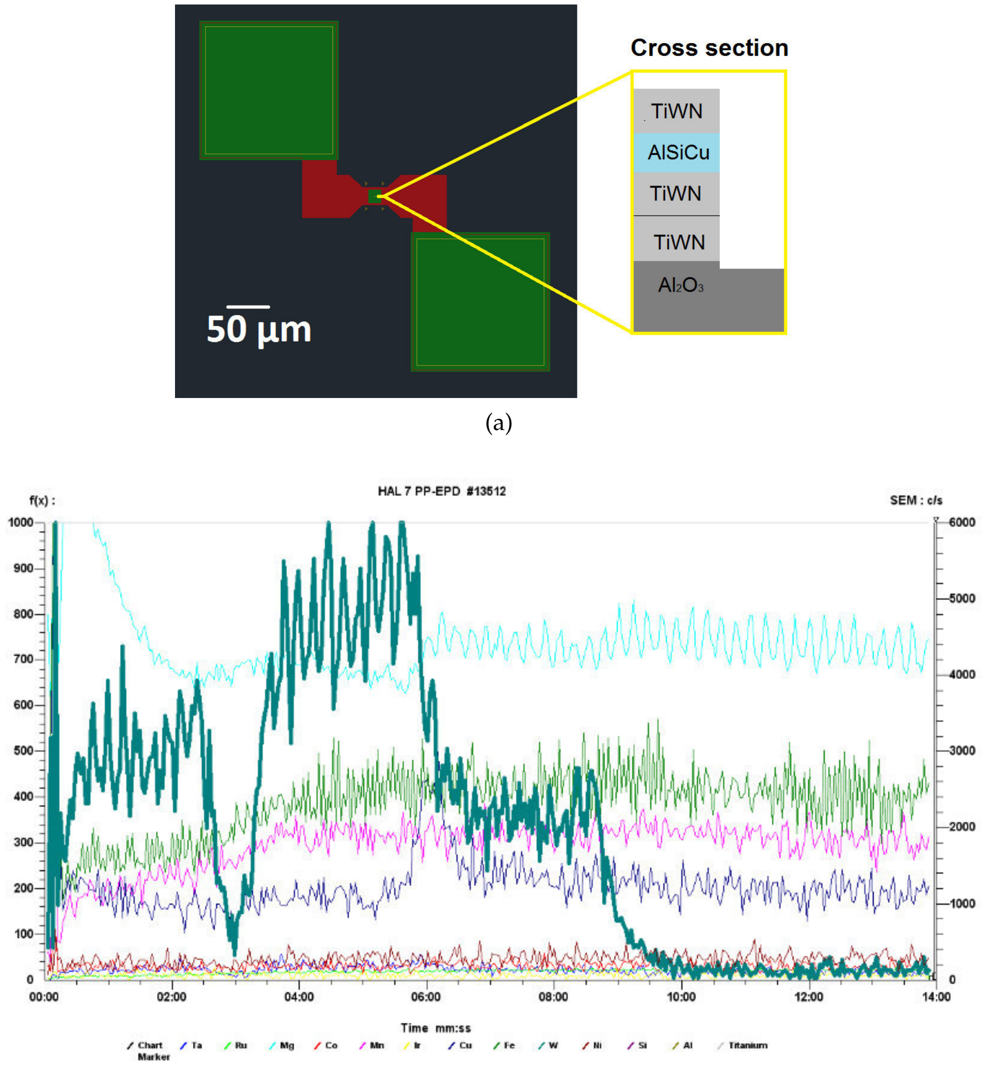

(a)

(b)

Figure 3.18: Sacrificial pillar cap definition. (a) Mask used to define the sacrificial caps (green part). The inset represents a cross sectional cut along the yellow line after step 9 is complete. (b) SIMS plot used to determine the etching stopping point after the definition of the sacrificial cap (and the extra TiWN layer deposited after IBP).

Step 10: side-wall insulation

After the definition of the sacrificial cap, and prior to the definition of the top contacts, the insulation of the sidewalls [inset of Fig. 3.15(a)] has to be performed. To do this, 300 nm of Al_2O_3 are deposited. This Al_2O_3 thickness was chosen so that it can effectively cover the sidewalls of the structure (with height of $\sim$200 nm). However, this insulating layer covers the sacrificial caps as well, preventing electrical contact to the bottom contacts and top of the MTJ. Therefore, a new lithography is performed (clear mode), where three square PR holes are defined on top of each sacrificial cap defined in step 9 [Fig. 3.19(a); orange part]. Again, using ion milling in conjugation with SIMS, an etch through the 300 nm of Al_2O_3 until the sacrificial caps are reached is performed, stopping in the AlSiCu between the TiWN layers. This is a difficult step because the SIMS signal is usually very low [since it arises from μm-sized structures; Fig. 3.19(b)]. Due to this issue, an extra Si piece with the sacrificial cap and the 300 nm of Al_2O_3 was sometimes used to detect the stopping point (depending on the number of dies). After etching, the PR is removed (using the plasma asher) and a structure with the sidewalls protected by Al_2O_3 [inset of Fig. 3.19(a)] and open on top of the bottom pads and MTJ is obtained.

Step 11: Top lead definition

Finally, we are in conditions to define the top lead that will allow the electrical contact with the top and bottom of the MTJ enabling the transport measurements to be performed. A trilayer consisting of TiWN (15 nm)/ AlSiCu (300 nm)/TiWN (15 nm) is deposited in the Timaris FTM. This thick AlSiCu layer is used to reduce the contact resistance and enhance the maximum current that can be injected. It is encapsulated between TiWN layers to prevent the Al diffusion to the pillar during annealing. After the deposition the last lithography is performed defining the top lead and the bottom pads (Fig. 3.20; blue part). This lithography is performed so that these structures are protected and the contacts can be defined by etching. After resist strip the device is complete and we can use it to perform electrical measurements in the MTJ with a 4-contact geometry.

3.5 ELECTRICAL MEASUREMENTS

The process described in the previous sections was used to nanofabricate several MTJ stacks. In particular, during the development of the process, it was necessary to nanofabricate a significant number of samples. In this section, we will focus on the electrical measurements performed on one MTJ stack that was nanofabricated over the maximum possible surface of the

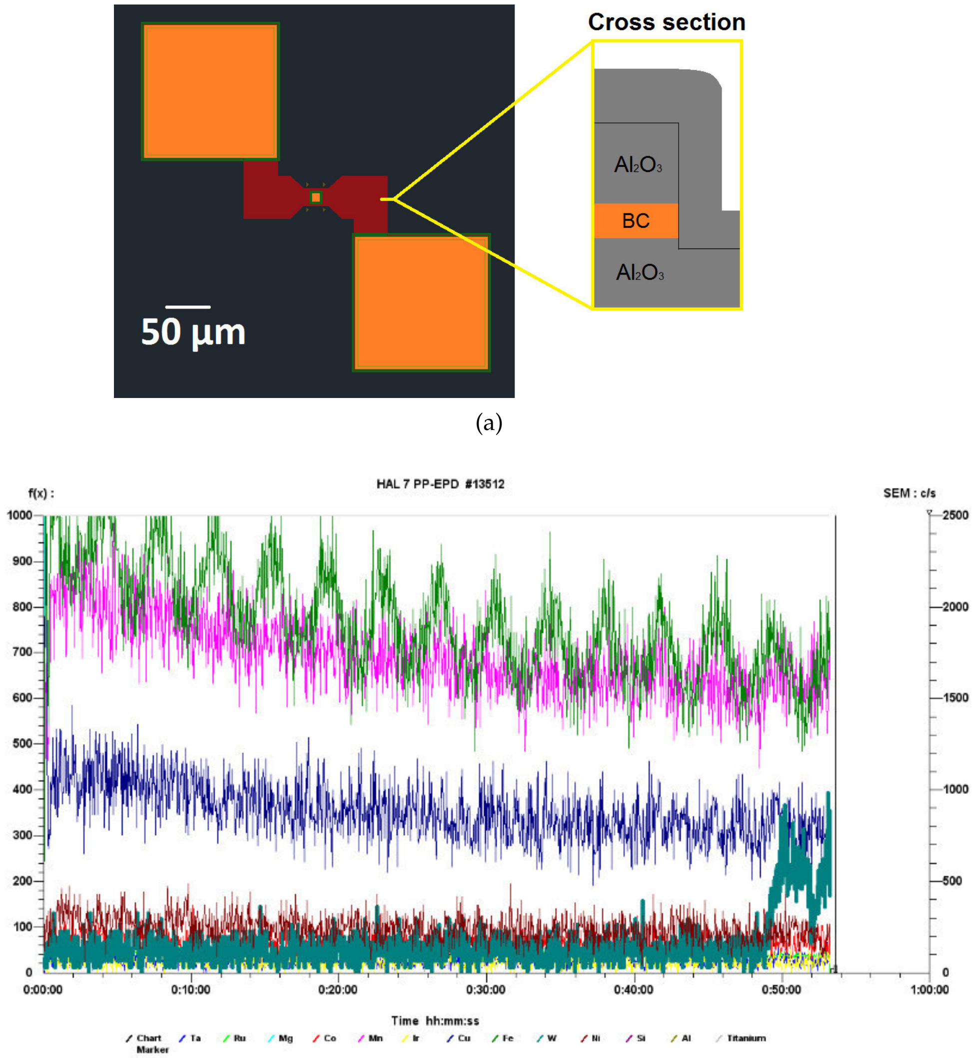

(a)

(b)

Figure 3.19: Open of via until sacrificial cap. (a) Mask used to define the holes that will be open by etch (orange part). The inset represents a cross sectional cut along the yellow line after step 10 is complete. (b) SIMS plot used to determine the etching stopping point within the sacrificial cap.

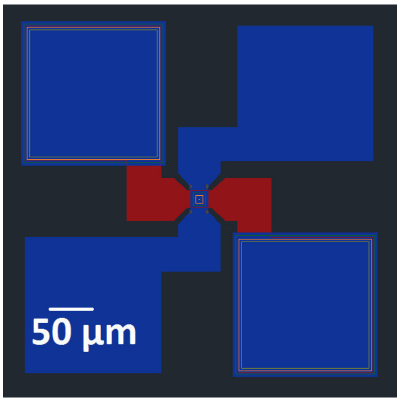

Figure 3.20: Top lead definition. Used mask to define the bottom and top contacts. After step 11 is finished the sample is ready to be measured.

wafer (the electrical properties of other samples will be also discussed in the following chapters). The goal of this sample was to determine the limits of the process in terms of achievable TMR (in the low *RA* region) and how the MTJ properties vary along the wafer position. The deposited stack was: 5 Ta/50 CuN/5 Ta/50 CuN/5 Ta/5 Ru/20 IrMn/2 $CoFe_{30}$/0.85 Ru/2.6 $CoFe_{40}B_{20}$/MgO [2×82 3kW 600sccm]/2.6 $CoFe_{40}B_{20}$/10 Ta/7 Ru, where the thicknesses are in nm. The sidewall cleaning time was 900 s and the capping layer consisted in 150 AlSiCu/5 TiWN. We fabricated 52 square dies with lateral dimensions of 2.2 cm occupying almost the totality of the 200 mm wafer. Each die has 1050 rectangular devices with lateral dimensions ranging from 100 × 40 nm^2 to 100× 450 nm^2. The electrical characterization was performed using the semi-automatic prober (section 2.7.2) and by measuring ~ 25% of all the devices equally distributed along the wafer. Using this process, we were able to extract full TMR from the MTJs in the low *RA* region for a large number of devices.

Sample miniaturization has a crucial importance for technological applications. Therefore, it is extremely important that even the smallest fabricated devices depict a very high TMR. Figure 3.21(a) shows the transfer curve for our record device, having a TMR of 156% for 1.8 $\Omega\mu m^2$ with a size of 130 × 50 nm^2. As an example, Fig. 3.21(b) shows the transfer curve at low bias for one of the smallest devices fabricated (40 × 100 nm^2), displaying a high TMR of 138% with an *RA* of 4.6 $\Omega\mu m^2$.

The uniformity of the etching process is fundamental to the electrical and magnetic properties of the MTJs over the whole wafer. To determine how the *RA* and TMR vary along the wafer, we calculated the mean value of these quantities in each of the 52 dies to all the functional devices. In Fig. 3.22(a) we schematically represent the TMR values for all die positions across the wafer. A TMR drop from the wafer center to the edge can be seen. In the central re-

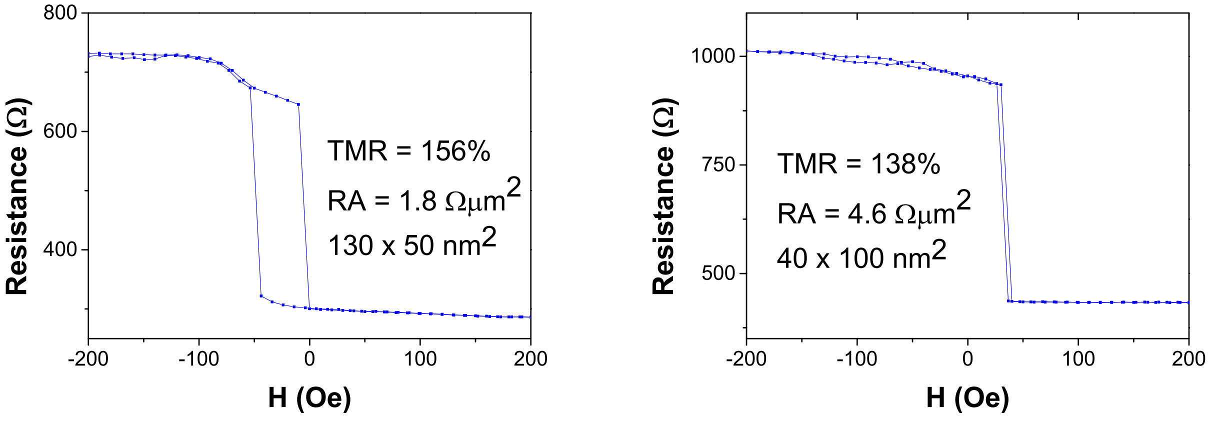

(a) (b)

Figure 3.21: Transfer curves of devices with (a) 130 × 50 nm^2 displaying a TMR of 156% and an RA of 1.8 Ωμm^2 and (b) 40 × 100 nm^2 displaying 138% and an RA of 4.6 Ωμm^2.

gion, in an area equivalent to 6 inch wafers (4×4 central dies), we achieved a mean TMR value above 100%. Although, there is a small loss of TMR in the next dies, a high value could still be achieved. However, in the outer most dies the TMR drops significantly. This loss of TMR as we approach the edge of the wafer is mostly related with the uniformity of the etching processes. Due to the presence of the clamps in the etching module, the etching of the wafer edge is not as effective as the one in the wafer center. This effect is particularly important during the sidewall cleaning due to the grazing angle etch. This results in the presence of a higher quantity of re-deposited material in the pillars of the outer dies than on those in the center, leading to a smaller TMR value.

Despite this straightforward relation of decreasing TMR as we approach the edge of the wafer, the RA relation is not as simple. In Fig. 3.22(b) we show the average RA for each die position. The central dies, that depict TMR values above 100% (4×4 central dies), also revealed a similar and low average RA value of around 1.6 Ωμm^2. In the following dies, the RA values increase to values above 2 Ωμm^2 and, in the outer most dies, RA decreases in 3 sides but remains high in the other. Since the average TMR drop when approaching the wafer edge was related with sidewall re-deposition, one expected the RA to also decrease. The RA distribution seems to indicate the overlap of two different factors. On one hand, the MgO thickness seems to increase from the wafer center leading to an increase of RA. On the other hand, as we approach the edge of the wafer, the effect of the re-deposited material becomes more important leading to an RA and TMR drop. The fact that the right edge revealed a high

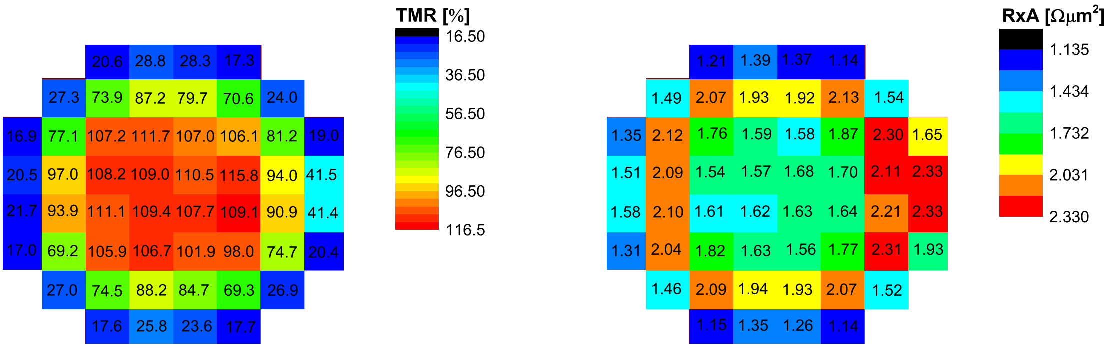

		20.6	28.8	28.3	17.3		
	27.3	73.9	87.2	79.7	70.6	24.0	
16.9	77.1	107.2	111.7	107.0	106.1	81.2	19.0
20.5	97.0	108.2	109.0	110.5	115.8	94.0	41.5
21.7	93.9	111.1	109.4	107.7	109.1	90.9	41.4
17.0	69.2	105.9	106.7	101.9	98.0	74.7	20.4
	27.0	74.5	88.2	84.7	69.3	26.9	
		17.6	25.8	23.6	17.7		

(a) TMR

		1.21	1.39	1.37	1.14		
	1.49	2.07	1.93	1.92	2.13	1.54	
1.35	2.12	1.76	1.59	1.58	1.87	2.30	1.65
1.51	2.09	1.54	1.57	1.68	1.70	2.11	2.33
1.58	2.10	1.61	1.62	1.63	1.64	2.21	2.33
1.31	2.04	1.82	1.63	1.56	1.77	2.31	1.93
	1.46	2.09	1.94	1.93	2.07	1.52	
		1.15	1.35	1.26	1.14		

(b) RA

Figure 3.22: Average (a) TMR and (b) RA for all the devices in each die position.

RA indicates that the MgO thickness variation is not completely radial as the TIMARIS MTM system uses horizontal movements during deposition. Despite the higher mean RA of the dies in the right edge, the distribution of the TMR vs RA graphs within these dies reveals an accentuated slope similar to the remaining dies on the edge of the wafer (not shown), which is an indication that some re-deposition might be present in the outer dies.

Due to the re-deposition phenomena taking place for the dies on the edge of the wafer, in the following analysis we exclude the outmost ones [see inset of Fig. 3.23(a)]. Figure 3.23(a) shows the TMR vs RA plot for devices with one lateral dimension of 100 nm and the other ranging from 40 nm to 450 nm and for which switching could be achieved with a field of 200 Oe (the maximum applied field). The results reveal that most of the MTJs have a TMR centered on 110% with an RA smaller than 2 Ωμm^2. The observed dispersion arises from the etching and e-beam steps of this highly sensitive nanofabrication process. One can also identify that some results deviate from the main cluster and are directed to the origin. This trend is the signature of electrical transport performed by other mechanisms rather than tunneling. The origin of such mechanisms can be either through re-deposited material on the surface of the pillars, or defects present in the MgO barrier (such as pin-holes). As will be shown in the next chapter, we have strong indication that the effect of the re-deposition can be completely overcome through the sidewall cleaning step (at least in the central part of the wafer). Hence, we believe that this trend of the TMR and RA decrease is mostly due to the presence of defects on the MgO barrier (which become more relevant for smaller pillar sizes). Nevertheless, the number of devices present in the slope region are a minor percentage of all the nanofabricated MTJs (~2%).

Different pillar sizes and aspect ratios depict different magnetic properties. Moreover, since the ion milling is a physical etching process, the variation of the pillar dimensions might affect the nanopillar definition leading to size dependent electrical properties. From Fig. 3.23(a) we observe that the dispersion of the TMR and RA decreases with the increase of one of the dimensions. This feature can derive from both the presence of re-deposited materials (mostly present in the edge of the wafer) and defects on the MgO barrier (also observed in the central part of the wafer). Note that the same amount of re-deposited material has a higher effect on smaller nanopillars and a defect in the MgO has a higher impact on a smaller area. Hence, in both cases, the dispersion is enhanced for smaller pillars. It was also verified that devices rotated by 90° have equivalent TMR vs RA graphs (not shown).

To take full profit from the 200 mm wafer nanofabrication, a high process yield is fundamental. Thus, a statistical analysis of the electrical and magnetic properties of the functional MTJs for all the measured sizes was performed. In Figs. 3.23(b) and (c) we show respectively TMR and RA histograms of the 100 × 100 nm^2 MTJs. The mean TMR value is 105% and the standard deviation (σ) is ~ 29%. As for the RA, the mean value is 1.7 $\Omega\mu$m^2 with σ ~ 0.37 $\Omega\mu$m^2. On the other hand, 100 × 450 nm^2 pillars have an average TMR of 105% and a decreased standard deviation of 18% (not shown). As for the RA, the mean value is 1.9 $\Omega\mu$m^2 with σ ~ 0.21 $\Omega\mu$m^2. As expected from Fig. 3.23(a), the standard deviations decrease for both TMR and RA. The mean TMR is remarkably constant for different sizes. In fact, it was observed that, for pillar dimensions equal or higher than 100 nm, the mean TMR was always between 104% and 110%, although it decreases down to ~ 40% for the 100 × 40 nm^2 pillars.

If we consider the TMR values within ± 2σ of their mean value for the 100 × 100 nm^2 pillars, 93% of the measured functional devices are contained within this range. In the case of the 100 × 450 nm^2 pillars, 95% of the devices fall in the ± 2σ range for TMR. Note that, in a perfect Gaussian distribution 95.44% of the values should be included within this range, which indicates that for the 100 × 450 nm^2 pillars the TMR distribution is very close to a Gaussian. If we define the yield of the process as the devices with a TMR within the range of ± 2σ and consider all the fabricated MTJs (functional and non-functional), a yield of 80% was achieved for both 100 × 100 nm^2 and 100 × 450 nm^2 pillars. This yield is remarkably high and revealed the same value for both dimensions. However, if we consider the 100 × 40 nm^2 pillars, the overall yield drops to 6%. Regarding the wafer position, the yield variation was negligible (in spite of the lower TMR). Therefore, we conclude that this variation is mostly related with the e-beam process due to the thick resist necessary for the milling steps, while the IBP process allowed a very efficient opening of the fabricated pillars.

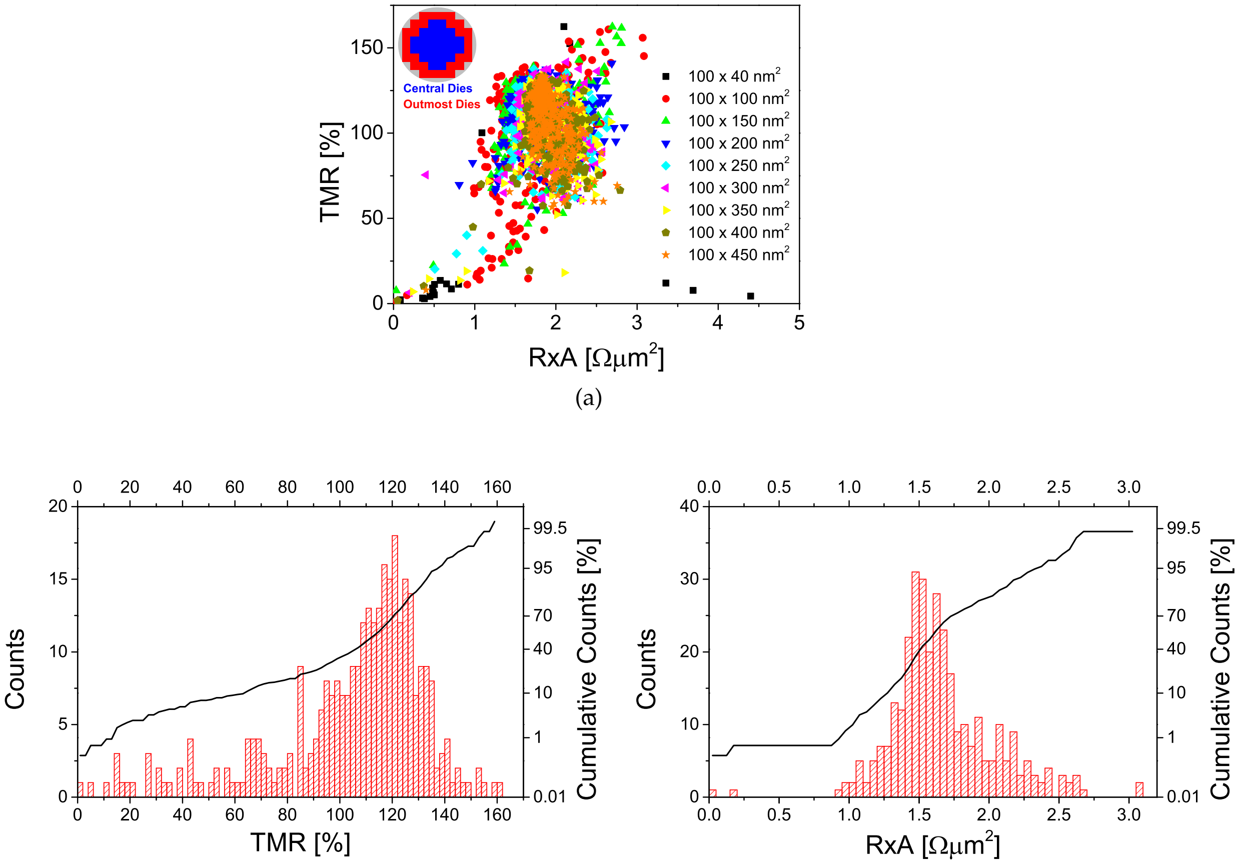

(a)

(b) TMR (100 × 100 nm^2)

(c) *RA* (100 × 100 nm^2)

Figure 3.23: (a) TMR as a function of *RA* for all the measured devices in the central dies (blue dies in the inset) with sizes ranging from 100 × 40 nm^2 to 100× 450 nm^2. Histogram of the (b) TMR and (c) *RA* for the 100 × 100 nm^2 MTJ pillars.

3.6 CONCLUSIONS

One of the milestones of this PhD thesis was the development of a sub-μm MTJ nanofabrication process. This goal was successfully fulfilled with the demonstration of the fabrication of MTJ pillars down to lateral dimensions of 40 × 100 nm^2 with full TMR conservation in the low RA region. In fact, even smaller dimensions (50 $\times$50 nm^2) could be achieved in other wafers with smaller stacks. In this chapter, a description of the developed protocol was performed including deposition, annealing, microfabrication of the contacts and nanofabrication of the MTJs. Higher emphasis was given to the most challenging nanofabrication part and the effect of the etching angle, sidewall cleaning and capping layers unveiled. The final process consists in a three step nanopillar definition in conjugation with a novel IBP process allowed us to achieve TMR values up to 156% with RA values below 2 Ωμm^2. The IBP reveals significant advantages when compared to the lift-off (lower process time and better for smaller pillars) and the CMP (smaller amount of residues and higher uniformity). Furthermore, a detailed and statistical description of the electrical performance of MTJ devices fabricated over a full 200 mm wafer was made. It was observed that the developed process is uniform, with average TMR values around or above 100% in 6 inch and that a more significant TMR decrease is only observed for the outmost dies. Process yields up to 80% were achieved for pillar dimensions down to 100 × 100 nm^2. Note that the electrical measurements studied here were the results that depicted the best full wafer uniformity with large TMR. In several wafers the results were not so homogeneous and in most cases it was not the goal (only central dies were fabricated). Some examples of other nanofabricated wafers will be given in the next chapters. This process constitutes the bedrock of this thesis and was used to obtain the performance of STNOs.

4

IMPACT OF THE MGO THICKNESS ON THE PERFORMANCE OF THE OSCILLATORS

To obtain steady-state microwave emission in spin transfer torque nano-oscillators (STNOs), most reports rely on very thin insulating barriers [resulting in a resistance × area product (RA) of ~1 $\Omega\mu m^2$] that are able to sustain large current densities and thus trigger large orbit magnetic dynamics. In STNOs with a homogeneous free layer configuration these dynamics occur in the GHz range of the frequency spectrum with integrated matched output powers (P_{out}) in the range of 1 - 40 nW. Such thin barriers are more prone to depict defects that hamper their tunnel magnetoresistance ratio (TMR). Moreover, despite the larger precession dynamics sustained by thinner insulating barriers, the associated voltage variation may be smaller due to the lower associated resistance. The effect of the RA on the performance of STNOs has been seriously overlooked since it is generally assumed that thinner insulating barriers maximize P_{out} due to the enhanced magnetization precessions.

In this chapter we used the process described in Chapter 3 to fabricate two tunnel junction (MTJ) stacks over 200 mm wafers. These MTJ stacks have the particularity of depicting an MgO wedge and thus the fabricated MTJ pillars depict a RA from ~1 $\Omega\mu m^2$ up to ~40 $\Omega\mu m^2$. We observed that intermediate insulating barriers (RA ~10 $\Omega\mu m^2$) result in an enhanced P_{out} (up to 200 nW) without compromising the ability to trigger self-sustained oscillations and without any noticeable degradation of the signal linewidth (Γ). Moreover, a significant decrease of the critical current densities for spin transfer torque induced dynamics (J_{STT}) was observed using thicker barriers, which have a larger TMR, a larger breakdown voltage and presumably a lower defect count. Further increase of the barrier thickness leads to low breakdown currents diminishing again the emitted power, leading to an optimal RA region (between 7.5 - 12.5 $\Omega\mu m^2$). These results mark a change of paradigm in STNOs since the RA target for increased P_{out} is no longer the very thin range. In fact, the unveiled optimal RA range uses thicker barriers easier to work with. Furthermore, the results shown here are cumulative and can be directly applied to other types of STNOs (vortices, with perpendicular anisotropy, synchronized, etc.).

4.1 MGO THICKNESS AND PERFORMANCE OF THE OSCILLATORS

The spin transfer torque (STT) effect [55, 156, 157, 158, 159, 160, 161, 162] allows the effective and selective manipulation of the magnetization of nano-magnets using local spin polarized electrical currents. It has been suggested as a key mechanism enabling a large number of spintronic devices, including magnetic random access memories (MRAM) [163], domain wall based storage [164] or spin transfer torque nano-oscillators (STNOs) [69, 61, 62, 137, 165, 68, 139, 86]. With respect to STNOs, these devices take advantage of the STT effect to achieve RF emission from persistent magnetic precession, driven by DC currents. They show major advantages over conventional complementary metal-oxide-semiconductor (CMOS) and crystal based oscillators, such as being tunable by both electrical currents and magnetic fields, working in a large range of temperatures, having a broadband output and a nanometric footprint while keeping the compatibility with a CMOS backend process. STNOs are thus versatile and compact RF oscillators that can be vertically integrated with CMOS, making them highly attractive for applications such as chip-to-chip or wireless communications, microwave sources for nanosensors or phase-array transceivers [69, 89].

There have been several proposals for alternative magnetic arrangements with different advantages explored in the context of specific applications. These include, homogenous in-plane oscillators [78], vortex oscillators [68], oscillators integrating perpendicular polarizers [88] or oscillators using free layers with canted magnetization [84, 85] and point-contact nano-oscillators [75, 106].

The STNOs with the largest reported integrated matched output power (P_{out}) are fabricated starting from magnetic tunnel junction (MTJ) stacks based on CoFeB/MgO/CoFeB which benefit from their high tunnel magnetoresistance ratio (TMR) [69, 84, 85, 81, 166]. However, the MTJ endurance is limited by the dielectric breakdown of the MgO insulating layer. This is a critical point for STNOs wherein, to observe persistent oscillations, one must apply large and continuous current densities. This is a fundamental difference with respect to other applications exploring the STT phenomena, such as MRAM, which can use short pulses of very large current (and voltage) amplitude to excite the free layer magnetization. The barrier is able to sustain large pulsed voltages with amplitudes well above the DC breakdown value whilst large angle magnetization dynamics can still be excited. For STNO applications, the excitation current must be maintained in the steady state and therefore large current densities, capable of exciting persistent dynamics, must be reached with DC voltages that the MgO barrier can endure.

Despite the fact that a small number of reports achieved large P_{out} values with relatively thick MgO barriers [resistance × area product (RA) > 4 $\Omega\mu m^2$] [84, 85, 81, 88], most works still rely on very thin MgO barriers ($RA \sim 1\ \Omega\mu m^2$) [68, 89, 78, 80, 90, 91, 92, 93, 76]. Hence, the consensus solution to excite STT excitations in nanofabricated MTJ stacks has been the use of ultra-low RA barriers. In that respect, these ultra-thin MgO barriers can sustain high current densities but the so far unavoidable presence of a large density of defects and pinholes at such low barrier thicknesses (and low RA) results in smaller TMR, lower breakdown voltage and an overall decrease in reliability and reproducibility. Apart from the requirement of having ultra-low *RA*, the role of the tunnel barrier on the properties of STNOs has been so far critically overlooked. The large majority of reported results rely in MTJs where transport properties are dominated by defects. These defects are present already on the as-deposited state [167] or, in some cases, are created prior to the dynamic characterization of the system by applying large currents that irreversibly change the transport properties of the device in a non-controlled way, which is required in order to observe STT persistent oscillations [168]. The effect of such defects on the dynamics is still not well accounted and, on top of that, the higher TMR and resistance of thicker MgO barriers should increase P_{out}. The assessment of such large unexplored region for STNO operation could reveal crucial operating conditions to boost their applicability and offer new fundamental physical insights.

In in this work, the role of the tunnel barrier on the STNO dynamics is studied using homogeneous in-plane magnetized STNOs. Such STNOs have output powers in in the range of 1 – 40 nW [78] and critical current densities required to excite auto-oscillations (J_{STT}) are often larger than 10^6 A/cm^2 [84, 81]. The STNOs were nanofabricated from MTJ stacks with an in-plane free layer magnetization, deposited on 200 mm diameter wafers, and incorporating an MgO wedge (resulting in measured *RA* values in the range 1 – 40 Ωμm^2). Two wedge samples have been processed into nano-pillars with diameters of 200 nm which were characterized statically (TMR, low bias *RA* and transfer curves, DC voltage/current breakdown) and dynamically (frequency spectrum versus bias current at fixed applied field). The results obtained in the two fabricated samples are consistent and clearly show that there is a trade-off between endurance to large currents (maximized for low *RA* MTJs) and large TMR (maximized for large *RA* MTJs), with an optimal *RA* region showing the largest P_{out} in the 7.5 – 12.5 Ωμm^2 range. In this region, STNOs with large impedance matched P_{out} values up to 200 nW are consistently found. This optimal *RA* region was corroborated by micromagnetic simulations that revealed a good agreement with the experimental data. Furthermore, a decrease by 2 orders of magnitude of J_{STT} was observed when going from very thin (below 5 Ωμm^2) to thicker MgO barriers. As a result, very small J_{STT} values (down to 1.17×10^5 A/cm^2) are achieved in the large *RA* and large TMR region, resulting in an enhancement of the STNOs operational window. More precisely, as the *RA* increases, the operational window [J_{STT} onset to breakdown current density (J_{break})] increases, contributing to an enhancement of the device robustness. Thus, the modification of the tunnel barrier thickness alone provides a mechanism to decrease the value of J_{STT}, and simultaneously increasing P_{out}, something of fundamental importance for all types of STNOs.

4.2 SAMPLE NANOFABRICATION

Two MTJ stacks incorporating MgO wedges were deposited over 200 mm Si <100> wafers in a Timaris Singulus tool, leading to a variable *RA* over the wafer from below 1 $\Omega\mu m^2$ up to 40 $\Omega\mu m^2$. The two deposited stacks were S1: substrate/100 Al_2O_3 5 Ta/50 CuN/10 Ru/50 CuN/20 Ru/17 $Pt_{38}Mn_{62}$/2 $CoFe_{30}$/0.85 Ru/2.6 $CoFe_{40}B_{20}$/MgO wedge/2 $CoFe_{40}B_{20}$/10 Ru/150 Cu/30 Ru and S2: substrate/100 Al_2O_3/3 Ta/30 CuN/5 Ta/17 $Pt_{38}Mn_{62}$/2 $CoFe_{30}$/0.85 Ru/2.6 $CoFe_{40}B_{20}$/MgO wedge/1.4 $CoFe_{40}B_{20}$/10 Ru/150 Cu/30 Ru (thicknesses in nm). Despite other differences in the stack, the only meaningful variation between the two deposited wafers concern the free layer thickness: for S1 t_{CoFeB} = 2.0 nm and for S2 and t_{CoFeB} = 1.4 nm. Both CoFeB layers have their magnetization in-plane, although in the case of S2 the CoFeB is already close to the transition between in-plane to out-of-plane magnetization (observed at ~1.1 nm of CoFeB). The majority of results reported here were collected from wafer S1 with S2 being mainly used to corroborate and demonstrate the reproducibility of the observed results. Upon deposition, the wafers were annealed for 2 h at 330 °C and cooled down under a magnetic field of 1 T along the easy axis defined during deposition.

Both stacks were then patterned into circular devices with diameters of 200 nm. To that end, the nanofabrication described in chapter 3 was used. Each nanopillar has four-dedicated contact pads which were used to measure the TMR and *RA* without any contribution of contact resistances. All the MTJ nanopillars produced were measured under quasi-static magnetic field sweeps (up to 200 Oe) in the semi-automatic DC prober. Figure 4.1(a) shows the *RA* values obtained from these transport measurements performed on the MTJ pillars along the MgO wedge position. The *RA* values extracted from transport measurements in patterned nanopillars follow the same trend observed in the current in-plane tester (CIPT) measurements with increasing *RA* along the wafer position. The TMR values obtained from the patterned nanopillars are plotted against the measured *RA* value, as shown in Fig. 4.1(b). Below 10 $\Omega\mu m^2$ a strong linear correlation between TMR and *RA* , which crosses the plot origin, is observed. This correlation is the signature of the presence of leakage currents through conduction channels that do not preserve the spin of the electrons. In nanometric sized nanopillars this role is usually attributed to re-deposited material in the nanopillar side-walls formed during the nanopillar ion milling etching. In this case, however, an effort to monitor and remove the extra material in the nanopillar sidewall was made during the nanofabrication process. The data in Fig. 4.1(b) indicates that this effort was successful: notice that the linear correlation between TMR and *RA* exists only in the region bellow 10 $\Omega\mu m^2$. If redeposited material were present in the fabricated nanopillars, it would affect all nanopillars, regardless of the *RA* value. In fact, it should lead to a much larger TMR reduction in pillars with a large *RA* compared to those with a small *RA*. Still, a distribution of data points linking the high *RA* data points to

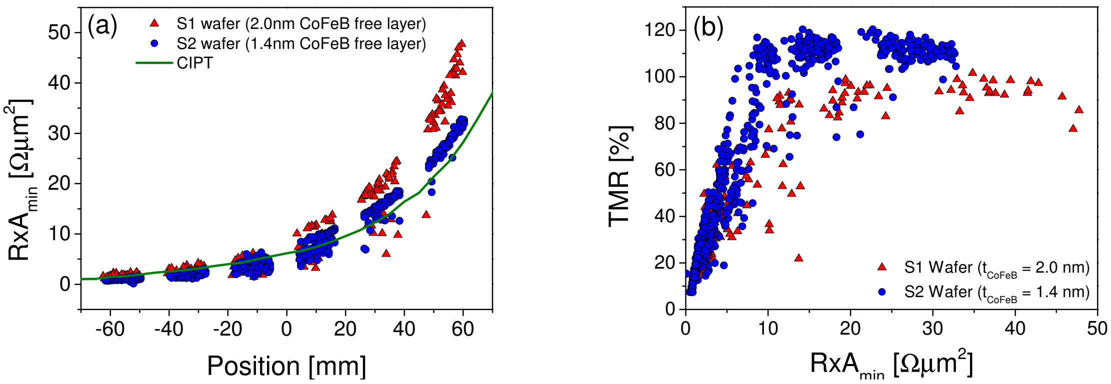

Figure 4.1: DC electrical characterization. *RA* and TMR values extracted from the measured transfer curves in a 4-point contact geometry (red triangles correspond to S1 with t_{CoFeB} = 2.0 nm and the blue circles to S2 with t_{CoFeB} = 1.4 nm). (a) *RA* of the measured MTJs and CIPT (of sample S1) measurements along the wafer position (green line) (b) TMR vs. *RA* measured for the full collection of 200 nm MTJ pillars.

the plot origin is not observed. Thus, the conclusion is clear: the nanofabrication process was successful in preventing the formation of redeposited material shorting the tunneling current through the MgO layer, but below the 10 Ωμm^2 value, the thin MgO barrier contains intrinsic defects that partially de-polarize the current that crosses it [167].

4.3 FERROMAGNETIC COUPLING

The transfer curve of the MTJ nanopillars is also dependent on the MgO thickness. Figure 4.2(a) shows three transfer curves for *RA* values of 11, 5, and 2 Ωμm^2 (for sample S1 with t_{CoFeB} = 2.0 nm). Besides the decrease in TMR with the decrease of MgO thickness, there is also an increase of the ferromagnetic coupling field (H_F) which displaces the center of the hysteresis curve and is increasingly more accentuated as the MgO becomes thinner. In Fig. 4.2(b) the H_F dependence as a function of the *RA* is shown for both samples. The origin of this coupling is twofold. The first contribution is related to the closure of the lateral magnetic flux arising from the synthetic antiferromagnet (SAF) that leads to stray fields that couple with the free layer. This coupling becomes significant for small MTJs and remains important for high MgO thicknesses [48]. The second contribution is related to Néel coupling induced by the roughness of the MgO/CoFeB interface and is more accentuated for smaller MgO thicknesses [169, 170].

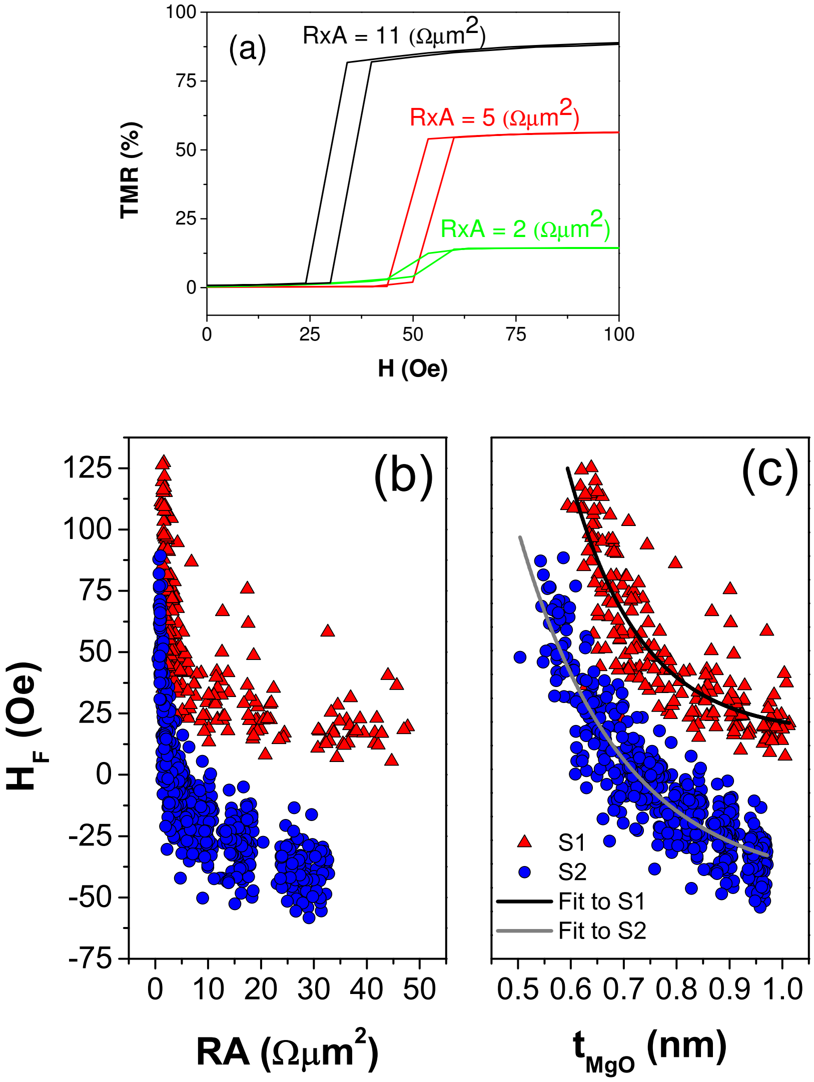

Figure 4.2: Ferromagnetic coupling. (a) TMR curves for different values of RA (11, 5, and 2 $\Omega\mu m^2$). Variation of H_F as a function of (b) RA and (c) calculated t_{MgO}. Red triangles correspond to S1 ($t_{CoFeB} = 2.0$ nm) and blue circles to sample S2 ($t_{CoFeB} = 1.4$ nm). Fit performed using Eq. (4.1) for S1 (black line) and S2 (gray line).

The Néel coupling can be estimated using the following equation [171]:

$$H_F = \frac{\pi^2}{\sqrt{2}}(\frac{h^2}{\lambda t_{CoFeB}})M_s exp(-\frac{2\pi\sqrt{2}}{\lambda}t_{MgO}), \tag{4.1}$$

where h is the roughness amplitude, λ is the roughness period, M_s is the magnetization saturation, and t_{MgO} is the MgO thickness. M_s was measured using the vibrating sample magnetometer (the obtained value was $M_s = 1.36 \times 10^6 A/m^2$), and the MgO thickness for different conditions of deposition was obtained using the exponential relation:

$$RA = A \cdot exp(B \cdot t_{MgO}), \tag{4.2}$$

where $A = 5 \times 10^{-3}\ \Omega\mu m^2$ and $B = 9.05\ nm^{-1}$. This relation was obtained by determining t_{MgO} from X-ray diffraction and RA from CIPT measurements in structures with thin MgO (<10 nm). Furthermore, it is well known that in ideal insulating barriers, there is an exponential relation between RA and t_{MgO} [172]. Therefore, from the measured values, a fit was extracted and Eq. (4.2) determined. The data in Fig. 4.2(c) were fitted to Eq. (4.1) for both samples, where h and λ were kept as free parameters. From the fitting (black line for sample S1 with $t_{CoFeB} = 2.0$ nm and gray line for sample S2 with $t_{CoFeB} = 1.4$ nm), the extracted values for the MgO roughness amplitude were $h_1 = 0.0482$ nm and $h_2 = 0.0225$ nm, and the value extracted for the period was $\lambda_1 = 1.20$ nm and $\lambda_2 = 1.72$ nm, for S1 and S2 respectively. Note that the small discrepancy with Ref. [79] for sample S1 is a consequence of the different RA ranges used in both cases. However, the values calculated here have a larger range and thus are, in principle, more reliable. We note that despite the simplicity of the model, sample S2 revealed a smaller MgO roughness amplitude with a larger period. This might explain the higher TMR observed in this case (despite the thinner free layer; Fig. 4.1) since such insulating barrier would be less prone to have defects. The reason why a smoother MgO barrier was observed in S2 might be related with the thinner bottom contact used in this case.

When t_{MgO} increases, the effect of the Néel coupling vanishes but H_F does not drop to zero. Instead, it goes to a stable value that is caused by the stray fields of the SAF. It is interesting to note that the this limit H_F value has a different sign for each sample. In fact, from the fittings we obtained the values of 14.5 Oe for S1 and -50 Oe for S2. This indicates that in the former case the parallel alignment is favored by the stray fields while in the latter the antiparallel (AP) alignment is favoured. One of the reasons for this difference might be the different thicknesses of the free layer. However, further work is still required to fully understand the mechanisms that lead to the distinct magnetic couplings observed.

4.4 CHARACTERIZATION OF THE RF OUTPUT IN THE FREQUENCY DOMAIN

To characterize the RF emission caused by STT excited oscillations of the free layer magnetization, a sub-set of the available MTJ nanopillars was selected. The emission was studied at room temperature in the frequency window 3 Hz – 10 GHz under a static bias current (I_{bias}) and bias field (H_{bias}) which were systematically swept within the limits of the experimental setup. As reported by other groups [61], it was verified that P_{out} is maximized when applying a large static magnetic field in a direction close, but with a slight offset from the direction that sets the free layer in the AP direction. In the case of the results reported here, an external applied field H_{bias} = 200 Oe applied along the plane (large enough to saturate the MTJ nanopillars in the AP direction) was used. The I_{bias} was then ramped up until STT persistent oscillations were observed in the frequency spectrum and then a small tilt of the magnetic field direction was introduced with the purpose of maximizing P_{out}. Once the magnetic field direction was optimized, the systematic characterization of the output spectrum was performed, sweeping I_{bias} at constant H_{bias}.

An example of a frequency spectrum can be seen in Fig. 4.3(a) along with the I_{bias} dependence of (b) resistance, (c) frequency, (d) linewidth and (e) power. This result concerns a nanopillar from wafer S1 with an RA of 11.5 $\Omega\mu m^2$ and a TMR of 87.8% exhibiting a P_{out} of 200 nW at I_{bias} = -2 mA. As shown, the spectrum is highly asymmetric with respect to the bias current polarity. Large amplitude, small linewidth peaks consistent with STT enabled auto-oscillations are observed only for negative bias currents (negative current is defined here as electrons traveling from the pinned to the free layer). In such configuration, the STT destabilizes the AP configuration which is set by the magnetic field. Besides the large P_{out}, the device also exhibits a reasonable linewidth (below 100 MHz). On the other hand, low power RF emissions with large linewidths consistent with thermal excitations are observed for positive currents, a configuration for which STT stabilizes the AP configuration. Note that, the studied nanopillars have a relatively large diameter (200 nm). Despite the common belief that smaller pillars (< 100 nm) have a better defined monodomain behaviour, it was observed in the work performed in this thesis that larger pillars usually depict larger P_{out}. In fact, recent results corroborate this observation with an optimal diameter for P_{out} optimization of 300 nm [76].

In order to compare the output power of nanopillars with different RA , care must be taken concerning the impedance mismatch in the acquired spectrum. The emission spectrum of the MTJ nanopillars is amplified by an amplifier with a 50 Ω input impedance before being injected into the spectrum analyzer where the spectrum is collected (section 2.7.3). Due to the resistance mismatch between the amplifier input impedance (R_L ~ 50 Ω) and the MTJ, the measured output power is only a fraction of that actually emitted by the MTJ. The fraction

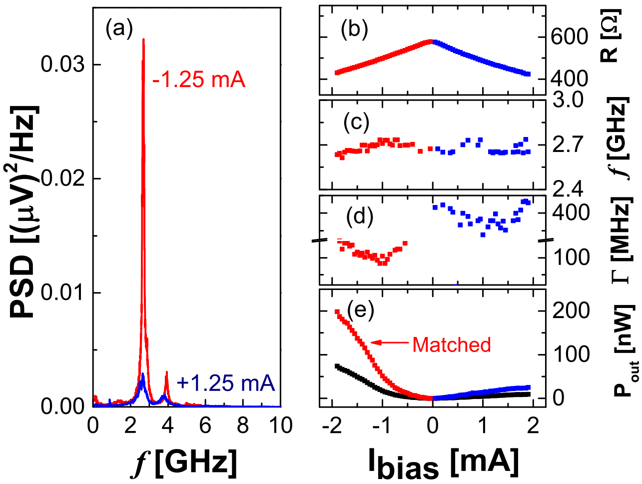

Figure 4.3: RF emission characterization. (a) Unmatched power spectral density (PSD) measured at the amplifier input with I_{bias} = ± 1.25 mA. (b) Resistance, (c) frequency, (d) linewidth and (e) P_{out} as a function of I_{bias}. The red (blue) points represent the integrated P_{out} matched to the load for negative (positive) I_{bias}, while the black points represent the non-matched power. The magnetic field was kept constant (200 Oe) in a direction close to the easy axis. (f) Schematic representation of the experimental setup used for the RF emission characterization.

of the amplified power depends on the absolute resistance of the MTJ. For this reason, the output power collected in the amplifier for nanopillars with different resistance values are not directly comparable. To account for the effect of the impedance mismatch the integrated matched output power P_{out} of each device was computed (see section 2.7.3). To that end, for each measurement of the voltage $[V(f)]$ at a certain I_{bias} and H_{bias}, the integrated non-matched power ($P_{non-matched}$) collected at the amplified input was calculated using:

$$P_{non-matched} = \int \frac{V^2(f) - V_0^2(f)}{BW \cdot g(f)} \frac{1}{R_L} df. \tag{4.3}$$

Here, $V_0(f)$ is the voltage measured at $I_{bias} = \emptyset$, BW the measurement bandwidth (the value used in these measurements was 3 MHz) and $g(f)$ the gain of the amplifier. The integrated matched output power P_{out} considering the measurement setup circuit is then calculated from [173]:

$$P_{out} = P_{non-matched} \cdot [\frac{(R + R_L)^2}{4R \cdot R_L}]. \tag{4.4}$$

The effect of this correction can be seen in Fig. 4.3(e). For a nanopillar with a resistance between 400 Ω and 600 Ω (depending on I_{bias}), P_{out} can be larger by a factor of 2 than $P_{non-matched}$ at the amplifier input.

4.5 RELATION BETWEEN TMR, RA AND P_{out}

In order to clarify the role of the MgO thickness in the RF emission of the final devices, the RF emission of a sub-set of the devices represented in Fig. 4.1 was characterized. Figure 4.4(a) shows the position of the selected devices in the TMR versus RA phase space together with the maximum measured P_{out} value which is represented as a colour scale. The size of each dot encodes the linewidth information at the I_{bias} value that maximizes the quality factor ($Q = P_{out}/\Gamma$) with larger dots representing larger linewidths. It is important to note that the maximum P_{out} represented in Fig. 4.4(a) were obtained under different I_{bias} values for different devices. Due to the different impedance values of the patterned nanopillars (which have all the same area, but different MgO thicknesses) the optimum current that maximizes P_{out} depends on the position of the devices on the wafer.

It is clear from Fig. 4.4(a) that P_{out} is maximized in the RA region between 7.5 - 12.5 Ωμm^2. In this region, P_{out} is larger by a factor of 5 when compared to that obtained in the ultra-low RA region close to 1 Ωμm^2 which is usually targeted in STNO devices. At a first look, one could argue that the optimal RA region that maximizes P_{out} is just the region that displays higher TMR with the lowest possible RA values. However, if we compare the STNO with the highest TMR in the region below 5 Ωμm^2 (69%) with the oscillator with the lowest TMR in

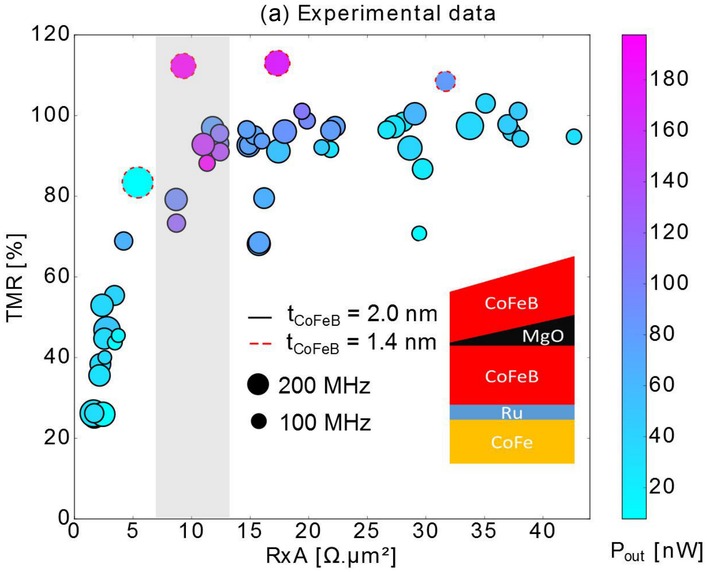

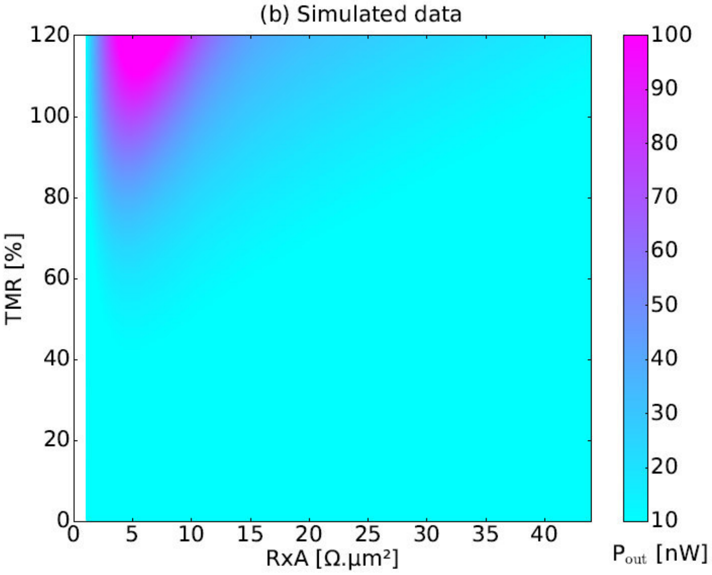

Figure 4.4: DC and RF electrical characterization. TMR versus RA for all the studied STNOs (circles with black border correspond to S1 with t_{CoFeB} = 2.0 nm and the circles with dashed red border to S2 with t_{CoFeB} = 1.4 nm). The color scale of the points represents the maximum P_{out} of the RF emission and the size of the points the linewidth for the oscillation with the highest Q. The inset shows a schematic representation of the deposited MTJ stack. (b) Simulated P_{out} at the breakdown voltage, versus RA and TMR (for t_{CoFeB} = 2.0 nm).

the optimal region (73%) the P_{out} values are still higher in the optimal region (65 and 121 nW, respectively). Furthermore, despite the fact that there is some variability in the P_{out} of oscillators with similar positions in the TMR vs RA plot, the lowest measured P_{out} value in the optimal region is always larger than the highest P_{out} for the small RA samples (below 5 $\Omega\mu m^2$). Therefore, one concludes that, even though lower RA values allow the use of higher currents that may excite larger oscillations, the decrease of RA is not always the best option to achieve optimal STNOs. In fact, the higher resistance characteristic of a thicker MgO results in a larger voltage variation of the oscillator even for similar TMR ratios. A similar conclusion can be extracted if the P_{out} for STNOs in the optimum RA region is compared with that of devices in the larger RA range. This occurs because for more resistive MTJs the J_{break} is achieved before the excitation of large magnetic precessions, leading to an optimal RA region. The observed variation of the P_{out} values likely results from the unavoidable process variability (small differences in sizes, density of defects or edge roughness). Despite this factor, the large number of characterized devices allowed us to determine clear trends as a function of RA. This behaviour was observed and reproduced in the two wedge wafers nanofabricated, despite the different magnetic configurations (t_{CoFeB} = 2.0 nm for S1 t_{CoFeB} = 1.4 nm for S2).

To further corroborate the observation of an optimal RA region where P_{out} is maximized, these experimental results were compared with micromagnetic simulations of the STT-induced dynamics. The simulations were performed using the object oriented micromagnetic framework (OOMMF) [174] to solve the Landau-Lifshitz-Gilbert-Slonczewski (LLGS) equation[55]. A 2.0 nm thick CoFeB free layer patterned in a 200 nm diameter pillar was considered (matching the stack and geometry of S1 devices). Apart from the geometry, the remaining parameters that were kept constant in the simulations were: Gilbert damping α = 0.01, free layer moment M_s = 1.36 × 10^6 A/m^2 and applied field H_{bias} = 200 Oe. The interfacial perpendicular magnetic anisotropy induced by the MgO layer was also taken into account (interfacial anisotropy constant of 1.5 × 10^{-3} J/m^2 extracted from magnetic measurements).

The free input parameters in the simulations were the TMR and RA, which were swept systematically within the limits of Fig. 4.4(a). The simulations were performed with a bias current density of $J_{bias} = V_{break}/RA$, which corresponds to the current at the dielectric breakdown of the MgO barrier. This is the maximum possible current density that can be reached and, theoretically, the current that maximizes P_{out} (within the range of the experimentally achievable values). In fact, it was verified that, for any given TMR and RA value, the simulations showed a continuous increase of the precession amplitude with the applied current. The values of this maximum current were experimentally measured as a function of RA using a ramp procedure (in a sub-set of devices of Fig. 4.1), in which the applied current was successively increased until dielectric breakdown is observed. This discrete data set was fitted to a continuous exponential law $V_{break} = V_0[1 - exp(RA/\tau)]$ which best described the experimental data, with V_0 = 1.15 V and τ = 7 Ωμm^2.

The P_{out} delivered to a load with impedance R_L was then calculated from the magnetization dynamics using [69, 73]:

$$\langle P_{out} \rangle \approx \frac{\langle V_{out}^2 \rangle}{R_L} = \frac{I_{bias}^2 \Delta R^2 R_L}{2(R + R_L)^2}. \tag{4.5}$$

Here, $V_{out}(t) = \Delta R \cdot cos(wt) I_{bias}$ is the RF output voltage, R stands for resistance of the STNO and ΔR stands for the peak-to-peak amplitude of the STNO impedance variation during an oscillation period.

Therefore, the input RA value will set the I_{bias} used, along with the value of R and ΔR (this last parameter also depends on the TMR). As for the input TMR value, it has a twofold influence on P_{out}. On one hand, ΔR for a given oscillation amplitude is proportional to the TMR value. On the other hand, the oscillation amplitude for a given current density depends on the spin current polarization (P) which is also linked to the TMR value. Here, Jullière´s model [10] was considered to correlate TMR with P $[TMR = 2P^2/(1 - P^2)]$

During the simulations, the P_{out} values delivered to a matched load were computed from equation (4.5) by setting $R_L = R$ with the result of this procedure being plotted in Fig. 4.4(b). Remarkably, the optimal RA region where P_{out} is maximized was also observed in the simulated case, although with the optimal region occurring for smaller RA values (maximum around 8 Ωμm^2). The calculated P_{out} values (up to 100 nW) are also lower than the ones that were experimentally measured (up to 200 nW). A part of this discrepancy can be attributed to the thermally-induced precessions that were neglected in the simulations. Note that an overall increase of the magnetization oscillation amplitude would increase P_{out} more significantly for larger RA values, moving the optimal RA region to values closer to the experimental data. Nevertheless, the simulations corroborate the observation of an RA region that maximizes P_{out}.

4.6 CRITICAL CURRENT DENSITIES FOR STT

To achieve very large amplitude oscillations before the dielectric breakdown of the MTJ, a very low critical current density for STT-induced magnetic precession J_{STT} is required. In fact, it was shown theoretically that P_{out} increases with J/J_{STT} [94]. The fact that STT excited oscillations are observed in the full measured RA range is surprising. Since these oscillations can only be obtained when the condition $J_{STT} < J_{break}$ is met, the observation of oscillations even for RA values of ~ 40 Ωμm^2 can only be understood if, in this large RA range, J_{STT} is unexpectedly small or J_{break} is unexpectedly large.

The values of J_{STT} can be calculated by identifying the deviation from the linear dependence of the inverse power on the bias current. An example of this derivation is plotted in Fig. 4.5(a), where the value of the critical current density J_{STT} was extracted by extrapolating the inverse power times the current squared ($I^2_{bias}/P_{out} \rightarrow 0$). J_{STT} can be derived using the relation $(J^2_{bias}/P_{out}) \propto (J_{STT} - J_{bias})$, valid in the thermally activated region and noting that, as the inverse power approaches zero, $J_{bias} \rightarrow J_{STT}$ [84, 94]. Thus, J_{STT} is determined by the x-axis intercept with the linear fit in the thermally excited region. In Figs. 4.5(b) and (c) the calculated values of J_{STT} are shown as a function of RA and TMR, respectively. From the RA dependence of S1 [Fig. 4.5(b); red triangles] one can observe that J_{STT} sharply decreases by 2 orders of magnitude as the MgO thickness is increased. In fact, the TMR dependence [Fig. 4.5(c)] indicates that large TMR values, characteristic of continuous MgO barriers, depict significantly lower values of J_{STT} with smaller error bars (note the logarithmic scale). The values of J_{STT} obtained for S2 (blue circles) corroborate the observed tendencies but with larger values of J_{STT} . Further work is still required to understand the reason of this discrepancy.

In the macrospin approximation, the critical current density for STT oscillations J_{STT} can be written as [74]:

$$J_{STT} = \frac{2e\mu_0 M_s \alpha d}{\hbar}\left(\frac{M_{eff}}{2} + H_{bias}\right) \cdot \frac{1}{P}, \tag{4.6}$$

where e is the charge of the electron, μ_0 is the permeability of free space, $\hbar$ the Planck constant, M_s the magnetization saturation, α the Gilbert damping constant, d the thickness of the free layer, M_{eff} the effective demagnetizing field (given by the demagnetizing factor minus the interface perpendicular magnetic anisotropy) and P the spin polarization.

The value of J_{STT} is expected to be inversely proportional to the spin polarization of the current [Eq. (4.6)]. Jullière´s model was used to correlate the TMR with the spin polarization and, in conjugation with Eq. (4.6), the expected trend of J_{STT} as a function of TMR was estimated. This was performed, using the value of J_{STT} measured for S1, with the calculated trend represented by the green line in Fig. 4.5(c). Despite the fact that the predicted trend indeed reveals a decrease of J_{STT} with TMR, the experimentally observed dependence is not completely consistent with the model. The discrepancy between the model and the experimental data can be attributed to different effects not accounted for in this simple model. As a first possibility, the TMR value used in the model was measured at low bias and decreases for higher bias voltages. It is expected that in conditions consistent with STT excitations the spin polarization of the current being injected in the free layer decreases compared to the low bias condition. However, this decrease in the spin polarization under STT conditions should be more pronounced for devices in the large RA range when compared to devices in the low RA range (which have lower breakdown voltages and therefore a smaller TMR decrease with increasing I_{bias}). So this effect should have a contribution which opposes the trend observed experimentally. Either

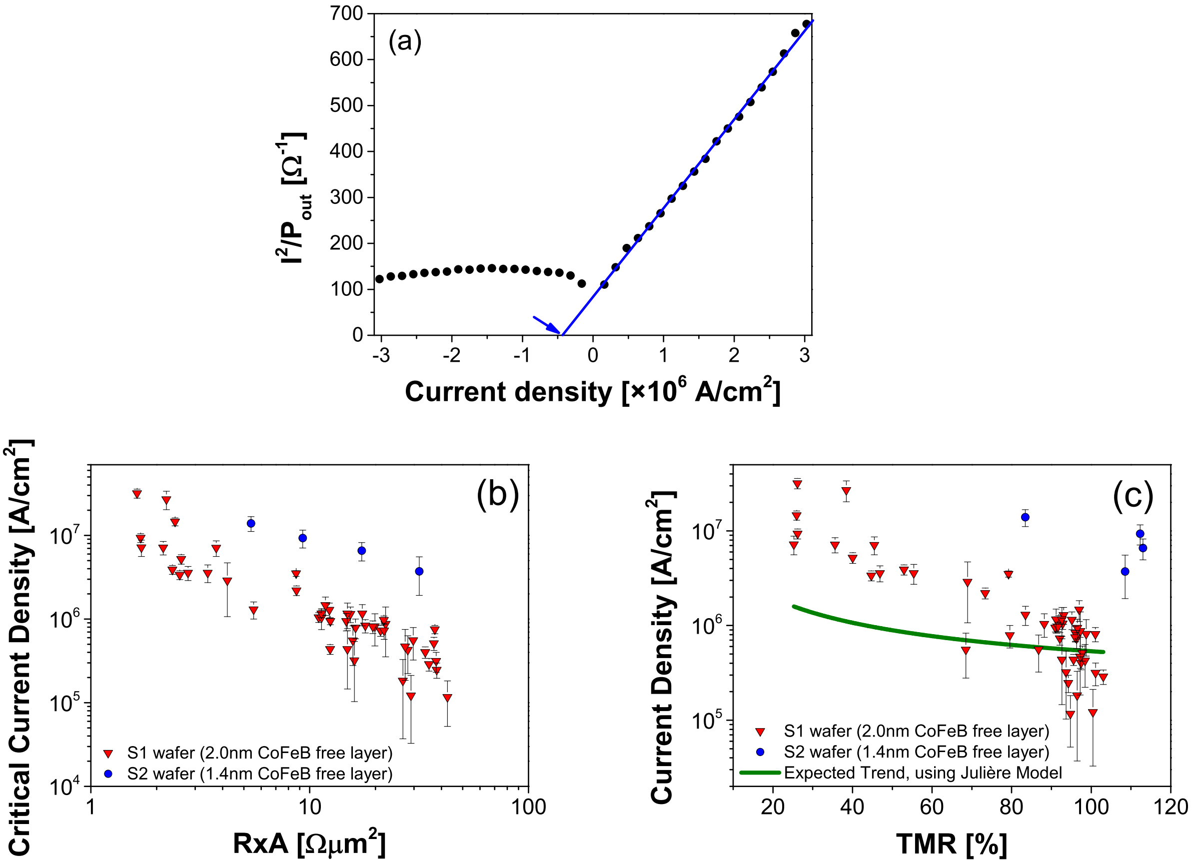

Figure 4.5: Critical current density for STT-induced oscillations. (a) Example of the determination of the critical current by the x-axis interception of the linear fit of I^2/P in the thermally activated region. Calculated values of J_{STT} as a function of (b) RA and (c) TMR for t_{CoFeB} = 2.0 nm (red triangles) and t_{CoFeB} = 1.4 nm (blue circles).

this effect has a small contribution or there are some other factors playing a more important role. A second possibility consists on the H_F which depends on the MgO thickness due to the orange peel coupling. The H_F field is larger for thinner barriers, and it can easily reach values of the order of 100 Oe near the 1 $\Omega\mu m^2$ range (see section 4.3), which is comparable to the applied field H_{bias} = 200 Oe, meaning that the effective field acting on the free layer can have a non-negligible dependence on RA as well. However, this effect is expected to be small since H_F is around one order of magnitude smaller than the effective demagnetizing field. Finally, as discussed previously, the data of Fig. 4.1 indicates that for devices with $RA <$ 10 $\Omega\mu m^2$ there are intrinsic defects in the MgO barrier which provide alternative conduction channels dominated by transport mechanisms other than tunneling [167]. Only the fraction of current which crosses the MgO barrier through tunneling is described by the Jullière model. In the presence of such defects, the fraction that is not described by the Jullière model and does not conserve the spin of the electrons increases as RA decreases. This is perceived as a decrease in the spin polarization which results in larger J_{STT} values compared to a scenario where spin conservative tunneling is the only transport mechanism. This effect is consistent with the mismatch observed in Fig. 4.5(c), although a better understanding of the different transport mechanisms and the fraction of current carried by each of them is required for a quantitative analysis.

4.7 OPERATIONAL WINDOW

For STNOs to reach commercial applications it is important to have a large P_{out} and a small bandwidth but also stable devices that achieve large oscillations for safe conditions with currents well below breakdown. To determine this range of operation, in Fig. 4.6 it is depicted the current density values at which the Q factor is maximized (white diamonds) along with J_{break} (red circles) and J_{STT} (blue triangles) for each STNO characterized in wafer S1.

For low RA values (below 5 $\Omega\mu m^2$) the current density that optimizes Q and the J_{break} values are quite large. However, the J_{STT} values are also significantly large so that the region for STNO operation (STNO region) is particularly thin. The reason for this is that despite the large J_{break}, the breakdown voltage (V_{break}) is smaller in this region. In fact, while for RA values bellow 5 $\Omega\mu m^2$ one has $V_{break} \approx 0.35$ V (due to the presence of small defects in the insulating layer), above 5 $\Omega\mu m^2$, V_{break} increases to ~ 1 V. As RA increases, the MgO barrier gets thicker and its quality improves (more continuous and better defined crystalline texture), the voltage endurance of the MTJ is higher and simultaneously the values of J_{STT} get significantly lower. As a result, although the maximum current density endured by the tunnel barriers decreases with RA, the value of J_{STT} also decreases but at an even faster rate which results in a broader STNO operating region. Moreover, the higher resistance of these MTJs gives rise to larger

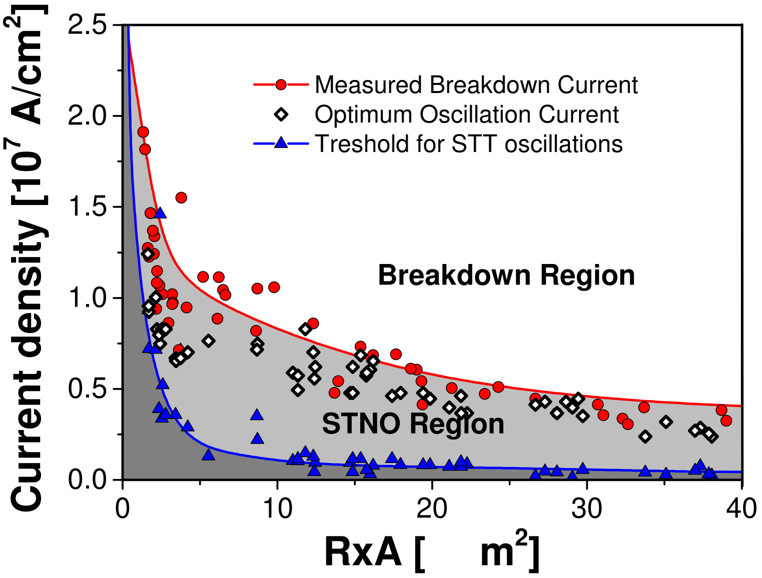

Figure 4.6: Range of operation of STNOs. Critical current density for STT-induced oscillations J_{STT} (blue triangles), breakdown current density J_{break} (red dots) and current for which the highest Q is achieved (white diamonds). The lines are splines fitted to the data separating the region without STT effects (dark gray), the STNO region (light gray) and the breakdown region (white). The considered sample was S1 with t_{CoFeB} = 2.0 nm.

voltage variations for the same magnetic precession amplitude leading to larger P_{out} values observed in the intermediate RA region.

From Fig. 4.6 one can also see that, for lower RA, the values of current that maximize Q are closer to the bottom limit of the STNO region whereas for higher RA they are closer (or even coincident) to the breakdown current. In Fig. 4.7, the characteristic resistance as a function of I_{bias} for two MTJs, one with thin MgO and another with MgO with intermediate thickness, are shown (constant field of 200 Oe; AP state). It is clear that, depending on the MgO thickness, different breakdown mechanisms take place. In the case of the thinner MgO, the breakdown is caused by increasing the size of defects or pin-holes (notice the more accentuated decrease of R after ~ - 4.75 mA). On the other hand, for thicker MgO, a sharp breakdown is observed, caused by dieletric rupture [167]. Furthermore, in the case of the thinner MgO, the value of current that leads to the highest Q and P_{out} occurs before the current breakdown (in agreement with Fig. 4.6). This can be caused either by the slower MgO degradation that progressively reduces the quality of the RF emission or because the oscillation with largest amplitude is achieved

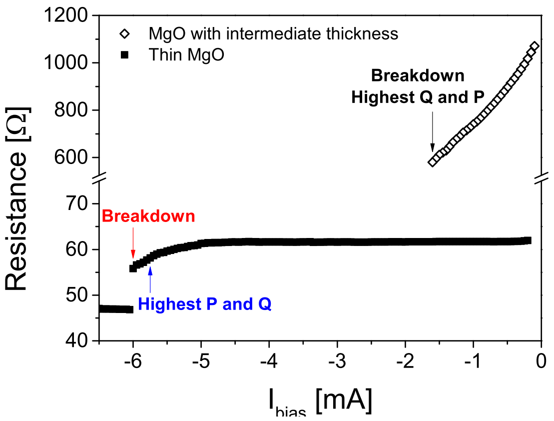

Figure 4.7: Breakdown mechanisms. Resistance as a function of the I_{bias} for a MTJ with thin MgO (black squares) and one with intermediate MgO thickness (white diamonds).

before breakdown. For the thicker MgO layers, the peak power increases until breakdown is reached, which indicates that the magnetic precession with largest amplitude was not achieved up to that point. This means that, for RA values above ~ 20 Ωμm^2, only small amplitude oscillations can be achieved before J_{break}, leading to a new decrease of P_{out} and confirming the optimal RA region between 7.5 and 12.5 Ωμm^2.

4.8 OPEN PROSPECTS

Despite the large effort of the STNOs community to work in the lowest possible RA range, this work presents a consistent set of data showing that thicker MgO barriers increase the P_{out} of these oscillators. From an application point of view this is a twofold advantage, since P_{out} is increased and thicker and more homogeneous MgO barriers have less defects and higher reproducibility. This optimal RA region is situated within 7.5 - 12.5 Ωμm^2 where P_{out} values up to 200 nW were observed, which are a factor of 5 larger than those obtained from devices with RA ~ 1 Ωμm^2. The results were corroborated by micromagnetic simulations and by a second fabricated MTJ incorporating an MgO wedge, both depicting the optimal region for maximized P_{out}. The main fact responsible for this large output is the low J_{STT} (down to 1.17 × 10^5 A/cm^2) obtained for the more continuous and crystalline MgO. Further investigation is still required to fully understand the mechanisms responsible for the ultra-low values of J_{STT}. Another worthwhile aspect of the results shown here is that the intermediate thickness of the MgO barrier can be applied to different STNOs geometries. The increase of the MgO thickness had no other discernible impact in the main operational figures of merit of the STNOs apart from the increase of P_{out} (frequency of operation and linewidth remained unchanged). It is therefore expected that the reported P_{out} increase in the intermediate MgO thickness range can have a cumulative effect when combined with other improvements of magnetic nature (such as vortex oscillators, STNOs incorporating perpendicular magnetic anisotropy or perpendicular polarizers) or device configurations (synchronized oscillators) that are also known to result in an increase of P_{out} when compared to homogeneous in-plane magnetization STNOs.

5

ALTERNATIVE GEOMETRIES FOR OSCILLATORS

Magnetic tunnel junction (MTJ) nanopillars with homogeneous magnetization were the main structures studied in the scope of this thesis. Nevertheless, the performance of other types of geometries (e.g. point-contacts) and magnetic configurations (e.g. magnetic vortices) as spin transfer nano oscillators (STNOs) have also been broadly studied. In this chapter, we will elaborate on these different configurations for STNOs. In particular, a novel geometry consisting on nanopillars with point-contacts for current confinement was developed. Such geometry implied some changes to the process described in Chapter 3. This changed process was successfully implemented and these novel structures fabricated. However, an undeniable conclusion of the effect of these nano-constrictions was hampered by the low yield and TMR obtained in this sample. Further work is thus still necessary to conclude if this geometry holds a significant advantage. Moreover, STNOs based on vortex magnetization were also successfully implemented. The conditions for the vortices formation (NiFe thickness and MTJ diameter) were unveiled. The measured vortex-based oscillators depicted output powers (P_{out}) 1.49 μW in conjugation with a small linewidth of 0.94 MHz at a frequency of 265 MHz. Hence, these oscillators cover a different frequency range and can be used as a complementary technology to STNOs based on homogeneous magnetization.

5.1 NANOPILLARS WITH POINT-CONTACTS FOR CURRENT CONFINEMENT

STNOs can be classified according to their electrical, magnetic and geometrical properties. Regarding the electric part, spin valves [61, 175, 176, 177] or MTJs [69, 84, 85, 81, 166, 79] can be used to retrieve an electrical signal from the current-induced oscillations. The main advantage of spin valves is their easier fabrication process, but higher P_{out} can be obtained using MTJs depicting high tunnel magnetoresistance ratio (TMR). The magnetic optimization is also of fundamental importance to the optimization of STNOs. Some configurations can be used such as the magnetic vortex configuration [68, 88, 139, 178, 105] and the homogeneous magnetization [84, 85, 81, 179]. The magnetic vortices, that will be studied in the next section, allow a higher ratio between P_{out} and linewidth (quality factor; Q) but their low frequency (below 1 GHz) is not suitable for most applications. The most common is the one based in in-plane (IP) homogeneous magnetic configuration. This configuration generates a high frequency but is usually associated with smaller amplitude and broader linewidth [61, 137].

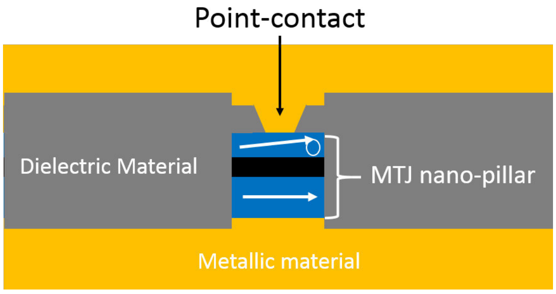

Figure 5.1: Alternative geometry for STNOs. Nanopillar with point-contact for current confinement.

It was demonstrated that the incorporation of magnetic layers with perpendicular magnetic anisotropy (PMA) leads to a decrease of the signal linewidth [84, 85]. Concerning STNO geometry, nanopillars [84, 85, 81] or point contacts [156, 159, 83, 180] can be used (see section 1.9.1). The nanopillars usually lead to a higher amplitude signal while the linewidth is usually smaller in structures incorporating point contacts. However, since MTJs are more resistive than spin valves, ballistic electron transport is difficult to achieve and the current spreads along the ferromagnetic (FM) mesa decreasing the current density. Therefore, point contacts are mainly used in spin valves but, in principle, can also be implemented in MTJ stacks depicting low resistance × area product (RA). In fact, a particular case of the point-contact geometry (the "sombrero-shaped" point-contact) was incorporated with an MTJ stack leading to a large P_{out} up to 2 µW [75]. Nevertheless, results with MTJs with a point-contact geometry are still scarce. The point-contact geometry also has the advantage to use the same FM mesa that facilitates the oscillator synchronization leading to an increased Q [105, 165, 62, 104, 106].

The nanofabrication processes used to obtain these geometries can also induce defects that deteriorate the magnetic and electrical properties of the STNOs. In the case of the nanopillar based-STNOs this effect is more drastic due to defects and redeposition generated during the nanopillar definition [116, 151, 150] (see chapter 3). However, the increased confinement of the current is advantageous when compared to the point-contact geometry, at least in MTJs. In this section, a hybrid structure consisting of a nanopillar with a point contact on top (Fig. 5.1) is proposed. Such a structure has a twofold advantage: (1) the smaller nanocontact on top of the pillar will increase the current density, maximizing the STT effect; (2) since the current is focused in the central part of the MTJ, the lateral sides of the pillar, which are more damaged during the etching process, will have a smaller contribution for the generated voltage. Note that, from a technical point of view, smaller point-contacts are easier to achieve than nanopillars since a thinner layer of e-beam resist can be used. Micromagnetic simulations of the current distribution of this hybrid geometry were performed [181]. The used geometry

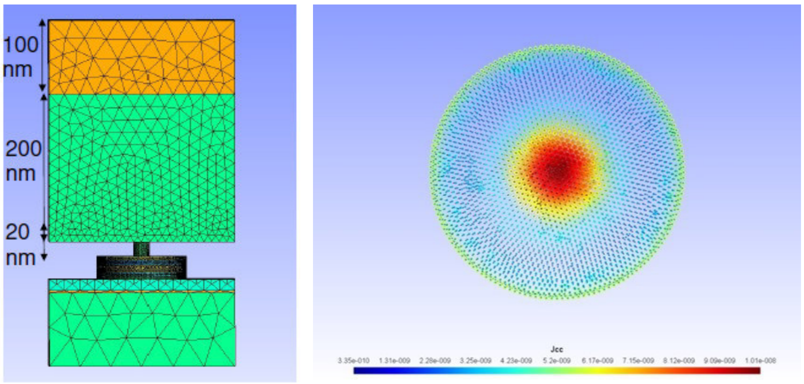

(a) (b)

Figure 5.2: Micromagnetic simulations of a current passing through a nanopillar with point contact. (a) Used geometry and (b) current profile within the pillar [181].

(similar to the dimensions and stack of the fabricated sample) is shown in Fig. 5.2(a). Figure 5.2(b) shows the simulated radial current distribution in the MTJ region, indicating that the current will be confined to the central region of the pillar after passing through the point-contact. These simulations suggest that ballistic electron transport occurs for low RA MTJs. Therefore, we expect the increased current density in the less damaged region of the MTJ to excite a large and coherent magnetic precession that might lead to a larger P_{out} in conjugation with a smaller linewidth.

5.1.1 *Nanofabrication of nanopillars with point contacts*

The fabrication scheme used to obtain these structures consisted on the definition of an insulating layer with a nano-sized hole (point-contact) on top of an MTJ stack and only then proceed to the nanopillar definition. The deposited stack was: [5 Ta / 25 CuN]$_{\times 6}$ / 5 Ta / 5 Ru / 20 IrMn / 2 $CoFe_{30}$ / 0.85 Ru / 2.2 $CoFe_{40}B_{20}$ / 0.5 $CoFe_{30}$ / MgO [9.8 $\Omega\mu m^2$] / 0.5 $CoFe_{30}$ / 2 $CoFe_{40}B_{20}$ / 10 Ta / 7 Ru (thicknesses in nm). After the stack deposition we deposited two extra layers: 15 TiWN / 10 Al_2O_3. The objective of this bilayer is to define the point contacts while stopping in a conductive layer (Ru oxide is still conductive). After this deposition, e-beam lithography was performed to define the point-contact structure. The simplest way to define the nanoholes would be by using positive resist (the exposed area during lithography is removed). However, the positive resist used in INL (PMMA) had very small selectivity to the physical etching and would be etched away before the nanoholes would be formed. Therefore,

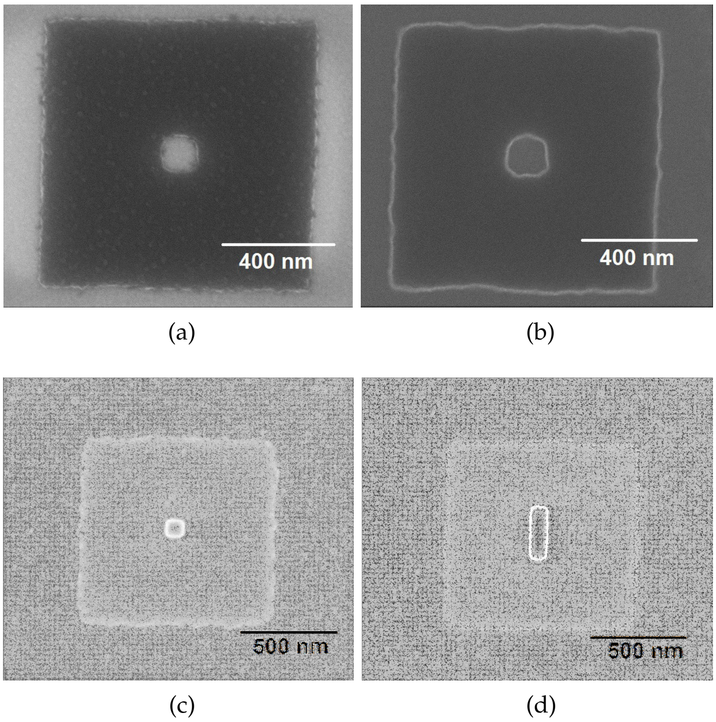

(a) (b) (c) (d)

Figure 5.3: SEM characterization of the point contact definition. Nanoring structure with a hole of 100 × 100 nm^2 after (a) e-beam lithography and (b) ion milling with an incident angle of 20° until the Ru below the Al_2O_3 and the TiWN layer. E-beam lithography of the pillar on top of a point contact (60 × 60 nm^2) with the dimensions of (c) 100 × 100 nm^2 and (d) 100 × 300 nm^2.

a negative resist was used to define a nanoring structure and use its hole as the point contact. The e-beam conditions had to be optimized and a different dilution (ARN7520 1+4) and dose (350 μCcm^2) were used in order to obtain the nanoring structure with a well-defined hole [Fig. 5.3(a) for a 100 nm hole]. The etching was performed using high energy conditions but with an incident angle of 20° with the normal direction of the sample. This angle was optimized to allow the etching inside the nanoscopic hole without redeposited material on its edges. The etching was performed until the signal of Ru was reached. Note that the majority of the signal comes from outside the nanoring structure and the etching rate inside the hole is smaller due to the constriction. Therefore, the hole might be in the TiWN layer or even closed. Thus, the TiWN layer allows a safer margin for the etching stopping point in a conductive layer. After etching and resist strip (plasma asher), the structure of Fig. 5.3(b) was obtained.

The ion beam planarization (IBP) step will require the use of a capping layer. Therefore, after the definition of the point-contacts a bilayer consisting of 150 AlSiCu / 15 TiWN was deposited. Afterwards, a new e-beam step (with the standard conditions; section 2.3.3) was performed to define the nanopillars. Figures 5.3(c) and (d) show the structure after e-beam lithography for two different pillar sizes. Despite the deposition of the thick capping layer, the profile of the nanoring structure defined previously is still visible. Moreover, a remarkable alignment between both e-beam lithographies could be achieved with the pillars defined on top of the point-contact.

The following step consists in the definition of the pillar by etching through the capping layer, the Al_2O_3 nanoring, the MTJ stack and finishing within the bottom contact. The objective of this etch is to obtain a structure as the one schematized in Fig. 5.1. However, since we had already defined nanostructures with different materials (and different etching selectivities) the final structure displays different steps [Fig. 5.4(a)-(c)]. It is clear that the nanorings defined previously passed their profile due to the slower etch rate of Al_2O_3 when compared to metals. However, it is only necessary for the MTJ to be restricted to the pillar region. In Figs. 5.4(d) and (e) we show cross sectional images of the structure showing that the MgO barrier is in fact confined to the nanopillar (despite the larger profile obtained in the bottom contact).

5.1.2 *DC measurements of pillars with and without point-contacts*

After finishing the nanofabrication process the transfer curves of the fabricated MTJ devices were measured and the RA and TMR values extracted. Both standard nanopillars (without constriction) and nanopillars incorporating a point-contact were fabricated. Both structures could be easily obtained in the same wafer just by not performing the first e-beam lithography for the structures without point contacts. In Fig. 5.5 we depict the TMR vs RA for all the measured devices (with different pillar sizes ranging from 100×100 to 200×300 nm^2). Two features are clear from this plot: (1) a relatively low TMR was achieved (below ~50%); (2) there are significantly more functional standard pillars than pillars incorporating a point-contact. Since the RA values of the MTJs are close or higher than the nominal value (9.8 $\Omega\mu m^2$) the sidewall redeposition does not seem to be responsible for the low TMR observed. Furthermore, in the TEM image of a non-functional device [Fig. 5.4(e)] one can verify that the top part of the pillar is not open, on the contrary, it is involved in the Al_2O_3 matrix leading to an open circuit. The fact that some of the MTJs with point-contacts were operational indicates that some of the MTJs with point contacts were open on top. In fact, in Fig. 5.4(d) we show one of these functional devices. Despite the fact that the top part of the pillar is already thinner due to the extensive etching [as can also be seen in Fig. 5.4(c)], the opening of the pillar could still be achieved in some cases. This indicates that the IBP step was performed in the limit, leading

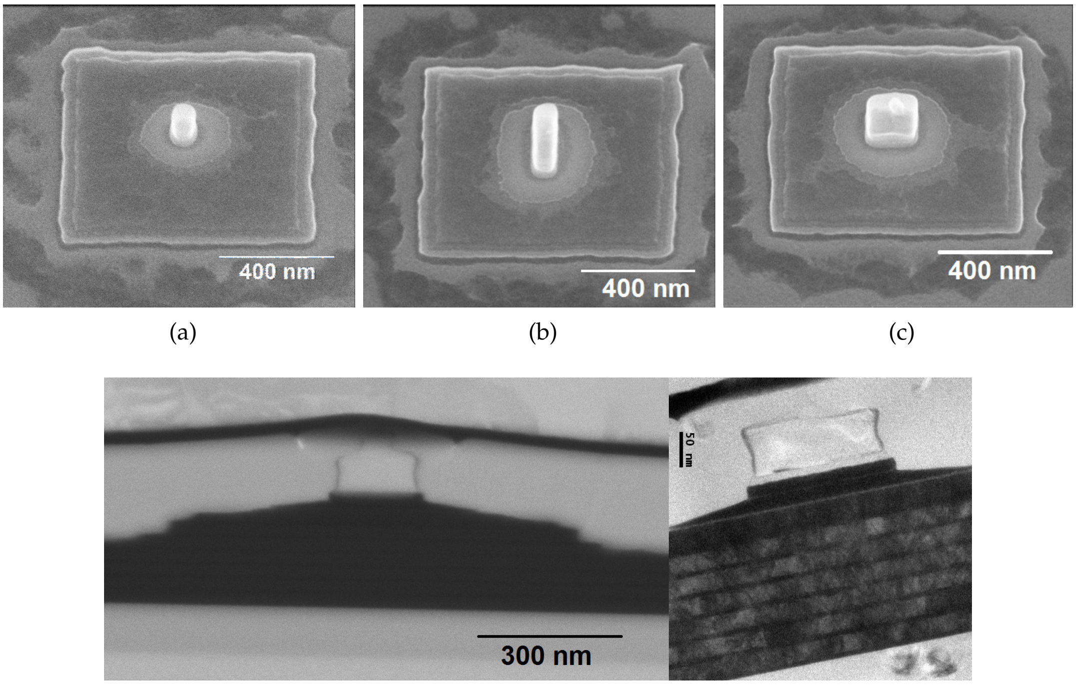

(a) (b) (c)

(d) (e)

Figure 5.4: Nanopillars with point-contacts. SEM characterization after the nanopillar definition through etch of pillars with (a) 100 × 100, (b) 100× 300 and (c) 200× 200 nm^2. (d) SEM cross section of a functional pillar with a point-contact. (e) TEM cross section of a non-functional pillar with point-contact.

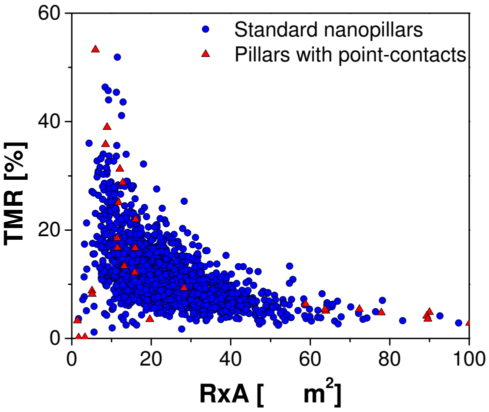

Figure 5.5: Static electrical measurements. TMR vs RA plot for all the measured functional devices (with different sizes). The black dots are standard pillars (without point contacts) and the red dots pillars incorporating point contacts.

to functional devices in some cases, open circuits in others and an overall increase of the *RA* and decrease of the TMR. More precisely, the case of pillars slightly open after planarization is equivalent to a resistance in series that increases the *RA* and reduces the TMR. Furthermore, it was also verified that all the nanopillars with point contacts smaller than 100 × 100 nm^2 led to open circuits. Thus, during the nanoring definition, the holes with dimensions below 100 × 100 nm^2 were not completely open. In spite of the significantly smaller number of devices with point-contacts, the TMR vs *RA* trend is similar. This indicates that, in the case of the open point-contacts, the devices seem to be functional both electrical and magnetically.

5.1.3 *Effect of the point-contact on STNOs*

After the characterization of the static electric and magnetic properties of the fabricated devices, a DC current was injected in some of the MTJ structures and the generated RF electrical signal was studied. This RF emission characterization was performed in both standard pillars and pillars with point-contacts. The objective of this study was to verify if the nanoconstriction is indeed beneficial for STNOs due to their increased current density and current confinement to the central (less damaged) region of the pillars. One also has to consider that the nanofabrication process has some associated variability due to magnetic domains, grains, defects of the MgO barrier, defects induced by the etching process, etc. Therefore, a full comparison between different types of oscillators requires some statistics. However, the small overall TMR and the low number of functional nanopillars with point-contacts hampered a deep statistical analysis. Nevertheless, we were able to select three pillars with different geometries: 200 × 300 nm^2 and 100 × 150 nm^2 standard pillars and 200 × 300 nm^2 pillars with 150 × 150nm^2 point-contacts. The pillars with 200 × 300 nm^2 with and without constriction allow us to compare directly the effect of the constriction. The smaller standard pillars (100 × 150 nm^2) allow us to verify if a larger pillar with a constriction is advantageous when compared to a pillar with dimensions identical to the constriction size. Note that a relatively large pillar size (200 × 300 nm^2) was studied so that the contrast between standard pillars and pillars with constriction would be enhanced. The smaller standard pillars (100 × 150 nm^2) do not have the same size as the studied constriction (150 × 150 nm^2) to minimize the effect of different aspect ratios of the studied pillar sizes.

Table 5.1 depicts the DC electrical properties [TMR, RA and breakdown current (I_{break})], along with the RF electrical properties [frequency, linewidth and maximum matched output power (P_{out})] of the characterized STNOs for each geometry (along with the average values). The different MTJs lie within the same TMR and RA region so that a straightforward comparison could be performed. The dynamic measurements were all performed with the same applied field of 200 Oe with a small tilting to maximize the microwave emission. Despite some variation of the measured parameters for the same geometry, the average values allow us to extract some trends. For instance, I_{break} is higher for the 200 × 300 nm^2 standard pillars than the other geometries. However, if we calculate the current density for breakdown (J_{break}), for the larger standard pillars we obtain 4.08×10^6 A/cm^2 while for the smaller ones we obtain 7.87×10^6 A/cm^2. If now we consider that the effective dimension of the pillar with the constriction is 200 × 300 nm^2 (pillar dimension) we obtain a J_{break} value of 3.20×10^6 A/cm^2, which is smaller than the one of both the standard pillars. On the other hand, if we consider that the effective dimension is the one of the nanoconstriction (150 × 150 nm^2), we obtain 8.53×10^6 A/cm^2, which is larger than both standard pillars. Thus, it is likely that the effective dimension of the current within the pillar with the point contact is in between the one of the pillar and the one of the constriction.

Due to the low TMR values of the MTJs (consequence of the incomplete planarization), a low average P_{out} (in the tens of pW range) and large linewidth (above 300 MHz) were obtained. Only in one MTJ pillar with the 100 × 150 nm^2 a smaller linewidth (120 MHz) was achieved. This coherent precession at larger frequency (6.30 GHz) was not observed in any other case. However, even in this case, P_{out} was limited below the nW range (0.370 nW). In Fig. 5.6(a) we show the evolution of P_{out} as a function of I_{bias} for the cases with largest output (MTJ1) for each geometry. The smallest standard pillar was the one that led to the largest P_{out} (with the smallest linewidth). This is consistent with the monodomain precession that is more likely to occur at smaller dimensions. However, we should point out that only one

Geometry	Parameters	MTJ1	MTJ2	MTJ3	Average
200 × 300 nm^2 (standard pillar)	TMR (%)	17.79	17.65	12.96	16.13
	RA ($\Omega\mu\text{m}^2$)	11.75	10.92	15.00	12.56
	I_{break} (mA)	2.70	2.75	1.90	2.45
	Frequency (GHz)	2.67	4.74	3.64	3.67
	Linewidth (MHz)	267	306	372	315
	P_{out} (pW)	156.3	94.3	43.9	98.2
200 × 300 nm^2 (with constriction)	TMR (%)	13.33	16.73	12.19	14.08
	RA ($\Omega\mu\text{m}^2$)	13.21	11.48	15.87	13.52
	I_{break} (mA)	1.95	1.95	1.85	1.92
	Frequency (GHz)	3.49	4.80	5.18	4.49
	Linewidth (MHz)	418	356	381	385
	P_{out} (pW)	108.2	66.7	56.4	77.1
100 × 150 nm^2 (standard pillar)	TMR (%)	16.52	15.55	13.89	15.32
	RA ($\Omega\mu\text{m}^2$)	18.58	5.37	18.52	14.15
	I_{break} (mA)	0.9	1.5	1.15	1.18
	Frequency (GHz)	6.30	3.63	2.28	4.07
	Linewidth (MHz)	120	411	390	307
	P_{out} (pW)	370.4	61.8	26.2	152.8

Table 5.1: Measured parameters (TMR, RA, I_{break}, frequency, linewidth and P_{out}) for three STNOs (and their average) for each geometry.

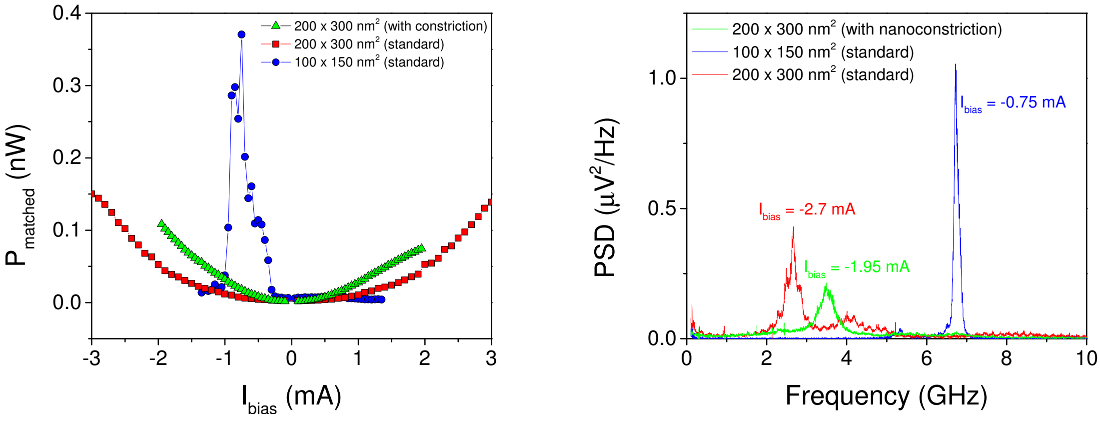

(a) (b)

Figure 5.6: RF emission characterization. Comparison between the different studied MTJ pillars (standard pillars with 200 × 300 and 100 × 150 nm^2 and pillar with 200 × 300 nm^2 with a nanoconstriction of 150 × 150 nm^2). (a) Integrated matched output power and (b) spectra for the largest output case for each geometry.

of the three measured MTJs with these dimensions led to this well-defined emission (MTJ2 and 3 led to results similar to the ones obtained with the other geometries). As for the pillars with dimensions of 200 × 300 nm^2, in the case of the pillar with point contact, P_{out} increases more sharply with I_{bias}, but, since I_{break} is smaller, a larger P_{out} is obtained in the case of the standard pillar. Figure 5.6(b) shows the measured spectra for each geometry at the I_{bias} values that maximized P_{out}. The RF emission arising from the smallest standard pillar is clearly larger and with a smaller linewidth than the remaining cases. A larger signal was obtained in the case of the larger pillar without constriction which is mainly related with the larger I_{break}.

5.1.4 *Challenges for future point-contact based geometries*

In summary, in this section a nanofabrication scheme to obtain nanopillars with point contacts for current confinement was demonstrated. The nanofabrication process was successfully implemented and functional MTJ pillars with point contacts (down to 100 × 100 nm^2) obtained. However, the yield of the process was low with most of the structures depicting open circuits (due to closed point contacts and incomplete IBP). The incomplete planarization also led to an increase of the RA and decrease of the TMR.

Due to the limited TMR of the fabricated MTJs and the relatively large dimensions and low yield of the functional nanoconstrictions, it is difficult to conclude if the point contact on top of a nanopillar is indeed beneficial for STNOs. The results seem to suggest a sharper increase of P_{out} with I_{bias} in the case with the point-contact. However, this variation might be within the dispersion of the results. As future directions to verify the effect of the point contact, it would be valuable to optimize the process to obtain smaller open point contacts (e.g. longer etching times during the nanoring definition). Furthermore, a thinner metallic layer between point contact and MTJ would perhaps minimize current dispersion within the pillar, regardless of the fact that the simulations indicate that the current is still confined with the used thickness (10 Ta / 7 Ru / 15 TiWN). Despite the fact that an intermediate RA is expected to increase P_{out} (see chapter 4), in this case it might be useful to use a smaller RA in order to allow a more ballistic current transport (leading to a smaller spreading of the current). Moreover, note that for the AP alignment (that maximizes P_{out}), negative current values (electrons from bottom to top) lead to a STT in the direction that enhances the precession. However, in the used geometry, the point contact is on top of the MTJ, minimizing the effect of the nanoconstriction for this current polarity. It was verified that the RF emission was not improved by using the P magnetic configuration and reversed current polarity. Finally, as a proof of concept of the point-contacts, perhaps the best strategy would be to use micrometric sized pillars. In such large structures, the current densities achieved without point-contacts would lead to negligible current-induced magnetic dynamics. Thus, we would be able to pinpoint the effect of the nanoconstriction and, only then, move to nanosized pillars with point-contacts on top.

5.2 MAGNETIC VORTEX OSCILLATORS

In all the STNOs previously discussed in this thesis, the FM layers depict homogeneous magnetization. In that case, the STT induces the magnetization dynamics that can be approximated to a macrospin precession [49] (neglecting inhomogeneties and magnetic domains). An alternative approach consists of using the STT-driven motion of a magnetic vortex to generate the RF signal (see section 1.8) [105, 68, 178, 52]. This magnetic configuration consists of a curling spin structure in the plane of the magnetization around a central region (core), where the magnetic moments are pointing out-of-plane (OOP) to avoid creating a singularity. The STT effect leads to a circular motion of the vortex core around its equilibrium position that generates a variation of the average magnetization of the free layer that results in an RF voltage variation [182]. This oscillation mode leads to very small linewidths (<1 MHz) in conjugation with a large P_{out} (in the μW range) [182, 54, 183]. On top of that, the STT-induced vortex oscillations depict a "textbook" behaviour in good agreement with the theoretical models [68, 184]. However, the oscillation frequency is limited to the sub-GHz range which is a less interesting range for technological applications. Nevertheless, novel approaches to excite higher frequency modes [185] and for RF sensor applications [178] have recently emerged. Another issue with vortex-based STNOs concerns the large OOP magnetic fields necessary to excite large oscillations and thus maximize P_{out} [68]. A solution to this problem consisted in the incorporation of a perpendicular polarizer that led to the achievement of large powers (0.6 μW) without an applied magnetic field [88]. Another configuration, consisting of a double vortex structure (i. e. a non homogeneous polarizer), showed narrow linewidths at zero field [186, 187]. Furthermore, relevant results concerning the synchronization of vortex oscillators have been also achieved [105, 108, 188].

The objective of the work described in this section was to use the developed nanofabrication process (Chapter 3) to obtain vortex-based STNOs. The goal was to demonstrate the feasibility of the vortex configuration, opening the prospect for future work performed with vortex-based STNOs. To achieve this structure, a soft FM with a weak magneto-crystalline anisotropy (such as NiFe) has to be incorporated in the magnetic stack. Two samples, whose main difference is the NiFe thickness (7 and 15 nm) on top of a high quality MTJ, were deposited and nanofabricated. From the measured transfer curves we explored the conditions (pillar size and NiFe thickness) that led to the vortex configuration. Moreover, preliminary RF electrical measurements of the fabricated vortex-based STNOs were performed. Large P_{out} values (1.49 μW) with a small linewidth (0.94 MHz) at a low frequency (265 MHz) were achieved. Hence, in this section we demonstrated both the feasibility of the vortex STNOs and the transversality of the nanofabrication process.

5.2.1 *Magnetic stack for magnetic vortices*

For the magnetic vortex configuration to be achieved, a NiFe layer was incorporated in the deposited stack. On top of that, an MTJ depicting large TMR was also used to retrieve a large P_{out} from the STT-induced magnetic oscillations. Moreover, the conditions to achieve magnetic vortices depend on both the nanopillar radius and NiFe thickness (see Fig. 1.10). Thus, some stack and pillar size optimization is required to achieve vortex-based STNOs. To fulfill this goal, two different stacks were deposited: (S1) 3 Ta / 30 CuN / 5 Ta / 20 PtMn / 2 $CoFe_{30}$ / 0.85 Ru / 2.2 $CoFe_{40}B_{20}$ / 0.5 $CoFe_{30}$ / MgO [1.45 $\Omega\mu m^2$] / 0.5 $CoFe_{30}$ / 2.0 $CoFe_{40}B_{20}$ / 0.21 Ta / 15 NiFe / 10 Ru /10 Ru / 150 CuN / 30 Ru and (S2) 5 Ta / 50 CuN / 5 Ta / 50 CuN / 5 Ta / 5 Ru / 6 IrMn / 2.6 $CoFe_{30}$ / 0.85 Ru / 1.8 $CoFe_{40}B_{20}$/ MgO [2.83 $\Omega\mu m^2$] / 2.0 $CoFe_{40}B_{20}$ / 0.2 Ta / 7 NiFe / 10 Ta / 30 CuN / 7 Ru (thicknesses in nm). Despite small differences between the stacks, the most relevant variation is the thickness of the NiFe layer where the vortex state will be generated. The thin Ta layer (0.2 nm) between the MTJ and the NiFe was used so that the vortex state of the soft FM (NiFe) is induced in the free layer magnetization.

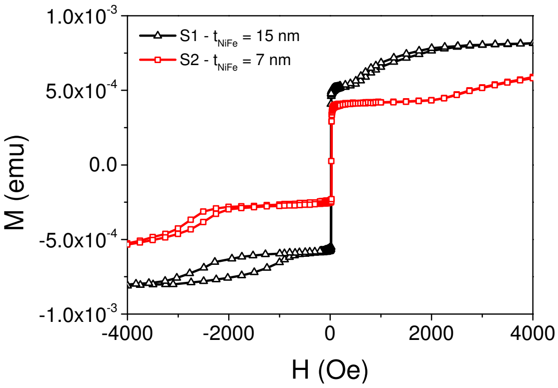

Figure 5.7: Magnetization curves of the stacks as a function of the IP magnetic field (prior to nanofabrication).

Thus, a vortex configuration can be achieved in conjugation with the high TMR characteristic of epitaxial CoFeB/MgO/CoFeB MTJs. The standard annealing (330 °C under 1 T for 2 h) was applied to both stacks.

In Fig. 5.7 we show the magnetization curves of both stacks with applied IP fields (prior to nanofabrication). In both cases the NiFe layer is coupled with the free layer of the MTJ. Thus, in the case of the thickest NiFe layer (S1) there is a larger magnetization jump at low fields (free layer + NiFe magnetization rotation). As for the synthetic antiferromagnets (SAFs), the one used in S2 (6 IrMn / 2.6 $CoFe_{30}$ / 0.85 Ru / 1.8 $CoFe_{40}B_{20}$) showed an increased stability when compared to the one used in S1 (20 PtMn / 2 $CoFe_{30}$ / 0.85 Ru / 2.2 $CoFe_{40}B_{20}$) since its rotation occurred for larger magnetic fields. Note that for the vortex state to appear, the MTJ nanofabrication is required and thus further information about the vortex formation is difficult to extract from the magnetization curves of unpatterned stacks.

5.2.2 *Transfer curve signature of magnetic vortices*

Both MTJ stacks (S1 and S2) were then nanofabricated into pillars of several sizes and their transfer curves measured. In Fig. 5.8 we show the TMR and RA extracted for the circular MTJs with diameters d ranging from 80 up to 500 nm for (a) S1 and (b) S2 (the same scales were used in both cases to facilitate the comparison). In the case of S1 [Fig. 5.8(a)], the smaller nanopillars have a well defined RA and a TMR ranging from 25 to 80%, while the bigger ones depict an increasing RA and a small TMR. To clarify the reason for the latter behaviour, in Fig. 5.9(a) we depict a typical transfer curve of this low TMR and high RA region, showing that complete

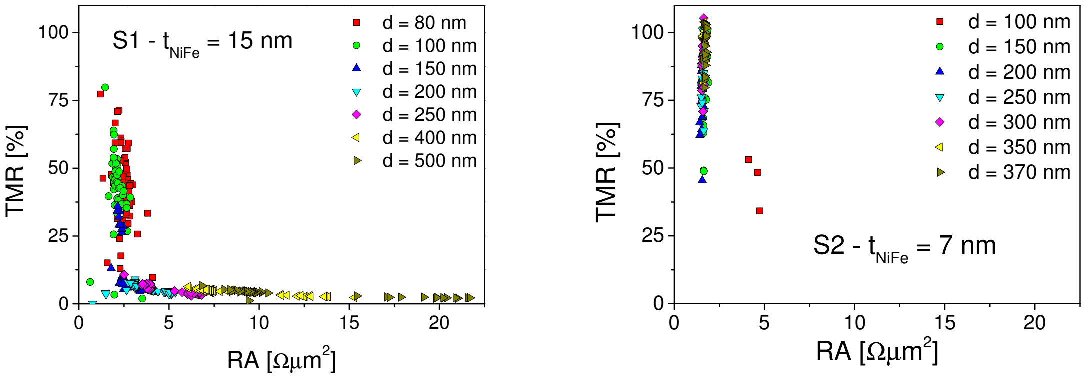

(a) (b)

Figure 5.8: DC electrical characterization. TMR vs *RA* map of the measured circular MTJs of samples (a) S1 and (b) S2 (applied magnetic IP field up to 200 Oe).

switching was not achieved (within the maximum field of 200 Oe). Note that the plotted *RA* values correspond to the lowest resistance state (P state in the case of complete switching), but since the magnetic reversal was not complete, the minimum resistance was not achieved and thus the measured *RA* is higher. Therefore, these measured values of *RA* and TMR are not the actual MTJ values. To confirm this hypothesis of incomplete switching, the transfer curves of some larger MTJs, falling in this region of high *RA* and low TMR, were measured with a manual setup with larger fields (up to 1.6 T). Figure 5.9(b) shows that in fact the full magnetic reversal of the free layer could be obtained with larger fields. However, the fact that these measurements were performed with 2-point contacts and the low statistics hamper a direct TMR comparison. Such a pronounced incomplete switching was not observed in S2 [Fig. 5.8(b)]. In the region with well defined *RA* (observed for both S1 and S2; below 3 $\Omega\mu m^2$), there is also a significant variation of the TMR values. The reasons for this TMR variation are some incomplete switching and sample variability. A higher average TMR and a better defined *RA* were obtained in sample S2. Note, however, that in S2 the larger MTJs led to the highest TMR. In the case of S1, the larger pillars depicted incomplete switching, it is thus likely that a higher TMR would be achieved for the larger MTJs of S1.

Let us now focus on the measured transfer curves where complete magnetization switching was obtained (S1 will be considered). In some cases, a sharp switching characteristic of homogeneous magnetization is observed [Fig. 5.9(c)]. In these cases, the magnetization of the free layer is homogeneous and a direct transition from the AP to the P state is induced. Other transfer curves, however, show a different behaviour [Fig. 5.9(d)]. In these cases, between the

AP and the P state, there is a linear resistance region where the vortex state is formed. Note that the net magnetization of a vortex is close to zero and thus the resistance of this state is in between the ones of the P and AP states. For a certain value of applied magnetic field, the vortex magnetization is destroyed and the free layer becomes homogeneous along the field direction. Note that the vortex configuration (but with some coercivity) was also achieved in the case of the larger pillars [Fig. 5.9(b)]. The vortex states could be achieved in both S1 and S2, although, some differences between the transfer curves obtained in each sample were observed. In Fig. 5.10 a typical transfer curve with vortex formation measured in S2 is shown. A large field range for the vortex formation was obtained, indicating that stable vortices could be achieved with t_{NiFe} = 7 nm. The complete transfer curves measured for the larger pillars of sample S1 [Fig. 5.9(b); blue line for the pillar with the same diameter (300 nm)] indicate that a thinner NiFe layer leads to a more stable vortex formation. Moreover, a positive (negative) FM coupling (H_F) was observed in the S1 (S2) which is likely caused by the different free layers used.

The formation of a magnetic vortex in a FM disc requires a balance between the dipolar and the exchange energies. Hence, the formation of this magnetic configuration depends on the disc radius (R) and the FM thickness (L), as was discussed in section 1.5. To compare our results with the theoretical framework, the transfer curves of nanopillars with different diameters for both samples were analysed to determine the conditions for vortex formation. In Fig. 5.11 an experimentally measured phase diagram, similar to the one of Fig. 1.10, is shown. The value of exchange length (L_E) that was considered was 5 nm (usual values are between 5 and 10 nm), L corresponds to the NiFe thickness of each sample and R the radius of the measured MTJ pillars. In some conditions the vortex state was achieved systematically (blue triangles) and in others only homogeneous magnetization was observed (red squares). In some cases, however, both behaviours (vortex and homogeneous magnetization) were observed for different MTJ pillars (green circles). The gray areas delimiting the regions of the vortex formation are an extrapolation of the expected behaviour. The case where the vortex formation is a metastable state (some vortices) was only observed in S2 for d = 150 and 200 nm, which is in agreement with the larger intermediate region for lower L values (red area of Fig. 1.10). Despite this qualitative behaviour in agreement with the theoretical state diagram (for NiFe discs), the actual values of R/L_E where the vortex state starts to be formed are higher than the theoretical case ($R/L_E \approx 1$). The first reason for this discrepancy might be a larger L_E than the one considered. The second reason is related to the fact that the vortex state is only measured electrically when the CoFeB is in this state. Thus, the vortex state might only be transferred to the CoFeB when it is very well defined within the NiFe layer (for larger R/L_E values). Moreover, the transfer curves indicate that the OOP magnetization state was not achieved (hard-axis behaviour was not observed). This is due to the relatively thick CoFeB

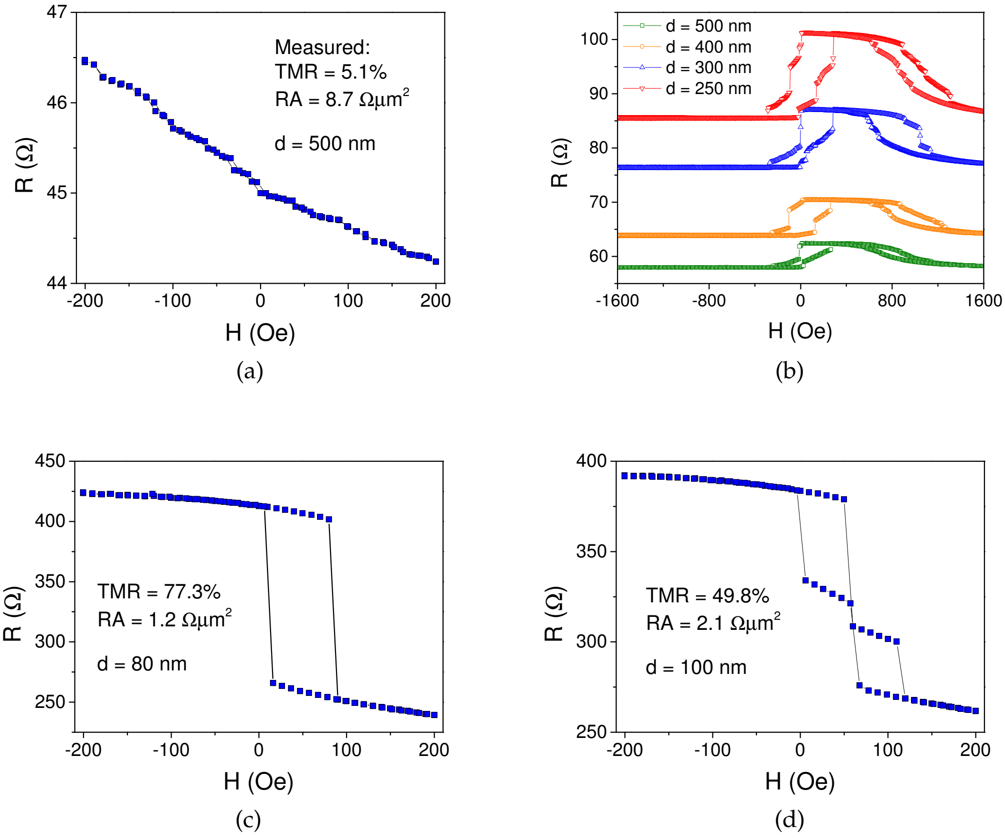

Figure 5.9: DC electrical characterization of S1. Transfer curves measured in the case of (a) incomplete switching, (b) MTJs depicting incomplete switching at low field (200 Oe) measured at higher fields, (c) homogeneous magnetization behaviour and (d) formation of the vortex magnetization.

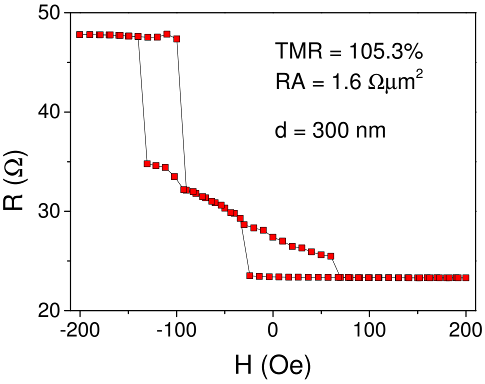

Figure 5.10: DC electrical characterization of S2. Transfer curve with vortex-state formation depicting a large field range.

free layer used, depicting an IP easy axis. More samples with different NiFe thicknesses would be necessary to build the complete state diagram. However, these results are already a very strong indication that magnetic vortices were successfully achieved.

5.2.3 *Vortex-based oscillators*

To further confirm that the magnetic vortex configuration was achieved, preliminary RF electrical measurements were performed. The maximization of the output deriving from vortex-based STNOs usually requires the presence of a large applied magnetic field in the OOP direction (H_{OOP}) [68]. Thus, the setup for RF electrical measurements with OOP fields (section 2.7.3.2) was used. In Fig. 5.12 a measured spectrum (black squares) obtained from an MTJ of S2 with a diameter of 350 nm along with a Lorentzian fit of the spectrum (red line) is shown. DC electrical measurements of this particular MTJ were not performed and thus the exact value of RA and TMR is not known. Nevertheless, the TMR map of this sample [Fig. 5.8(b)] indicates that the TMR of this MTJ is most certainly above 75%. A very large P_{out} of 1.49 μW in conjugation with a very small linewidth (0.94 MHz) could be obtained. Note that a large H_{OOP} (0.4 T) was necessary and the low RA allowed the injection of a large I_{bias} (13.8 mA). The frequency of the RF emission is, however, limited to 265 MHz. This low frequency value in conjugation with the large output and small linewidth demonstrates the successful implementation of the vortex configuration.

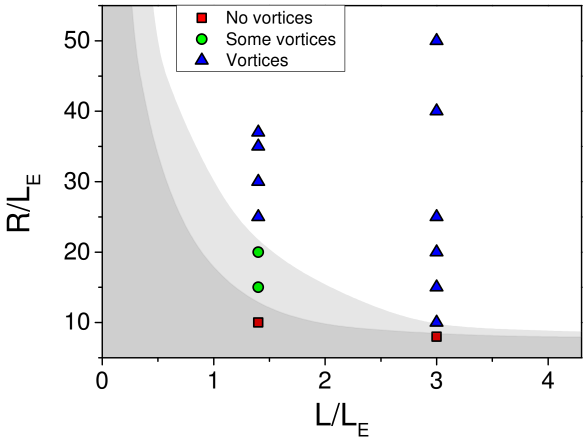

Figure 5.11: State diagram of the measured nanosized MTJs. Three states with no vortices (red squares), some vortices (green circles) and vortices (blue triangles) were observed. The gray areas are guides to the eye of the extrapolated behaviour.

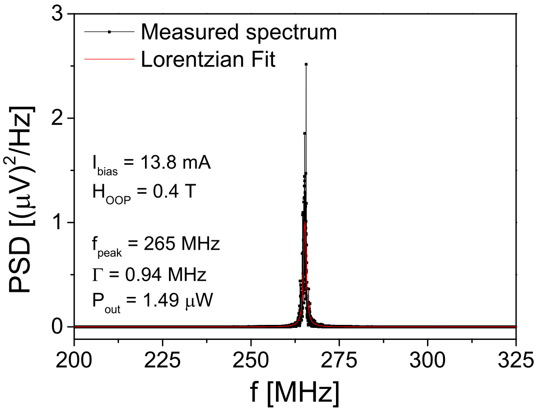

Figure 5.12: RF emission characterization of the vortex-based STNOs. Unmatched power spectral density (PSD) measured at the amplifier input with I_{bias} = 13.8 mA, H_{OOP} = 0.4 T.

5.2.4 *Open prospects with the vortex configuration*

In this section, it was demonstrated that the nanofabrication process can be adapted for different geometries and magnetic configurations. In particular, MTJs with vortex magnetization could be achieved just by incorporating a relatively thick permalloy layer (7 and 15 nm of NiFe). The measured transfer curves revealed the signature of magnetic vortex formation. Moreover, the state diagram of the magnetic states as a function of the nanopillar size and NiFe thickness is in qualitative agreement with the expected behaviour. The RF emission generated by the vortex-based STNOs depicted a large P_{out} of 1.49 μW with a small linewidth of 0.94 MHz. The measured frequency was 265 MHz which lies within the typical range for such STNOs. These were the first preliminary measurements of an ongoing work on vortex-based STNOs and further results are expected.

6

OSCILLATORS INCORPORATING A PERPENDICULAR POLARIZER

The performance of spin transfer torque nano oscillators (STNOs) depends on several characteristics of the oscillators (electrical, magnetic, structural, etc.). For instance, in chapter 4 the output power (P_{out}) was maximized by tuning the MgO barrier thickness thickness [or resistance × area product (RA)] range of the magnetic tunnel junction (MTJ), whereas in chapter 5 nanopillars incorporating point-contacts and magnetic vortices were used. Another approach consists in optimizing the magnetic properties of the deposited stack to enhance the magnetization precession of the free layer, while maintaining a coherent oscillation. In this chapter, such magnetic configuration, leading to an increased precession amplitude, is pursued. To do so, the incorporation of materials with strong perpendicular magnetic anisotropy (PMA) was used. More precisely, a magnetic stack comprising an MTJ with in-plane homogeneous magnetization [depicting large tunneling magnetoresistance (TMR)] and a perpendicular polarizer was developed. The goal of such magnetic structure is to achieve an orthogonal magnetic polarization of the electron spins and the MTJ, inducing a large out-of-plane (OOP) precession of the free layer magnetization. Within the materials that can be used as a perpendicular polarizer, Co/Pt multilayers are one of the most common choices due to their strong PMA. However, the Timaris multi target module (section 2.1.1.1) does not incorporate a Pt target. Hence, the Kenosistec deposition tool (section 2.1.1.2) had to be used to deposit the perpendicular polarizer. Therefore, an ex-situ deposition scheme (with two vacuum breaks) taking profit of both deposition tools was used. The deposition was optimized, the stack nanofabricated and the RF emission of the STNOs characterized.

6.1 OSCILLATORS WITH PERPENDICULAR MAGNETIC ANISOTROPY

The concept of using the spin of electrons to operate electronic devices, instead of only their charge, led to the creation and quick expansion of the field of spintronics [5, 6, 17]. A novel development consisted of the use of the spin transfer torque (STT) effect to generate magnetization precessions in the magnetic layers at the microwave range [55, 189, 61, 70, 175]. These dynamics are created by spin polarized currents that transfer their angular momentum to the magnetic layers. STNOs [69] use magnetoresistive structures (such as spin valves and MTJs) to obtain an RF signal associated with the magnetic precession of the free magnetic layer.

Since the STT effect is a vectorial quantity, its direction and magnitude depend on the relative direction between the current spin polarization and the magnetization of the free layer. More precisely, if a magnetic polarizer with magnetization direction ($\vec{m}_1$) in conjugations with a free layer with magnetization $\vec{m}$ is used, the STT-induced anti-damping torque can be expressed as [190]:

$$\vec{\tau}_{STT} = a_J(J,\theta)\vec{m} \times (\vec{m} \times \vec{m}_1), \tag{6.1}$$

where J is the current density, θ the angle between the magnetic orientation of the polarizer and free layer and a_J is the STT amplitude that depends on the used materials and TMR. Note that Eq. (6.1) shows that an angular deviation between the magnetization of the magnetic layers is necessary for a significant torque. Nevertheless, some misalignment is always present due to thermal fluctuations of the magnetization and thus the magnetic precession can be started even with parallel configurations (such as the results shown in the previous chapters). Furthermore, two classes of magnetization trajectories can be obtained: in-plane (IP; oscillation around the IP static magnetization ground state) and out-of-plane (OOP; oscillation around the OOP excited magnetization state) [55, 86, 191, 192]. The OOP mode usually has a trajectory with a larger amplitude (the magnetization can oscillate almost between the P and AP states), leading to a larger emitted output power (P_{out}). Another difference between these precession modes consists of their frequency dependence with the applied current (I_{bias}). While, the OOP mode is characterized by a frequency increase with I_{bias} (blue shift), a frequency decrease (red shift) is observed in the IP mode [193].

Therefore, the STNOs configurations where both the free and pinned magnetic layers have an in-plane easy axis [61, 70, 79] profit from the large TMR achieved in these structures but neglect the enhancement of the magnetic precession. Moreover, these magnetic precessions are usually IP, restraining further the oscillation amplitude. On top of that, this configuration requires a relatively large magnetic field to produce a high microwave signal [61, 80]. The incorporation of layers with perpendicular magnetic anisotropy (PMA) can be used to improve the performance of STNOs and several configurations have already been tried. A fully perpendicular device is not advantageous for STNOs, since the relative orientation of both layers is still the same, and thus a large applied magnetic field is still required [82]. Promising results have been achieved using a pinned layer with IP magnetization and free layer with tilted magnetization leading to P_{out} values up to 280 nW with a linewidth of 25 MHz [84] and bias field free emission with 36 nW with a linewidth of 28 MHz [85]. However, the tilted magnetization was achieved by decreasing the thickness of the free layer which also decreases the TMR value and thus limits the extracted power. Another approach to maximize the amplitude of the magnetic precession with limited TMR loss, consists in using IP magnetized MTJs incorporating a perpendicular polarizer. In fact, this configuration has already been successfully implemented in spin valves [86] and MTJ with magnetic vortex configuration [88]. In the case of the MTJ-based vortex configuration, a large P_{out} (600 nW) was obtained without applied magnetic field. However, the oscillation frequency was limited to the 180 MHz range which is less appealing for technological applications. In the measurements performed with spin valve structures it was observed that an OOP steady state precession trajectory could be obtained by using the perpendicular polarizer, which indicates that a larger precession amplitude can be achieved through this magnetic configuration. The effect of a perpendicular polarizer on the STT-induced magnetic dynamics of a free magnetic layer has already been thoroughly studied using both a macrospin model [194] and micromagnetic simulations [195].

In this chapter, the fabrication of an MTJ with homogeneous IP magnetization in conjugation with a perpendicular polarizer is described. Note that in this geometry the IP pinned layer of the MTJ is still present, shaping the polarization of the current injected in the free layer. However, as will be demonstrated, the determinant effect of the perpendicular polarizer could be demonstrated. Thus, the IP pinned layer has a more important role as analyser (due to the TMR), than as a current polarizer. The stack deposition used in this work was performed ex-situ, i.e., using two deposition tools with vacuum breaks. We performed this ex-situ deposition in order to take profit from two distinct deposition tools: one for the deposition of MTJs with large TMR (Timaris multi target mode; section 2.1.1.1) and another for deposition of Co/Pt multilayers depicting large PMA (Kenosistec tool; section 2.1.1.2). This deposition scheme represents an important asset due to the prohibitive costs of targets of materials such as Pt or Pd necessary to achieve large PMA [196]. The magnetic and electric properties of the stack were optimized and a full wafer was nanofabricated. MTJ devices with low RA (5 - 6 Ω μm^2) and large TMR (up to ~ 90%) could be obtained. Moreover, the transfer curves revealed the formation of an intermediate resistance plateau, which is a signature of the generation of OOP oscillations of the free layer. It was shown that this region depicting the OOP oscillations of the free layer maximizes the P_{out} up to 60 nW. However, the minimum linewidth was limited to the ~500 MHz region. Nevertheless, the largest P_{out} was obtained without applied field, which is a relevant aspect for practical applications.

6.2 STACK OPTIMIZATION

Two physical vapor deposition systems were used to deposit the magnetic stacks: the Timaris system (S1) with a base pressure of 2.0×10^{-9} mbar for the MTJ deposition; and a Kenosistec system (S2) with a base pressure of 5.0×10^{-8} Torr incorporating a Pt target used for the deposition of the perpendicular polarizer. The stack deposition was performed in 3 steps (Fig. 6.1). (1) The deposition of a low resistance bottom contact (BC; 5 Ta / 50 CuN / 5 Ta / 50 CuN / 5 Ru; thicknesses in nm) in the S1 tool. The Ru layer on top allowed us to maintain the low resistance of the BC after vacuum break since the oxidized Ru is still conductive. (2)

Deposition of the perpendicular polarizer (PMA1) with strong OOP anisotropy (3 Ta / 3 Pt / $[0.4\ \text{Co}\ /\ 0.9\ \text{Pt}]_{\times 2}$ / 0.4 Co / 3 Pt) in the S2 tool. The deposition of the last Pt layer allows for another vacuum break since Pt does not oxidize. It was verified that 3 nm is the minimum safe thickness that prevents the oxidation of the Co layer underneath. (3) After the deposition of the perpendicular polarizer we move again to the S1 tool for the MTJ deposition. However, it has to be considered that the spin diffusion length of Pt is between 1.2 - 3.7 nm at room temperature [197, 198, 199, 200, 201], and so, most of the spin polarization is lost after passing through the 3 nm Pt layer. Therefore, a new perpendicular polarizer (PMA2) is deposited prior to the MTJ with the stack: 0.9 CoFe / 5 Cu to compensate the spin polarization lost while passing through the Pt layer. The CoFe thickness (0.9 nm) was optimized, as will be shown later, and the Cu layer (5 nm) does not de-polarize the current (Cu spin diffusion length is above 36 nm but can go up to 700 nm depending on the reports [202, 203, 204]) and it assures that PMA2 and the MTJ are not strongly coupled. Afterwards, a thin Ta seed layer, the MTJ and capping layers (0.2 Ta / 2.0 CoFeB / $\sim$1 MgO / 2.6 CoFeB / 0.85 Ru / 2 CoFe / 20 MnIr / 10 Ta / 100 CuN / 7 Ru) were deposited sequentially and without vacuum break. An annealing at 330°C with an applied field of 1 T during 2 h was performed in order to assure the epitaxial bcc (0 0 1) crystalline growth of the MTJ that allows large TMR values.

In Fig. 6.2 we show the magnetization curves for (a) PMA1, (b) PM1+PMA2, (c) PMA2 without PMA1 underneath and (d) PMA1 + PMA2 + MTJ of unpatterned samples after annealing. It is clear that the Co/Pt multilayer [PMA1; Fig. 6.2(a)] depicts a strong PMA. The PMA1 + PMA2 magnetization curve also reveals a strong anisotropy indicating that PMA2 depicts OOP magnetization as well (only a small decrease of the coercive field from $\sim$520 to $\sim$450 Oe was observed). Thus, this structure will, in principle, be able to polarize the electrons traveling to the MTJ. One could argue that, since PMA2 has OOP magnetization, PMA1 is not necessary and an in-situ deposition scheme could be used. However, in Fig. 6.2(c) it is shown that the magnetization curve of a structure with PMA2 without PMA1 underneath depicts IP magnetization. The conclusion is that PMA1 is necessary to magnetically couple with PMA2, inducing the OOP magnetization orientation. The magnetization curve of the full structure (with the MTJ) is shown in Fig. 6.2(d). The curve for the field applied in-plane shows that the MTJ has the expected behavior with the rotation of the three magnetic layers (MTJ and synthetic antiferromagnet; black arrows). The magnetic behaviour with the OOP field reveals a more elongated hysteretic curve than in the case of the polarizer without MTJ [Fig. 6.2(b)]. This is most likely a consequence of the effect of the field lines arising from the IP MTJ. Nevertheless, an OPP coercive field of $\sim$150 Oe could still be achieved. Moreover, note that these measurements were performed in unpatterned samples (necessary to have a measurable signal). The nanopillar fabrication is expected to increase further the OOP magnetic component due the reduction of the demagnetizing field.

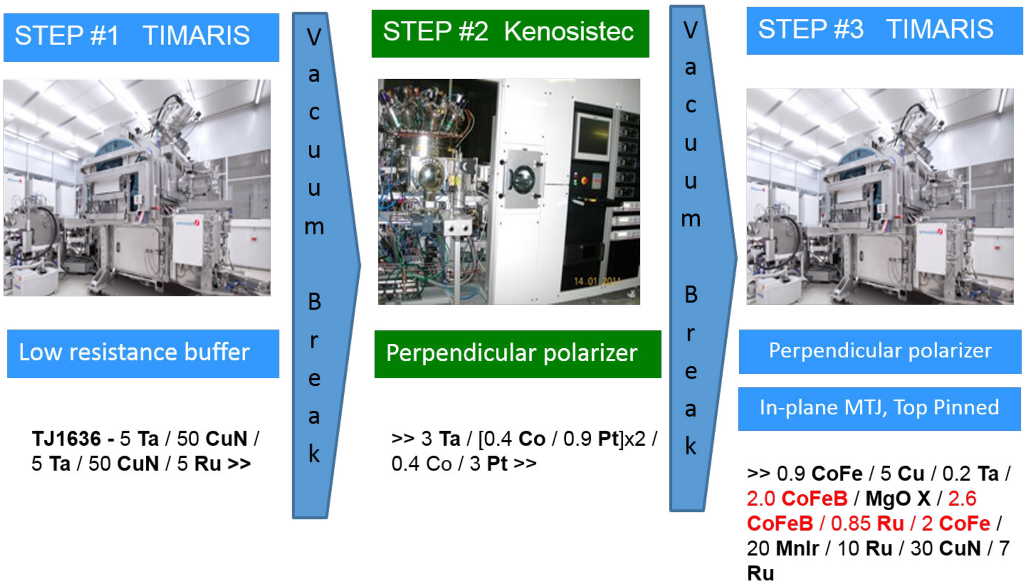

Figure 6.1: Deposition scheme used to obtain an MTJ with homogeneous IP magnetization in conjugation with a perpendicular polarizer. Deposition of the bottom contact (Timaris), deposition of the materials with strong PMA (Kenosistec) and deposition of the second polarizer and the IP MTJ (Timaris).

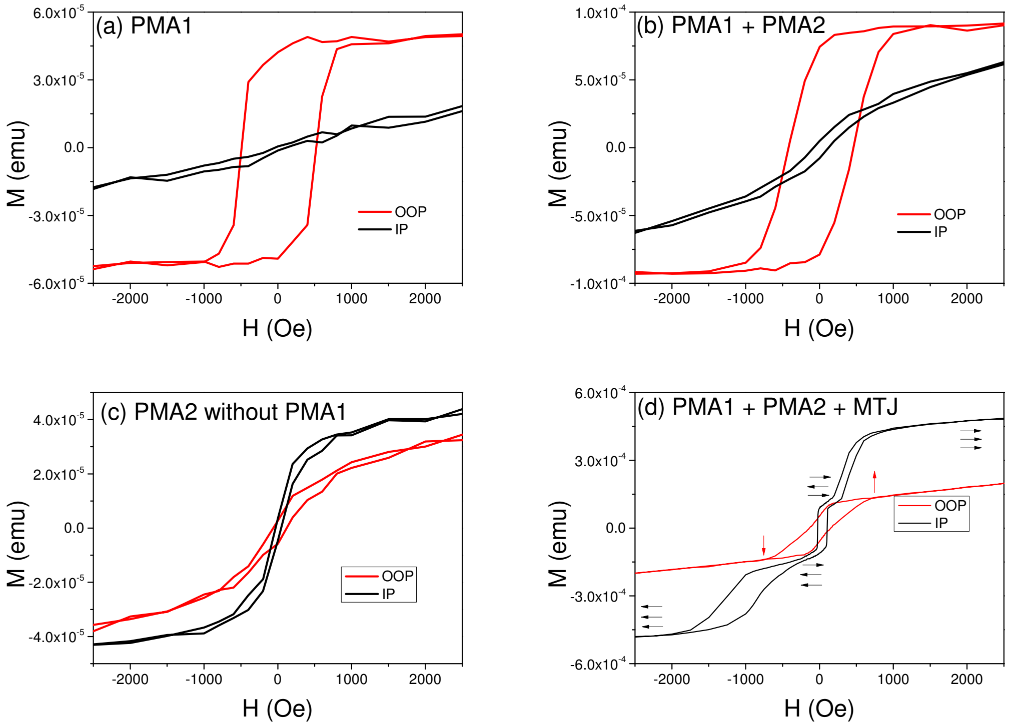

Figure 6.2: Magnetic curves of the polarizers and MTJ. Magnetic moment as a function of the applied magnetic field in the OOP direction (red line) and IP direction (black line) for the (a) PMA1 multilayer (3 Ta / 3 Pt / [0.4 Co / 0.9 Pt]$_{\times 2}$ / 0.4 Co / 3 Pt); (b) PMA1 + PMA2 (0.9 CoFe / 5 Cu); (c) PMA2 without PMA1 underneath; and (d) PMA1 + PMA2 + MTJ (0.2 Ta / 2.0 CoFeB / MgO [13.7 $\Omega\mu m^2$] / 2.6 CoFeB / 0.85 Ru / 2 CoFe / 20 MnIr). All the measurements had a protective layer of 10 Ta (thicknesses in nm) and were performed after annealing. The black arrows represent the magnetization of the FM layers of the MTJ and the red arrows represent the magnetization of the perpendicular polarizer.

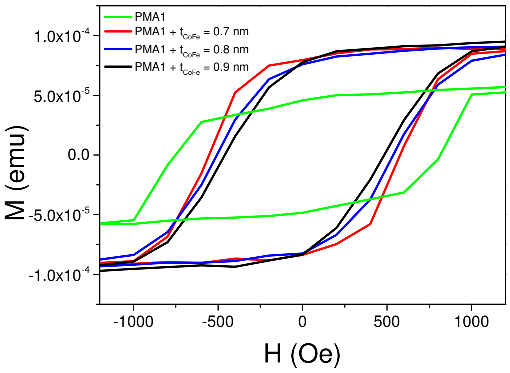

Figure 6.3: Optimization of PMA2. Magnetization curves measured with OOP applied magnetic fields of PMA1 (green line) and PMA1 + PMA2 with different CoFe thicknesses of 0.7, 0.8 and 0.9 nm (red, blue and black line, respectively).

The full polarizer (PMA1+PMA2) was optimized to achieve a significant perpendicular anisotropy, while using the thickest possible PMA2 so that the current is effectively polarized. In Fig. 6.3 the magnetization curves measured in the OOP direction for PMA1 (green line) and PMA2 with CoFe thicknesses of 0.7, 0.8 and 0.9 nm (red, blue and black line, respectively) are shown. As the CoFe thickness increases, the curve becomes more elongated and the coercive field decreases, unveiling a slight decrease of the PMA. However, a relatively thick layer is necessary to fully polarize the current. Hence, the 0.9 nm of CoFe were chosen for PMA2 since it is already relatively thick while maintaining the OOP magnetization.

Besides the magnetic behaviour, it is important to verify that the electric counterpart of the MTJ is functioning with a large TMR in order to retrieve a high output signal from the STNO. To do that, the current in-plane tester (CIPT; section 2.7.1) was used to determine to a good approximation the TMR of the deposited (unpatterned) samples. In Fig. 6.4 we depict the TMR as a function of RA for different types of MTJ stacks and different MgO thicknesses. For all the deposited structures it was verified that the thinner the MgO, the higher the density of defects and worse the crystallinity, leading to a TMR drop. This TMR drop is more accentuated for RA values below 2 $\Omega\mu m^2$. Reference structures without perpendicular polarizer, bottom pinned and with IP magnetization were deposited (5 Ta / 50 CuN / 5 Ta / 50 CuN / 5 Ta / 5 Ru / 20 PtMn / 2 $CoFe_{30}$ / 0.85 Ru / 2.5 $CoFe_{40}B_{20}$ / MgO [X $\Omega\mu m^2$] / 2.0 $CoFe_{40}B_{20}$ / 10 Ta / 30 CuN / 7 Ru). A high TMR above 150% could be obtained in this standard deposition process (black squares). For the stacks incorporating a perpendicular polarizer, a TMR decrease was observed. This occurs because the deposition of the perpendicular polarizer requires vacuum

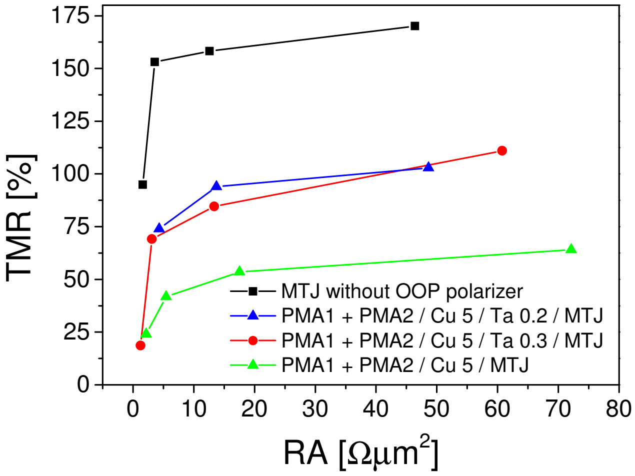

Figure 6.4: Electrical response of the MTJs. TMR as a function of RA for several MTJ stacks: MTJs without perpendicular polarizer (black squares); MTJ with perpendicular polarizer and interface Ta layer with 0.2 nm (blue triangles) and 0.3 nm (red circles).

breaks between depositions leading to the oxidation of Ru and, possibly, partial oxidation of the Pt layer that may alter the surface morphology. Moreover, PMA1 is deposited in a deposition tool with smaller targets and higher vacuum pressure, leading to an increased roughness that induces defects in the MgO barrier, decreasing further the TMR. It was verified that the seed layer (interface between the Cu of PMA2 and the CoFeB of the MTJ) also has a crucial role in the measured TMR. Without this layer, the TMR drops to values below 50% (green triangles). This happens because the Cu layer prevents the proper crystalline growth of the MTJ. An interface layer is thus necessary between the Cu and the CoFeB in order to obtain epitaxial MTJs depicting large TMR. If we introduce a thin Ta seed layer with a nominal thickness of 0.2 nm (blue triangles), a TMR above 90% can be achieved. A thicker Ta layer with a nominal thickness of 0.3 nm was also tried without any noticeable advantage in terms of TMR (red dots). The Ta seed layer is thus necessary to achieve large TMR; however, it will introduce some spin de-polarization. In fact, the spin diffusion length in Ta is estimated to be between 1 - 2.7 nm [205, 206]. Therefore, we chose to use the thinnest Ta layer (0.2 nm) in order to minimize the spin de-polarization of the current coming from the perpendicular polarizer. Such a thin Ta barrier is most likely discontinuous and thus some electrons might even be injected into the FM layer without any interaction with the Ta atoms (preventing de-polarization).

6.3 NANOFABRICATION

After the magnetic and electric optimization of the IP MTJ incorporating a perpendicular polarizer, a stack was deposited on a 200 mm Si wafer and the nanofabrication performed. The deposited stack for fabrication was: 5 Ta / 50 CuN / 5 Ta / 50 CuN / 5 Ru / 3 Ta / 3 Pt / [0.4 Co / 0.9 Pt]$_{\times 2}$ / 0.4 Co / 3 Pt / 0.9 CoFe / 5 Cu / 0.2 Ta / 2.0 CoFeB / MgO [2 × 75 3kW 600 sccm] / 2.6 CoFeB / 0.85 Ru / 2 CoFe / 20 MnIr / 10 Ta / 100 CuN / 7 Ru and the deposition was performed as described previously. The MgO deposition parameters were chosen so that the RA would fall into the optimal region for the output power (P_{out}; 8 $\Omega\mu m^2$) as shown in chapter 4. From the CIPT measurements, we also verified that this RA value depicts a TMR above 80% (Fig. 6.4). In Fig. 6.5 we show the TMR and the RA measured for every fabricated circular MTJ with different diameters (d). This graph shows that larger pillars depict larger TMR and smaller dispersion of the results. This effect is probably associated with some redeposition on the sidewalls, or defects on the MgO barrier (as discussed in chapter 3); note that both effects are maximized for smaller nanopillars. The average RA for the higher dimensions is between 5 - 6 $\Omega\mu m^2$, which is consistent with the presence of a small amount of redeposition (target RA was 8 $\Omega\mu m^2$). Another reason for this small RA variation might be related with the fact that the pillar size can be slightly larger than the nominal one (from the scanning electron microscope images the actual size is $\sim$10 nm larger than the nominal one for 100 nm diameter pillars).

6.4 DC CHARACTERIZATION WITH IN-PLANE FIELDS

If we consider the deposited and nanofabricated magnetic stack (polarizer + MTJ), it is expected that the electrons coming from the polarizer will have a spin polarization orthogonal to the free layer static magnetization. Moreover, when the current direction is reversed, the electrons reflected by the perpendicular polarizer will also depict OOP spin orientation. This will induce a torque in the free layer magnetization that will excite its OOP precession. However, a certain value of critical current (I_C) is required to excite this OOP precession of the free layer magnetization. Moreover, an IP magnetic field applied along the easy axis might suppress the OOP oscillations. Therefore, the OOP precessions are excited for a current above I_C and by increasing the current this region with OOP oscillations becomes broader, until a certain value of the IP magnetic field suppresses it. [86]. During oscillation the average magnetization is pointing in the OOP direction and thus the MTJ resistance should have a value between the one of the parallel (P) and antiparallel (AP) state.

In Fig. 6.6 we show several transfer curves at different positive bias current (I_{bias}; 0.1, 0.5, 1.0, 1.5, 2.0 and 2.5 mA) for a circular MTJ with 200 nm of diameter depicting a TMR of 84%

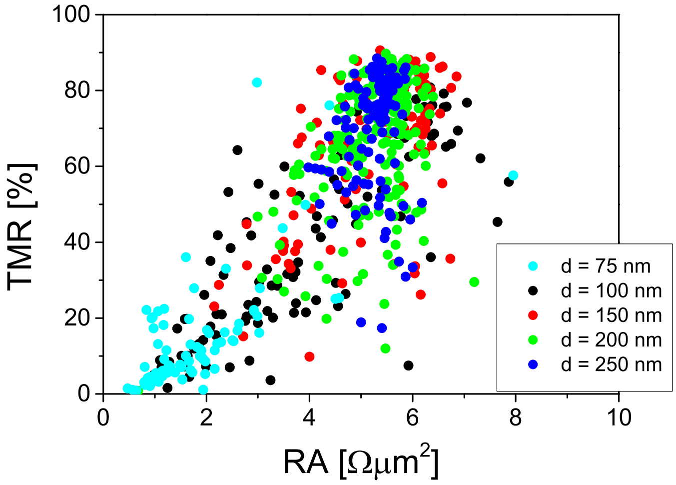

Figure 6.5: TMR and *RA* of the nanofabricated MTJs. Circular MTJs with diameters (*d*) from 75 nm to 250 nm.

(at low I_{bias}) and an *RA* of 4.8 Ωμm^2. Here, positive I_{bias} corresponds to electrons traveling from the polarizer to the free magnetic layer. As I_{bias} increases, the TMR decreases due to the enhancement of thermal effects and the magnetization dynamics. Let us first consider the transfer curves measured at lower I_{bias} (0.1, 0.5 and 1.0 mA). In these cases, a transition between a high resistance (AP) state and a low resistance (P) state was observed. However, if I_{bias} is increased above 1.5 mA, a plateau with an intermediate resistance state appears. This resistance plateau corresponds to a region where the free layer magnetization is tilted (leading to a resistance between the P and AP state) and thus it is one signature of the OOP precession region. This plateau region is observed in different field regions when sweeping from the AP to the P state than the other way around due to the coercivity inherent to the FM free layer. Dipolar stray fields arising from the polarizer might induce further the OOP orientation of the free layer. However, this contribution is not current dependent. One could experimentally determine the role of the perpendicular dipolar stray fields by keeping the polarizer as an extended film and patterning only the MTJ part.

It was observed that the transfer curves measured with negative I_{bias} for the same MTJ pillar, also showed the plateau region but for larger I_{bias} values (absolute value; -2.0 mA). This happens because, in this case, the OOP spin polarization is transferred through the electrons reflected by the perpendicular polarizer. Due to the metallic nature of the polarizer, less electrons are reflected than transmitted and thus the plateau formation requires larger currents.

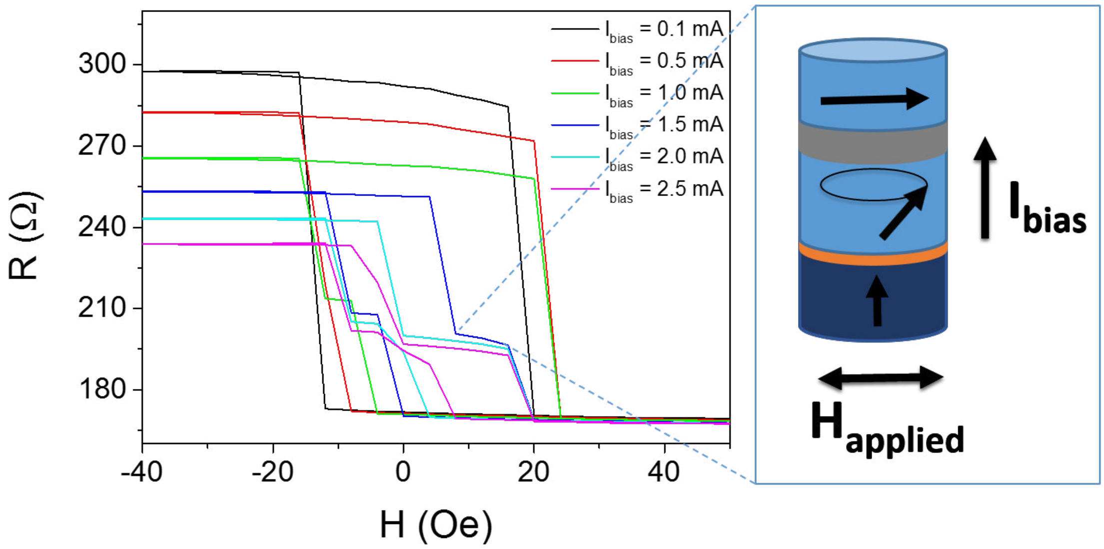

Figure 6.6: Transfer curves as a function of the applied field obtained for positive I_{bias} values (from 0.1 to 2.5 mA). The inset represents the magnetic configuration in the resistance plateau region.

One could argue that the plateau region is caused by the incoherent rotation of magnetic grains or domains. However, the observed bias and field dependence corroborates further the OOP precession mechanism. In Fig. 6.7(a) we show the state diagram of the magnetic states for different values of applied field and I_{bias}. This diagram was obtained by saturating to the AP state (negative fields) for a certain I_{bias} and gradually increasing the IP field. In agreement with Fig. 6.6, larger I_{bias} values lead to the formation of a plateau resistance state. This plateau broadens for increasing current values, corroborating the formation of the region with the OOP magnetization precession of the free layer. A slight asymmetry of these triangular regions is observed, with a broader region for positive bias (electrons traveling from the polarizer to the free layer). In Fig. 6.7(b) we show the resistance of the different magnetic states formed as a function of I_{bias} (average resistance within the magnetic field range for each state), with the plateau region with an intermediate resistance being formed due to the induced OOP oscillations of the free layer.

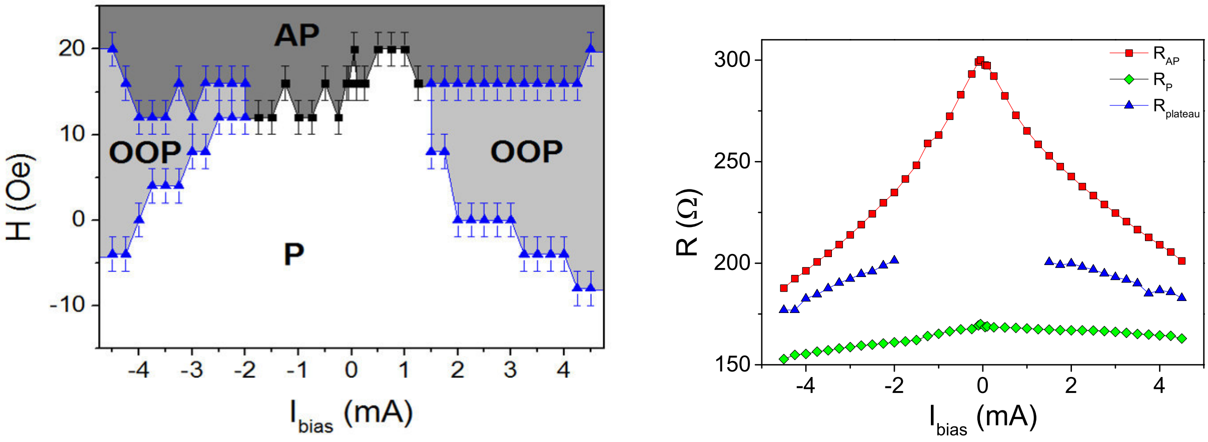

(a)

(b)

Figure 6.7: State diagram of the observed magnetic states. (a) Resistance states observed as a function of applied IP field and I_{bias}. (b) Resistance as a function of I_{bias} for the P, AP and the plateau state.

6.5 RF EMISSION CHARACTERIZATION

To further corroborate the hypothesis of the OOP precession induced by the perpendicular polarizer, we fixed I_{bias} to the highest used value (4 mA) and swept the magnetic field after negative saturation for each measurement. A spectrum was measured for each field value and the integrated non-matched and matched output power was determined. In Fig. 6.8(a) we depict the P_{out} dependence on the IP applied field with maximum values of 60 nW (matched; red squares). Most importantly, it is observed that there is a region where P_{out} is maximized. This region of maximum P_{out} coincides with the field region where the plateau is present [Fig. 6.8(b)]. Note that the formation of another smaller plateau with higher resistance was also observed (-14 to -4 Oe). This plateau is most likely a metastable state where the free layer magnetization is slightly tilted (it is not always present, as can be seen in Fig. 6.6).

In Fig. 6.8(c) we depict the measured spectra for the different values of magnetic field. The plateau region has clearly a larger emission than the P or AP states. Another signature of the effect of the perpendicular polarizer corresponds to a parabolic dependence of the peak frequency with the magnetic field [86]. Although the frequency dependence does not show a fully parabolic behaviour, a curvature of the peak frequency with the applied field was indeed observed, which corroborates further the effect of the polarizer. The tilting of the parabola might be attributed to the current polarization induced by the IP pinned layer of

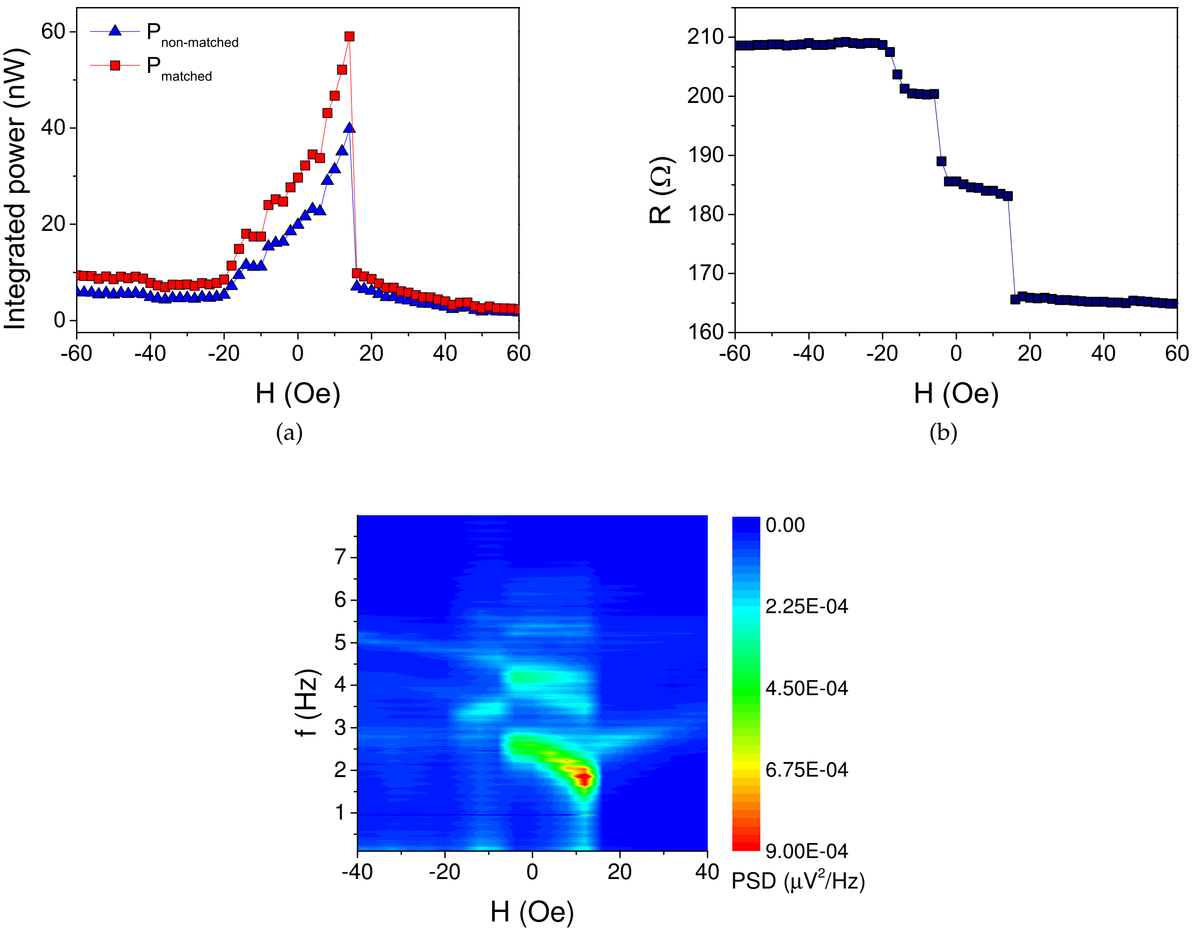

(a)

(b)

(c)

Figure 6.8: Effect of the applied magnetic field on the STNO performance. Field dependence of the STT-induced RF emission for I_{bias} = 4 mA. (a) Integrated output power matched to a load of 50 Ω (red squares) and non-matched (blue triangles), (b) resistance and (c) spectra as a function of the IP applied magnetic field.

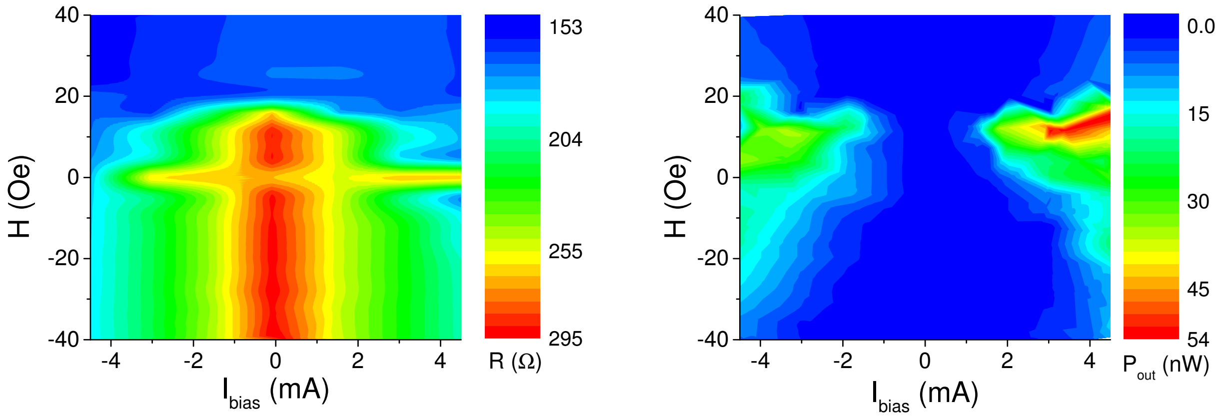

(a) Resistance map.

(b) P_{out} map.

Figure 6.9: Resistance and power correlation. 3D maps of (a) the resistance and (b) integrated matched P_{out} as a function of I_{bias} and applied field.

the MTJ. Despite the frequency behaviour, the linewidth is still large (~ 500 MHz). A similar linewidth was also observed in other characterized STNOs from the same wafer. Moreover, a second smaller peak was also observed (at ~ 4 GHz). This considerable linewidth might be a consequence of the ex-situ fabrication that leads to a non-uniform precession mode. We point out that, since the OOP polarizer enhances the oscillation amplitude, local variations of the polarizer topography or magnetic grains might generate different precession modes within the free magnetic layer and thus generate a large linewidth and additional modes. Also, it is possible that this magnetic configuration generates incoherent magnetic oscillations.

To summarize the effect of the magnetic states on the RF emission, in Fig. 6.9 we plot the 3D map of the resistance [Fig. 6.9(a)] and the integrated matched P_{out} [Fig. 6.9(b)] as a function of the applied magnetic field and I_{bias}. In the resistance map we can identify the AP (P) state for larger negative (positive) fields. As expected, as I_{bias} increases the resistance decreases (due to phonon excitation and magnetic precession). This resistance dependence with I_{bias} makes it more difficult to identify the plateau region from this map. Nevertheless, by comparison with Fig. 6.8(b), it is clear that this plateau corresponds to the cyan region obtained for low positive fields and larger I_{bias} values. If we now compare this map with the P_{out} map, it is clear that the largest output values were achieved in the plateau region.

The low field value necessary to reach the plateau with maximized P_{out} (below 14 Oe) is an important asset of these STNOs. In fact, for other MTJs characterized on the same wafer, the largest P_{out} was obtained without an applied magnetic field. Figure 6.10 depicts (a) a spectra obtained for I_{bias} = 4 mA; and the evolution of key parameters of the measured RF emission [(b) frequency, (c) P_{out}, (d) linewidth and (e) resistance] as a function of I_{bias} for a small applied field (8 Oe). Once again, it is observed that P_{out} increases in the plateau region (resistance decrease for I_{bias} above $\sim$ 2 mA for both polarities).

Concerning the frequency dependence, the expected behaviour corresponds to a linear increase of f with I_{bias} while a uniform precession is present [194]. For larger current values, a non-uniform configuration appears, depicting higher frequency that slightly decreases with I_{bias} [195]. In fact, a frequency jump between modes was observed [86, 195]. This behaviour was not observed in this sample, instead a stepwise increase of f was obtained for positive I_{bias}. The frequency increase (blue shift) is consistent with the OOP precessions [193]. The f increase in discrete jumps might be a consequence of the dipolar interaction field from the polarizer [195]. In respect to the higher f mode expected at higher currents, the peak at 4 GHz [Fig. 6.10(a)] becomes more pronounced for larger I_{bias}. It is possible that this peak corresponds to the higher f mode caused by the non-uniform configuration. Higher I_{bias} (not achievable before MTJ breakdown) would be necessary to confirm this hypothesis. There is also a f and linewidth jump between the AP and the plateau states, which correspond to a change of the precession modes due to the enhanced OOP precession. Large linewidths (above ~ 500 MHz) were observed.

It is usually possible to estimate the critical current density for STT-induced magnetic precession (J_{STT}) by identifying the deviation from the linear dependence of the inverse power on I_{bias} [207, 94, 158, 78]. This estimation is performed using the inverse power value measurements performed in the thermally activated precession region [as shown in Fig. 4.5(a)]. Since the OOP precessional state is obtained for both polarities, such calculation could not be performed for this mode. One can thus consider that the critical current for the OOP state occurs in the transition to the plateau region at 1.8 mA (critical current density of 5.73×10^6 A/cm^2). Nevertheless, it is possible to use the inverse power to estimate J_{STT} for the IP precessions with smaller P_{out}. A value of 8.57×10^5 A/cm^2 was obtained, which is in line with the results of section 4.6.

Hence, it was shown that different magnetic states could be achieved depending on I_{bias} and applied field. The state diagram is mostly in agreement with the macrospin picture for an IP magnetized free layer in conjugation with a perpendicular polarizer [194]. It is also expected the formation of an OOP stable state after a certain current threshold. In this state, the magnetization is pointing in the OOP direction (without significant precession). In fact, micromagnetic simulations showed the possibility to achieve a vortex configuration with this structure [195]. The larger P_{out} values in the GHz range at the plateau region indicate that such states were not achieved in this device.

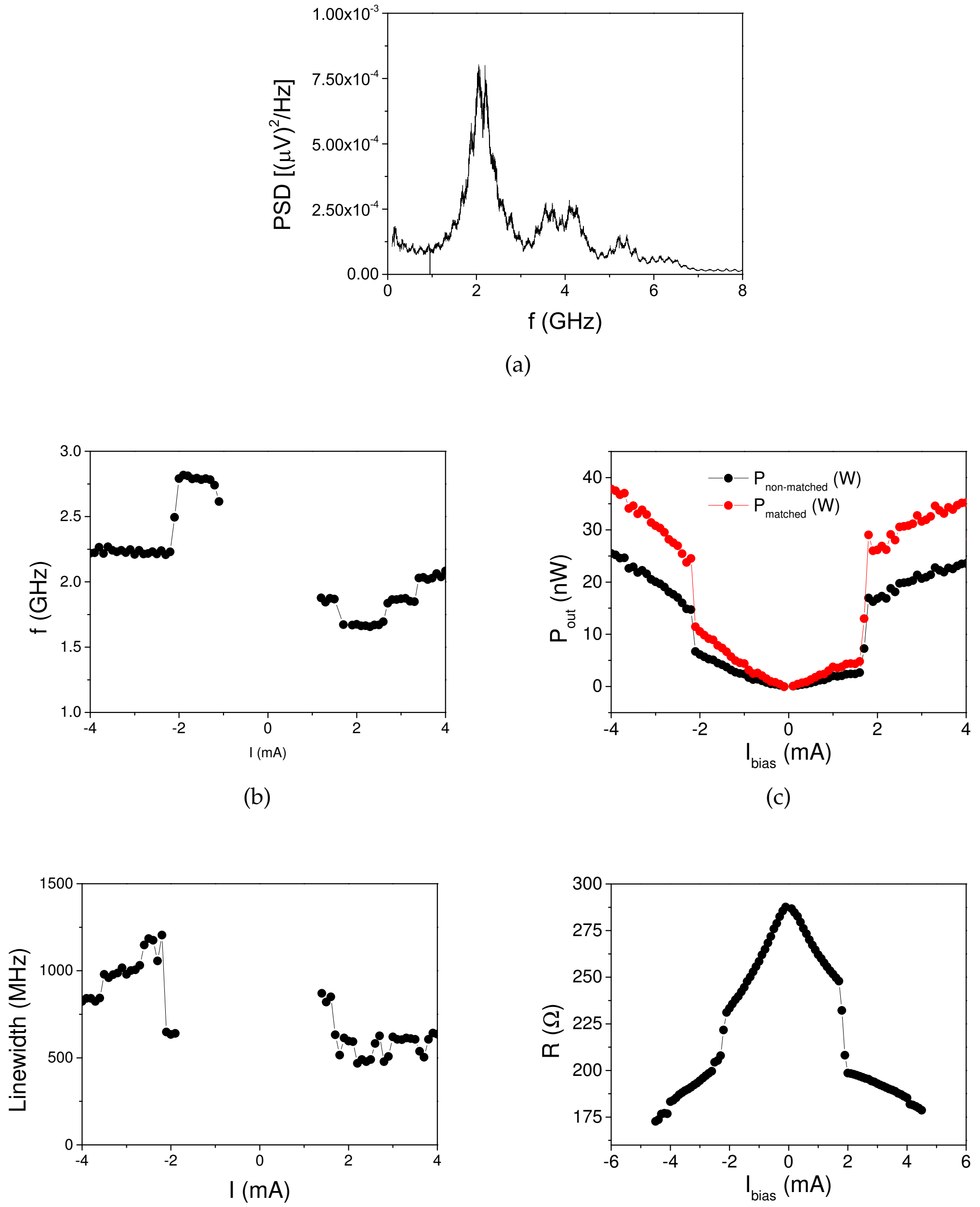

(a)

(b) (c)

(d) (e)

Figure 6.10: RF emission characterization. (a) Power spectral density (PSD) measured at I_{bias} = 2 mA. (b) Frequency, (c) integrated matched (black dots) and non-matched (red squares) P_{out}, (d) linewidth and (e) resistance a function of I_{bias}. No magnetic field was applied.

Note that several STNOs were characterized, with the majority of them depicting the plateau formation. The increase of P_{out} in the plateau region was also observed in some cases (but not in all the measured STNOs). It is possible that in the pillars where the plateau state does not lead to an increase of P_{out}, a perpendicular stable state is achieved. Further work is still necessary to confirm this hypothesis [194]. Other MTJ structures depicted results similar to the ones shown here. It was also verified that smaller pillars were not advantageous to obtain a macrospin behaviour, possibly due to the increased density of defects.

6.6 CONCLUSIONS

An ex-situ deposition process was successfully used to obtain IP MTJs incorporating a perpendicular polarizer. This deposition scheme takes profit of two deposition tools: one for the deposition of high quality MTJs and another, incorporating a Pt target, for the perpendicular polarizer deposition. The development of such configuration required the optimization of the magnetic and electric counterparts of the stack. After nanofabrication, these structures depicted low RA (5 - 6 Ω μm^2) and large TMR (up to ~ 90%). The presence of plateau states, with resistances between the P and the AP states, were observed. These plateau states are a signature of the OOP magnetization precession of the free layer. It was shown that P_{out} was maximized (up to 60 nW) in the plateau region. These observations strongly suggest that the perpendicular polarizer is effectively polarizing the current injected into the MTJ. Moreover, the state diagram of the different magnetic states as a function of I_{bias} and IP applied field could be built. Besides the interesting physical behaviour, it was also observed that the largest P_{out} was obtained for low applied magnetic field, which represents a significant asset for practical applications of STNOs.

7

EXPLORATORY PATH TOWARDS THZ SPINTRONICS

As it has been shown in the previous chapters, the principle of functioning of the spin transfer nano oscillators (STNOs) relies on the conversion of the magnetic dynamics into an electrical signal due to magnetoresistive (MR) effects. In that respect, the correlation between the real-time dynamics of the magnetic and electric counterparts is relevant for understanding spintronic phenomena and, in particular, STNOs. Moreover, in the scope of this thesis, the frequency domain was almost always used to characterize these oscillators. Thus, a complementary approach based on time domain measurements is also of interest. Despite the fact that electrical techniques allow measurements in the time-domain, the sub-ps range is still only accessible using optical techniques. Therefore, the main goal of this work was to determine how the electrical and magnetic dynamics correlate in spintronics materials. This fundamental study was performed using different optical characterization tools. This work was performed in the Institute for Molecules and Materials (IMM) in the Netherlands under the supervision of Dr. Alexey Kimel and involved the development of setups for spectral measurements (with the help of Tonnie Toonen), for magneto-optical Kerr effect (MOKE) measurements (with the help of Dr. Ilya Razdolski) and for THz-time domain spectroscopy (TDS) setup (with the help of Thomas Huisman and Dr. Rostislav Mikhaylovskiy) and the measurements reported in this chapter. Due to the exploratory nature of this work, we chose the simplest possible structures depicting MR and thus magnetic tunnel junctions (MTJs), which consist on a multilayered system, were not studied here. Instead discontinuous metal-insulator multilayers (DMIMs) that depict tunnel magnetoresistance (TMR) values at room temperature (RT) up to 7% were used. These structures consist on $Co_{80}Fe_{20}/Al_2O_3$ multilayers, where the CoFe thickness is varied so that for some values it is discontinuous and the electrons tunnel between CoFe grains, leading to MR effects.

The THz-time domain spectroscopy (TDS) setup was the spectroscopic tool of reference used in the work described in this chapter. The THz (10^{12} Hz; corresponding to 4.14 meV) are the typical energy range of electronics intraband transitions, thus allowing the probing of the charge carrier dynamics. Moreover, the wavelengths in the optical region of the spectrum are sensitive to the magnetization. Therefore, by using the THz-TDS and the optical pump-probe setups we were able to characterize and correlate the electric and the magnetic counterparts of the studied samples. However, the THz transmission could only be measured with the sample with thickest and continuous CoFe layers (with negligible TMR). Nevertheless, by performing temperature dependent measurements, we were able to correlate electrical resistance and THz transmission. Furthermore, the Maxwell equations were used to associate the THz emission spectrum to the measured magnetic dynamics. The good agreement obtained supports the hypothesis that the THz emission originates from the ultrafast laser-induced demagnetization. These results pave a way to THz probing of the MR state and push spintronics to the THz regime.

7.1 ULTRAFAST CHARGE AND MAGNETIZATION DYNAMICS

The demand for ever faster and energy efficient data processing has continuously fueled applied and fundamental research on magnetism over the last decades and resulted in the emergence and rapid development of spintronic technology [208]. At the same time, the engineering of spintronic devices operating at THz frequencies remains a major challenge, [209, 210] that can be met by the optical manipulation of spins at sub-picosecond timescales. In fact, there is a strong need for STNOs working in the THz regime, although, this field of research is still on its infancy [211].

One of the most efficient ways to study ultrafast dynamics of magnetic materials and structures is based on the pump-probe technique, in which ultrashort optical laser pulses are used to induce and probe magnetization dynamics [212]. With the help of pump-probe techniques many exciting phenomena have been demonstrated, such as ultrafast demagnetization [213], coherent manipulation of spins with the help of circularly polarized light [214] or helicity dependent all-optical magnetic switching [215]. Such studies of the magnetic dynamics have gained renewed importance with the development of practical applications that rely on these dynamics to operate, being one of the most relevant cases the technologies that exploit the spin transfer torque (STT) effect (STT controlled magnetic random access memories and STNOs).

At the same time, THz time domain spectroscopy (TDS) [216] is a technique that has been broadly used to characterize material properties in the THz spectral region. In fact, since this frequency range corresponds to the characteristic energy of electronic intraband transitions [217], it allows the probing of charge carrier dynamics. There are several known examples of this kind of studies for bulk semiconductors and semiconductor nanostructures [218, 219, 220, 221, 222, 223]. Moreover, THz-TDS can be used to investigate magnetic phenomena, like ultrafast demagnetization [224, 225], precessional modes of magnetic sublattices [226, 227, 228], as well as novel phenomena for the generation and control of ultrafast electrical currents [229, 230].

Despite the amount of reports on either ultrafast spin dynamics or THz-TDS, the combined investigation of the dynamics of spins and charges in technologically relevant materials is still scarce [231, 232]. The conjugation of both measurements in materials that depict magnetoresistance may elucidate the role of the electrical and magnetic counterpart in transport phenomena and even push spintronics to the THz region. Here, we study how charges (i.e. free electrons) and spins respond to ultrafast stimuli such as an electric field at THz frequencies or a femtosecond laser pulse in CoFe/Al_2O_3 multilayered structures. These nanometric layers are widely used in the fabrication of spintronic devices, such as magnetic tunnel junctions [10, 233]. The main objective of this work consisted in establishing a bridge between the magnetic dynamics and the resistance counterpart in relevant materials for spintronics applications. Since the principle of functioning of the STNOs consists on the conversion of the magnetic dynamics into voltage oscillations, a deeper knowledge of how the electric and magnetic counterparts are correlated is interesting for the study of this type of devices. Certainly, the THz regime (10^{12} Hz) is considerably faster than the GHz regime (10^9 Hz). However, it was not the objective of this study to observe the real time dynamics induced by the STT effect, but instead to get insight on the relation between magnetic and electrical dynamics.

7.2 GRANULAR SAMPLES

Due to the exploratory nature of this task, our main objective was to study simple materials depicting MR. A multilayered structure such as MTJs or spin valves were thus not ideal since the emitted signals might correspond to different layers (only very recently some results have been reported regarding THz transmission on spin valves [232]). Thus, a set of $[Co_{80}Fe_{20}$ $(t)/Al_2O_3$ (3 nm)$]_{\times 10}$ multilayers that were prepared by ion beam sputtering on 0.7 mm thick glass substrates in a Nordiko 3000 tool were used (their static magnetic and electrical properties were reported previously [234, 235, 236]). The values of nominal CoFe thickness t are 1.0, 1.1, 1.2, 1.4, 1.6 and 1.8 nm. For the smaller values of t (from 1.0 to 1.6 nm) the CoFe layer is organized as a granular layer [Fig. 7.1(a)]. These type of structures are known as discontinuous metal-insulator multilayers (DMIMs). Despite their simplicity, these type of structures display interesting properties for spintronics applications. For instance, tunnel magnetoresistance (TMR) of 7% at RT for optimized composition and nanogranular structure, with special sensitivity to low (or moderate) magnetic fields, were reported. The structure with thickest CoFe (1.8 nm) is already a continuous layer [234].

7.3 SPECTRAL MEASUREMENTS

To access distinct properties of the materials, different wavelengths can be used. For instance, the THz range can be used to extract information regarding the charge carriers while the optical part is used to access the magnetization. The probing of the magnetization is performed using MOKE, which consists in the rotation of the light polarization after reflected

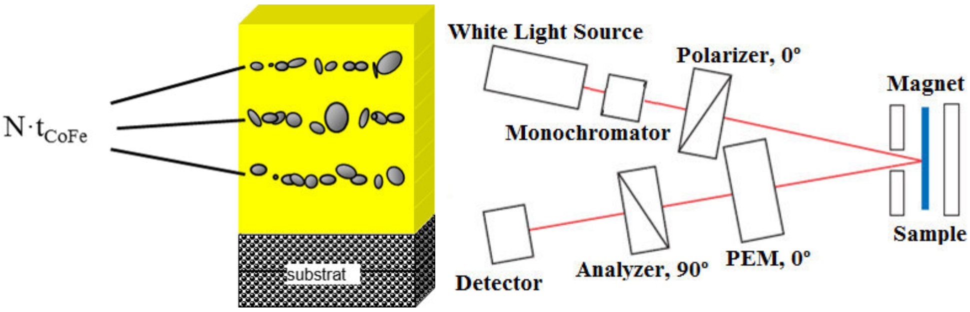

(a) DMIM samples

(b) Spectral MOKE setup

Figure 7.1: Samples studied and used setup. (a) Schematic representation of the DMIM. The yellow part represents the Al_2O_3 and the grey structures the granular CoFe. (b) Representation of the setup used to perform spectral MOKE measurements.

by a magnetic surface. This effect is broadly used to investigate magnetic materials (in static magnetization loops, pump-probe techniques and even as a microscopy tool). However, even within the optical region of the spectrum, the MOKE rotation angle of the polarization might depend on the used wavelength. On top of that, the dependence of the MOKE rotation with the used frequency might also reveal insights on the magnetic properties of the samples. Such magnetic and spectral correlation is still mostly unexplored territory.

Therefore, as a first characterization tool for the studied samples, we developed a spectral MOKE setup [Fig. 7.1(b)] [237] incorporating a white light source and a monochromator to control the used wavelength. The light is then polarized and reflected by the sample. Then, a photo-elastic modulator (PEM) is used to modulate the polarization of the light for a certain frequency f. After that, using the analyser and the detector, three voltages are measured: V_{DC}, V_{1f} and V_{2f} for the continuous, at frequency f and $2f$, respectively. Using the ratios between the DC and the AC terms, we can measure quantities that are not affected by light intensity fluctuations, changes in the transmission, among others. The MOKE rotation (θ_k) and ellipticity (ε_k) can then be calculated using [237]:

$$\theta_k = \frac{\sqrt{2}}{4J_2}\frac{V_{2f}}{V_{DC}}, \tag{7.1}$$

and

$$\varepsilon_k = \frac{\sqrt{2}}{4J_1}\frac{V_{1f}}{V_{DC}}, \tag{7.2}$$

where J_1 and J_2 are, respectively, the first and second order terms of the Fourier expansion of the light intensity that can be extracted by ramping the intensity values. Both θ_k and ε_k give

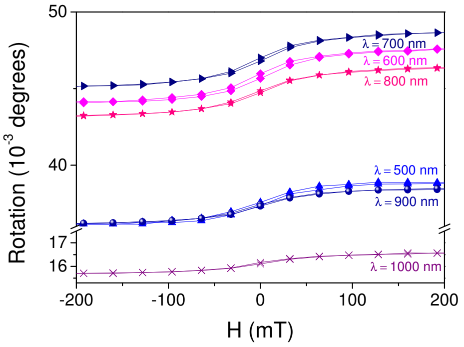

(a) t = 1.0 nm

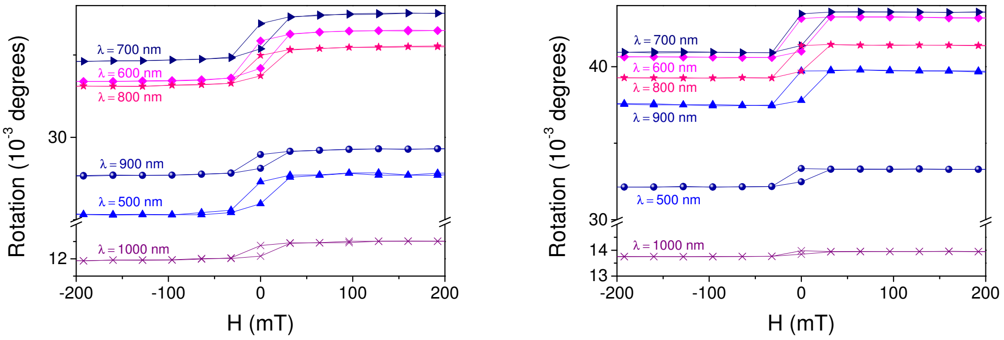

(b) t = 1.6 nm

(c) t = 1.8 nm

Figure 7.2: MOKE rotation as a function of the magnetic field measured for different wavelengths and (a) t = 1.0, (b) 1.6 and (c) 1.8 nm.

information regarding the magnetization of the sample (in-plane and out-of-plane component, respectively). Here, we extracted the MOKE rotation using Eq. (7.1) for different wavelengths. Figure 7.2 shows magnetization curves measured for different wavelengths for samples with CoFe thicknesses of t = 1.0 , 1.6 and 1.8 nm [Figs. 7.2(a), (b) and (c), respectively]. It is clear that different wavelengths lead to different values of MOKE rotation. Moreover, it was observed that the nominal thickness of the CoFe layer leads to different magnetic behaviours. In fact, for t = 1.0 nm a superparamegnetic behaviour was observed, while for the remaining values a ferromagnetic behaviour was obtained. This behaviour is in line with the reported properties of these samples [234].

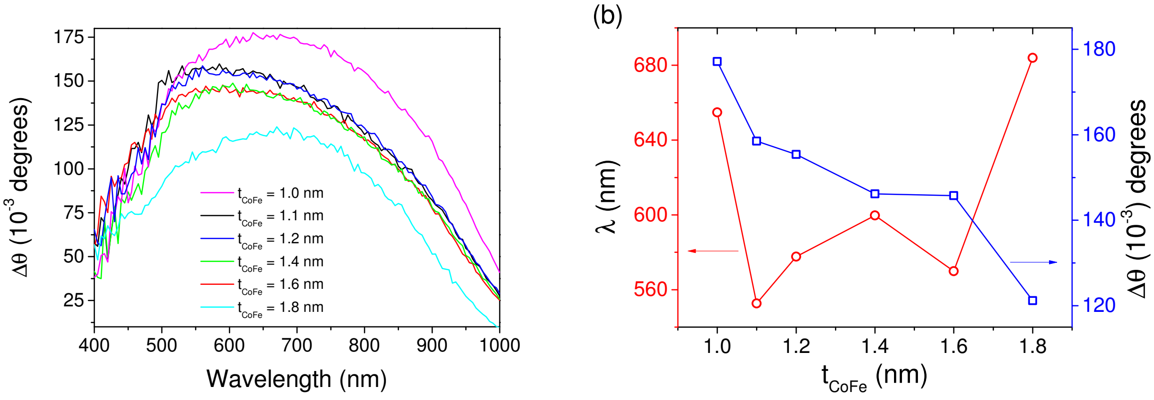

Figure 7.3: Spectral MOKE measurements. (a) MOKE rotation difference between the high and low resistance state as a function of the wavelength for all the samples. (b) Maximum MOKE rotation and corresponding wavelength as a function of the CoFe thickness.

A systematic study of the MOKE rotation as a function of the wavelength for all the samples was then performed. More precisely, the angular MOKE rotation as a function of the magnetic field from 400 nm to 1000 nm (with 5 nm steps) was determined [Fig. 7.3(a)]. The obtained MOKE rotation was larger in these measurements (when compared to those shown in Fig. 7.2) because the alignment was improved between measurements. The observed dependence of the maximum MOKE rotation with the CoFe thickness [Fig. 7.3(b)] reveals some interesting features. First, the MOKE rotation (blue squares) decreases with increasing CoFe thickness, which indicates that the rotation of the polarization depends not only on the quantity of magnetic material but also on its magnetic properties. Moreover, the value of frequency that maximizes the MOKE rotation (red circles) revealed a trend that depends on the magnetic and structural properties of the samples. More precisely, the samples with t between 1.1 and 1.6 nm reached the maximum rotation for lower frequency values. On the other hand, the samples with t = 1.0 and 1.8 nm reached this maximum for higher frequency values. Note that the sample with t = 1.0 nm is the only displaying a superparamegnetic behaviour, being all the others ferromagnetic. Furthermore, the sample with t = 1.8 nm has a continuous CoFe layer, whereas the others have a granular structure. These features indicates that the spectral response of the MOKE rotation depends on both the magnetic and structural properties of the samples. Hence, this tool can in principle be used as a simple characterization tool of magnetic and structural properties. A deeper study of these spectral dependence was not performed since the main focus of this work consisted on the characterization of the carrier dynamics using THz-TDS.

7.4 THZ - TIME DOMAIN SPECTROSCOPY (TDS) SETUP

The THz spectrometer used for these measurements was based on a Ti:Sapphire regenerative amplifier which generates 50 fs laser pulses at the central wavelength of 800 nm with a repetition rate of 1 kHz and a pump fluence of 1 mJ/cm^2. A schematic representation of the THz-TDS setup is shown in Fig. 7.4. Two different configurations were used with very few modifications: one for THz transmission measurements (shutter open) and another for THz emission measurements (shutter closed). The red line represents the optical beam and the yellow the THz field. Small holes in the parabolic mirrors allow the optical beam to pass without significant loss of the THz field. The optical laser is divided in three branches: one for detection (1), one for THz generation (2) and one for optical pump excitation of the sample (3). For the measurements we employed an electro-optical detector which allows us to determine the THz electric field. The electro-optical linear effect generates birefringence in materials with inversion symmetry upon the application of an electric field. In this case, the THz radiation induces the birefringence causing the rotation of the optical probe polarization. The THz signal is thus measured by resolving the polarization of the optical probe [238]. In the transmission measurements a THz emitter (a ZnTe crystal) is excited generating THz radiation. This radiation is focused on the sample and one can study how the THz transmission of the sample changes as a function of the optical pump delay time. In the case of the THz emission measurements, the optical beam that would lead to the THz radiation of the ZnTe crystal is blocked and one can study the THz emission of the sample itself. The optical pump was focused onto the sample at normal incidence. The THz waves emitted from the optically pumped sample were measured after propagating through the glass substrate of the sample. An optical filter (transparent to THz radiation) was used to block the optical pulses. The purge box that involves the measurement setup was used to avoid the presence of water molecules that absorb THz radiation (N_2 was injected into the box). A cryostat was used to change the temperature of the sample from 300 to 15 K; the cryostat was only used in the temperature dependent measurements, the remaining experiments were performed at room temperature. A schematic representation of the magnetic field direction applied during the measurements is also shown in Fig. 7.4.

The full set of samples were measured using the THz-TDS setup (both in the emission and transmission mode). It was observed that the the emission results were similar to all the measured samples but with a higher signal for the sample with the thickest CoFe (t = 1.8 nm). As for the transmission measurements, only the sample with the thickest and continuous CoFe depicted a variation of the THz transmission upon optical pump incidence. The reason for this lack of THz transmission variation for the remaining samples may be due to the fact that the signal was too small to be measured or because the continuous multilayers have a

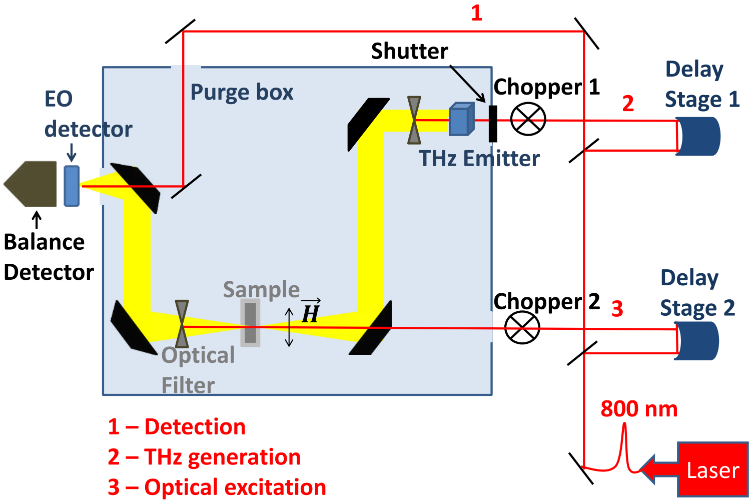

Figure 7.4: Schematic representation of the THz-TDS setup. The inset shows how each optical beam is used (1 - detection, 2 - THz generation and 3 - optical excitation).

different behaviour. Further investigation with different granular samples would be necessary to clarify this issue. Therefore, from now on, the shown results only concern the sample with continuous CoFe layers (t = 1.8 nm).

7.5 OPTICAL PUMP-PROBE TECHNIQUE

In order to probe the ultrafast magnetization dynamics, a time-resolved stroboscopic magneto-optical pump-probe technique was employed [239]. A Ti:sapphire laser system in combination with an amplifier was used to generate laser pulses similar to the optical pump used in the THz measurements with a repetition rate of 250 kHz (and the same pump fluence of 1 mJ/cm^2). The same pulse was used as optical probe but with a beam intensity at least 100 times lower.

7.6 THZ TRANSMISSION

With the aim of understanding to what extent THz transmission measurements can serve as a probe of transport properties in CoFe/Al$_2$O$_3$ multilayers at THz frequencies, we measured the THz transmission through the multilayer structure as a function of temperature T. In order

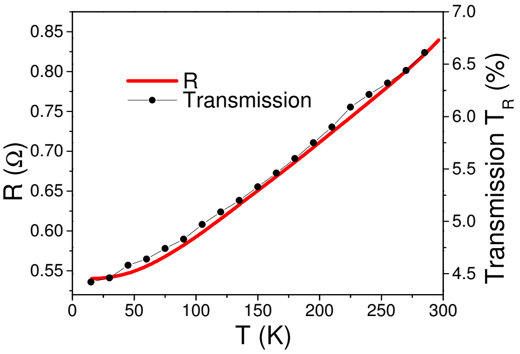

Figure 7.5: THz transmission (T_R) and resistance (R) as a function of temperature. The black dots represent the THz transmission normalized to the transmission of the substrate and the red line the resistance behaviour for the same sample as reported elsewhere [234].

to deduce the signal originating from the CoFe/Al_2O_3 multilayer, we normalized the electric field transmission of the sample with that of the substrate. The result is shown in Fig. 7.5 (black dots). One sees that the THz transmission through the CoFe/Al_2O_3 multilayer increases with temperature. This can be understood if one assumes that the transmission is dominated by the real part of the electric conductivity. As temperature decreases, the scattering rate of free electrons becomes smaller thereby leading to an increase of the conductivity and thus a decrease of the transmission of the electromagnetic radiation at THz frequencies. There is a remarkable correlation between the temperature dependencies of the THz transmission with the DC electrical resistance, see Fig. 7.5. This finding confirms that the THz transmission can serve as a probe of the transport properties of spintronics materials at THz frequencies.

To understand if it is possible to control the transport properties of the multilayer structure with the aid of a femtosecond laser pulse, we performed time-resolved pump-probe measurements in which the sample was first excited by a 50 fs laser pulse and the laser-induced changes were probed with a pulse of THz radiation. Varying the delay between the pump and probe pulses we measured how the maximum electric field of the transmitted THz pulse changes as a function of the delay. The results are shown in Fig. 7.6(a), where the change in the transmission is measured with respect to the transmission without pump pulses present. It is seen that the femtosecond laser excitation can indeed cause ultrafast dynamics of the THz transmission. In particular, the time-resolved measurements reveal three different regimes of the dynamics: the steep change of the THz transmission on a time-scale of ~500 fs, a fast decay on a time-scale of ~0.8 ps and a slower relaxation with the characteristic time of about 140 ps. The dynamics can be understood using the two-temperature model, which describes the temporal evolution of the system in terms of two coupled reservoirs of energy representing free electrons and lattice, respectively [240]:

$$C_e(T_e)\frac{dT_e}{dt} = -G(T_e - T_l) + P(t), \tag{7.3}$$

and

$$C_l(T_l)\frac{dT_l}{dt} = G(T_e - T_l), \tag{7.4}$$

where C_l and C_e are heat capacities of the lattice and the electrons, respectively. T_l is the lattice temperature, T_e is the temperature of the electrons, G the electron-lattice coupling factor and $P(t)$ the laser heating source. When an intense 50 fs laser pulse is absorbed in the medium, its energy is transferred to the electron gas, increasing its temperature/energy. This leads to an increase of the scattering rate and results in a decrease of the conductivity. As a result, the THz transmission increases and, as can be seen from the experiment in the studied materials, this increase occurs faster than 0.5 ps (τ_0 < 0.5 ps). From the differential equations it is seen that the time-scale of the process is defined by the time dependence of the source $P(t)$. After that, due to electron-phonon coupling, the electrons will effectively transfer their energy to the lattice on a time-scale below 1 ps ($\tau_1 \sim$ 0.8 ps) [241, 242]. Phenomenologically, we were able to describe the transmission change due to a pump pulse using:

$$\frac{\Delta T_R}{T_R} = [0.5erf(\frac{t}{\tau_0} - 0.5)][A_1exp(-\frac{t}{\tau_1}) + A_2exp(-\frac{t}{\tau_2})], \tag{7.5}$$

where τ_0 is the rise time of the error function, A_1 and A_2 are exponential amplitudes, and τ_1 and τ_2 are exponential decay times. The first term between brackets in Eq. (7.5) describes the sudden change in the resistivity, while the exponential decays account for the different relaxation processes. The function described in Eq. (7.5) can perfectly describe our photo-induced transmission change, as shown by the solid line in Fig. 7.6(a). The decay time τ_1 can be interpreted as the characteristic time of the electron-phonon coupling, the strength of which is described by the factor G [see Eqs. (7.3) and (7.4})]. The observed decrease of the THz transmission originates from an increase of the THz conductivity and indicates that this electron-lattice thermalization leads to a temperature decrease of the system. One should point out that the resistance of a metal is governed by both electron-electron and electron-phonon scattering. It is expected that the electron-electron scattering rate is proportional to T^2, while the electron-phonon scattering rate is proportional to T^5 [243]. Thus, it is not obvious at the first sight that the conductivity should increase and the THz transmission drop as the electrons transfer energy to phonons. The conductivity increase on a time-scale of the electron-phonon interaction can be assigned to the fact that the drop in the electronic temperature is substantially larger than the increase in the phonon temperature. After the temperatures of the electrons and the lattice are equilibrated, the whole excited area will cool down on the time-scale of the heat-transfer ($\tau_2 \sim 140$ ps). Therefore, τ_2 is assigned to the cooling of the lattice, which results in the coupling of the lattice to an infinite reservoir at room temperature and is not explicitly shown in this restricted two-temperature model. As the electron scattering decreases (due to electron-phonon coupling and heat transfer) the conductivity increases and thus the THz transmission decreases. This behaviour is consistent with Fig. 7.5.

In Fig. 7.6(b) we show τ_1 and τ_2 as a function of temperature; τ_0 appears to be temperature independent ($\tau_0 \sim 0.16$ ps). The fast recovery (τ_1) on a sub-ps time-scale is nearly independent of the sample temperature, whereas the slow cooling rate (τ_2) increases by almost 15% when going from 300 to 15 K. Since τ_2 corresponds to the characteristic time of the longer thermal relaxation process, as the temperature increases, the thermal relaxation is more efficient and τ_2 decreases. On the other hand, τ_1 (which is related to the electron-phonon coupling) is independent on the temperature since it is mainly affected by the ultrafast heating caused by the optical laser pulse. As for the exponential decay amplitudes of the transmission (A_1 and A_2), a decrease is observed with increasing temperatures [Fig. 7.6(c)]. This result is expectable since, for high temperatures, the transmission limit is enhanced and thus the decay amplitudes decrease.

Measurements with different in-plane magnetic fields were also performed (not shown). For the best sensitivity of our setup we could not detect any dependence of the THz transmission, with or without pump, on the magnetic field. This is probably related with the small magnetoresistance exhibited by this sample [234]. Furthermore, while MR effects are claimed to be abundantly observed in the mid-infrared optical range [244, 245, 246, 247], less is known for the THz spectral range [248, 249, 250].

7.7 THZ EMISSION

To understand the effect of the optical pump on the CoFe/Al_2O_3 multilayer structure we also studied THz emission from the sample after it has been excited by a femtosecond laser pulse at room temperature. Figure 7.7(a) shows the THz emission waveforms measured at different azimuthal angles (θ) between magnetization and the axis of the electro-optical detector (polarization of the detection beam). The polarization of the detection beam was maintained constant and the sample rotated. In order to elucidate the origin of the emission, we performed the measurements for different orientations of the magnetization with respect to the axis of the detector. Although we clearly observe THz emission when the polarization of the detector axis and the magnetization are orthogonal, no THz emission is observed with the axis parallel to the magnetization. To reveal the full angular dependence we measured the strength of the electric field of the emitted THz radiation as a function of the angle θ between the detector axis

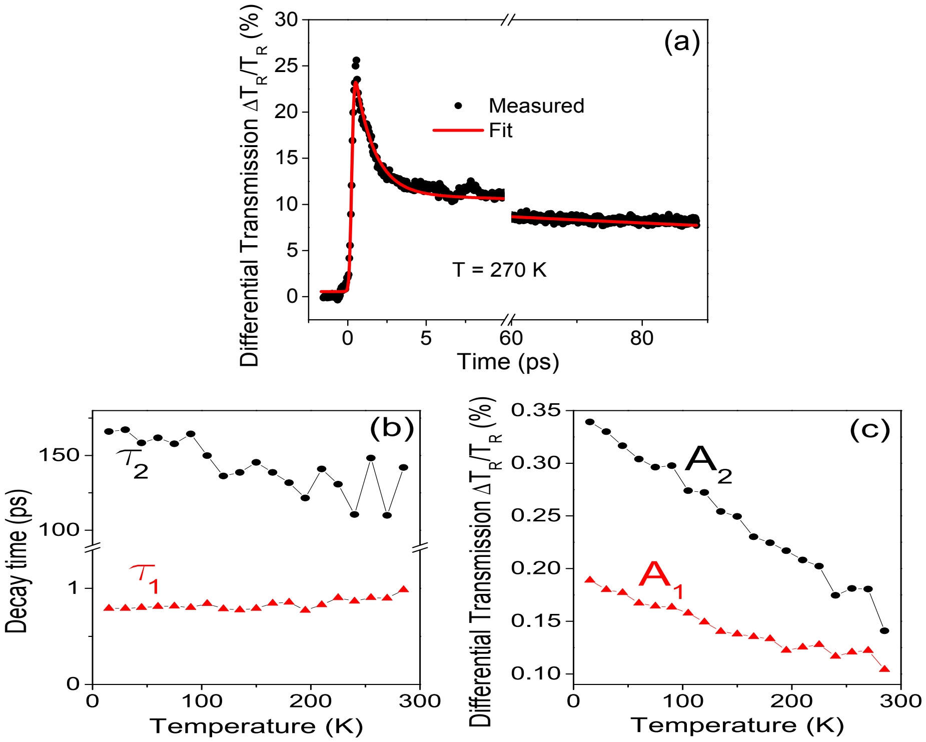

Figure 7.6: Change in THz peak transmission after an incident optical pump pulse. (a) The change in THz transmission (relatively to the transmission without the pump pulse, $\Delta T_R/T_R$) can be fitted with Eq. (7.5). (b) Characteristic times and (c) amplitude of the decays of the photo-induced transmission change during the fast recovery (τ_1) and the slow cooling rate (τ_2).

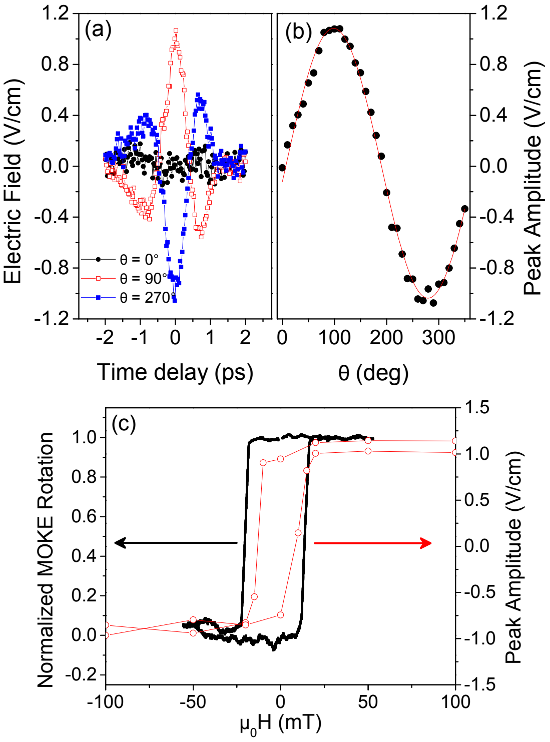

Figure 7.7: Ultrafast demagnetization results in THz emission. (a) THz emission for different azimuthal angles θ. (b) Experimental peak intensity as a function of θ (dots) and respective sinusoidal fit (line). (c) Comparison between the near-infrared MOKE rotation and the THz peak amplitude as a function of the applied magnetic field.

and the magnetization. Figure 7.7(b) reveals a periodic dependence which can be accurately fitted with a sine function. A similar sinusoidal relation to the laser-induced THz emission was already observed in Fe [251] and Ni films [224]. While the former report claimed that this emission is generated by an optical nonlinearity due to symmetry breaking at the surfaces of the films, the latter suggests that the THz emission originates from the ultrafast laser-induced demagnetization of the metallic magnet. Indeed, it follows from Maxwells's equations that a time varying magnetization (M) results in the emission of electromagnetic radiation.

To confirm that the origin of the THz emission is the ultrafast demagnetization, we performed experiments at different applied magnetic fields (H). Since CoFe is a ferromagnetic material, the dependence of the magnetization M on the field H shows a hysteretic behaviour. Using MOKE measurements [252] in which the angle of incidence of light was set to 45 degrees and the magnetic field applied in the plane of the sample, we obtained the dependence of the magnetization on the magnetic field $M(H)$ [see Fig. 7.7(c)]. The figure also shows that the peak amplitude of the emitted THz radiation as a function of H reveals a similar hysteretic-like behaviour. It should be noted, however, that since the THz emission measurements run in a stroboscopic mode with pump pulses present, the interpretation of the outcome of the measurements in fields lower than the coercive field is ambiguous.

We have also checked if the THz emission is sensitive to the polarization of the optical pump and found no polarization dependence of the emission signals which again confirms the hypothesis that the ultrafast changes of the magnetization are due to the laser-induced demagnetization and not opto-magnetic phenomena similar to those described in Ref. [253]. It was observed (using wiregrid polarisers) that the emission is always purely polarized perpendicular to the magnetization. These measurements support the hypothesis that demagnetization induced THz emission is observed.

To support the idea of THz radiation being emitted due to ultrafast laser-induced demagnetization, we have compared our experimental results obtained with the help of the MOKE and THz emission spectroscopy. In particular, taking the data on ultrafast demagnetization from the MOKE measurements we calculated the electric field of the THz wave emitted as a result of such a rapid change of the magnetization of the medium. Starting from the derivation of the plane wave equation for an infinite plane, using Faraday's and Ampère's laws and taking into account the fact that the generated THz radiation before being detected first propagates through a glass substrate, it is possible to arrive to the following expression for the electric field of the THz radiation [254]:

$$\tilde{E}_y(\omega, z) = \frac{4\pi\omega}{c} i\tilde{m}_x(\omega) d \frac{1}{n+1} exp(-i\frac{\omega}{c}nz), \tag{7.6}$$

where $\tilde{E}_y(w, z)$ is the generated complex electric field, $\tilde{m}_x$ is the complex magnetization, ω the angular frequency, d is the thickness of the magnetic layer, n is the refractive index of the substrate and c the speed of light in vacuum.

In order to find the electric field of the generated THz radiation, we experimentally found how the magnetization of the medium changes in time after the sample was excited by a 50 fs laser pulse at room temperature. In particular, we performed all optical pump-probe experiments in which the medium was excited by a 50 fs laser pulse with a central wavelength of 800 nm and the temporal evolution of the laser-induced changes was probed with the help of a similar but weaker probe pulse. Using the procedure described in Ref. [239], we were able to determine the time-scale and the degree of the laser-induced demagnetization [Fig. 7.8(a)]. The dynamics of the demagnetization obtained at different magnetic fields are shown in Fig. 7.8(a), revealing that it is relatively insensitive to the external magnetic field.

Taking the dependence of the demagnetization from Fig. 7.8(a) we calculated the spectrum of the THz emission. The outcome of the calculations is shown in Fig. 7.8(b), together with the

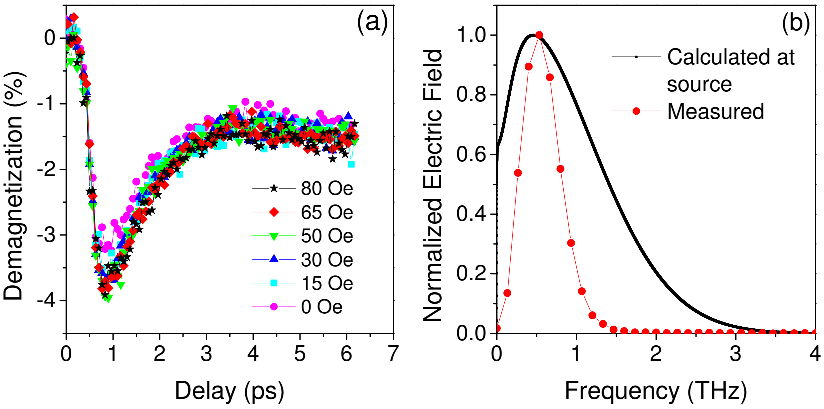

Figure 7.8: Ultrafast demagnetization results in a near-infrared pump-probe system. (a) Pump-probe measurements of the demagnetization at different applied magnetic fields and (b) comparison between the spectrum of the THz emission and the spectrum calculated through the demagnetization measurements (both normalized to their highest value).

measured trace of the THz spectrum. Regarding the fact that, in the calculation procedure of the THz trace no fit parameters are used and the propagation and ZnTe response are neglected, the similarity between these two spectra is quite satisfactory. However, the spectral width of the calculated spectrum is broader than the measured one. This can be explained taking into account that the propagation response will attenuate lower frequencies, while the propagation through the substrate and the response of the ZnTe detection will attenuate higher frequencies.

7.8 CONCLUSIONS

In this work, several optical and THz characterization techniques were developed and employed to understand the charge and magnetic dynamics of materials used in spintronics applications. The spectral MOKE measurements revealed interesting features. Specifically, they revealed that the spectral dependence of the MOKE rotation depends on the magnetic and structural properties of the samples and thus it can be used as a characterization tool. Furthermore, we performed a detailed study of the THz transmission and emission in CoFe/Al_2O_3 multilayers. It was verified that the THz transmission has the same temperature dependence as the electrical resistance, opening the possibility of probing the resistance state in the ps timescale using THz transmission. In fact, posteriorly to this work it was demonstrated the possibility of probing the resistance state of spin valves using THz spectroscopy [232]. Moreover, the effect of a femtosecond laser excitation on the THz transmission, and thus the electrical resistivity, was studied. Besides the observed sub-ps change in the resistivity, we also observed an emission of linearly polarized THz radiation triggered by the ultrafast optical excitation. To reveal the origin of the emission, we compared the near-infrared MOKE rotation with the THz peak amplitude. Both these observables appear to show quite similar hysteresis dependencies on the applied magnetic field. Moreover, the magnetization dynamics deduced from the time-resolved MOKE measurements was used to calculate the spectrum of the THz emission which must accompany such a laser-induced magnetization dynamics. The calculated spectrum is in good agreement with the experimentally obtained spectrum of the electric field of the emitted radiation. These facts strongly support the hypothesis that the THz emission originates from the ultrafast laser-induced demagnetization.

8

CONCLUSIONS AND FUTURE DIRECTIONS

Spin transfer torque nano-oscillators (STNOs) are in the forefront of current spintronic applications. In this thesis, these novel devices were thoughtfully studied from their fabrication to their RF emission characterization. As for the nanofabrication process, nanometric magnetic tunnel junctions (MTJs) with tunnel magnetoresistance (TMR) values up to 156% in the low RA range (below 2 Ωμm^2), were successfully obtained in industrial 200 mm wafers. Higher yields and uniformities were achieved with dimensions above 100 × 100 nm^2 (above 80%), but functional devices down to 50 × 50 nm^2 could still be obtained. Moreover, a novel ion beam planarization (IBP) step, to confer physical and electrical stability to the nanopillars, was implemented. This IBP step is an important new contribution to the groups working on MTJ nanofabrication since it has significant advantages when compared to lift-off (lower process time and better for smaller pillars) and CMP (fewer residues and higher uniformity) processes. This fabrication protocol was fully developed and applied to STNOs. Nevertheless, it can be applied to a different range of applications, such as nanosensors, magnetic random access memories (MRAMs) and novel devices that explore pure spin currents for memories and oscillators. Hence, this process is not only relevant for the work shown in this thesis, it can also be the foundation from which new projects will blossom.

Arguably, the strongest contribution of this thesis to the development of STNOs, consisted in unveiling the effect of the MgO barrier thickness on the performance of the oscillators. It was until now broadly assumed that thinner MgO barriers (RA ~ 1 Ωμm^2), that are able to sustain larger currents, would enhance the maximum output power (P_{out}) due to the larger STT-excited magnetization precessions. Nevertheless, thicker and more continuous MgO barriers depict a larger TMR, smaller defect count and higher breakdown voltage. Moreover, the larger resistance leads to a larger voltage variation for the same amplitude of the magnetization orbits. Still, if the MgO barrier thickness is increased further, the current values sustained by the MTJ are too small and the STT-induced magnetic precessions are restrained. In fact, it was determined that there is an optimal MgO barrier thickness (equivalent to an RA range within 7.5 - 12.5 Ωμm^2) where P_{out} was maximized up to 200 nW (while frequency of operation and linewidth remained unchanged). These values are 5 times larger than the ones obtained from devices with RA ~ 1 Ωμm^2. These results were corroborated by micromagnetic simulations and by a second fabricated MTJ incorporating an MgO wedge, both depicting the optimal region for maximized P_{out}. The main feature responsible for this increased output is the very low values of critical current density required to excite auto-oscillations J_{STT} (down to 1.17×10^5 A/cm^2) that were obtained for the more continuous and crystalline MgO. There are still open strings left from this work, in particular, further theoretical and experimental work is still necessary to fully understand the mechanisms that lead to the low measured J_{STT} values and their dependence with the TMR and RA. A key aspect of these results, is that this approach is cumulative with other improvements and STNOs geometries (such as vortex oscillators, STNOs incorporating perpendicular anisotropy, or synchronized oscillators). Furthermore, this RA range facilitates the MTJ nanofabrication with large TMR values, when compared to the lower RA region. Hence, this approach represents a simple and beneficial way to maximize P_{out}, that is transversal to different STNO configurations. We expect that these results will have a significant impact in the future research and implementation of STNOs.

The broad application of the nanofabrication process to different geometries and magnetic configurations was also tested. A novel geometry incorporating MTJ pillars with point-contacts (down to 100×100 nm^2) was successfully obtained. Despite the limited TMR and yield of this particular sample (due to incomplete planarization), interesting possibilities arise from such structure. Namely, achieving the synchronization of oscillators is one of the most promising ways to increase P_{out} and decrease the linewidth of STNOs. So far, synchronization was mainly achieved with point-contact geometries sharing the same ferromagnetic (FM) mesa. Therefore, we believe that the used fabrication methodology could be applied to μm-sized pillars incorporating point-contacts. Such structures would allow a clearer understanding of the effect of the nanoconstriction (since large STT-induced magnetic precessions are not achievable with μm-sized pillars). Moreover, pillars with 2 or more point-contacts could be envisaged to obtain oscillator synchronization. Hence, this work opens the prospect of synchronized MTJ-based STNOs. If this structure is demonstrated to be beneficial for STNOs (even without synchronization), the original geometry of a nano-sized pillar incorporating a point-contact could be further explored.

The nanofabrication process was also employed to achieve vortex-based STNOs, which is one of the most well-established sub-fields of the research on oscillators. This configuration was successfully implemented by incorporating relatively thick NiFe layers (7 and 15 nm) into the magnetic stack. The obtained state diagram (magnetic state for different pillar radius and NiFe thicknesses) was coherent with the theoretical framework. Moreover, the RF emission of vortex-based STNOs was measured and large P_{out} values of 1.49 μW in conjugation with a small linewidth below 1 MHz obtained. As expected for this configuration, the signal frequency was limited to 265 MHz. This work opens the prospect for further investigation concerning vortex-based STNOs. In fact, collaborations with partner organizations working on magnetic vortices are ongoing and these results have been recently published [255].

The last STNO configuration, developed in the scope of this thesis, consisted in MTJs with in-plane (IP) homogeneous magnetization incorporating a perpendicular polarizer (so far, such configuration had only been applied to spin valves). In what concerns this thesis, the development of such magnetic stack was the most complex in terms of the deposition scheme. Nevertheless, an ex-situ deposition process was successfully implemented, taking profit of the two available thin film deposition tools: one for the deposition of MTJs and another incorporating a Pt target. After nanofabrication, MTJ structures depicting low RA (5-6 $\Omega\mu\text{m}^2$) and TMR values up to ~ 90% were obtained. Note that, taking into account that two vacuum breaks were necessary during the stack deposition, a considerable TMR was obtained. The presence of a plateau state, with resistance between the P and the AP states, is a strong evidence that the perpendicular polarizer is effectively working and OOP magnetic precessions are obtained in this region. Furthermore, the state diagram of the different magnetic states as a function of I_{bias} and the IP applied field is in agreement with the expected polarizer effect. The excitation of the out-of-plane (OOP) magnetic precessions led to a maximized P_{out} up to 60 nW (values ~ 10 nW were obtained outside the plateau region). Moreover, this larger P_{out} was obtained with low magnetic field (in some structures even without applied field), which is a significant asset for practical applications. The large measured linewidth ~ 500 MHz is the most limitative factor of this approach. Further work is still necessary to understand if the large linewidths are a consequence of this magnetic configuration or the ex-situ fabrication process.

The key principle of operation of STNOs resides on the magnetization dynamics associated to a magnetoresistive structure. To further understand these dynamics and their correlation with the electrical counterpart, an exploratory work using pump-probe techniques in materials used in spintronics applications, was performed. The main tool used in this study was the THz-time domain spectroscopy setup (TDS) and the most disruptive results obtained with CoFe/Al_2O_3 multilayers. The THz-TDS setup can be set for the study of the THz transmission or emission of the samples. This wavelength corresponds to the range of electronics intraband transitions, thus allowing the probing of the charge carrier dynamics. An impressive correlation between the THz transmission and the electrical resistance (as a function of the temperature) was observed. This opens the possibility of electrical transport probing in the ps time-scale using THz transmission. In fact, posteriorly another group demonstrated the possibility of probing the resistance state of spin valves using THz spectroscopy [232]. Furthermore, we could correlate the THz emission with the laser-induced ultrafast demagnetization. This was performed by performing time-resolved magneto optical Kerr effect (MOKE) measurements and comparing the calculated spectrum with the measured THz emission. The good correlation achieved supports the hypothesis that THz emission originates from the ultrafast demagnetization. The collaboration with the group of Dr. Alexey Kimel and Prof. Theo Rasing remains active with significant results being already achieved [230].

In summary, the results obtained in this thesis open a broad range of possibilities for future research directions. Different approaches for STNOs (point-contacts, magnetic vortices, perpendicular anisotropy) can be explored, pushing even further the limits of this technology. The intermediate MgO thickness can be applied to maximize the output of STNOs and is transversal to the different geometries. Moreover, further spintronics applications (sensors and MRAMs) can be envisaged using the developed fabrication process. Finally, the continuation of fundamental research on magnetic and electric dynamics might push these technologies to even faster regimes.

A

TIMARIS MULTI TARGET MODE DEPOSITION CONDITIONS

Contrary to the remaining deposition schemes, where a static deposition is performed (besides rotation), the depositions performed in Timaris multi target mode (MTM) are dynamic (based on horizontal movements of the wafer under a plasma). These horizontal movements are performed along the deposition chamber with a length L. The deposited thickness will thus depend on the speed of those movements and the plasma power. More precisely, larger powers increase the quantity of sputtered material, increasing the deposition rate, while larger speeds minimize the deposition time, decreasing the deposition rate. Hence, the dynamic deposition rate R_{dyn} is defined as:

$$R_{dyn} = \frac{tv}{nP}, \tag{A.1}$$

where t is the film thickness, v the speed, n the number of passes and P the power used during calibration. R_{dyn} was calculated for each material target and the material thickness obtained for each deposition can be obtained using:

$$t_i = \frac{1}{R_{dyn}} \frac{n_i P_i}{v_i}. \tag{A.2}$$

Usually, the power P was maintained constant (the one used for the calibration) and n and v were changed accordingly to the desired thickness. In Table A.1 we show the values of R_{dyn} obtained for each material.

The MgO calibration was performed in a similar way but considering the resistance × area product (RA) instead of the measured thickness. The exponential law for the RA is given by:

$$RA = A_1 exp(\frac{nP}{v}\frac{1}{B_1}), \tag{A.3}$$

where A_1 and B_1 are constants. By plotting RA as a function of $\frac{nP}{v}$ (where P was maintained constant with a value of 3 kW), the values of A_1 and B_1 could be determined (4.94×10^{-3} $\Omega\mu m^2$ and 10.8306 W·mm/s, respectively). Finally, by adjusting the values of n and v we are able to deposit MgO barriers with different RA values.

Material	P (kW)	R_{dyn} (nm/kW·mm/s)
Cu	1.10	548.5
CuN	3.00	467.3
Ta	1.10	216.1
IrMn	2.60	364.4
PtMn	0.35	343.8
Ru	0.60	299.5
CoFe	0.35	187.8
CoFeB	0.40	164.1
NiFe	0.70	203.1

Table A.1: Deposition parameters of the Timaris MTM.

BIBLIOGRAPHY

[1] T. McGuire and R. Potter, "Anisotropic magnetoresistance in ferromagnetic 3d alloys," *IEEE Transactions on Magnetics*, vol. 11, no. 4, pp. 1018 – 1038, 1975. (Cited on page 1.)

[2] J. Smit, "Magnetoresistance of ferromagnetic metals and alloys at low temperatures," *Physica*, vol. 17, no. 6, pp. 612–627, 1951. (Cited on page 1.)

[3] L. Berger, "Influence of spin-orbit interaction on the transport processes in ferromagnetic nickel alloys, in the presence of a degeneracy of the 3d band," *Physica*, vol. 30, no. 6, pp. 1141–1159, 1964. (Cited on page 1.)

[4] J.-G. Zhu, "New heights for hard disk drives," *Materials Today*, vol. 6, no. 7-8, pp. 22–31, 2003. (Cited on page 1.)

[5] M. N. Baibich, J. M. Broto, A. Fert, F. N. Van Dau, and F. Petroff, "Giant Magnetoresistance of (001)Fe/(001)Cr Magnetic Superlattices," *Physical Review Letters*, vol. 61, pp. 2472–2475, nov 1988. (Cited on pages 2 and 149.)

[6] G. Binasch, P. Grünberg, F. Saurenbach, and W. Zinn, "Enhanced magnetoresistance in layered magnetic structures with antiferromagnetic interlayer exchange," *Physical Review B*, vol. 39, pp. 4828–4830, mar 1989. (Cited on pages 2 and 149.)

[7] J. C. Slonczewski, "Currents and torques in metallic magnetic multilayers," *Journal of Magnetism and Magnetic Materials*, vol. 247, no. 3, pp. 324–338, 2002. (Cited on page 3.)

[8] M. Jullière, "Tunneling between ferromagnetic films," *Physics Letters A*, vol. 54, pp. 225–226, sep 1975. (Cited on pages 4 and 6.)

[9] T. Miyazaki and N. Tezuka, "Giant magnetic tunneling effect in Fe/AlzO3/Fe junction," *Journal of Magnetism and Magnetic Materials*, vol. 139, pp. 94–97, 1995. (Cited on page 4.)

[10] J. Moodera, L. R. Kinder, T. M. Wong, and R. Meservey, "Large Magnetoresistance at Room Temperature in Ferromagnetic Thin Film Tunnel Junctions," *Physical Review Letters*, vol. 74, no. 16, pp. 3273–3276, 1995. (Cited on pages 4, 121, and 169.)

[11] D. Wang, C. Nordman, J. Daughton, Z. Qian, and J. Fink, "70% TMR at Room Temperature for SDT Sandwich Junctions with CoFeB as Free and Reference Layers," *IEEE Transactions on Magnetics*, vol. 40, pp. 2269–2271, jul 2004. (Cited on pages 4 and 5.)

[12] H. Jin and T. Miyazaki, "Tunnel Magnetoresistance Effect," in *The Physics of Ferromagnetism*, vol. 158 of *Springer Series in Materials Science*, ch. 12, pp. 403–432, Springer Berlin Heidelberg, 2012. (Cited on page 4.)

[13] W. Butler, X.-G. Zhang, T. Schulthess, and J. MacLaren, "Spin-dependent tunneling conductance of Fe/MgO/Fe sandwiches," *Physical Review B*, vol. 63, pp. 1–12, jan 2001. (Cited on pages 4, 7, 9, and 10.)

[14] J. Mathon and a. Umerski, "Theory of tunneling magnetoresistance of an epitaxial Fe/MgO/Fe(001) junction," *Physical Review B*, vol. 63, pp. 1–4, may 2001. (Cited on page 4.)

[15] M. Bowen, V. Cros, F. Petroff, a. Fert, C. Martínez Boubeta, J. L. Costa-Krämer, J. V. Anguita, a. Cebollada, F. Briones, J. M. De Teresa, L. Morellón, M. R. Ibarra, F. Güell, F. Peiró, and a. Cornet, "Large magnetoresistance in Fe/MgO/FeCo(001) epitaxial tunnel junctions on GaAs(001)," *Applied Physics Letters*, vol. 79, no. 11, pp. 1655–1657, 2001. (Cited on page 4.)

[16] J. Faure-Vincent, C. Tiusan, C. Bellouard, E. Popova, M. Hehn, F. Montaigne, and a. Schuhl, "Interlayer Magnetic Coupling Interactions of Two Ferromagnetic Layers by Spin Polarized Tunneling," *Physical Review Letters*, vol. 89, p. 107206, aug 2002. (Cited on page 4.)

[17] S. Yuasa, A. Fukushima, T. Nagahama, K. Ando, and Y. Suzuki, "High Tunnel Magnetoresistance at Room Temperature in Fully Epitaxial Fe/MgO/Fe Tunnel Junctions due to Coherent Spin-Polarized Tunneling," *Japanese Journal of Applied Physics*, vol. 43, pp. 588–590, apr 2004. (Cited on pages 5 and 149.)

[18] S. Ikeda, J. Hayakawa, Y. Ashizawa, Y. M. Lee, K. Miura, H. Hasegawa, M. Tsunoda, F. Matsukura, and H. Ohno, "Tunnel magnetoresistance of 604% at 300 K by suppression of Ta diffusion in CoFeBMgOCoFeB pseudo-spin-valves annealed at high temperature," *Applied Physics Letters*, vol. 93, no. 8, p. 082508, 2008. (Cited on pages 5, 7, 10, and 74.)

[19] P. M. Tedrow and R. Meservey, "Spin-dependent tunneling into ferromagnetic nickel," *Physical Review Letters*, vol. 26, no. 4, pp. 192–195, 1971. (Cited on page 5.)

[20] P. M. Tedrow and R. Meservey, "Spin polarization of electrons tunneling from films of Fe, Co, Ni and Gd," *Physical Review B*, vol. 7, no. 1, pp. 318–326, 1973. (Cited on page 5.)

[21] R. Meservey, P. M. Tedrow, and P. Fulde, "Magnetic field splitting of the quasiparticle states in superconducting aluminum films," *Physical Review Letters*, vol. 25, no. 18, pp. 1270–1272, 1970. (Cited on page 5.)

[22] N. Mott, "The electrical conductivity of transition metals," *Proceedings of the Royal Society of London A*, vol. 153, no. 880, pp. 699–717, 1936. (Cited on page 6.)

[23] I. A. Campbell, A. Fert, and A. R. Pomeroy, "Evidence for Two Current Conduction in Iron," *Philosophical Magazine*, pp. 1–6, 2007. (Cited on page 6.)

[24] A. Fert and A. Campbell, "Two-Current Conduction in Niquel," *Physical Review Letters*, vol. 21, no. 16, pp. 15–17, 1968. (Cited on page 6.)

[25] M. F. Gillies, a. E. T. Kuiper, J. B. a. Van Zon, and J. M. Sturm, "Magnetic tunnel junctions with tantalum oxide barriers displaying a magnetoresistance ratio of up to 10% at room temperature," *Applied Physics Letters*, vol. 78, no. 22, pp. 3496–3498, 2001. (Cited on page 7.)

[26] C. L. Platt, B. Dieny, and a. E. Berkowitz, "Spin polarized tunneling in reactively sputtered tunnel junctions," *Journal of Applied Physics*, vol. 81, no. 8, p. 5523, 1997. (Cited on page 7.)

[27] Y. Lu, X. Li, G. Gong, G. Xiao, a. Gupta, P. Lecoeur, J. Sun, Y. Wang, and V. Dravid, "Large magnetotunneling effect at low magnetic fields in micrometer-scale epitaxial La0.67Sr0.33MnO3 tunnel junctions," *Physical Review B*, vol. 54, no. 12, pp. R8357–R8360, 1996. (Cited on page 7.)

[28] J. Wang, P. P. Freitas, E. Snoeck, P. Wei, and J. C. Soares, "Spin-dependent tunnel junctions with ZrOx barriers," *Applied Physics Letters*, vol. 79, no. 26, p. 4387, 2001. (Cited on page 7.)

[29] J. Wang, S. Cardoso, and P. P. Freitas, "Tunnel junctions with AlN barriers and FeTaN electrodes," *Journal of Applied Physics*, vol. 89, no. 11, pp. 6868–6870, 2001. (Cited on page 7.)

[30] J. M. D. Teresa, A. Barthélémy, A. Fert, J. P. Contour, R. Lyonnet, F. Montaigne, P. Seneor, A. Vaurès, and R. R. P. Ap, "Inverse Tunnel Magnetorresistance in Co. New Ideas on Spin-Polarized Tunnelling," *Physical Review Letters*, pp. 80–83, 1999. (Cited on page 7.)

[31] J. M. De Teresa, "Role of Metal-Oxide Interface in Determining the Spin Polarization of Magnetic Tunnel Junctions," *Science*, vol. 286, pp. 507–509, oct 1999. (Cited on page 7.)

[32] I. I. Oleinik, E. Y. Tsymbal, and D. G. Pettifor, "Structural and Electronic Properties of Cobalt / Alumina Tunnel Junctions from First Principles," *Physical Review B*, vol. 62, no. 6, pp. 3952–3959, 2000. (Cited on page 7.)

[33] I. Oleinik, E. Tsymbal, and D. Pettifor, "Atomic and electronic structure of Co/SrTiO3/Co magnetic tunnel junctions," *Physical Review B*, vol. 65, no. 2, pp. 1–4, 2001. (Cited on page 7.)

[34] E. Y. Tsymbal, I. I. Oleinik, and D. G. Pettifor, "Oxygen-induced positive spin polarization from Fe into the vacuum barrier," *Journal of Applied Physics*, vol. 87, no. 9, pp. 5230–5232, 2000. (Cited on page 7.)

[35] P. Mavropoulos, N. Papanikolaou, and P. Dederichs, "Complex Band Structure and Tunneling through Ferromagnet /Insulator /Ferromagnet Junctions," *Physical Review Letters*, vol. 85, no. 5, pp. 1088–1091, 2000. (Cited on page 7.)

[36] S. Yuasa and D. D. Djayaprawira, "Giant tunnel magnetoresistance in magnetic tunnel junctions with a crystalline MgO (0 0 1) barrier," *Journal of Physics D: Applied Physics*, vol. 40, pp. 337–354, nov 2007. (Cited on page 8.)

[37] W. H. Butler, "Tunneling magnetoresistance from a symmetry filtering effect," *Science and Technology of Advanced Materials*, vol. 9, p. 014106, apr 2008. (Cited on page 9.)

[38] X. G. Zhang and W. H. Butler, "Large magnetoresistance in bcc Co/MgO/Co and FeCo/MgO/FeCo tunnel junctions," *Physical Review B*, vol. 70, no. 17, pp. 1–4, 2004. (Cited on page 10.)

[39] K. Tsunekawa, D. D. Djayaprawira, M. Nagai, H. Maehara, S. Yamagata, N. Watanabe, S. Yuasa, Y. Suzuki, and K. Ando, "Giant tunneling magnetoresistance effect in low-resistance CoFeBMgO (001) CoFeB magnetic tunnel junctions for read-head applications," *Applied Physics Letters*, vol. 87, no. 7, p. 072503, 2005. (Cited on pages 10 and 75.)

[40] B. Rodmacq, S. Auffret, B. Dieny, S. Monso, and P. Boyer, "Crossovers from in-plane to perpendicular anisotropy in magnetic tunnel junctions as a function of the barrier degree of oxidation," *Journal of Applied Physics*, vol. 93, no. 10 2, pp. 7513–7515, 2003. (Cited on page 13.)

[41] B. Rodmacq, A. Manchon, C. Ducruet, S. Auffret, and B. Dieny, "Influence of thermal annealing on the perpendicular magnetic anisotropy of Pt/Co/AlOx trilayers," *Physical Review B*, vol. 79, no. 2, pp. 1–8, 2009. (Cited on page 13.)

[42] H. X. Yang, M. Chshiev, B. Dieny, J. H. Lee, a. Manchon, and K. H. Shin, "First-principles investigation of the very large perpendicular magnetic anisotropy at Fe|MgO and Co|MgO interfaces," *Physical Review B*, vol. 84, pp. 1–5, aug 2011. (Cited on page 13.)

[43] S. Monso, B. Rodmacq, S. Auffret, G. Casali, F. Fettar, B. Gilles, B. Dieny, and P. Boyer, "Crossover from in-plane to perpendicular anisotropy in Pt/CoFe/AlOx sandwiches as a function of Al oxidation: A very accurate control of the oxidation of tunnel barriers," *Applied Physics Letters*, vol. 80, no. 22, pp. 4157–4159, 2002. (Cited on page 13.)

[44] A. Manchon, C. Ducruet, L. Lombard, S. Auffret, B. Rodmacq, B. Dieny, S. Pizzini, J. Vogel, V. Uhlír, M. Hochstrasser, and G. Panaccione, "Analysis of oxygen induced anisotropy crossover in Pt/Co/MOx trilayers," *Journal of Applied Physics*, vol. 104, no. 4, 2008. (Cited on page 13.)

[45] J. M. Teixeira, J. Ventura, J. P. Araujo, J. B. Sousa, P. Wisniowski, S. Cardoso, and P. P. Freitas, "Resonant tunneling through electronic trapping states in thin MgO magnetic junctions," *Physical Review Letters*, vol. 106, no. 19, pp. 1–4, 2011. (Cited on page 14.)

[46] J. Ventura, J. M. Teixeira, E. Paz, J. S. Amaral, J. D. Costa, a. Apolinario, J. P. Araujo, S. Cardoso, R. Ferreira, and P. P. Freitas, "The influence of annealing on the bimodal distribution of blocking temperatures of exchange biased bilayers," *Physica Status Solidi - Rapid Research Letters*, vol. 7, no. 9, pp. 676–680, 2013. (Cited on page 14.)

[47] B. G. Park, J. Wunderlich, X. Martí, V. Holý, Y. Kurosaki, M. Yamada, H. Yamamoto, a. Nishide, J. Hayakawa, H. Takahashi, a. B. Shick, and T. Jungwirth, "A spin-valve-like magnetoresistance of an antiferromagnet-based tunnel junction.," *Nature materials*, vol. 10, no. 5, pp. 347–351, 2011. (Cited on page 14.)

[48] A. Anguelouch, B. D. Schrag, G. Xiao, Y. Lu, P. L. Trouilloud, R. a. Wanner, W. J. Gallagher, and S. S. P. Parkin, "Two-dimensional magnetic switching of micron-size films in magnetic tunnel junctions," *Applied Physics Letters*, vol. 76, no. 5, p. 622, 2000. (Cited on pages 15 and 113.)

[49] B. Lacoste, *Mastering the influence of thermal fluctuations on the magnetization switching dynamics of spintronic devices*. PhD thesis, Ecole Doctorale de Physique de Grenoble, 2013. (Cited on pages 15 and 139.)

[50] K. Y. Guslienko, G. R. Aranda, and J. Gonzalez, "Spin torque and critical currents for magnetic vortex nano-oscillator in nanopillars," *Journal of Physics: Conference Series*, vol. 292, no. 1, p. 012006, 2011. (Cited on page 16.)

[51] N. D. Mermin, "The topological theory of defects in ordered media," *Reviews of Modern Physics*, vol. 51, pp. 591–648, jul 1979. (Cited on page 16.)

[52] G. Hrkac, P. S. Keatley, M. T. Bryan, and K. Butler, "Magnetic vortex oscillators," *Journal of Physics D: Applied Physics*, vol. 48, no. 45, p. 453001, 2015. (Cited on pages 16, 74, and 139.)

[53] K. L. Metlov and K. Y. Guslienko, "Stability of magnetic vortex in soft magnetic nano-sized circular cylinder," *Journal of Magnetism and Magnetic Materials*, vol. 242-245, no. 0, pp. 1015–1017, 2002. (Cited on page 17.)

[54] K. Yu. Guslienko, "Magnetic Vortex State Stability, Reversal and Dynamics in Restricted Geometries," *Journal of Nanoscience and Nanotechnology*, vol. 8, no. August, pp. 2745–2760, 2008. (Cited on pages 17 and 139.)

[55] J. Slonczewski, "Current-driven excitation of magnetic multilayers," *Journal of Magnetism and Magnetic Materials*, vol. 159, pp. 1–7, jun 1996. (Cited on pages 18, 74, 109, 120, 149, and 150.)

[56] A. V. Chumak, V. I. Vasyuchka, A. A. Serga, and B. Hillebrands, "Magnon spintronics," *Nature Physics*, vol. 11, no. 6, pp. 453–461, 2015. (Cited on page 18.)

[57] M. Kläui, C. A. F. Vaz, J. A. C. Bland, W. Wernsdorfer, G. Faini, E. Cambril, and L. J. Heyderman, "Domain wall motion induced by spin polarized currents in ferromagnetic ring structures," *Applied Physics Letters*, vol. 83, no. 1, pp. 105–107, 2003. (Cited on page 18.)

[58] J. Grollier, P. Boulenc, V. Cros, A. Hamzić, A. Vaurès, A. Fert, and G. Faini, "Switching a spin valve back and forth by current-induced domain wall motion," *Applied Physics Letters*, vol. 83, no. 3, pp. 509–511, 2003. (Cited on page 18.)

[59] S. Ikeda, K. Miura, H. Yamamoto, K. Mizunuma, H. D. Gan, M. Endo, S. Kanai, J. Hayakawa, F. Matsukura, and H. Ohno, "A perpendicular-anisotropy CoFeB-MgO magnetic tunnel junction.," *Nature materials*, vol. 9, pp. 721–724, sep 2010. (Cited on pages 18 and 74.)

[60] S. Mangin, D. Ravelosona, J. A. Katine, M. J. Carey, B. D. Terris, and E. E. Fullerton, "Current-induced magnetization reversal in nanopillars with perpendicular anisotropy," *Nature Materials*, vol. 5, pp. 210–215, feb 2006. (Cited on pages 18 and 74.)

[61] S. I. Kiselev, J. C. Sankey, I. N. Krivorotov, N. C. Emley, R. J. Schoelkopf, R. A. Buhrman, and D. C. Ralph, "Microwave oscillations of a nanomagnet driven by a spin-polarized current.," *Nature*, vol. 425, pp. 380–3, sep 2003. (Cited on pages 18, 25, 74, 110, 116, 129, 149, and 150.)

[62] S. Kaka, M. R. Pufall, W. H. Rippard, T. J. Silva, S. E. Russek, and J. A. Katine, "Mutual phase-locking of microwave spin torque nano-oscillators.," *Nature*, vol. 437, pp. 389–92, sep 2005. (Cited on pages 18, 29, 30, 74, 110, and 130.)

[63] J. Grollier, *From Spin Torque Nano-Oscillators to Memristors*. PhD thesis, Université Pierre et Marie Curie, 2013. (Cited on page 19.)

[64] S.-C. Oh, S.-Y. Park, A. Manchon, M. Chshiev, J.-H. Han, H.-W. Lee, J.-E. Lee, K.-T. Nam, Y. Jo, Y.-C. Kong, B. Dieny, and K.-J. Lee, "Bias-voltage dependence of perpendicular spin-transfer torque in asymmetric MgO-based magnetic tunnel junctions," *Nature Physics*, vol. 5, no. 12, pp. 898–902, 2009. (Cited on page 20.)

[65] D. L. Huber, "Dynamics of spin vortices in two-dimensional planar magnets," *Physical Review B*, vol. 26, no. 7, pp. 3758–3765, 1982. (Cited on page 22.)

[66] F. Garcia-Sanchez, J. Sampaio, N. Reyren, V. Cros, and J. V. Kim, "A skyrmion-based spin-torque nano-oscillator," *New Journal of Physics*, vol. 18, no. 7, pp. 1–10, 2016. (Cited on page 22.)

[67] A. A. Thiele, "Steady-state motion of magnetic domains," *Physical Review Letters*, vol. 30, no. 6, pp. 230–233, 1973. (Cited on page 22.)

[68] A. Dussaux, B. Georges, J. Grollier, V. Cros, A. V. Khvalkovskiy, A. Fukushima, H. Kubota, K. Yakushiji, S. Yuasa, K. A. Zvezdin, K. Ando, A. Fert, M. Konoto, H. Kubota, K. Yakushiji, S. Yuasa, K. A. Zvezdin, K. Ando, and A. Fert, "Large microwave generation from current-driven magnetic vortex oscillators in magnetic tunnel junctions.," *Nature communications*, vol. 1, p. 8, jan 2010. (Cited on pages 23, 25, 27, 29, 74, 110, 129, 139, 140, and 145.)

[69] Z. Zeng, G. Finocchio, and H. Jiang, "Spin transfer nano-oscillators.," *Nanoscale*, vol. 5, no. 6, pp. 2219–31, 2013. (Cited on pages 22, 27, 74, 110, 121, 129, and 149.)

[70] W. H. Rippard, M. R. Pufall, S. Kaka, S. E. Russek, and T. J. Silva, "Direct-current induced dynamics in Co90 Fe10/Ni80 Fe20 point contacts.," *Physical Review Letters*, vol. 92, no. 2, p. 027201, 2004. (Cited on pages 22, 25, 29, 149, and 150.)

[71] P. Villard, U. Ebels, D. Houssameddine, J. Katine, D. Mauri, B. Delaet, P. Vincent, M. C. Cyrille, B. Viala, J. P. Michel, J. Prouvée, and F. Badets, "A GHz spintronic-based RF oscillator," *IEEE Journal of Solid-State Circuits*, vol. 45, no. 1, pp. 214–223, 2010. (Cited on page 23.)

[72] S. A. Wolf, A. Y. Chtchelkanova, and D. M. Treger, "Spintronics - a retrospective and perspective," *IBM Journ. Res. Dev.*, vol. 50, p. 101, 2006. (Cited on page 23.)

[73] S. E. Russek, W. H. Rippard, T. Cecil, and R. Heindl, *Handbook of Nanophysics: Functional Nanomaterials*. CRC PrIlic, 2010. (Cited on pages 23, 27, and 121.)

[74] M. D. Stiles and J. Miltat, "Spin Dynamics in Confined Magnetic Structures III," *Topics in Applied Physics*, vol. 101, pp. 225–308, 2006. (Cited on pages 23, 28, and 122.)

[75] H. Maehara, H. Kubota, Y. Suzuki, T. Seki, K. Nishimura, Y. Nagamine, K. Tsunekawa, A. Fukushima, A. M. Deac, K. Ando, and S. Yuasa, "Large emission power over 2 μW with high Q factor obtained from nanocontact magnetic-tunnel-junction-based spin torque oscillator," *Applied Physics Express*, vol. 6, no. 11, p. 113005, 2013. (Cited on pages 24, 26, 74, 110, and 130.)

[76] B. Wang, H. Kubota, K. Yakushiji, S. Tamaru, and H. Arai, "Diameter dependence of emission power in MgO-based nano-pillar spin-torque oscillators," *Applied Physics Letters*, vol. 108, p. 253502, 2016. (Cited on pages 24, 25, 110, and 116.)

[77] A. V. Nazarov, H. M. Olson, Z. Gao, H. Cho, S. Stokes, and B. B. Pant, "Spin transfer stimulated microwave emission in MgO magnetic tunnel junctions," *Applied Physics Letters*, vol. 88, no. 162504, p. 273, 2006. (Cited on pages 24 and 29.)

[78] D. Houssameddine, S. H. Florez, J. A. Katine, J. P. Michel, U. Ebels, D. Mauri, O. Ozatay, B. Delaet, B. Viala, L. Folks, B. D. Terris, and M. C. Cyrille, "Spin transfer induced coherent microwave emission with large power from nanoscale MgO tunnel junctions," *Applied Physics Letters*, vol. 93, no. 2, pp. 2006–2009, 2008. (Cited on pages 24, 27, 29, 75, 110, 111, and 163.)

[79] J. D. Costa, S. Serrano Guisan, J. Borme, L. Francis, T. Zaman, E. Paz, J. Ventura, R. Ferreira, and P. Freitas, "Impact of MgO thickness on the performance of Spin Transfer Torque Nano-Oscillators," *IEEE Transactions on Magnetics*, vol. 9464, no. c, pp. 1–1, 2015. (Cited on pages 24, 25, 115, 129, and 150.)

[80] Z. M. Zeng, P. Upadhyaya, P. Khalili Amiri, K. H. Cheung, J. a. Katine, J. Langer, K. L. Wang, and H. W. Jiang, "Enhancement of microwave emission in magnetic tunnel junction oscillators through in-plane field orientation," *Applied Physics Letters*, vol. 99, no. 3, p. 032503, 2011. (Cited on pages 24, 25, 27, 29, 75, 110, and 150.)

[81] A. M. Deac, A. Fukushima, H. Kubota, H. Maehara, Y. Suzuki, S. Yuasa, Y. Nagamine, K. Tsunekawa, D. D. Djayaprawira, and N. Watanabe, "Bias-driven high-power mi-

crowave emission from MgO-based tunnel magnetoresistance devices," *Nature Physics*, vol. 4, pp. 803–809, aug 2008. (Cited on pages 24, 27, 74, 75, 110, 111, 129, and 130.)

[82] C. H. Sim, S. Y. H. Lua, T. Liew, and J. G. Zhu, "Current driven oscillation and switching in Co/Pd perpendicular giant magnetoresistance multilayer," *Journal of Applied Physics*, vol. 109, no. 7, pp. 1–4, 2011. (Cited on pages 25 and 150.)

[83] W. H. Rippard, A. M. Deac, M. R. Pufall, J. M. Shaw, M. W. Keller, S. E. Russek, G. E. W. Bauer, and C. Serpico, "Spin-transfer dynamics in spin valves with out-of-plane magnetized CoNi free layers," *Physical Review B*, vol. 81, no. 1, pp. 1–8, 2010. (Cited on pages 25, 29, and 130.)

[84] Z. Zeng, P. K. Amiri, I. N. Krivorotov, H. Zhao, G. Finocchio, J.-P. Wang, J. a. Katine, Y. Huai, J. Langer, K. Galatsis, K. L. Wang, and H. Jiang, "High-power coherent microwave emission from magnetic tunnel junction nano-oscillators with perpendicular anisotropy.," *ACS nano*, vol. 6, pp. 6115–21, jul 2012. (Cited on pages 25, 26, 27, 28, 29, 74, 110, 111, 122, 129, 130, and 150.)

[85] Z. Zeng, G. Finocchio, B. Zhang, P. K. Amiri, J. A. Katine, I. N. Krivorotov, Y. Huai, J. Langer, B. Azzerboni, K. L. Wang, and H. Jiang, "Ultralow-current-density and bias-field-free spin-transfer nano-oscillator," *Scientific Reports*, vol. 3, p. 1426, 2013. (Cited on pages 25, 27, 28, 29, 74, 110, 129, 130, and 150.)

[86] D. Houssameddine, U. Ebels, B. Delaët, B. Rodmacq, I. Firastrau, F. Ponthenier, M. Brunet, C. Thirion, J.-P. Michel, L. Prejbeanu-Buda, M.-C. Cyrille, O. Redon, and B. Dieny, "Spin-torque oscillator using a perpendicular polarizer and a planar free layer.," *Nature materials*, vol. 6, pp. 441–7, jun 2007. (Cited on pages 25, 110, 150, 157, 160, and 163.)

[87] P. Bortolotti, A. Dussaux, J. Grollier, V. Cros, A. Fukushima, H. Kubota, K. Yakushiji, S. Yuasa, K. Ando, and A. Fert, "Temperature dependence of microwave voltage emission associated to spin-transfer induced vortex oscillation in magnetic tunnel junction," *Applied Physics Letters*, vol. 100, no. 4, p. 042408, 2012. (Cited on pages 25 and 29.)

[88] A. Dussaux, E. Grimaldi, B. Rache Salles, A. S. Jenkins, A. V. Khvalkovskiy, P. Bortolotti, J. Grollier, H. Kubota, A. Fukushima, K. Yakushiji, S. Yuasa, V. Cros, and A. Fert, "Large amplitude spin torque vortex oscillations at zero external field using a perpendicular spin polarizer," *Applied Physics Letters*, vol. 105, no. 2, p. 022404, 2014. (Cited on pages 25, 26, 27, 29, 74, 110, 129, 140, and 150.)

[89] H. S. Choi, S. Y. Kang, S. J. Cho, I.-Y. Oh, M. Shin, H. Park, C. Jang, B.-C. Min, S.-I. Kim, S.-Y. Park, and C. S. Park, "Spin nano-oscillator-based wireless communication," *Scientific Reports*, vol. 4, pp. 1–7, 2014. (Cited on pages 27 and 110.)

[90] S. Y. Martin, N. de Mestier, C. Thirion, C. Hoarau, Y. Conraux, C. Baraduc, and B. Diény, "Parametric oscillator based on nonlinear vortex dynamics in low-resistance magnetic tunnel junctions," *Physical Review B*, vol. 84, p. 144434, oct 2011. (Cited on pages 27, 30, 68, and 110.)

[91] M. Quinsat, F. Garcia-Sanchez, A. S. Jenkins, V. S. Tiberkevich, A. N. Slavin, L. D. Buda-Prejbeanu, A. Zeltser, J. A. Katine, B. Dieny, M. C. Cyrille, and U. Ebels, "Modulation bandwidth of spin torque oscillators under current modulation," *Applied Physics Letters*, vol. 105, no. 15, 2014. (Cited on pages 27 and 110.)

[92] S. Tamaru, H. Kubota, K. Yakushiji, T. Nozaki, M. Konoto, A. Fukushima, H. Imamura, T. Taniguchi, H. Arai, T. Yamaji, and S. Yuasa, "Magnetic field angle dependence of the self-oscillation of spin torque oscillators having a perpendicularly magnetized free layer and in-plane magnetized reference layer," *Applied Physics Express*, vol. 7, no. 6, 2014. (Cited on pages 27 and 110.)

[93] S. Tamaru, H. Kubota, K. Yakushiji, M. Konoto, T. Nozaki, A. Fukushima, H. Imamura, T. Taniguchi, H. Arai, S. Tsunegi, S. Yuasa, and Y. Suzuki, "Observations of thermally excited ferromagnetic resonance on spin torque oscillators having a perpendicularly magnetized free layer," *Journal of Applied Physics*, vol. 115, no. 17, pp. 2014–2017, 2014. (Cited on pages 27 and 110.)

[94] A. Slavin and V. Tiberkevich, "Nonlinear auto-oscillator theory of microwave generation by spin-polarized current," *IEEE Transactions on Magnetics*, vol. 45, no. 4, pp. 1875–1918, 2009. (Cited on pages 28, 121, 122, and 163.)

[95] H. G. Silva, A. M. Pereira, J. M. Teixeira, J. M. Moreira, G. N. Kakazei, J. P. Araújo, Y. G. Pogorelov, J. B. Sousa, M. E. Braga, B. Raquet, H. Rakoto, C. Gatel, E. Snoeck, S. Cardoso, and P. P. Freitas, "Magnetic field strength and orientation effects on Co-Fe discontinuous multilayers close to percolation," *Physical Review B*, vol. 82, no. 14, pp. 1–8, 2010. (Cited on page 28.)

[96] J. V. Kim, V. Tiberkevich, and A. N. Slavin, "Generation linewidth of an auto-oscillator with a nonlinear frequency shift: Spin-torque nano-oscillator," *Physical Review Letters*, vol. 100, no. 1, pp. 1–4, 2008. (Cited on page 28.)

[97] K. V. Thadani, G. Finocchio, Z. P. Li, O. Ozatay, J. C. Sankey, I. N. Krivorotov, Y. T. Cui, R. a. Buhrman, and D. C. Ralph, "Strong linewidth variation for spin-torque nano-oscillators as a function of in-plane magnetic field angle," *Physical Review B*, vol. 78, no. 2, pp. 1–7, 2008. (Cited on page 28.)

[98] M. W. Keller, a. B. Kos, T. J. Silva, W. H. Rippard, and M. R. Pufall, "Time domain measurement of phase noise in a spin torque oscillator," *Applied Physics Letters*, vol. 94, no. 19, pp. 12–15, 2009. (Cited on page 28.)

[99] D. Houssameddine, U. Ebels, B. Dieny, K. Garello, J. P. Michel, B. Delaet, B. Viala, M. C. Cyrille, J. a. Katine, and D. Mauri, "Temporal coherence of MgO based magnetic tunnel junction spin torque oscillators," *Physical Review Letters*, vol. 102, no. 25, 2009. (Cited on page 29.)

[100] S. Bonetti, P. Muduli, F. Mancoff, and J. Åkerman, "Spin torque oscillator frequency versus magnetic field angle: The prospect of operation beyond 65 GHz," *Applied Physics Letters*, vol. 94, no. 10, 2009. (Cited on page 29.)

[101] K. K. Likharev, *Dynamics of Josephson Junctions and Circuits*. CRC Press, 1991. (Cited on page 29.)

[102] J. Fell and N. Axmacher, "The role of phase synchronization in memory processes," *Nature Review Neuroscience*, vol. 12, pp. 105–118, feb 2011. (Cited on page 29.)

[103] A. Pikovsky, M. Rosenblum, and J. Kurths, *Synchronization - A universal concept in nonlinear sciences*. Cambridge University Press, 2001. (Cited on page 29.)

[104] F. B. Mancoff, N. D. Rizzo, B. N. Engel, and S. Tehrani, "Phase-locking in double-point-contact spin-transfer devices.," *Nature*, vol. 437, pp. 393–5, sep 2005. (Cited on pages 29 and 130.)

[105] A. Ruotolo, V. Cros, B. Georges, A. Dussaux, J. Grollier, C. Deranlot, R. Guillemet, K. Bouzehouane, S. Fusil, and A. Fert, "Phase-locking of magnetic vortices mediated by antivortices.," *Nature nanotechnology*, vol. 4, pp. 528–32, aug 2009. (Cited on pages 29, 74, 129, 130, 139, and 140.)

[106] A. Houshang, E. Iacocca, P. Dürrenfeld, S. R. Sani, J. Åkerman, and R. K. Dumas, "Spin-wave-beam driven synchronization of nanocontact spin-torque oscillators," *Nature nanotechnology*, no. December, 2015. (Cited on pages 29, 110, and 130.)

[107] R. Lebrun, A. Jenkins, A. Dussaux, N. Locatelli, S. Tsunegi, E. Grimaldi, H. Kubota, P. Bortolotti, K. Yakushiji, J. Grollier, A. Fukushima, S. Yuasa, and V. Cros, "Understanding of Phase Noise Squeezing Under Fractional Synchronization of a Nonlinear Spin Transfer Vortex Oscillator," *Physical Review Letters*, vol. 017201, no. July, pp. 1–5, 2015. (Cited on pages 30 and 68.)

[108] A. Dussaux, A. V. Khvalkovskiy, J. Grollier, V. Cros, A. Fukushima, M. Konoto, H. Kubota, K. Yakushiji, S. Yuasa, K. Ando, and A. Fert, "Phase locking of vortex based spin transfer oscillators to a microwave current," *Applied Physics Letters*, vol. 98, no. 13, p. 132506, 2011. (Cited on pages 30, 68, and 140.)

[109] S. Tamaru, H. Kubota, K. Yakushiji, S. Yuasa, and A. Fukushima, "Extremely Coherent Microwave Emission from Spin Torque Oscillator Stabilized by Phase Locked Loop," *Scientific Reports*, vol. 5, p. 18134, 2015. (Cited on page 30.)

[110] D. L. Smith, *Thin-Film Deposition: Principles and Practice*. New York: New-York: McGraw-Hill, inc, 1995. (Cited on page 31.)

[111] M. Zeise and M. J. Thornton, "Thin Film Deposition Techniques," in *Spin Electronics*, pp. 298–315, Springer, 2001. (Cited on page 31.)

[112] P. Kelly and R. Arnell, "Magnetron sputtering: a review of recent developments and applications," *Vacuum*, vol. 56, no. 3, pp. 159–172, 2000. (Cited on page 32.)

[113] R. Ferreira, *Ion Beam Deposited Magnetic Spin Tunnel Junctions targeting HDD Read Heads, Non-volatile Memories and Magnetic Field Sensor Applications*. PhD thesis, Instituto Superior Técnico, 2008. (Cited on page 33.)

[114] P. Revell and G. Goldspink, "A review of reactive ion beam etching for production," *Vacuum*, vol. 34, pp. 455–462, mar 1984. (Cited on page 40.)

[115] A. Pimpin and W. Srituravanich, "Reviews on micro- and nanolithography techniques and their applications," *Engineering Journal*, vol. 16, no. 1, pp. 37–55, 2012. (Cited on page 43.)

[116] D. C. Leitao, R. J. Macedo, A. V. Silva, D. Q. Hoang, D. A. MacLaren, S. McVitie, S. Cardoso, and P. P. Freitas, "Optimization of exposure parameters for lift-off process of sub-100 features using a negative tone electron beam resist," *Proceedings of the IEEE Conference on Nanotechnology*, no. August, 2012. (Cited on pages 44, 75, and 130.)

[117] G. L.-T. Chiu and J. M. Shaw, "Optical lithography: Introduction," 1997. (Cited on page 46.)

[118] M. Altissimo, "E-beam lithography for micro-nanofabrication.," *Biomicrofluidics*, vol. 4, jan 2010. (Cited on page 49.)

[119] A. Tseng, K. Chen, C. D. Chen, and K. J. Ma, "Electron beam lithography in nanoscale fabrication: Recent development," *IEEE Transactions on Electronics Packaging Manufacturing*, vol. 26, no. 2, pp. 141–149, 2003. (Cited on page 49.)

[120] E. Paz, R. Ferreira, and P. Freitas, "Linearization of Magnetic Sensors with a Weakly Pinned Free Layer MTJ Stack Using a Three-Step Annealing Process," *IEEE Transactions on Magnetics*, vol. 9464, no. c, pp. 1–1, 2016. (Cited on page 52.)

[121] D. C. Joy, "Scanning electron microscopy for materials characterization," *Current Opinion in Solid State and Materials Science*, vol. 2, pp. 465–468, 1997. (Cited on page 54.)

[122] K. Vernon-Parry, "Scanning electron microscopy: an introduction," *III-Vs Review*, vol. 13, no. 4, pp. 40–44, 2000. (Cited on page 54.)

[123] D. R. Clarke, "Review: transmission scanning electron microscopy," *Journal of Materials Science*, vol. 8, no. 2, pp. 279–285, 1973. (Cited on page 55.)

[124] L. A. Giannuzzi and F. A. Stevie, "A review of focused ion beam milling techniques for TEM specimen preparation," *Micron*, vol. 30, no. 3, pp. 197–204, 1999. (Cited on page 56.)

[125] C. S. Kim, S. H. Ahn, and D. Y. Jang, "Review: Developments in micro/nanoscale fabrication by focused ion beams," *Vacuum*, vol. 86, no. 8, pp. 1014–1035, 2012. (Cited on page 56.)

[126] S. Foner, "Versatile and Sensitive Vibration-Sample Magnetometer," *The Review of scientific instruments*, vol. 30, no. 7, pp. 550–557, 1959. (Cited on page 62.)

[127] A. A. Tulapurkar, Y. Suzuki, A. Fukushima, H. Kubota, H. Maehara, K. Tsunekawa, D. D. Djayaprawira, N. Watanabe, and S. Yuasa, "Spin-torque diode effect in magnetic tunnel junctions," *Nature*, vol. 438, pp. 339–342, nov 2005. (Cited on page 68.)

[128] S. D. Bader and S. S. P. Parkin, "Spintronics," *Annual Review of Condensed Matter Physics*, vol. 1, pp. 71–88, jul 2010. (Cited on page 74.)

[129] P. P. Freitas, R. Ferreira, S. Cardoso, and F. Cardoso, "Magnetoresistive sensors," *Journal of Physics: Condensed Matter*, vol. 19, no. 16, p. 165221, 2007. (Cited on page 74.)

[130] C. Albon, A. Weddemann, A. Auge, K. Rott, and A. Hütten, "Tunneling magnetoresistance sensors for high resolutive particle detection," *Applied Physics Letters*, vol. 95, no. 2, p. 023101, 2009. (Cited on page 74.)

[131] M. Pannetier, C. Fermon, G. Le Goff, J. Simola, and E. Kerr, "Femtotesla magnetic field measurement with magnetoresistive sensors," *Science*, vol. 304, no. 5677, pp. 1648–1650, 2004. (Cited on page 74.)

[132] L. Jiang, E. Nowak, P. Scott, J. Johnson, J. Slaughter, J. Sun, and R. Dave, "Low-frequency magnetic and resistance noise in magnetic tunnel junctions," *Physical Review B*, vol. 69, p. 054407, 2004. (Cited on page 74.)

[133] W. Shen, X. Liu, D. Mazumdar, and G. Xiao, "In situ detection of single micron-sized magnetic beads using magnetic tunnel junction sensors," *Applied Physics Letters*, vol. 86, no. 25, p. 253901, 2005. (Cited on page 74.)

[134] P. P. Freitas, F. A. Cardoso, V. C. Martins, S. A. M. Martins, J. Loureiro, J. Amaral, R. C. Chaves, S. Cardoso, L. P. Fonseca, A. M. Sebastião, M. Pannetier-Lecoeur, and C. Fermon, "Spintronic platforms for biomedical applications.," *Lab on a chip*, vol. 12, pp. 546–57, feb 2012. (Cited on page 74.)

[135] R. S. Gaster, L. Xu, S.-J. Han, R. J. Wilson, D. A. Hall, S. J. Osterfeld, H. Yu, and S. X. Wang, "Quantification of protein interactions and solution transport using high-density GMR sensor arrays.," *Nature nanotechnology*, vol. 6, no. 5, pp. 314–20, 2011. (Cited on page 74.)

[136] D. C. Leitao, A. V. Silva, E. Paz, R. Ferreira, S. Cardoso, and P. P. Freitas, "Magnetoresistive nanosensors: controlling magnetism at the nanoscale," *Nanotechnology*, vol. 27, no. 4, p. 045501, 2016. (Cited on page 74.)

[137] W. H. Rippard, M. R. Pufall, S. Kaka, T. J. Silva, S. E. Russek, and J. a. Katine, "Injection locking and phase control of spin transfer nano-oscillators," *Physical Review Letters*, vol. 95, no. 6, pp. 10–13, 2005. (Cited on pages 74, 110, and 129.)

[138] M. M. Waldrop, "The chips are down for Moore's law," *Nature*, vol. 530, pp. 145–7, 2016. (Cited on page 74.)

[139] V. S. Pribiag, I. N. Krivorotov, G. D. Fuchs, P. M. Braganca, O. Ozatay, J. C. Sankey, D. C. Ralph, and R. A. Buhrman, "Magnetic vortex oscillator driven by dc spin-polarized current," *Nature physics*, vol. 3, pp. 498 – 503, 2007. (Cited on pages 74, 110, and 129.)

[140] J. Wunderlich, B. Kaestner, J. Sinova, and T. Jungwirth, "Experimental observation of the spin-hall effect in a two-dimensional spin-orbit coupled semiconductor system," *Physical Review Letters*, vol. 94, no. 4, p. 047204, 2005. (Cited on page 74.)

[141] Y. K. Kato, R. C. Myers, A. C. Gossard, and D. D. Awschalom, "Observation of the Spin Hall," *Science*, vol. 306, pp. 1910–1913, 2004. (Cited on page 74.)

[142] J. Sinova, S. O. Valenzuela, J. Wunderlich, C. H. Back, and T. Jungwirth, "Spin Hall effects," *Reviews of Modern Physics*, vol. 87, no. 4, pp. 1213–1260, 2015. (Cited on page 74.)

[143] L. Liu, "Spin-torque switching with the giant spin Hall effect of tantalum," *Science*, vol. 336, pp. 555–558, 2012. (Cited on page 74.)

[144] A. V. Penumatcha, S. R. Das, Z. Chen, and J. Appenzeller, "Spin-torque switching of a nano-magnet using giant spin hall effect," *AIP Advances*, vol. 5, no. 10, p. 107144, 2015. (Cited on page 74.)

[145] Z. Zhao, M. Jamali, A. K. Smith, and J. P. Wang, "Spin Hall switching of the magnetization in Ta/TbFeCo structures with bulk perpendicular anisotropy," *Applied Physics Letters*, vol. 106, no. 13, p. 132404, 2015. (Cited on page 74.)

[146] L. Liu, O. J. Lee, T. J. Gudmundsen, D. C. Ralph, and R. A. Buhrman, "Current-induced switching of perpendicularly magnetized magnetic layers using spin torque from the spin hall effect," *Physical Review Letters*, vol. 109, no. 9, p. 096602, 2012. (Cited on page 74.)

[147] V. E. Demidov, H. Ulrichs, S. V. Gurevich, S. O. Demokritov, V. S. Tiberkevich, A. N. Slavin, A. Zholud, and S. Urazhdin, "Synchronization of spin Hall nano-oscillators to external microwave signals.," *Nature communications*, vol. 5, p. 3179, 2014. (Cited on page 74.)

[148] V. E. Demidov, S. Urazhdin, A. Zholud, A. V. Sadovnikov, and S. O. Demokritov, "Nanoconstriction-based spin-Hall nano-oscillator," *Applied Physics Letters*, vol. 105, no. 17, p. 172410, 2014. (Cited on page 74.)

[149] S. Isogami, M. Tsunoda, K. Komagaki, K. Sunaga, Y. Uehara, M. Sato, T. Miyajima, and M. Takahashi, "In situ heat treatment of ultrathin MgO layer for giant magnetoresistance ratio with low resistance area product in CoFeB/MgO/CoFeB magnetic tunnel junctions," *Applied Physics Letters*, vol. 93, no. 19, pp. 2006–2009, 2008. (Cited on page 75.)

[150] S. W. Chun, D. Kim, J. Kwon, B. Kim, S. Choi, and S. B. Lee, "Multi-step ion beam etching of sub-30 nm magnetic tunnel junctions for reducing leakage and MgO barrier damage," *Journal of Applied Physics*, vol. 111, no. 7, pp. 2010–2013, 2012. (Cited on pages 75 and 130.)

[151] X. Peng, S. Wakeham, A. Morrone, S. Axdal, M. Feldbaum, J. Hwu, T. Boonstra, Y. Chen, and J. Ding, "Towards the sub-50 nm magnetic device definition: Ion beam etching (IBE) vs plasma-based etching," *Vacuum*, vol. 83, no. 6, pp. 1007–1013, 2009. (Cited on pages 75 and 130.)

[152] X. Peng, Z. Wang, Y. Lu, B. Lafferty, T. McLaughlin, and M. Ostrowski, "On the geometry control of magnetic devices: Impact of photo-resist profile, shadowing effect, and material properties," *Vacuum*, vol. 84, no. 9, pp. 1075–1079, 2010. (Cited on page 75.)

[153] S. Ishibashi, T. Seki, T. Nozaki, H. Kubota, S. Yakata, A. Fukushima, S. Yuasa, H. Maehara, K. Tsunekawa, D. D. Djayaprawira, and Y. Suzuki, "Large Diode Sensitivity of CoFeB/MgO/CoFeB Magnetic Tunnel Junctions," *Applied Physics Express*, vol. 3, p. 073001, jun 2010. (Cited on page 75.)

[154] W. Zhao, X. Zhao, Y. Wang, M. Wang, S. Peng, and B. Zhang, "Failure Analysis in Magnetic Tunnel Junction Nanopillar with Interfacial Perpendicular Magnetic Anisotropy," *Materials*, pp. 1–15, 2016. (Cited on page 75.)

[155] R. Macedo, J. Borme, R. Ferreira, S. Cardoso, P. P. Freitas, B. Mendis, and M. MacKenzie, "Nanofabrication of 30 nm Devices Incorporating Low Resistance Magnetic Tunnel Junctions," *Journal of Nanoscience and Nanotechnology*, vol. 10, no. 9, pp. 5951–5957, 2010. (Cited on page 75.)

[156] M. Tsoi, a. Jansen, J. Bass, W.-C. Chiang, M. Seck, V. Tsoi, and P. Wyder, "Excitation of a Magnetic Multilayer by an Electric Current," *Physical Review Letters*, vol. 80, no. 19, pp. 4281–4284, 1998. (Cited on pages 109 and 130.)

[157] E. B. Myers, "Current-Induced Switching of Domains in Magnetic Multilayer Devices," 1999. (Cited on page 109.)

[158] J. Katine, F. Albert, R. Buhrman, E. Myers, and D. Ralph, "Current-Driven Magnetization Reversal and Spin-Wave Excitations in Co /Cu /Co Pillars," *Physical Review Letters*, vol. 84, no. 14, pp. 3149–3152, 2000. (Cited on pages 109 and 163.)

[159] M. Tsoi, A. G. M. Jansen, J. Bass, W.-C. Chiang, V. Tsoi, and P. Wyder, "Generation and detection of phase-coherent current-driven magnons in magnetic multilayers," *Nature*, vol. 406, pp. 46–48, jul 2000. (Cited on pages 109 and 130.)

[160] J. Iwasaki, W. Koshibae, and N. Nagaosa, "Colossal spin transfer torque effect on skyrmion along the edge," *Nano Letters*, vol. 14, no. 8, pp. 4432–4437, 2014. (Cited on page 109.)

[161] A. R. Mellnik, J. S. Lee, A. Richardella, J. L. Grab, P. J. Mintun, M. H. Fischer, A. Vaezi, A. Manchon, E.-A. Kim, N. Samarth, and D. C. Ralph, "Spin-transfer torque generated by a topological insulator," *Nature*, vol. 511, no. 7510, pp. 449–451, 2014. (Cited on page 109.)

[162] S. Urazhdin, V. E. Demidov, H. Ulrichs, T. Kendziorczyk, T. Kuhn, J. Leuthold, G. Wilde, and S. O. Demokritov, "Nanomagnonic devices based on the spin-transfer torque.," *Nature nanotechnology*, vol. 9, no. 7, pp. 509–13, 2014. (Cited on page 109.)

[163] D. Bradley, "A new spin on magnetic control," *Materials Today*, vol. 14, no. 12, p. 580, 2011. (Cited on page 110.)

[164] S. S. P. Parkin, M. Hayashi, and L. Thomas, "Magnetic Domain-Wall Racetrack Memory," *Science*, vol. 320, no. April, pp. 190–195, 2008. (Cited on page 110.)

[165] S. Sani, J. Persson, S. M. Mohseni, Y. Pogoryelov, P. K. Muduli, A. Eklund, G. Malm, M. Käll, A. Dmitriev, and J. Åkerman, "Mutually synchronized bottom-up multi-nanocontact spin-torque oscillators.," *Nature communications*, vol. 4, p. 2731, 2013. (Cited on pages 110 and 130.)

[166] H. Kubota, A. Fukushima, K. Yakushiji, T. Nagahama, S. Yuasa, K. Ando, H. Maehara, Y. Nagamine, K. Tsunekawa, D. D. Djayaprawira, N. Watanabe, and Y. Suzuki, "Quantitative measurement of voltage dependence of spin-transfer torque in MgO-based magnetic tunnel junctions," *Nature Physics*, vol. 4, no. 1, pp. 37–41, 2008. (Cited on pages 110 and 129.)

[167] J. Ventura, J. P. Araujo, J. B. Sousa, R. Ferreira, and P. P. Freitas, "Competing spin-dependent conductance channels in underoxidized tunnel junctions," *Applied Physics Letters*, vol. 90, no. 3, pp. 3–5, 2007. (Cited on pages 111, 113, 124, and 125.)

[168] T. Devolder, L. Bianchini, J. V. Kim, P. Crozat, C. Chappert, S. Cornelissen, M. Op De Beeck, and L. Lagae, "Auto-oscillation and narrow spectral lines in spin-torque oscillators based on MgO magnetic tunnel junctions," *Journal of Applied Physics*, vol. 106, no. 10, 2009. (Cited on page 111.)

[169] C. Tiusan, M. Hehn, and K. Ounadjela, "Magnetic-roughness-induced magnetostatic interactions in magnetic tunnel junctions," *The European Physical Journal B*, vol. 26, pp. 431–434, apr 2002. (Cited on page 113.)

[170] B. D. Schrag, A. Anguelouch, S. Ingvarsson, G. Xiao, Y. Lu, P. L. Trouilloud, A. Gupta, R. a. Wanner, W. J. Gallagher, P. M. Rice, and S. S. P. Parkin, "Néel "orange-peel" coupling in magnetic tunneling junction devices," *Applied Physics Letters*, vol. 77, no. 15, p. 2373, 2000. (Cited on page 113.)

[171] L. Néel, "A new method of coupling the magnetization of two thin ferromagnetic films," *Academy of Sciences Paris*, vol. 255, p. 1676, 1962. (Cited on page 115.)

[172] S. Yuasa, T. Nagahama, A. Fukushima, Y. Suzuki, and K. Ando, "Giant room-temperature magnetoresistance in single-crystal Fe/MgO/Fe magnetic tunnel junctions.," *Nature materials*, vol. 3, pp. 868–71, dec 2004. (Cited on page 115.)

[173] C. Bowick, J. Blyler, and C. Ajluni, *RF circuit design*, vol. 53. Elsevier, 2008. (Cited on page 118.)

[174] M. J. Donahue and D. G. Porter, "OOMMF User's Guide version 1.0," 1999. (Cited on page 120.)

[175] I. N. Krivorotov, N. C. Emley, J. C. Sankey, S. I. Kiselev, D. C. Ralph, and R. a. Buhrman, "Time-domain measurements of nanomagnet dynamics driven by spin-transfer torques.," *Science*, vol. 307, no. 5707, pp. 228–231, 2005. (Cited on pages 129 and 149.)

[176] R. Okura, Y. Sakuraba, T. Seki, K. Izumi, M. Mizuguchi, and K. Takanashi, "High-power rf oscillation induced in half-metallic Co2MnSi layer by spin-transfer torque," *Applied Physics Letters*, vol. 99, no. 5, pp. 2013–2016, 2011. (Cited on page 129.)

[177] J. Sinha, M. Hayashi, Y. K. Takahashi, T. Taniguchi, M. Drapeko, S. Mitani, and K. Hono, "Large amplitude microwave emission and reduced nonlinear phase noise in Co2Fe(Ge0.5Ga0.5) Heusler alloy based pseudo spin valve nanopillars," *Applied Physics Letters*, vol. 99, no. 16, pp. 2013–2016, 2011. (Cited on page 129.)

[178] A. S. Jenkins, R. Lebrun, E. Grimaldi, S. Tsunegi, P. Bortolotti, H. Kubota, K. Yakushiji, A. Fukushima, G. de Loubens, O. Klein, S. Yuasa, and V. Cros, "Spin torque resonant vortex core expulsion for an efficient radio-frequency detection scheme," *Nature nanotechnology*, no. January, pp. 1–10, 2015. (Cited on pages 129, 139, and 140.)

[179] Y. Zhang, H. Zhao, A. Lyle, P. a. Crowell, and J.-P. Wang, "High power and low critical current spin torque oscillation from a magnetic tunnel junction with a built-in hard axis polarizer," *Applied Physics Letters*, vol. 100, no. 3, p. 032405, 2012. (Cited on page 129.)

[180] G. Finocchio, O. Ozatay, L. Torres, R. Buhrman, D. Ralph, and B. Azzerboni, "Spin-torque-induced rotational dynamics of a magnetic vortex dipole," *Physical Review B*, vol. 78, p. 174408, nov 2008. (Cited on page 130.)

[181] A. V. Silva, *Towards sub-100nm Magnetoresistive Devices: From Simulations to Applications*. PhD thesis, Instituo Superior Técnico, 2016. (Cited on pages 130 and 131.)

[182] K. Y. Guslienko, B. A. Ivanov, V. Novosad, Y. Otani, H. Shima, and K. Fukamichi, "Eigenfrequencies of vortex state excitations in magnetic submicron-size disks," *Journal of Applied Physics*, vol. 91, no. 10 I, pp. 8037–8039, 2002. (Cited on page 139.)

[183] Y. Gaididei, V. P. Kravchuk, and D. D. Sheka, "Magnetic vortex dynamics induced by an electrical current," *International Journal of Quantum Chemistry*, vol. 110, no. 1, pp. 83–97, 2010. (Cited on page 139.)

[184] A. V. Khvalkovskiy, J. Grollier, A. Dussaux, K. A. Zvezdin, and V. Cros, "Vortex oscillations induced by spin-polarized current in a magnetic nanopillar: Analytical versus micromagnetic calculations," *Physical Review B*, vol. 80, no. 14, pp. 10–13, 2009. (Cited on page 139.)

[185] M. Kammerer, M. Weigand, M. Curcic, M. Noske, M. Sproll, A. Vansteenkiste, B. Van Waeyenberge, H. Stoll, G. Woltersdorf, C. H. Back, and G. Schuetz, "Magnetic vortex core reversal by excitation of spin waves.," *Nature communications*, vol. 2, p. 279, 2011. (Cited on page 140.)

[186] A. V. Khvalkovskiy, J. Grollier, N. Locatelli, Y. V. Gorbunov, K. A. Zvezdin, and V. Cros, "Nonuniformity of a planar polarizer for spin-transfer-induced vortex oscillations at zero field," *Applied Physics Letters*, vol. 96, no. 21, pp. 9–12, 2010. (Cited on page 140.)

[187] N. Locatelli, V. V. Naletov, J. Grollier, G. De Loubens, V. Cros, C. Deranlot, C. Ulysse, G. Faini, O. Klein, and A. Fert, "Dynamics of two coupled vortices in a spin valve nanopillar excited by spin transfer torque," *Applied Physics Letters*, vol. 98, no. 6, pp. 2012–2015, 2011. (Cited on page 140.)

[188] N. Locatelli, A. Hamadeh, F. Abreu Araujo, A. D. Belanovsky, P. N. Skirdkov, R. Lebrun, V. V. Naletov, K. A. Zvezdin, M. Muñoz, J. Grollier, O. Klein, V. Cros, and G. de Loubens, "Efficient Synchronization of Dipolarly Coupled Vortex-Based Spin Transfer Nano-Oscillators," *Scientific Reports*, vol. 5, p. 17039, 2015. (Cited on page 140.)

[189] L. Berger, "Emission of spin waves by a magnetic multilayer traversed by a current," *Physical Review B*, vol. 54, pp. 9353–9358, oct 1996. (Cited on page 149.)

[190] D. Ralph and M. Stiles, "Spin transfer torques," *Journal of Magnetism and Magnetic Materials*, vol. 320, pp. 1190–1216, dec 2007. (Cited on page 150.)

[191] Z. Li and S. Zhang, "Magnetization dynamics with a spin-transfer torque," *Physical Review B*, vol. 68, no. 2, p. 024404, 2003. (Cited on page 150.)

[192] A. Slavin and V. Tiberkevich, "Current-induced bistability and dynamic range of microwave generation in magnetic nanostructures," *Physical Review B*, vol. 72, no. 9, p. 094428, 2005. (Cited on page 150.)

[193] E. Monteblanco, D. Gusakova, J. F. Sierra, and U. Ebels, "Redshift and Blueshift Regimes in Spin-Transfer-Torque Nano-Oscillator Based on Synthetic Antiferromagnetic Layer," *IEEE transactions on Magnetics*, vol. 4, p. 3500204, 2013. (Cited on pages 150 and 163.)

[194] U. Ebels, D. Houssameddine, I. Firastrau, D. Gusakova, C. Thirion, and B. Dieny, "Macrospin description of the perpendicular polarizer-planar free-layer spin-torque oscillator," *Physical Review B*, vol. 78, p. 024436, 2008. (Cited on pages 151, 163, and 165.)

[195] J. Toussaint, "Modeling of the perpendicular polarizer-planar free layer spin torque oscillator: Micromagnetic simulations," *Physical Review B*, vol. 78, p. 024437, 2008. (Cited on pages 151 and 163.)

[196] P. F. Carcia, "Perpendicular magnetic anisotropy in Pd/Co and Pt/Co thin-film layered structures," *Journal of Applied Physics*, vol. 63, no. 10, pp. 5066–5073, 1988. (Cited on page 151.)

[197] M. Isasa, E. Villamor, L. E. Hueso, M. Gradhand, and F. Casanova, "Temperature dependence of spin diffusion length and spin Hall angle in Au and Pt," *Physical Review B*, vol. 91, no. 2, p. 024402, 2015. (Cited on page 152.)

[198] A. Azevedo, L. H. Vilela-Leão, R. L. Rodríguez-Suárez, a. F. Lacerda Santos, and S. M. Rezende, "Spin pumping and anisotropic magnetoresistance voltages in magnetic bilayers: Theory and experiment," *Physical Review B*, vol. 83, no. 14, p. 144402, 2011. (Cited on page 152.)

[199] W. Zhang, V. Vlaminck, J. E. Pearson, R. Divan, S. D. Bader, and A. Hoffmann, "Determination of the Pt spin diffusion length by spin-pumping and spin Hall effect," *Applied Physics Letters*, vol. 103, no. 2013, pp. 2–6, 2013. (Cited on page 152.)

[200] M. Obstbaum, M. Härtinger, H. G. Bauer, T. Meier, F. Swientek, C. H. Back, and G. Woltersdorf, "Inverse spin Hall effect in Ni81Fe19 normal-metal bilayers," *Physical Review B*, vol. 89, no. 6, p. 060407, 2014. (Cited on page 152.)

[201] J.-C. Rojas-Sánchez, N. Reyren, P. Laczkowski, W. Savero, J.-P. Attané, C. Deranlot, M. Jamet, J.-M. George, L. Vila, and H. Jaffrès, "Spin Pumping and Inverse Spin Hall Effect in Platinum: The Essential Role of Spin-Memory Loss at Metallic Interfaces," *Physical Review Letters*, vol. 112, no. 10, p. 106602, 2014. (Cited on page 152.)

[202] J. Bass and W. P. Pratt Jr., "Spin-diffusion lengths in metals and alloys, and spin-flipping at metal/metal interfaces: an experimentalist's critical review," *Journal of Physics: Condensed Matter*, vol. 19, no. 18, p. 183201, 2007. (Cited on page 152.)

[203] F. J. Albert, N. C. Emley, E. B. Myers, D. C. Ralph, and R. A. Buhrman, "Quantitative study of magnetization reversal by spin-polarized current in magnetic multilayer nanopillars.," *Physical Review Letters*, vol. 89, no. 22, p. 226802, 2002. (Cited on page 152.)

[204] T. Kimura, J. Hamrle, and Y. Otani, "Estimation of spin-diffusion length from the magnitude of spin-current absorption: Multiterminal ferromagnetic/nonferromagnetic hybrid structures," *Physical Review B*, vol. 72, pp. 1–6, 2005. (Cited on page 152.)

[205] L. Liu, R. A. Buhrman, and D. C. Ralph, "Review and Analysis of Measurements of the Spin Hall Effect in Platinum," *arXiv:1111.3702*, 2011. (Cited on page 156.)

[206] M. Morota, Y. Niimi, K. Ohnishi, D. H. Wei, T. Tanaka, H. Kontani, T. Kimura, and Y. Otani, "Indication of intrinsic spin Hall effect in 4d and 5d transition metals," *Physical Review B*, vol. 83, no. 17, p. 174405, 2011. (Cited on page 156.)

[207] M. D. Stiles and J. Miltat, "Spin-transfer torque and dynamics," *Topics in Applied Physics*, vol. 101, pp. 225–308, 2006. (Cited on page 163.)

[208] I. Žutić and S. Das Sarma, "Spintronics: Fundamentals and applications," *Reviews of Modern Physics*, vol. 76, pp. 323–410, apr 2004. (Cited on page 168.)

[209] T. Jungwirth, X. Marti, P. Wadley, and J. Wunderlich, "Antiferromagnetic spintronics," *Nature nanotechnology*, vol. 11, no. 3, pp. 231–241, 2016. (Cited on page 168.)

[210] P. Wadley, B. Howells, J. Elezny, C. Andrews, V. Hills, R. P. Campion, V. Novak, K. Olejnik, F. Maccherozzi, S. S. Dhesi, S. Y. Martin, T. Wagner, J. Wunderlich, F. Freimuth, Y. Mokrousov, J. Kune, J. S. Chauhan, M. J. Grzybowski, A. W. Rushforth, K. W. Edmonds, B. L. Gallagher, and T. Jungwirth, "Electrical switching of an antiferromagnet," *Science*, vol. 351, no. 6273, pp. 587–590, 2016. (Cited on page 168.)

[211] R. Cheng, D. Xiao, and A. Brataas, "Terahertz Antiferromagnetic Spin Hall Nano-Oscillator," *Physical Review Letters*, vol. 116, p. 207603, 2016. (Cited on page 168.)

[212] A. Kirilyuk, A. Kimel, and T. Rasing, "Ultrafast optical manipulation of magnetic order," *Reviews of Modern Physics*, vol. 82, pp. 2731–2784, sep 2010. (Cited on page 168.)

[213] E. Beaurepaire, J.-C. Merle, A. Daunois, and J.-Y. Bigot, "Ultrafast Spin Dynamics in Ferromagnetic Nickel," *Physical Review Letters*, vol. 76, pp. 4250–4253, may 1996. (Cited on page 168.)

[214] A. Kimel, A. Kirilyuk, P. a. Usachev, R. V. Pisarev, a. M. Balbashov, and T. Rasing, "Ultrafast non-thermal control of magnetization by instantaneous photomagnetic pulses.," *Nature*, vol. 435, pp. 655–7, jun 2005. (Cited on page 168.)

[215] C. Stanciu, F. Hansteen, a. Kimel, a. Kirilyuk, a. Tsukamoto, a. Itoh, and T. Rasing, "All-Optical Magnetic Recording with Circularly Polarized Light," *Physical Review Letters*, vol. 99, pp. 1–4, jul 2007. (Cited on page 168.)

[216] R. Ulbricht, E. Hendry, J. Shan, T. F. Heinz, and M. Bonn, "Carrier dynamics in semiconductors studied with time-resolved terahertz spectroscopy," *Reviews of Modern Physics*, vol. 83, no. 2, pp. 543–586, 2011. (Cited on page 168.)

[217] M. A. Ordal, R. J. Bell, R. W. Alexander, L. L. Long, and M. R. Querry, "Optical properties of fourteen metals in the infrared and far infrared: Al, Co, Cu, Au, Fe, Pb, Mo, Ni, Pd, Pt, Ag, Ti, V, and W.," *Appl. Opt.*, vol. 24, pp. 4493–4499, dec 1985. (Cited on page 168.)

[218] M. Beard, G. Turner, and C. Schmuttenmaer, "Transient photoconductivity in GaAs as measured by time-resolved terahertz spectroscopy," *Physical Review B*, vol. 62, pp. 15764–15777, dec 2000. (Cited on page 168.)

[219] E. Hendry, F. Wang, J. Shan, T. Heinz, and M. Bonn, "Electron transport in TiO2 probed by THz time-domain spectroscopy," *Physical Review B*, vol. 69, p. 081101, feb 2004. (Cited on page 168.)

[220] E. Hendry, M. Koeberg, J. Pijpers, and M. Bonn, "Reduction of carrier mobility in semiconductors caused by charge-charge interactions," *Physical Review B*, vol. 75, p. 233202, jun 2007. (Cited on page 168.)

[221] S. W. Koch, M. Kira, G. Khitrova, and H. M. Gibbs, "Semiconductor excitons in new light," *Nature materials*, vol. 5, pp. 523–531, jul 2006. (Cited on page 168.)

[222] M. Van Exter and D. Grischkowsky, "Carrier dynamics of electrons and holes in moderately doped silicon," *Physical Review B*, vol. 41, no. 17, pp. 12140–12149, 1990. (Cited on page 168.)

[223] T. I. Jeon and D. Grischkowsky, "Characterization of optically dense, doped semiconductors by reflection THz time domain spectroscopy," *Applied Physics Letters*, vol. 72, no. 23, pp. 3032–3034, 1998. (Cited on page 168.)

[224] E. Beaurepaire, G. M. Turner, S. M. Harrel, M. C. Beard, J.-Y. Bigot, and C. a. Schmuttenmaer, "Coherent terahertz emission from ferromagnetic films excited by femtosecond laser pulses," *Applied Physics Letters*, vol. 84, no. 18, p. 3465, 2004. (Cited on pages 168 and 179.)

[225] J. Shen, X. Fan, Z. Chen, M. F. DeCamp, H. Zhang, and J. Q. Xiao, "Damping modulated terahertz emission of ferromagnetic films excited by ultrafast laser pulses," *Applied Physics Letters*, vol. 101, no. 7, p. 072401, 2012. (Cited on page 168.)

[226] R. Mikhaylovskiy, E. Hendry, F. Ogrin, and V. Kruglyak, "Low-temperature time-domain terahertz spectroscopy of terbium gallium garnet crystals," *Physical Review B*, vol. 87, p. 094414, mar 2013. (Cited on page 168.)

[227] K. Mori, T. Satoh, R. Iida, T. Shimura, and K. Kuroda, "Terahertz Time-Domain Spectroscopy of Antiferromagnetic Resonance in Orthoferrite," in *Proceedings of the International Quantum Electronics Conference and Conference on Lasers and Electro-Optics Pacific Rim 2011*, p. C567, Optical Society of America, 2011. (Cited on page 168.)

[228] K. Yamaguchi, T. Kurihara, Y. Minami, M. Nakajima, and T. Suemoto, "Terahertz time-domain observation of spin reorientation in orthoferrite ErFeO3 through magnetic free induction decay," *Physical Review Letters*, vol. 110, no. 13, pp. 1–5, 2013. (Cited on page 168.)

[229] T. Kampfrath, M. Battiato, P. Maldonado, G. Eilers, J. Nötzold, S. Mährlein, V. Zbarsky, F. Freimuth, Y. Mokrousov, S. Blügel, M. Wolf, I. Radu, P. M. Oppeneer, and M. Münzenberg, "Terahertz spin current pulses controlled by magnetic heterostructures.," *Nature nanotechnology*, vol. 8, pp. 256–60, apr 2013. (Cited on page 168.)

[230] T. J. Huisman, R. V. Mikhaylovskiy, J. D. Costa, F. Freimuth, E. Paz, J. Ventura, P. P. Freitas, S. Blügel, Y. Mokrousov, T. Rasing, and a. V. Kimel, "Femtosecond control of electric currents in metallic ferromagnetic heterostructures," *Nature nanotechnology*, no. February, pp. 2–6, 2016. (Cited on pages 168 and 186.)

[231] J. Kono, "Spintronics: Coherent terahertz control," *Nature Photonics*, vol. 5, pp. 5–6, jan 2011. (Cited on page 168.)

[232] Z. Jin, A. Tkach, F. Casper, V. Spetter, H. Grimm, A. Thomas, T. Kampfrath, M. Bonn, M. Kläui, and D. Turchinovich, "Accessing the fundamentals of magnetotransport in metals with terahertz probes," *Nature Physics*, no. July, 2015. (Cited on pages 168, 169, 181, and 185.)

[233] J. Ventura, a. M. Pereira, J. P. Araujo, J. B. Sousa, Z. Zhang, Y. Liu, and P. P. Freitas, "Three-state memory combining resistive and magnetic switching using tunnel junctions," *Journal of Physics D: Applied Physics*, vol. 40, no. 19, pp. 5819–5823, 2007. (Cited on page 169.)

[234] J. B. Sousa, J. A. M. Santos, R. F. A. Silva, J. M. Teixeira, J. Ventura, J. P. Araújo, P. P. Freitas, S. Cardoso, Y. G. Pogorelov, G. N. Kakazei, and E. Snoeck, "Peculiar magnetic and electrical properties near structural percolation in metal-insulator granular layers," *Journal of Applied Physics*, vol. 96, no. 7, pp. 3861–3864, 2004. (Cited on pages 169, 171, 175, and 177.)

[235] W. Kleemann, O. Petracic, C. Binek, G. N. Kakazei, Y. G. Pogorelov, J. B. Sousa, S. Cardoso, and P. P. Freitas, "Interacting ferromagnetic nanoparticles in discontinuous Co80Fe20 / Al2O3 multilayers: From superspin glass to reentrant superferromagnetism," *Physical Review B*, vol. 63, no. 13, p. 134423, 2001. (Cited on page 169.)

[236] G. Kakazei, P. Freitas, S. Cardoso, A. Lopes, M. P. de Azevedo, Y. Pogorelov, and J. Sousa, "Transport properties of discontinuous Co80Fe20/Al2O3 multilayers, prepared by ion beam sputtering," *IEEE Transactions on Magnetics*, vol. 35, pp. 2895–2897, 1999. (Cited on page 169.)

[237] T. Oakberg, "Magneto-optic Kerr effect," *HINDS Instruments*, pp. 1–6, 2005. (Cited on page 170.)

[238] K. Reimann, "Table-top sources of ultrashort THz pulses," *Reports on Progress in Physics*, vol. 70, no. 10, pp. 1597–1632, 2007. (Cited on page 173.)

[239] R. Medapalli, I. Razdolski, M. Savoini, A. R. Khorsand, A. Kirilyuk, A. V. Kimel, T. Rasing, A. M. Kalashnikova, A. Tsukamoto, and A. Itoh, "Efficiency of ultrafast laser-induced demagnetization in Gd xFe 100-x-yCo y alloys," *Physical Review B*, vol. 86, no. 5, pp. 1–7, 2012. (Cited on pages 174 and 180.)

[240] J. K. Chen and J. E. Beraun, "Numarical study of ultrashort laser pulse interactions with metal films," *Numerical Heat Transfer, Part A: Applications*, vol. 40, no. 1, pp. 1–20, 2001. (Cited on page 176.)

[241] K. O. B. Hillebrands, *Spin Dynamics in Confined Magnetic Structures I*. 2002. (Cited on page 176.)

[242] A. Ellens, H. Andres, A. Meijerink, and G. Blasse, "Spectral-line-broadening study of the trivalent lanthanide-ion series.I. Line broadening as a probe of the electron-phonon coupling strength," *Physical Review B*, vol. 55, no. 1, pp. 173–179, 1997. (Cited on page 176.)

[243] J. M. Ziman, *Electrons and Phonons, the Theory of Transport Phenomena in Solids*. Oxford University Press, 1960. (Cited on page 176.)

[244] R. F. C. Marques, P. R. Abernethy, J. A. D. Matthew, C. O. Paiva-Santos, L. Perazolli, M. Jafelicci, and S. M. Thompson, "Contactless measurement of colossal magnetoresistance in la 1-xSrxMnO3 using the infrared magnetorefractive effect," *Journal of Magnetism and Magnetic Materials*, vol. 272-276, no. III, pp. 1740–1741, 2004. (Cited on page 177.)

[245] A. B. Granovsky, I. V. Bykov, E. A. Gan'shina, V. S. Gushchin, M. Inoue, Y. E. Kalinin, A. A. Kozlov, and A. N. Yurasov, "Magnetorefractive effect in magnetic nanocomposites," *Journal of Experimental and Theoretical Physics*, vol. 96, no. 6, pp. 1104–1112, 2003. (Cited on page 177.)

[246] R. T. Mennicke, D. Bozec, V. G. Kravets, M. Vopsaroiu, J. A. D. Matthew, and S. M. Thompson, "Modelling the magnetorefractive effect in giant magnetoresistive granular and layered materials," *Journal of Magnetism and Magnetic Materials*, vol. 303, no. 1, pp. 92–110, 2006. (Cited on page 177.)

[247] S. Uran, M. Grimsditch, E. E. Fullerton, and S. D. Bader, "Infrared spectra of giant magnetoresistance Fe / Cr / Fe trilayers," *Physical Review B*, vol. 57, no. 5, pp. 2705–2708, 2000. (Cited on page 177.)

[248] R. Shimano, Y. Ino, Y. P. Svirko, and M. Kuwata-Gonokami, "Terahertz frequency Hall measurement by magneto-optical Kerr spectroscopy in InAs," *Applied Physics Letters*, vol. 81, no. 2, pp. 199–201, 2002. (Cited on page 177.)

[249] K. J. Chau and A. Y. Elezzabi, "Photonic anisotropic magnetoresistance in dense Co particle ensembles," *Physical Review Letters*, vol. 96, no. 3, pp. 2–5, 2006. (Cited on page 177.)

[250] C. J. E. Straatsma, M. Johnson, and A. Y. Elezzabi, "Terahertz spinplasmonics in random ensembles of Ni and Co microparticles," *Journal of Applied Physics*, vol. 112, no. 10, 2012. (Cited on page 177.)

[251] D. J. Hilton, R. D. Averitt, C. a. Meserole, G. L. Fisher, D. J. Funk, J. D. Thompson, and a. J. Taylor, "Terahertz emission via ultrashort-pulse excitation of magnetic metal films.," *Optics letters*, vol. 29, no. 15, pp. 1805–1807, 2004. (Cited on page 179.)

[252] J. M. Teixeira, R. Lusche, J. Ventura, R. Fermento, F. Carpinteiro, J. P. Araujo, J. B. Sousa, S. Cardoso, and P. P. Freitas, "Versatile, high sensitivity, and automatized angular dependent vectorial Kerr magnetometer for the analysis of nanostructured materials.," *The Review of scientific instruments*, vol. 82, p. 043902, apr 2011. (Cited on page 179.)

[253] A. V. Kimel, A. Kirilyuk, and T. Rasing, "Femtosecond opto-magnetism: ultrafast laser manipulation of magnetic materials," *Laser & Photonics Reviews*, vol. 1, no. 3, pp. 275–287, 2007. (Cited on page 180.)

[254] T. J. Huisman, R. V. Mikhaylovskiy, A. Tsukamoto, T. Rasing, and A. V. Kimel, "Simultaneous measurements of terahertz emission and magneto-optical Kerr effect for resolving ultrafast laser-induced demagnetization dynamics," *Physical Review B*, vol. 92, no. 10, pp. 1–8, 2015. (Cited on page 180.)

[255] M. Romera, P. Talatchian, R. Lebrun, K. J. Merazzo, P. Bortolotti, L. Vila, J. D. Costa, R. Ferreira, P. P. Freitas, M. Cyrille, U. Ebels, V. Cros, and J. Grollier, "Enhancing the injection locking range of spin torque oscillators through mutual coupling," *Applied Physics Letters*, vol. 109, no. 252404, 2016. (Cited on page 184.)